AQUEOUS DEPOSITION OF GOLD NANOFILM FOR SOLAR CONTROL

By

Xiaoda Xu

A THESIS SUBMITTED FOR THE REQUIREMENTS FOR

THE DEGREE OF

DOCTOR OF PHILOSOPHY

FACULTY OF SCIENCE
UNIVERSITY OF TECHNOLOGY, SYDNEY
AUSTRALIA

2006

CERTIFICATE OF ORIGINALITY

I certify that the work in this thesis has not previously been submitted for a degree, nor has it been submitted as part of the requirements for a degree, except as fully acknowledged within the text.

I also certify that the thesis has been written by me. Any help that I have received in this research work and the preparation of the thesis itself has been fully acknowledged. In addition, I certify that all information sources and literature used are indicated in this thesis.

Xiaoda Xu

5/08/2015

ACKNOWLEDGEMENTS

I must first thank Professor Mike Cortie, my supervisor, who has helped me in many and various ways. He has not only contributed his ideas and initiatives but has also supported me at every stage of this project. I should say that this thesis is also the fruit of his dedication: from idea to design; from experiment to discussion; from result to format. His guidance has greatly improved the quality of this research.

I also thank Dr Mike Stevens, my co-supervisor, for his time and effort. He read the first draft of this thesis and made critical comments. Other academics, Associate Professor Mike Ford, Professor Geoff Smith and Dr Abbas Maaroof, also provided useful suggestions and comments for this research.

I am grateful also to all the other staff who helped me, especially Dr Richard Wuhrer in SEM imaging, Geoff McCredie in XPS and optical properties characterisation, Dr Ronald Shimmon in chemical synthesis, and Jean-Pierre Guerbois in thermal analysis. My fellow students and friends Donald Maclurcan, Dr Benjamin SouleDeBas, Rainer Hoft, Dakrong Pissuwan and Burak Cankurtaran helped me in different ways, either with brainstorm discussions or in experiments. I would like to thank them all for their help. Thanks also to Hysitron Incorporation, which provided an analysis of certain properties.

A three-year doctoral candidature is a long time. My family members also supported my study physically and psychologically. My parents and Alice and Mark Sawyer, as well as my son Bowen, sustained my efforts all the time. Without their support, it would have been impossible for me to focus on the research.

Finally, I wish to thank the University of Technology Sydney, the Australian Research Council and Anglogold Ashanti Australia for their financial support of this project.

PREFACE

Part of this thesis have been published in the following journals and peer-reviewed conference proceedings:

[1] X. Xu, T. H. Gibbons and M. B. Cortie, *Spectrally-selective gold nanorod coatings for window glass.* Gold Bulletin, 2006. **in press**.

[2] X. Xu and M. Cortie, *Shape change and color gamut in gold nanorods, dumbbells, and dog bones.* Advanced Functional Materials, 2006. **in press**.

[3] M. Cortie, X. Xu and M. Ford, *Effect of composition and packing configuration on the dichroic optical properties of coinage metal nanorods.* Physical Chemistry Chemical Physics, 2006. **8**: 3520

[4] X. Xu, M. B. Cortie and M. Stevens, *Effect of glass pre-treatment on the nucleation of semi-transparent gold coatings.* Materials Chemistry and Physics, 2005. **94**: 266.

[5] K. E. Peceros, X. Xu, S. R. Bulcock and M. B. Cortie, *Dipole-dipole plasmon interactions in gold-on-polystyrene composites.* Journal of Physical Chemistry B, 2005. **109**: 21516

[6] M. Cortie, X. Xu, H. Zareie, H. Chowdhury and G. Smith. *Plasmonic heating of gold nanoparticles and its exploitation*. Smart Materials, Nano-, and Micro-Smart Systems II. 2005. Sydney, Australia.

[7] H. Chowdhury, X. Xu, P. Huynh and M.B. Cortie, *Radiative heat transfer across glass coated with gold nanoparticle.* ASME Journal of solar energy engineering, 2005. **127**: 70.

[8] X. Xu, M. Stevens and M. B. Cortie, *In situ precipitation of gold nanoparticles onto glass for potential architectural applications.* Chemistry of Materials, 2004. **16**: 2259.

ABSTRACT

In this study, I have demonstrated two ways to deposit nanoscale gold coatings on glass for solar control purposes. Coatings produced by *in situ* deposition showed a variation in colour from red, to purple to blue in transmission, caused by the surface plasmons of isolated particles and the inter-particle interaction of gold nanospheres. The absorption peak was in the upper visible and near-infrared. The colour and transmission spectrum of these coatings were controlled by nucleation, growth and aggregation of the gold nanospheres. The optical spectrum was simulated by Discrete Dipole Analysis (DDA), which revealed that the absorption peaks were strongly influenced by the ratio of particle size to interparticle spacing. The mechanical properties of these gold nanoparticle coatings were also investigated by nanoindentation. This indicated the film of gold nanoparticles showed similar mechanical properties to those of bulk gold.

The seed-mediated method for synthesis of gold nanorods was also investigated. It was found that the pH, Ag^+, surfactant and seed solution play important roles in controlling the aspect ratio. Ag^+ is strongly absorbed by the gold nanorods. Ag/Au in as-prepared rods changed only slightly from 1:1.78 to 1:1.35, while the ratio in solution changed greatly from 1:10 to 1:2.5. A double-layer micellar structure in the surfactant solution was proposed as the explanation for the synthesis of gold nanorods by the seed-mediated method. The transmission spectra of different shapes of gold nanorods were also simulated by the DDA method, while the gamut of colours of gold nanorods during growth was mapped onto the CIE-LAB colour space. Self-assembled coatings of gold nanorods provided better spectral selectivity between infrared and visible region than was possible with spheres. Numerical simulations confirmed this, and showed that a mixture of nanorods of varying aspect ratio could achieve better spectral selectivity with a low gold loading. However, the further development of gold nanorod coatings requires the availability of an effective method to produce long rods.

TABLE OF CONTENTS

LIST OF FIGURES

LIST OF TABLES

1. Introduction

Ordinary window glass of 4 mm thickness transmits about 90% of incident-visible and near-infrared light [1]. Solar radiation, as received on Earth [2], is a continuous spectrum ranging from ultraviolet to near infrared (Figure 1-1). Only a small portion of the spectrum is visible (380 nm ~ 740 nm). This indicates that a considerable amount of energy can be transmitted into a building interior through windows from sunlight without being sensed by human eyes. For example, at 32° latitude an unshaded east-or west-facing window can receive up 700 W/m^2 of solar energy during daylight hours [1]. This can cause a heat load of tens of kilowatts into a residence or office space. This energy, while welcome in winter, is generally not desired in summer. Efforts to remove it by air-conditioning contribute significantly to national energy consumption, and hence greenhouse gas emissions, in many warmer regions of the developed world [3, 4].

A possible solution is to modify windows so that they attenuate incoming solar radiation [5]. There are different solutions available to attenuate the transferring of solar heat to buildings, from relatively cheap tinted films to expensive low-emissivity (low-e) coatings [1]. Technically, both infrared absorbing and reflection coatings could be utilised for this purpose. “Pyrolytic” coatings are examples of infrared reflecting coatings. Tin and/or indium oxide coatings on glass are applied to plate glass substrates at approximately 600°C. The transparent oxide is formed *in situ* by pyrolysis. The oxides provide strong infrared blocking capability [1] by reflecting a proportion of the infrared (IR) radiation while transmitting most of the visible light. Pyrolytic coatings are durable, however, the disadvantage of the process is the requirement that they can only be manufactured in a glass production line. Thin metallic films are another example of infrared reflective coatings, with deposition of continuous thin films of Au, Ag etc. by the sputtering process. The coatings reflect part of the infrared while permitting transparency of the coatings in the visible region [1, 6]. In this case, the glass is at ambient temperature during the process. The advantage of the method is that it is flexible and the coatings have a high efficiency of spectral selectivity. These films are usually sandwiched between layers of transparent dielectrics of high refractive index, such as ZnO, Nb_2O_5, Bi_2O_3, or TiO_2 [6, 7] and/or a special frame has to be designed to protect the vulnerable film from erosion and oxidation. Since 1980, industrial-scale production of large areas of such coated glasses, using magnetron sputtering, has been growing steadily [7]. Unfortunately, the high cost of applying these coatings (for example, ~\$10 per m^2) and complex installation requirements inhibit the enlargement of market share, even though the actual cost of the raw materials used, about \$1 or less per m^2, is hardly significant.

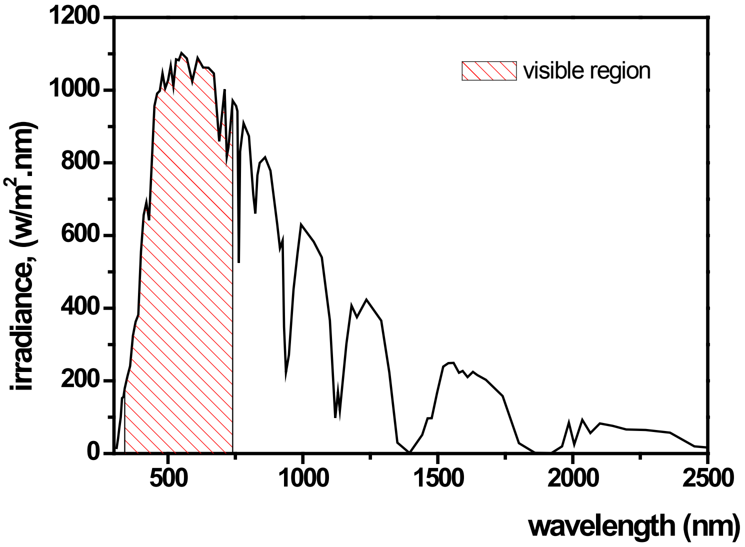

Figure 1-1 Direct normal solar spectral irradiance at air mass 1.5 for a 37^o tilted surface

(Redrawn from [2].)

FeO_x or LaB_6 nanoparticle-based coatings are examples of strong infrared-absorbing films [8]. The nanoparticles can be either dispersed in a glass matrix or into plastic thin films, which can be applied to glass substrate as required [8, 9]. The advantage of a plastic film is that it can be retro-fitted to a glass pane at any time. A significant drawback to IR-absorbing coatings is that roughly 50% of their absorbed energy passes into the interior environment. This deteriorates their infrared-shielding efficiency [1].

The challenge for my research project is to develop new, gold-based solar screening coatings that can be applied at relatively low cost. However, it may be helpful at this point to justify the usage of gold as the main material for solar glazing coatings. First of all, gold is uniquely resistant to oxidation or corrosion, so coatings made from it will last a very long time. Secondly, gold just happens to have the right electronic properties to allow it to be used in spectrally-selective reflective and (as I will show) absorptive coatings. Its high value is not an insurmountable obstacle either. A layer of gold nanoparticles equivalent in volume to a continuous coating of 10 nm of Au (a useful thickness for solar glazing) would contain US$3.72 /m^2 of gold, calculated at US$600/troy ounce, which is at the top end of the band in which gold has traded over the last 50 years. This is much less than the total cost (capital plus operating) of vacuum-coating glass with any material. It is also less than 2% of the retail cost of retrofitted film-based schemes. Therefore, I believe that such a product would be viable in a competitive market. Additionally, the gold nanofilm gives a pleasant neutral blue tone (in transmission), which is acceptable in the community from the viewpoint of aesthetics.

Gold nanoparticles in colloidal suspension display an interesting red colour because they exhibit a plasmon resonance with light at a wavelength of around 520 nm. This phenomenon has been known for hundreds of years and has been much studied. This colour is not desirable for architectural applications. Fortunately, a particle-to-particle interaction in densely packed coatings develops a second plasmon resonance peak, starting from 650 nm and which moves into the near-infrared region as packing density increases. The colour of such colloids or coatings is blue to blue-grey, which is much more acceptable for architectural use. However, there appears to have been no previous study into exploiting gold nanoparticles for spectrally selective architectural coatings. Such interest as there has been in depositing gold nanoparticles onto glass has been targeted on developing photonic materials [10-12] or towards enhancing the Raman response of gold in order to provide a more sensitive analytical technique for organic molecules. However, I will show in this thesis that coatings based on gold nanoparticles can have reasonable IR-blocking capability. The wet chemical process to deposit such gold nanosphere coatings *in situ* on plate glass [13] provides a low-cost process, since it does not require any costly investments on vacuum equipment for physical vapour deposition (PVD) or chemical vapour deposition (CVD)[14, 15].

More complex gold nanoparticles, such as gold nanorods [16], nanoshells [17, 18] and “caps” [19] , also provide good potential for solar control purposes. These shapes of gold nanoparticles have both transverse and longitudinal plasmon resonance peaks, which may give them better spectral selectivity between the infrared and the visible region. I will show that gold nanorods may be especially useful for solar control applications. High yield mass production and a tunable aspect ratio make them an ideal material for this application.

In this study we will show how coatings of variously shaped gold nanoparticles on glass can serve for solar screening applications. Both *in situ* deposited gold nanosphere coatings and self-assembled gold nanorod coatings will be investigated. The thesis includes:

Chapter 2. Literature review, in which I describe past and current progress in electroless deposition of gold coatings on insulated surface, surface pre-treatment, post-treatment of gold coating, fabricating and properties of gold nanorods, and Immobilisation of gold nanorods on glass.

Chapter 3. Gold nanosphere coatings by wet chemical process for solar-glazing purposes, in which I address *in situ* deposition of coatings of hemispherical gold nanoparticles onto glass, the optical properties of coatings of gold nanoparticles, the colour imparted to the coating by surface plasmons, and the adhesion and mechanical properties of gold nanoparticles on glass.

Chapter 4. Nucleation of semi-transparent gold nanosphere coatings on glass, in which I explore the effect of pre-treatment on optical properties of gold nanoparticle coatings, simulation of the nucleation of gold spherical nanoparticles coating by classical nucleation theory, and the relation of the emissivity of gold nanocoating to infrared screening capability.

Chapter 5. Synthesis and mechanism of formation of gold nanorods, in which I describe the making of gold nanorods by the seed-mediated method, the control of optical properties of gold nanorods, the growth mechanism for the formation of gold nanorods and a simulation of the optical properties of the gold nanorods by Discrete Dipole Analysis (DDA).

Chapter 6. Spectrally selective coatings on windows by self-assembled gold nanorods, in which the production of coatings of gold nanorods on glass by self-assembly is described, as are the optical properties for both high-packing-density and low-packing-density coatings, the thermal stability of the coatings, and the evolution of the optical properties of these coatings.

2. Literature review

Solar heat penetrates window glass and causes an increase in the interior temperature. This is undesirable in tropical areas, and might require air-conditioning to control. The deposition of gold nanofilms as infrared reflective coatings on the glass is one of the choices for energy saving in hot climates. In this chapter, technology relating to the deposition of gold nanofilms on glass is reviewed. Current technologies for depositing gold nanofilms on glass substrates, synthesising gold nanorods, and assembling coatings of gold nanorods are discussed.

2.1 Gold nanosphere coatings on glass by aqueous deposition

Aqueous deposition of gold on substrates can be classified into electroplating and electroless plating [20]. Electroless deposition is more practical to achieve transparent gold thin films on glass, since the substrate is non-conductive, whereas conductive substrates are essential to galvanic deposition.

The electroless gold deposition is widely used in the microelectronic and decorative industry; most of its function is to obtain a layer of “flash gold” to obtain good conductivity for interconnections [21-23] or to obtain a decorative layer [24]. Former and current studies have focused on improving the deposition rate [25] and plating-bath stability [26, 27]. Furthermore, most recipes are for depositing “flash gold” on nickel, and may not function on insulating substrates such as glass. Until now, there has been little work relating to the infrared reflective, aqueous gold nanofilms on glass. The concept of an aqueous process to precipitate transparent gold coatings for architectural applications is not new, and dates from at least the patent of Miller in 1977 [28]. However, many of the early methods required the use of highly toxic chemicals such as cyanides and/or soluble salts of lead, mercury or cadmium. As a result, these processes in recent times have not been widely exploited. The optical properties of gold nanofilms and the mechanism of their formation have not so far been explored.

The typical electroless gold process on glass is illustrated in Figure 2-1 [26].

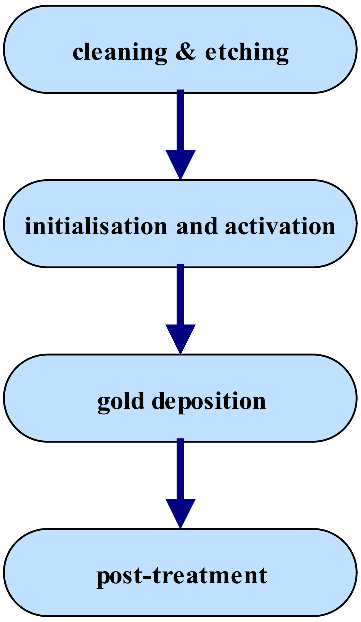

Figure 2-1 General procedure for gold deposition on glass

2.1.1 Cleaning and etching

Glass substrates have a high surface energy, therefore they are easily contaminated. Thus, the cleaning process is critical for the successful deposition of a uniform gold film on the glass.

The most popular processes include cleaning and etching by strong basic, for example NaOH, acidic oxidising solution (aqua regia, piranha solution, chromate solution), plumbite [29], hydrofluoric acid [30-32], solvent immersion [33], and controlled plasma etching [25, 34-37]. The impact of cleaning processes on the electroless gold deposition is still not clear, and its influence requires systematic investigations.

2.1.2 Initialisation and activation

The gold deposition is usually performed in an aqueous solution and can be initiated on the surface of most metals automatically. Unfortunately, glass is non-catalytic to gold deposition. However, the surfaces of such non-catalytic materials can be rendered catalytic by producing a film of particles of appropriate materials, which is a so-called sensitisation or initialisation procedure.

The well-established process for glass is to catalytically activate the substrate surface by stannous and/or palladium adsorption, that will subsequently initialise the metal deposition.

However, electroless gold has poor adhesion to the glass substrate, unlike the significant adhesion obtained from the electroless deposition of silver to glass. Some researchers suggest the use of an Sn/Ag treatment for the initialisation of the gold deposition on glass and to enhance adhesion [28, 38]. The typical treatment consisted of contacting the glass surface with $SnCl_2$ solution for 1–3 minutes, rinsing, and then immersing the glass in the silver solution to obtain an invisible "seed" layer of silver on the glass substrate [39].

The mechanism proposed for the silver treatment is as follows [20]:

The exchange reaction of the Sn^{2+} ion occurs on the surface of the glass according to Equations 2-1 to 2-3, then silver deposits onto the glass in the early stages of the plating reactions as shown in Equation 2-4:

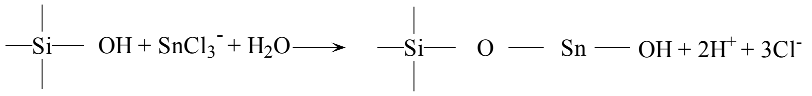

$$-Si-OH + SnCl_3^- + H_2O \longrightarrow -Si-O-Sn-OH + 2H^+ + 3Cl^-$$

(eq. 2-1)

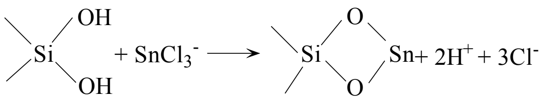

(eq. 2-2)

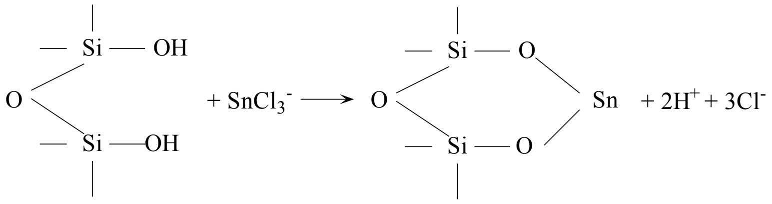

(eq. 2-3)

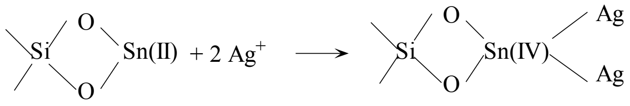

(eq. 2-4)

In this manner, the deposition of silver onto the glass surface is induced early in the reduction reaction. Also, the Ag is a catalyst for the gold reduction, and the reaction progresses thereafter.

An alternative method is to deposit an active interlayer, especially silane, on the glass before gold deposition [40]. The process is illustrated in Figure 2-2 and exploits the presence of a self-assembled monolayer (SAM). In the SAM process, the glass surface was functionalised by the attachment of a silane layer containing radicals of NH_2 or SH_2. With the silane as the interlayer between the gold particles and glass surface, a gold monolayer can be established on the glass surface. There are a number of research papers and patents on SAM-functionalised glass surfaces for gold deposition [41, 42]. It is believed that reactive groups such as $-NH_2$, $-SH_2$, in the silane attach to the gold nanoparticles to form a thin film on the glass surface. The attached gold nanoparticles on the interlayer can serve as "seed" and catalyst for further electroless deposition of gold film.

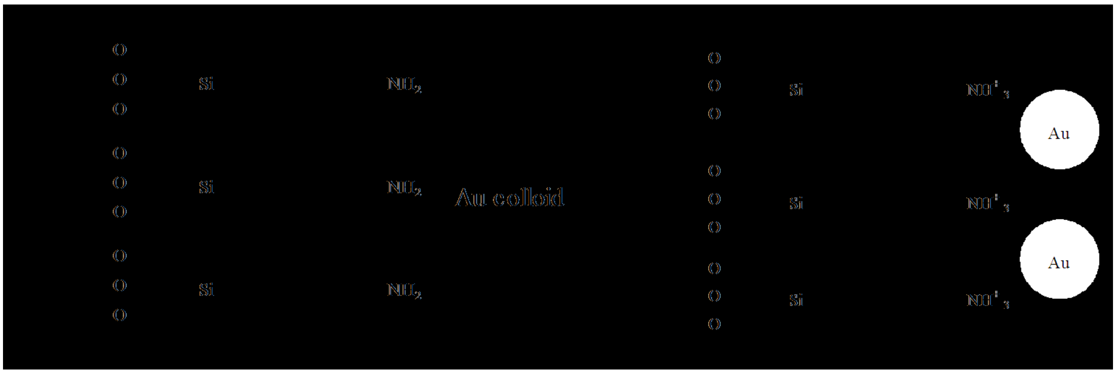

Figure 2-2 Schematic diagram of forming of Au seed layer on glass

(Redrawn from [42].)

2.1.3 Gold deposition

There are many recipes available for the gold aqueous deposition process [23, 43]. The ingredients in the solution include a soluble gold salt, reducing agent, a stabiliser to keep the bath solution from decomposing, a complexing agent to control the concentration of $Au(OH)_4^-$ in the bath, and surfactants to obtain better performance of the deposition process. According to the reaction mechanisms, there are three types of electroless gold, that is, a) galvanic displacement [44], b) autocatalytic deposition and c) substrate-catalysed process. Some of the processes [43] may include one or more mechanisms mentioned above. For the dielectric properties of the glass, only the last two types of reaction mechanism are possible, and their potential influence on the formation of gold nanofilms on the glass surface will be investigated during the study [45].

The control of the initial deposition process is necessary to subsequently obtain a 10 nm film. Unfortunately, there is little successful work on this aspect of film development. Recently, Matsubara *et al.* used a quartz crystal microbalance method to study the initial stage of electroless nickel deposition process. According to their *in situ* monitoring, the deposition rate would ramp up quickly at the first stage (around 50 nm) then slow down to a certain level later [46], which means the average deposition rate may not be applied to the initial stage of deposition. Some process parameters have a significant impact on the deposition rate, including ligands, additives, pH value, and reactant concentration. It is known that CN^- is a good stabiliser in the gold plating bath and significantly affects the deposit rate [20]. Unfortunately CN^- is highly toxic, and thus safety regulations must be strictly followed. The substitution of cyanide by a safer chemical to control the reaction is of vital importance for experimental work.

Electroless gold deposits with a high two-dimensional character along the gas/liquid interface have been reported [47, 48]. Their application to nanofilms needs further investigation.

2.1.4 Post-treatment

Levy, Davlin *et al*. [49, 50] found that both the adhesion and abrasion resistance of gold deposited on glass could be considerably improved by a heat treatment cycle. The typical test method applied is the tape adhesion test [51]. For sound adhesion, during the test, the gold film should not separate or lift from the glass when a pressure-sensitive adhesive tape is adhered to the film and pulled off at a controlled low rate. However, the standard Scotch-tape method has limited application for nanofilms, because the method is qualitative and hardly reveals the failure mechanism of the adhesion.

2.1.5 Characterisation of gold thin film

Field Emission Microscopy (FEM), Atomic Force Microscopy (AFM) [52], and image-analysis software have been applied to characterise the morphology of gold on glass; X-Ray Photoemission Spectrometer (XPS) and Energy Dispersive Spectroscopy (EDS) provide useful elemental information; X-Ray Diffraction (XRD) gives useful structural information. Near-field Optical Scanning Microscopy (NSOM) [53], UV-Vis and FT-IR spectroscopy determine optical properties [2, 54]. The papers of Warren and Miyake *et al.* provide good background reference material on the characterisation of gold thin films [55, 56].

In summary, although the process of electroless gold deposition has the advantage of being simple and cheap, the challenges include the incompatibility of chemical and mechanical properties between the substrate and coating, and the fact that the substrate is normally exceedingly smooth [36].

2.2 Gold nanorods in colloid

Gold nanospheres [57, 58] have been studied for many years, long before gold nanorods attracted attention for their effectiveness in tuning the electronic, magnetic, optical [59], optoelectronic [60], chemical-sensing [61] and catalytic properties [62] of gold nanoparticles. For example: the optical properties of gold nanorods in the application of chemical sensing and imaging is reviewed by Murphy [61]; the drastic reduction of plasmon damping in gold nanorods [63] is examined by Sonnichsen *et al.*. The surface plasmon resonance of gold nanorods is highly dependent on their aspect ratios [64, 65]. The sensitivity of Surface Enhanced Raman Scattering (SERS) is also related to the morphology of gold and silver nanoparticles [66, 67]. Techniques relating to the synthesis of mono-dispersed nanorods have been under intensive investigation. Synthesis of gold nanorods, such as rigid template synthesis, electrochemical methods, and surfactant mediation methods have been reported extensively during the last few years [61].

2.2.1 Seed-mediated synthesis method

The seed-surfactant-mediated method of Jana and Murphy is now the most popular method for producing gold nanorods [64, 68-71]. It is a relatively straightforward bench-top process with mass production potential. The disadvantage of the method is the size distribution and aspect ratio of the products [72]. It is difficult to control the process to obtain a mono-dispersed product. Much of the current work in the literature is focused on overcoming the need to separate coexisting spherical nanoparticles, controlling the size distribution, aspect ratio, and shape variations [72].

The current recipe remains quite similar since the original conception. It includes a) a gold source such as $AuCl_4^-$; b) a mild reducing agent for example ascorbic acid; c) a seed solution to initialise the reaction; d) a high concentration of surfactant or co-surfactant such as cetyl trimethyl ammonium bromide (CTAB); and e) other additives to improve yield and control the shape of the particles. However, the yield of gold nanorods from the original recipe was very low, so centrifugation was an essential step in order to separate the nanorods from the more abundant nanospheres [64, 72, 73]. All the above factors are critical for the production of gold nanorods. There are a number of different versions of the recipe based on this popular method [74]. Various aspect ratios of gold nanorods can now be synthesised.

(a) $AuCl_4^-$

$AuCl_4^-$ is the source of gold to form gold nanorods. It was also found that the aspect ratio of gold nanorods could be influenced by the concentration of $AuCl_4^-$. In addition, the aspect ratio of gold nanorods could be raised by increasing the gold content of the growth solution up to a limiting point, beyond which a further increase in the concentration of $AuCl^-_4$ resulted in a decrease in the length of the gold nanorods [72]. A similar trend was found when varying the silver ion content [72].

A related finding was published by Gou and Murphy, who used sub-stoichiometric quantities of ascorbic acid. They found that the rest of the gold ions in the solution could still be reduced by heating the original solution, without the need to introduce extra ascorbic acid. The longitudinal peak at around 840 nm was shifted to the blue side in their initial heating stage, and was diminished with longer times of heat treatment. The resulting shapes were called “dogbones”. This is in contradiction to the situation for the purified gold nanorods, in which there was no obvious shape change and spectral shift in such heat treatment [75].

According to their experiments, a surplus amount of $AuCl_4^-$ existed in the growth solution of gold nanorods, which might explain the change of morphologies of gold nanorods observed with a long aging time.

(b) Reducing agent

Ascorbic acid is the most frequently used reducing agent for preparing gold nanorods. Busbee *et al*. [74] reported an improved method to synthesise the high-aspect ratio of the nanorods. The addition of equimolar amounts of sodium hydroxide to the ascorbic acid used as a reductant increased its pH to 3.5 and resulted in a “dramatic increase” in the relative proportion of nanorods. The authors reported that only one round of purification centrifugation was required in order to produce gold nanorods with an aspect ratio of 19. It was also reported that a further increase in the pH to 5.6 resulted in nanorods with an aspect ratio of 25 but an increased polydispersity. Using CTAB as the directing molecule, gold nanorods with aspect ratios as high as 200 could be achieved. However, the authors reported that the yields were very low in this case [74]. It was thought that the abrupt change in the yield and shape of gold nanorods with the increase of pH from 2.8 to 3.5 was due to the first pKa of ascorbic acid. At pH 3.5, a significant increase in the fraction of ascorbate led to the higher aspect ratio of gold nanomaterials. They speculated that the ascorbate was a more effective reductant on the five-fold {111} end faces than on the other faces of the growing nanorod.

(c) Seed solution

Some investigators have studied the effect of different kinds of seeds on the growth of gold nanorods. The most commonly used seed is positively charged gold nanospheres reduced by a strong reducing agent such as $NaBH_4$ [76]. The published TEM images of seed particles show that they are less than 4 nm in diameter, whereas the diameter of nanorods is generally about 7 to 12 nm [72].

In addition, lower aspect ratio gold nanorods functioned as seeds (nuclei) for higher aspect ratio gold nanorods. Gold nanorods with aspect ratios as high as 18 could be produced in this way with cycles of centrifugation to separate the different shape [68].

It was found that citrate-reduced seed could also grow into rods. However, the yield was relatively low [77]. Gole and Murphy [78] studied the effect of seeds for large aspect ratio gold nanorods, using their well-known three-step synthesis recipe. Gold seeds of both negative and positive surface charge proved to produce gold nanorods of high aspect ratio. The length of the nanorods produced with the three-step procedure with different seeds ranged from 150 nm to 660 nm, with aspect ratios of 16 to 36. However, once again, citrate-stabilised seed tended to produce a poor yield of nanorods.

(d) Surfactant

CTAB is an essential surfactant to produce gold nanorods. The dependence of the aspect ratio of gold nanorods on the surfactant used was studied by Gao *et al.* [79]. The analogues of C_{16}TAB with different hydrocarbon chains were applied to the syntheses of the nanorods. It was found that the length of surfactant tail had a strong influence on the aspect ratio of gold nanorods. The longer surfactant hydrocarbon tails tended to produce higher aspect ratio gold nanorods within the range of the authors" investigation.

There is also a study using poly(vinyl pyrrolidone) (PVP) and/or ethylene glycol to synthesise the gold nanorods or nanocubes [80].

(e) Additives

Ag^+ and cyclohexane are the most frequently used additives in the synthesis of gold nanorods to improve both productivity and uniformity. It was found that $AgNO_3$ [70] and cyclohexane [81] could be introduced to control the aspect ratio of gold nanorods.

However, the role of Ag^+ is very controversial. The majority of researchers agree that the introduction of silver ions to the solution will improve the nanorod yield and aspect ratio markedly, while an excess amount of Ag^+ halts the growth of gold nanorods [64, 72, 73].

A modified version of the method of Murphy *et al.* [16, 70] has been applied and has been proved to be an effective way to produce a short aspect ratio of (2–4) gold nanorods, 40 to 50 nm in length, in high yield. This method can also generate the dogbone shape if required.

Wu *et al.* believe the contribution of $AgNO_3$ in the synthesis of gold nanorods came from NO_3^- ions rather than from Ag^+ [82]. Their result suggested that, by varying the amount of NO_3^-, a long aspect ratio of gold nanorods could be obtained. The researchers used HNO_3 and/or $NaNO_3$ to synthesise the long aspect ratio of gold nanorods.

(f) Others

The shape-changing that occurs on the aging of rods can also occur during specimen preparation. Zweifel and Wei have reported a method to introduce sulphide to stop the growth of nanorods. Again, their results caused more perplexment than clarity, since they evidently showed that the gold nanoparticles became dumbbell-shaped firs,t before finally turning into cylindrical rods [83].

2.2.2 Other gold nanorod synthesis methods

(a) Templated methods

The earliest method to manufacture rods was based on having a porous alumina template, the cavities of which were back-filled with gold [84]. Although the method has been quite highly developed [85, 86], it has been largely supplanted by the other synthesis techniques. Templated synthesis methods have been reported to produce nanowires [87]. Composite nanorods such as Au/Ag [88, 89], Au/SiO_2 [90], Au/Fe_3O_4 [91], Au/Fe [92], Au/Fe_2O_3 [93] core/shell structures have been investigated by various research groups.

(b) Electrochemical synthesis

The electrochemical method [81, 94, 95] was another early way used to make gold nanorods. Gold is used as the anode and CTAB as both electrolyte and shape-stabiliser. The gold nanorods are synthesised under appreciable current density and temperature. Song *et al.* synthesised gold nanorods in a 0.08 M CTAB aqueous solution by electrochemical reaction. With an increasing of concentration of $AuCl_4^-$ the overgrowth of gold nanorods turns the rod into dumbbells [96]. The shape change is similar to what was observed by Gou and Murphy using the seed-mediated method [75]. In that experiment, excess $AuCl_4^-$, existed in the solution. After adding extra amounts of ascorbic acid, dogbone and dumbbell shapes dominated in the solution. Compared with ordinary gold nanorods, the new shapes showed a strong blue shift in the longitudinal peak. As a result, the colour of the colloid changed from blue to purple [75].

Similar to the seed-mediated method, the surfactants also play an important role in forming the morphology of gold nanorods. It was found that tetrabutylammonium bromide (TC_4AB) was a better co-surfactant than tetradodecylammonium bromide ($TC_{12}AB$) on synthesising rods [97].

(c) Photochemical synthesis

Photon-reduction has also been investigated for synthesis of gold nanorods [98, 99]. For example, Miranda and Ahmadi [100] reported an unusual procedure in which $AuCl^-_4$ was reduced under the different wavelengths of UV radiation. There were some interesting findings in their research: 1) acetone played a critical role in this photolytic reduction reaction; otherwise spherical particles dominated in the final product. Interestingly, acetone was also found to play an important role in the electrochemical synthesis, that is, forming the rod shape [95]; 2) for the reduction under 300 nm radiation, the maximum rod length occurred in 6 hours, and the rods became shorter afterwards; 3) no seed was required in this photochemical reaction; nucleation was initialised by photo-reduction; 4) there was a higher yield of gold nanorods under 300 nm radiation than under 254 nm radiation. There is also a report (Niidome *et al.*) on the combination of chemical reduction and photo-irradiation processes to produce gold nanorods [101].

(d) Microwave synthesis

Gold nanorods have also been synthesised by microwave heating [102, 103], either in cationic surfactant or ethylene glycol. It was found that both surfactant concentration and reaction procedure played an important role during the process [103]. Liu *et al*. believed that with higher surfactant concentration and faster ramping of the reaction temperatures, gold nanorods with a higher aspect ratio could be produced. There is no seed or template requirement during this process. However, the mechanism of the reaction to form the nanorods remains unclear. The method has a relatively low yield. From the SEM and TEM images shown in the paper, a broad size distribution of particles was presented in the final product.

(e) Other methods

Carnizal *et al.* described how rods could be obtained by reduction in the presence of biological materials. This method might be useful in bio-applications [104].

2.2.3 Shape transition of gold nanorods

It has been reported that gold nanorods could further grow to form low symmetry shapes such as dumbbells and dogbones [75, 96]. The overgrowth occurred in either the seed-mediated method or electrochemical method. With an increasing concentration of $AuCl_4^-$, the overgrowth of gold nanorods turned the rod into dumbbells (Song *et al.*). [96]. The shape change is similar to what was observed by Gou and Murphy using the seed-mediated method [75]. In that experiment, excess gold existed in the solution. After adding extra amounts of ascorbic acid, dogbone and dumbbell shapes dominated in the solution. Compared with ordinary gold nanorods, the new shapes showed a strong blue shift in the longitudinal peak. As a result, the colour of the colloid changed from blue to purple [75].

There is still controversy over how to consistently produce the dumbbell shape. It has been shown ([75, 81, 96]) that the ends of the rods consist of a mix of {111} and {100} facets, while the flanks present the {110} plane to the environment. Due to weaker binding of CTAB to {111} than to {110}, the overgrowth rate along <111> directions should be higher than that of <110>, which results in a dumbbell shape.

It is not clear, however, why this growth would not happen at the outset in the seed process, thereby preventing the formation of rod-like shapes.

2.2.4 Separation of gold nanorods

Since the product of synthesis is a mixture of gold nanorods with different aspect ratios and nanospheres, it was essential to separate them before they could be applied to any further work. Some separation methods have been proposed, such as nanoporous filters, centrifuging and a combination of recrystallisation and centrifuging. Nanorods can be partially separated from spheres of significantly different size by centrifuging. The method may be used to separate small nanospheres (range 1–10 nm) [69], in which case the pellet contains the desired rods, or oversize spheres, in which case the supernatant contains the desired rods. Nanoporous filters do not work well for separating nanorods and spheres with similar diameters. There were studies utilising size exclusion chromatography to separate rods from spheres. However, only a partial separation was achieved [105, 106].

Jana *et al.* used a combination of centrifuge and recrystallisation to achieve better separation of gold nanorods. Rods and large spheres were collected from a pellet produced by low-speed centrifuging at 6,000 rpm. All the precipitates collected were dissolved in hot (40–50 °C), 0.1 M CTAB solution and crystallised during cooling, and the procedure was repeated a few times. The long rods collected in the precipitate, whereas short nanorods preferred to stay in the supernatant [69].

There is no satisfactory method that can separate similar sizes of gold nanospheres and short nanorods. The separation process is a very tedious, time-consuming process, which suggests that a new method for achieving mono-dispersed nanorods is required.

2.2.5 Mechanism of growth of gold nanorods

At this time, the seed-mediated method is the most popular and practical method to synthesise gold nanorods. The mechanisms of formation of gold nanorods discussed here all apply to this method, except where otherwise specified. There are many variables in the synthesis of gold nanorods by the seed-mediated method, as already mentioned. Different growth mechanisms have been proposed to explain the growth.

(a) Soft micellar template mechanism

Nikoobakt *et al*. suggested two possible growth mechanisms [72] for the seed-mediated method. In one mechanism, the surfactants form a soft template due to their micellar structure [107], in which the template has a size dependent on the surfactant concentration and the ionic strength of the solution. By introducing the seed to the growth solution, the surfactant-capped seed becomes part of the soft template, and growth starts by gold atoms diffusing into the template. In this mechanism [72], the authors believed that growth of nanorods took place simultaneously in all directions: growth in the longitudinal direction takes place parallel to the {001} plane, which is accompanied by the formation of four relatively unstable {110} facets and four {111} facets. Once the seed grows to a critical size, the facets become large enough for surfactant binding. The growth rate of different facets in the presence of the surfactant determines the final shape of the nanoparticles. Jana *et al*. [68, 70] have argued in support of this soft templating mechanism, and have drawn attention to the similarity of shape of the CTAB micellar structure and the gold nanorods [70].

(b) Passive protection mechanism

The other possible mechanism for the seed-mediated method is that the surfactant-capped seed starts growing, however, the {110} facets are restricted from growth by a preferential coverage of CTAB monomers coming from the solution [72], that is, passivation of certain crystal facets of the gold seed by CTAB to promote anisotropic growth [108].

Gao *et al*. proposed a “zipping” mechanism to explain the growth of gold nanorods. which is illustrated below. By this mechanism, the surfactant is adsorbed as a bi-layer, rather than monolayer, on the flanks of the gold nanorod, with the trimethylammonium headgroup of the first monolayer of surfactant facing the gold surface. In this case, the authors believed that the growth of gold nanorods was attributed to the absorption of surfactant rather than to a soft micellar template [79]. Nikoobakht *et al.* [109] have provided evidence of CTAB bi-layers on gold nanorods.

The contradictory evidence to this mechanism was provided by Gou and Murphy. They found the aspect ratio of gold nanorods in their original growth solution decreased when the solution of gold nanorods was heated. From TEM images, it could be observed that the length of gold nanorods did not change substantially, whereas the width increased significantly [75]. This finding presents a challenge to the passivation mechanism for rod growth, since most agree that the rods are caused by selective growth on their ends. What factor(s) has (have) changed in this experiment to make growth along the flanks preferable?

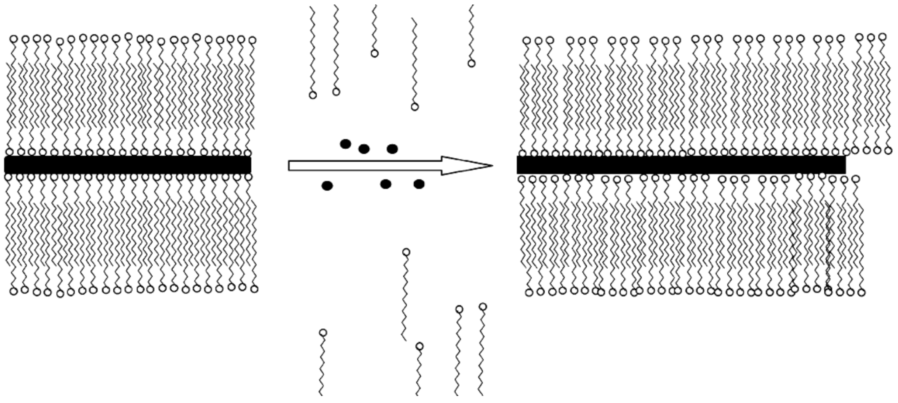

Figure 2-3 Illustration for growth of gold nanorods by bi-layer passivation mechanism

(From Gao *et al.* [79].)

Gou *et al.* further use their CTAB double monolayer selective adsorption mechanism to explain the growth of dogbone-shaped particles [75].

(c) Electric-field enhanced diffusion mechanism

Another proposed mechanism for the anisotropic growth of gold nanorods in the seed-mediated method is by electric-field enhanced diffusion of Au(I)-CTAB [77]. However, this theory does not offer any role for Ag^+, even though there are many reports that silver can increase the yield and aspect ratio of gold nanorods [72]. Nevertheless, the authors assumed that the rate of rod formation was determined by the frequency at which $AuCl_2^-$-laden cationic micelles impinged on the cationic gold seed particles, which was inturn controlled by the electrical double-layer interaction between the micelles and gold rods. There are some difficulties in relation to this theory. Firstly, the diffusion layer is usually around micron level or sub-micron level, and whether it works effectively at the order of nanometers is still unknown. Secondly, the theory could not explain the role of silver, which most researchers found improved the yield of rods [16]. Thirdly, Wei and Zamborini [108] found that the growth of nanorods could at times proceed from one end rather than two from opposite directions. This is in contradiction to the electric field theory [77].

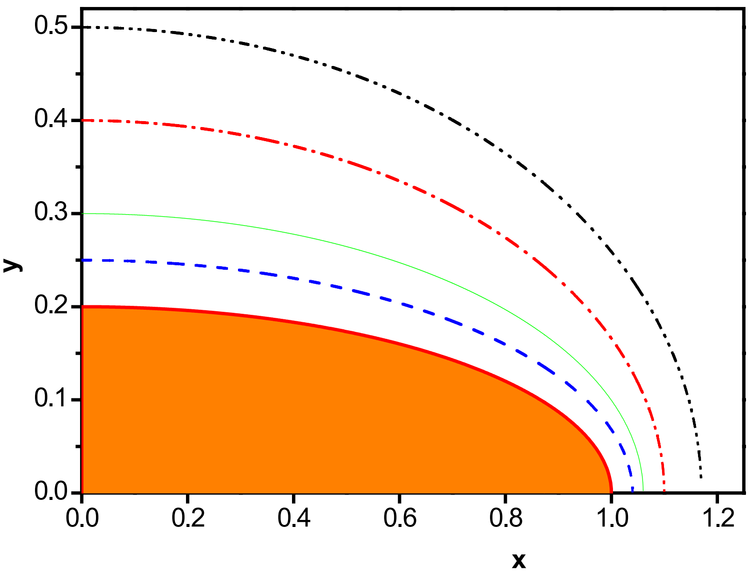

Figure 2-4 Contour plot of scaled potential around nanorod

(Redrawn from [77])

Gai *et al.* [76] claimed that the classic theory of surface energy minimisation is responsible for the nucleation and growth of the nanorods. In electrochemical synthesis, Yao *et al.* also found the growth axial direction of gold nanorods was <110>, which was normal to the high-energy surface [97]. The energy minimisation with the reduction to a stable form of Au was the driving force for the formation of nanorods. Initially, multiple twinned particles were formed that had weaker bonding in the twinned areas and provided sites for Au diffusion to those sites. This led to the growth of the nanorod along the <100> direction. However, their argument was not convincing, given the well-known fact that Au {110} surfaces on the flanks have higher energy than the {111}.

With all these theories, there is no clear explanation for the function of silver, which most researchers believe has an essential role in the synthesis of gold nanorods [71]. There remains the puzzle of why introducing Ag^+ could significantly improve the yield of gold nanorods [72].

2.2.6 Crystal structure of gold nanorods

There are some disputes concerning the crystal structure of gold nanorods. According to available reports, there are different crystal structures for gold nanorods made by different methods. At the moment, most characterisation methods are focusing on gold nanorods prepared by the seed-mediated method and the electrochemical method.

(a) Seed-mediated method

The crystal structure of gold nanorods made via the seed-mediated method is illustrated in Figure 2-5 [76]. The structure was constructed using a pentagonal arrangement of {111} faces on the ends and unstable {110} facets as sides. Surface diffraction of the particles indicated the highly unstable {110} surface is protected by a surfactant. Work in this area has supported the concept of a pentagonal structure for gold nanorods. Canizal *et al.* used “bio-reduction”, that is, reductant was an extraction of the milled plant *Mediicago sativa* [104]. They obtained twinning along the <112> and the authors believed the gold nanorods in this case were growing as decahedra along <112>. Nikoobakht *et al.* suggested the sides of gold nanorods were composed by four stable {111} facets and four relatively unstable {110} facets [72]. Hernandez *et al.* facets, using lead underpotential deposition (LUD), which is one of the electrochemical characterisation techniques, confirmed that gold nanorods are composed of (111) and (110), and practically no (100) planes [60].

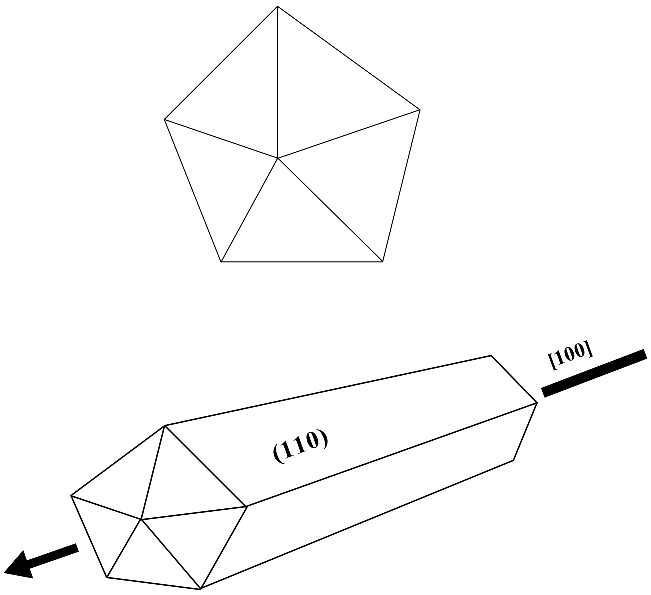

Figure 2-5 Illustration of crystal structure of gold nanorods via seed-mediated methods

(Redrawn from [76])

(b) Electrochemical method

For the gold nanorods made via the electrochemical method, different crystal structures were found for short rods and long rods [110]. Short gold nanorods with aspect ratios of (3–7) are enclosed mainly by {100} and {110} facets and their growth axial direction is <001>, whereas long gold nanorods of aspect ratios 20–35 are dominated by {111} and {110} facets and their growth axial direction is <112>. Wang *et al*. found gold nanorods prepared electrochemically and capped in micelles had an axial growth direction of <001> and have surfaces made of {100} and the unstable {110} facets [111] were mostly untwinned [110]. {100} showed no reconstruction while unstable {110} showed missing-row reconstruction [111]. However, Yao *et al.* suggested that the growth of rods was along <110> [97].

(c) Other methods

Different from the electrochemical method, the gold nanorods synthesised from "bio-reduction" [112] are mostly twinned. Yacaman *et al*. believed the difference may occur by higher stress introduced during a bio-reduction process. XRD results revealed for the gold nanorods, synthesised from the microwave method, a "well-crystallised elemental

Au with FCC structure" [102, 105]. Coura *et al.* [113] utilised high-resolution TEM and simulation to study the elongation of gold nanowires and their crystallographical orientation change.

2.2.7 Thermal stability of gold nanorods

Since nanorods are thermodynamically an unstable structure, their stability for long-term service, particularly at high temperatures, has attracted attention. From section 2.2.6, there are unstable {110} facets in gold nanorods which have to be protected by surfactant to stabilise the rod structure. If this capping layer is removed or destroyed by heating to 200°C, the diffusion of gold atoms may reshape the gold nanoparticles [111].

(a) Laser and other radiation

The gold nanorod is a vulnerable structure. Link *et al.* found melting of gold nanorods could occur within 30–35 ps, when irradiating with a 400 nm laser at 20 μJ [114]. When gold nanorods are exposed to low-energy laser pulses, they undergo shape transitions at temperatures below melting.

Chang *et al*. reported significant shape change in gold nanorods that were exposed to laser radiation at 532 nm and 1054 nm [81]. A phi (ϕ)-shaped particle, was found, which they believed was a transition stage from gold nanorods to gold nanospheres. In other work, gold nanorods synthesised by reduction with biomaterials (fresh alfalfa, *Medicago sativa*) were irradiated under the electron beam of a TEM [112]. Surface relaxation, reconstruction and faceting were observed during the process, due to electron beam-induced heating. Link *et al.* also investigated the melting process of electrochemically synthesised gold nanorods under laser radiation [114, 115]. They believed the process could be described in the scheme shown in Figure 2-6.

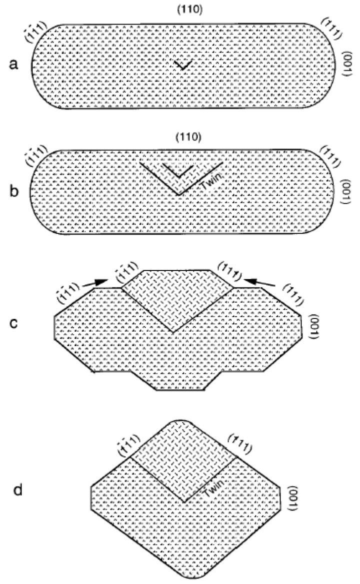

Figure 2-6 Physical model of shape change of gold nanorods under radiation

(From Link *et al.* [115].)

Takahashi *et al.* [116] investigated the fusion of gold nanoparticles on a substrate under cyclohexane. It was found that with radiation from a 532 nm laser beam, the thiol-capped gold nanoparticles aggregated and fused in the organic solvent. The morphologies of the particles altered dramatically after the laser radiation.

(b) Heat-treatment process

There are very few reports on the thermal stability of gold nanoparticles at ambient temperatures, which would be very important for their use in applications such as window-glass coatings. Thermogravimetric (TGA) results indicated the gold nanoparticles were stabilised by a surfactant. The weight losses peak showed there are different modes of binding between Au surfaces and surfactant. The situation was caused by absorption of the stabiliser on different crystal planes [117].

Mohamed *et al.* [118] studied the thermal stability of gold nanorod suspensions with average aspect ratio of 3.3 in glycerol aqueous solutions. The activation energy for shape change was reported as 88.2 kJ/mol in the range of 60°C to 100°C. Al-sherbini *et al.* used a similar system to study the thermal stability of gold nanorods (with aspect ratio of 2 to 4) [119], and showed that the longitudinal plasmon blue-shifted and decreased in intensity as the suspensions were aged at various temperatures up to 100 °C. The active energy of gold nanorods was reported as 54.18 kJ/mol. The explanation given was that aging destroyed the protective micellar structure of the longest rods, causing them to be selectively and progressively precipitated out of the suspension. The net reduction in average aspect ratio caused the blue-shifting of the longitudinal plasmon peak. The gold nanorods used in their studies were both prepared by the electrochemical method.

(c) Simulation

There have been attempts to simulate thermally induced shape changes in gold nanorods [120]. In the simulation of Wang and Dellago, gold nanorods containing 1,000 to 10,000 atoms were assessed. The results showed that the morphology started to change at temperatures as low as 517K. Another study has reproduced such transitions using molecular dynamics simulations of gold nanorods consisting of approximately one hundred atoms [120]. The authors found that the shape change was accompanied by a structural change. On the basis of the simulation results, a mechanism was suggested that explains the intermediate products and the internal defects of gold nanorods observed in laser heating experiments [121].

2.3 Gold nanorod coatings on glass

In section 2.2, we discussed the different methods and mechanisms of synthesising suspensions of gold nanorods [61, 105]. Ordered arrays of particles possess more exciting properties for possible applications [122], but the application of such particles in the form of coatings has received less attention. In this section, I will review the progress that has been made in respect of the producing and properties of such coatings.

There are two routes to achieve coatings of gold nanorods on substrates such as glass, mica and silica. In the first method the rods are produced separately, using the methods described in section 2.2, and then transferred to the substrate. In the second, the rods are grown *in situ*, possibly onto pre-existing seed particles that have been placed on the substrate. I will discuss these two technical methods separately.

2.3.1 Route 1: Immobilisation of gold nanorods on glass

Technically, gold nanorods, dispersing phase and substrate must be compatible before we can deposit continuing gold nanorods on them [123, 124]. Since gold nanorods are synthesised mostly in the aqueous phase, transferring them to the organic phase will be very useful on certain non-linear optical surfaces Transferring gold nanorods from the aqueous to the organic phase was studied by Wei *et al.*. The process did not require any other surface monolayer of thiol or amine as usual. The morphology of gold nanorods was reported as persisting after the transfer [125].

Immobilisation of gold nanorods on surfaces has been investigated by a number of researchers [126-130]. Kwon *et al.* reported the method which used Cl^- as an aggregating agent to assemble the gold nanorods into linearly aligned structures of linear bundles on TEM grids [126]. In contrast to the seed-mediated method, nanorods from the electrochemical reduction method were employed which contained 8.4 mM of CTAB, less than one tenth the concentration of the seed-mediated method. The gold nanorods were oriented in close to head-to-tail shapes on the microscopic scale. Other factors, such as pH, have also been found to trigger the immobilisation of gold nanorods. For example, Orendorff *et al.* found that at pH 8.0, rods formed side-to-side assemblies rather than the isolated disorder aggregation that formed at pH 3.0 [131]. Diffusion of gold nanorods has also been observed on chemically functionalised surface [132].

Gole *et al.* [133] published a method for immobilising f gold nanorods onto acid-terminated surfaces via electrostatic interactions. The authors claimed the density of rods assembled on the surface can be controlled simply by pH variation. In their work, gold nanorods were synthesised by the seed-mediated method. The typical size of gold nanorods produced was 400 nm × 25 nm, with aspect ratios of (16 ± 2.5). Nanorods were purified by centrifuging to remove excess CTAB. A glass slide was first coated with 10 nm nickel and then 200 nm thickness gold film by sputtering, and then dipping into 10^{-3}M 16-mercaptohexadecanoic acid ethanol solution to allow an SAM to form. The authors used five different pH values, that is, 1, 3.3, 6.5, 8 and 11, in their control experiments, and found that the density of the immobilised nanorods varied according to the pH. According to their findings, the maximum dispersed nanorods density occurred in pH 6.5, while after pH 8, aggregation of gold nanorods occurred. Although the authors realised the potential influence of CTAB, a cationic surfactant, its function remains unclear. Even though centrifugation was applied to remove most of the free CTAB from the gold nanorod suspension, it has not been established whether the changes in density of rod deposition were caused by changes in the pH itself or in the ionic strength induced by the change of pH. Another Immobilisation method was reported by Gole and Murphy, in which the authors coated the gold nanorods with polyelectrolyte. This converted the surface charge of gold nanorods from positive to negative. Control of the surface charge of gold nanorods allows more flexibility for application of the nanorods in immobilisation processes [134].

Murphy has recently reviewed [61] the methods to immobilise or align gold nanorods in one, two or three dimensions [135-137]. To achieve the one-dimensional alignment, one strategy was to use streptavidin as an end-to-end "glue" to join the gold nanorods (Figure 2-7) [135]. Alternatively, alignment of the rods could be achieved by physical stretching of a polymer film containing gold nanorods [138].

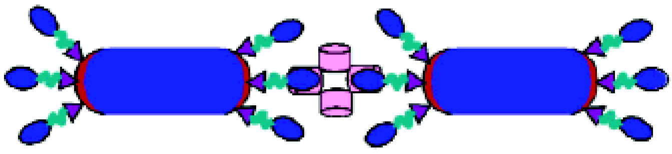

Figure 2-7 One-dimensional assembly of gold nanorods

(From Caswell *et al.* [135].)

Two dimensional, side-by-side assembling could be achieved by incubation of gold nanorods with thioalkylcarboxylic acid based bifunctional molecules or diallyldimethyl ammonium chloride [129, 139].

2.3.2 Route 2: Growth and manipulation of gold nanorods on surfaces

It has been demonstrated that growth of gold in the interface of gas and liquid is controllable [140]. However, the literature contains a few articles concerned with the growth of gold nanorods onto a surface. Small gold nanoparticles are self-assembled on the functionalised surface as seed (Process illustrated in Figure 2-2), and the seed develops into a rod shape on the substrate surface [108, 141, 142]. For example, Taub *et al*. [141] self-assembled 3.5 nm diameter gold nanoseed on mica and silica surfaces functionalised with 0.01% aminopropyltrimethoxysilane. The seeded substrate was then immersed in the growth solution containing 0.06 M CTAB, 0.5 mL of 2.5×10^{-4} M $HAuCl_4$ and 25 μL of 0.1 M ascorbic acid. There are two important issues in this article. First, for the self-assembled monolayer, only a very sparse coverage of gold nanoparticles was attached to the silane (1-10 per μm^2). Second, similar to the other seed-surfactant-mediated methods, the yield of gold nanorods on the surface was not high. Contrary to the report of Nikoobakht [72], the authors found that the change of $AgNO_3$ concentration did not influence the aspect ratio of gold nanorods in their experimental conditions. In order to observe well-separated particles, they used a lower density seeded surface (1–10 particles/μm^2). Gold nanorods grown with this method are neither arrayed nor erect. So, currently, the nanorods cannot be used as the “brick” for nano-architecture. Wei *et al.* immobilised (3–5) nm gold seed on a surface of glass by a mercaptolpropyltrimethoxy-silane monolayer and observed the growth of gold nanorods on the surface by AFM [108]. In this work, the authors did not add Ag^+ in their growth solution. A relatively low yield of nanorods on glass (5~15%) was obtained and the authors found that the Au rods grew in either one direction or two directions. There was a strong positive correlation of seed and nanorod diameters. Although the authors claimed that initial seed structure rather than size was more important in the synthesis of nanorods, there was no direct evidence to support their hypothesis.

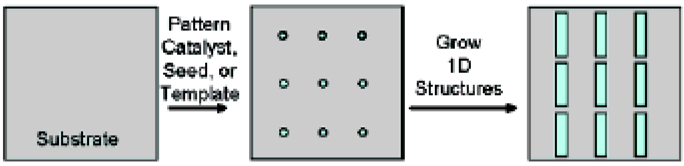

Figure 2-8 Growth and manipulation of gold nanorods on the substrate

(From Mieszawska *et al.* [143].)

Some workers have used poly(dimethylsiloxame) (PDMS) stamps to transfer gold nanoparticle seed onto functionalised Si/SiO$_x$ as a micro-feature pattern. The seeds were then grown into gold nanorods (Figure 2-8). Unfortunately, the yield of gold nanorods in this work was as low as 7% [143].

A report on the manipulation of gold nanorods on the substrate surface by AFM has been published by Hsieh *et al.*. Such techniques may result in nanofabrication in the future [144].

2.4 Simulation for optical properties of gold nanoparticles and their coatings

The simulation of optical properties of the gold nanorods has been of much interest recently [145]. Link *et al.* tried to use Mie theory to explore the relationship of the aspect ratio of gold nanorods to their surface plasmon peak position [146-148]. The quasi-static calculation method was also applied to simulate the optical properties of the nanorods with the increasing aspect ratio [149]. The common problem for all workers in this field is that there is no simple geometric shape of real gold nanorods. Therefore, they opted to use a prolate spheroid or a right cylinder instead. However, real rods have more complex shapes [75]. Due to obvious mathematical difficulties in processing the dumbbell, there is no specific simulation on how shape change (except aspect ratio) caused the change in the spectrum of gold nanorods. Brioude *et al.* used the Discrete Dipole Approximation (DDA) method of Draine and Flateau to simulate the spectra of rods [150]. The advantage for this method is apparent; the optical properties of any shapes can be simulated by this method with the only limitation relating to the computing capability.

3. Gold nanosphere coatings by wet chemical process for solar-glazing purposes

3.1 Introduction

The adhesion of colloidal gold nanoparticles to ordinary glass is poor [151], and merely dipping a glass surface into such a solution will not result in any significant adhesion of gold nanoparticles. Generally, there are two strategies for applying gold nanoparticle coatings on glass substrates by the wet chemical process. In the first strategy, gold nanoparticles are separately synthesised and glass substrates are functionalised with special chemicals, such as silane or thiol organic compounds. The prepared gold nanoparticles bind to the functionalised substrate [12, 151, 152]. In general, relatively complex reagents, such as aminoalkylalkoxysilanes [12, 151, 152] are required to achieve this. This is the self-assembling process. In this method, the adhesion of the particles to the glass is improved by the interlayer. In the second strategy, the gold nanoparticles are deposited directly onto the catalysed glass substrate. This *in situ* process is closely related to electroless plating.

In this chapter, the second approach is utilised. Inspired by the now-lapsed patent literature on the electroless deposition of gold, the reduction of Au(III) to form nanoparticles is arranged to occur heterogeneously on the surface of the glass, rather than homogeneously in the solution. The basic concept may be found in the patents of Levy [49] for decorative, non-transparent coatings, from which I have drawn the idea of using ethylene diamine as a complexing agent. The work of Miller [38] provided the pre-treating method of using a stannous chloride. The work of Franz and Vanek [45] suggested buffering the solution to control the pH. The work of Luce [153] prompted me to use less toxic $HAuCl_4$ as a source of Au(III) and hydrazine as the reducing agent.

The idea of an aqueous process to precipitate transparent gold coatings onto glass for architectural applications is not new, and dates from at least the patent of Miller in 1977 [28]. However, many of the early methods required the use of currently unattractive chemicals such as cyanides, and/or soluble salts of lead, mercury or cadmium. For whatever reason, these processes seem not to have been widely exploited. The interest at

UTS has been to explore whether, with the benefit of the current knowledge of nanotechnology, a coating of gold nanoparticles could be developed that was simple to apply, useful for solar glazing, and which did not require the use of hazardous raw materials. Miyake *et al.* also pointed out that the adhesion of electroless gold on silicon is superior to that of sputtered gold [56].

The crystal structure and mechanical properties of gold nanocoatings from aqueous deposition are very important. The crystal growth preference, Young's modulus, microhardness and adhesion provide important information on durability for architectural applications. However, these data seem not to have ever been previously reported.

3.2 Experimental

3.2.1 Materials

The ethylene diamine, hydrazine, and sodium hydroxide were obtained from Aldrich, while HCl, H_2SO_4, HNO_3, potassium hydrogen phthalate, KCl, $SnCl_2 \cdot 6H_2O$, and gold were sourced from diverse suppliers. All chemicals were used as-received. Generic soda-lime glass microscope slides were obtained from Livingstone. All H_2O used was purified by double-distillation.

3.2.2 Synthesis of $HAuCl_4$

$HAuCl_4$ was prepared by dissolving pure gold in aqua regia (HCl: HNO_3 3:1 volume/ volume). The method may be found elsewhere [154]. A brief description of the procedure is as follows: 9.85 g pure gold was dissolved in 80 mL of aqua regia and the solvent was evaporated under aspirator vacuum on a water bath. For removal of nitric acid, the product was strongly heated twice with concentrated HCl in the same manner; the excess hydrochloric acid was separated by concentrating the remaining solution to around 15 mL. Finally, the solution was diluted to 500 mL to obtain a 0.10 M $HAuCl_4$ solution. It is accepted that some residual HCl content will have been present in the solution (Figure 3-1).

3.2.3 Gold deposition

The glass surface was pretreated by immersing for one hour in 5% NaOH/methanol solution and then two minutes in 0.1% of aqueous $SnCl_2$. The slide was rinsed with pure water before deposition of the gold from a solution of 0.0004 M $HAuCl_4$, 0.015 M N_2H_4 and 0.03 M ethylene diamine. This solution was buffered to pH values of 5.1, 8.0 or 10.0. The pH 5.1 buffer solution was prepared by mixing 100 mL of 0.1 M potassium hydrogen phthalate and 51 mL of 0.1 M NaOH. The pH 8.0 buffer was prepared by mixing 100 mL 0.025 M $Na_2B_4O_7 \cdot 10H_2O$ (borax) with 41 mL 0.1 M HCl. The pH 10.0 buffer solution was prepared by mixing 100 mL 0.05 M $NaHCO_3$ with 21.4 mL 0.1 M NaOH. It was confirmed that the pH of these solutions stayed constant during the deposition.

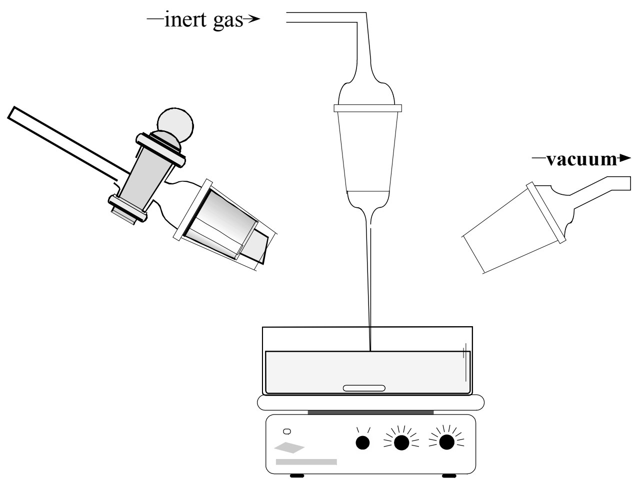

Figure 3-1 Experimental setup for preparation of $HAuCl_4$

The coating solution must be made up immediately prior to use, and has a short lifetime of a few minutes to an hour, depending on the pH. The published Pourbaix diagram for $[AuCl_4]^-$ shows that the gold should form soluble complexes in the buffered environments provided that the $[Cl^-]$ concentration was greater than about 10^{-2} M [155]. The soluble species in the pH 5.1 environment was likely to have been $[AuCl_3OH]^-$ or $[AuCl_2(OH)_2]^-$, whereas that in the alkaline buffer was likely to have been $[AuCl(OH)_3]^-$.

3.2.4 Thin film characterisation

(a) Transmittance

A Cary 5E UV/Vis/IR spectrophotometer, working in the range of 170 nm to 4300 nm, and with a resolution of 0.5 nm, was used to inspect the visible-IR transmission spectrum of the samples. The scanning rate was 5 nm/s with spectral bandwidth (SBW) of 2 nm.

(b) Surface composition and morphology

The coverage and nature of the coating of gold nanoparticles was assessed using a combination of X-ray photoelectron spectroscopy (XPS), scanning electron microscopy (SEM) and atomic force microscopy (AFM). XPS spectra of the Au nanoparticles were recorded using Al Kα radiation (1486.6 eV) at 20 eV. The sample was placed in an ultra-high vacuum chamber at 10^{-9} Torr housing the analyser. The experimental data were calibrated with the carbon peak that was always shown as a contamination at 285 eV. The morphology of deposited gold was characterised by JEOL 6300F field emission scanning electron microscopy (FESEM), with secondary electron images at 30 kV, and with Digital Instruments 3100 atomic force microscopy (AFM) in contact mode.

(c) Crystal orientation of gold nanoparticles

The crystal orientation of gold nanoparticles was measured by X-ray diffractrometer (XRD).

(d) Spectral data analysis

An objective measure of the wavelength at which maximum extinction occurred was obtained by taking a numerical first derivative, $\frac{dT}{d\lambda}$ of the transmission intensity through the coating, versus wavelength. The maximum absorption was taken as occurring at the wavelength for which $\frac{dT}{d\lambda}=0$.

(e) Volume fraction

The volume fraction of the gold in our coatings could not be properly determined by simple areal analysis, since the coatings were three-dimensional at the nanoscale. Therefore, it was determined by constructing a geometric model of the surface, using numerous measurements of particle diameter, position and shape made from the SEM and AFM images, using custom-written software. The software allowed the user to map an image of the coating into an array of hemispheres. Since many of the particles were close together or overlapping, double-counting of gold was avoided by rendering the list of hemispherical particles into an array of voxels which represented a slab of thickness, t. The volume fraction, ϕ, occupied by gold was then estimated from this array by point counting, and was influenced by the value chosen for t. Two measures of volume fraction were estimated. The first, ϕ_{surface}, is simply the areal fraction of the surface at z=0, that is, covered by gold. The second is the volume fraction, ϕ_{box}, of gold in the slab bounded by z=0 and z=t, where t is the maximum height of any particle in the relevant sample. Obviously $\phi_{\text{surface}} > \phi_{\text{true}} > \phi_{\text{box}}$, where ϕ_{true} is the actual volume fraction of gold encountered by a photon.

(f) Scratch test

Scratch tests (illustrated in Figure 3-2) were performed on a Hystron Ubi 1®, Hysitron Inc. The system has an *in situ* Atomic Force Microscopy (AFM) unit to locate interesting areas of the samples. During the test, both normal and lateral forces were applied to the diamond indenter tip while the sample was examined. Both forces were measured and recorded during the displacement of the surface coating or nanoparticles. The morphologies of the sample before and after the scratch were imaged by the *in situ* AFM unit. Normal force, lateral force and displacement were recorded as a function of time.

Normal forces ranging from 20 to 30 µN were applied to the different areas of the sample to ensure the displacement of gold nanoparticles from the substrate occurs. Each scratch lasted for 30 seconds and the path of scratch was 2 µm. The built-in AFM image capacity of the instrument monitored the dislocation of particles after every scratch.

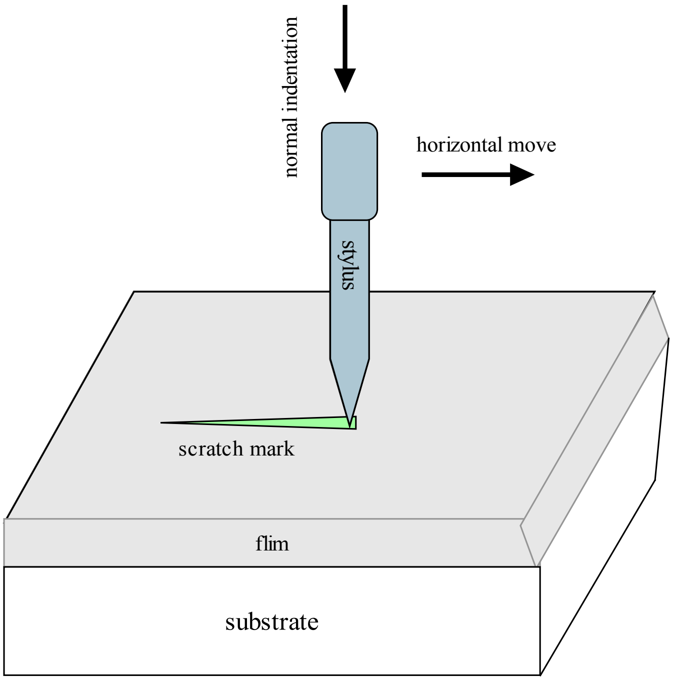

Figure 3-2 Illustration of scratch test process

(g) Nanoindentation

Nanoindentation tests were also performed with a Hystron Ubi 1®, Hysitron Inc. A Diamond NorthStar® indenter tip was utilised in performing the indentation tests. The testing spot was also imaged by an *in situ* AFM unit before and after the test. The peak load of indentation was 5 µN and each indent process included stages of five seconds of linear loading, two seconds of load-holding and five seconds of linear unloading [156].

3.3 Results

3.3.1 XPS results of gold nanoparticle coating

The surface composition of gold nanoparticle coatings in different deposition stages was examined by XPS, as per the procedure described in 3.2.4(b). Typical XPS spectra of Au (4f) as-deposited onto the glass are shown in Figure 3-3, for different processing times. Au ($4f_{7/2,\ 5/2}$) peaks at 84.0 and 87.9 eV correspond to pure gold. With increasing immersion time in the coating solution, the height of the gold peaks increased (Figure 3-4), while the height of the silicon (2s, 2p) peaks reduced, which indicates an increase in the coverage of the gold nanoparticles on the glass substrate.

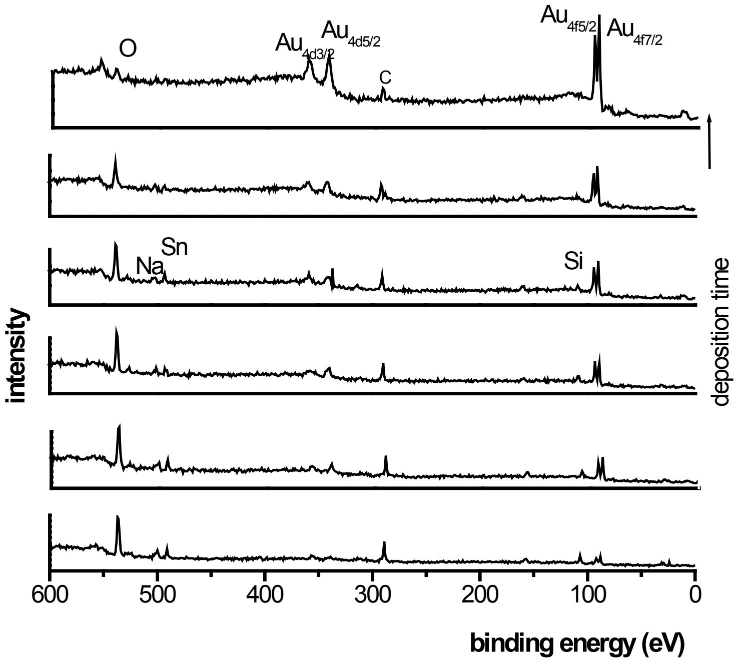

Figure 3-3 XPS spectra of glass surfaces coated at pH 5.1

(From bottom to top 6, 12, 18, 24, 30 and 50 minutes respectively.)

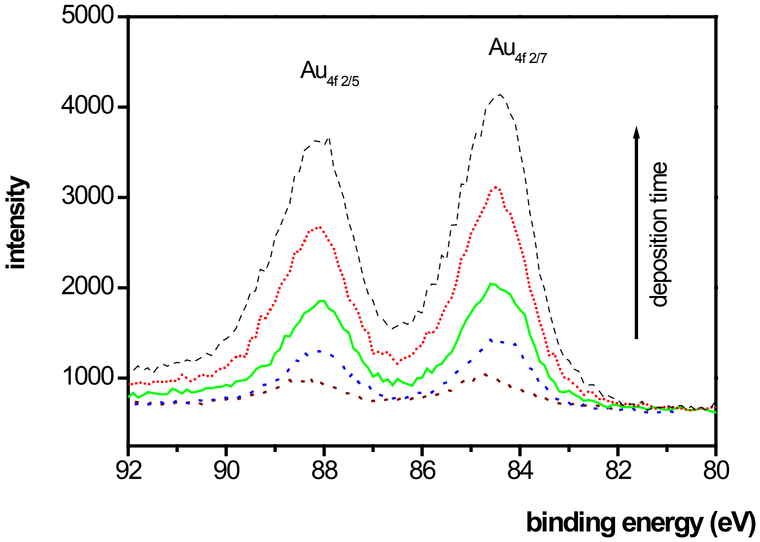

Figure 3-4 Gold peaks on XPS spectra

(Deposited in pH 5.1 solution for 6, 12, 30, 40, 60 minutes respectively, showing development of the coating of gold nanoparticles as a function of deposition time.)

3.3.2 AFM image of gold nanoparticles on the glass

The dimensions of the gold nanoparticles deposited on the glass surface were measured by AFM, according to the procedure in section 3.2.4(b). An AFM image of the coating is shown in Figure 3-5, while the measured aspect ratios of the particles in that image are plotted in Figure 3-6. For a perfect hemisphere, the ratio of height and diameter of sphere is 0.5, while the ratio for a sphere is 1. The measurements indicate an average ratio of 0.33 (Figure 3-6). Since the radii of the AFM tip are comparable to those particles, the raw data of the measurements from AFM were further corrected by the hardball model described in section 4.2.3(d). It is evident that the particles are “caps” or hemispheres caused by heterogeneous nucleation [157]. This indicates that the reaction takes place *in situ*.

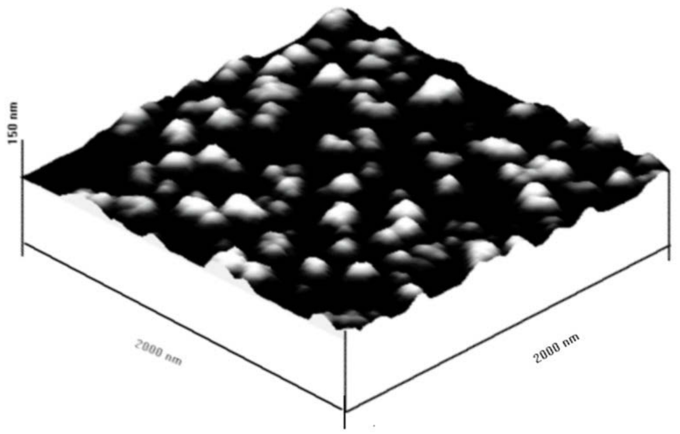

Figure 3-5 AFM morphology of gold nanoparticles deposited on glass

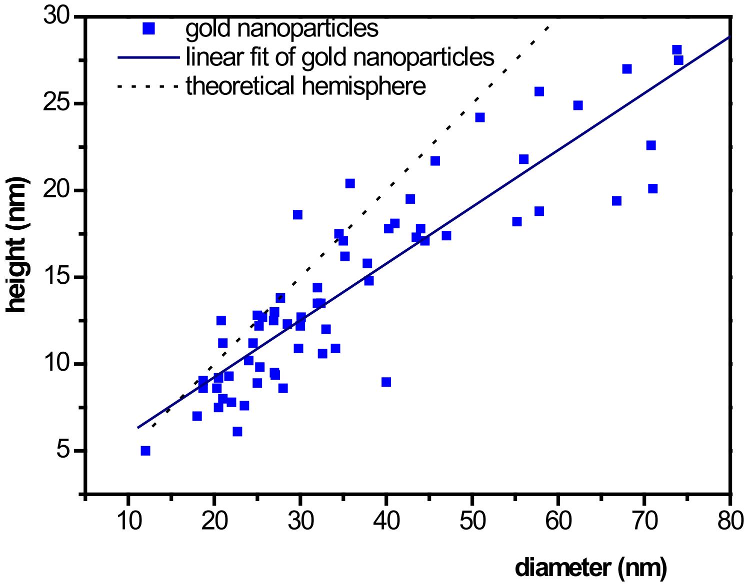

Figure 3-6 Height and diameter of particles demonstrating hemisphere

3.3.3 Optical properties of gold nanoparticle coatings on glass by different processes

Figure 3-7 to Figure 3-9 show the visible and infrared spectra of glass slides coated with gold at pH 5.1, pH 8.0 and pH 10.0 respectively. From these Figures it is evident that the longer the deposition time, the lower the transmittance in both the visible and the infrared area. It is worth noting that the surface of the glass slides became coloured well before any colloidally induced colouring became visible in the coating solution. We interpret this as evidence that the nucleation and growth of the nanoparticles occurred first on the surface of the glass before it took place in the solution.

For the deposition at pH 5.1, the spectrum can be grouped into three stages. In the initial stage, there is the appearance of the first absorbance peak at 520 nm, which included spectra I and II in Figure 3-7. After prolonged immersion time, a second peak appeared at 700 nm while the first peak was still visible (Figure 3-7 - III, IV and V). In this phase, the first peak is still at 520 nm while the second peak shifted gradually to 750 nm during the deposition. In the last stage, the second peak broadened and shifted further to longer wavelengths, and the first peak was no longer discernible on the spectrum. Meanwhile, the transmittance of the glass slide at 2500 nm (in the infrared region) rapidly dropped from 78% to 7% (Figure 3-7 - VI, VII, VIII and IX). In these three stages, the colour of the glass slide varied in hue from pink through violet to blue.

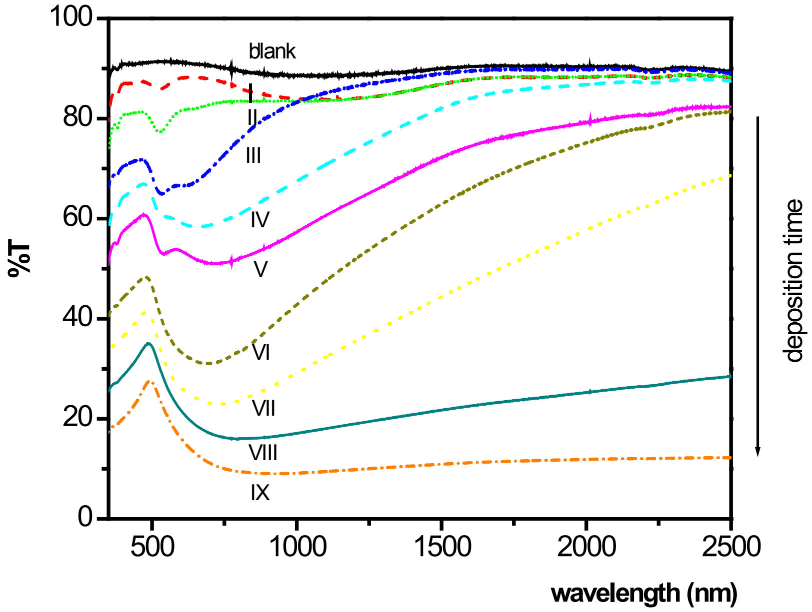

Figure 3-7 Transmittance spectra of gold nanoparticles deposited at pH 5.1

(Shown for deposition times of 6, 12, 18, 24, 30, 36, 40, 50, 60 minutes, corresponding to spectra I through IX respectively.)

For the deposition at pH 8.0, the spectra can be grouped into two types. The first absorbance peak appeared at 520 nm (Figure 3-8 I). This peak broadened during the deposition process (Figure 3-8 II). The second peak appeared at ~700 nm and moved further to the infrared area during the deposition process (Figure 3-8 III– VIII). The transmittance of the glass in the near-infrared (2500 nm) dropped from 85% to 10%.

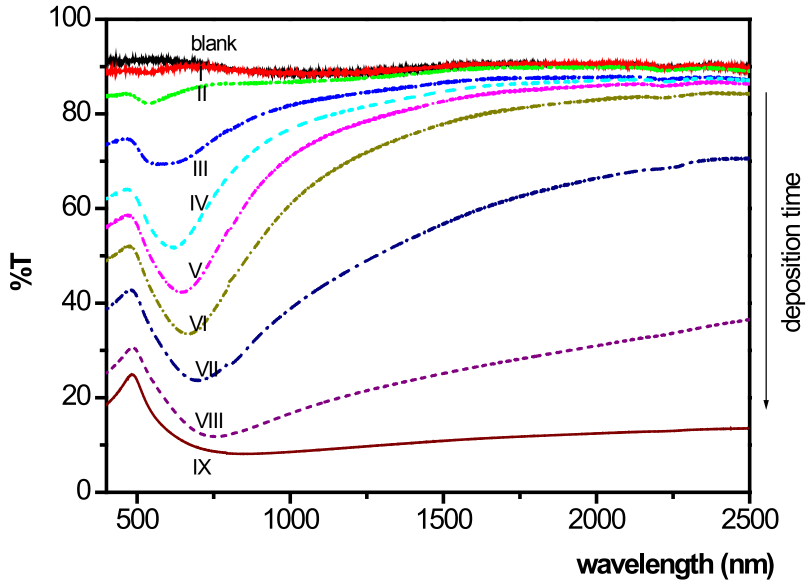

Figure 3-8 Transmittance spectra of gold nanoparticles deposited at pH 8.0

(Shown for deposition times of 2, 6, 12, 18, 24, 30, 42, 45 and 50 minutes, corresponding to spectra I through IX respectively.)

For the deposition at pH 10.0, the spectra are quite similar to those of pH 8.0. There was no clear coexistence of the first and second peaks on the spectra. The first absorbance peak appeared at 520 nm (Figure 3-9 I), but was overwhelmed by the development of the second peak during the deposition process. The second peak appeared at ~720 nm and moved further to the infrared area as the coating thickened (Figure 3-9 II– VIII). The transmittance of the glass in the near-infrared area (2500 nm) dropped from 85% to 10%.

The colour of the glass slide varied in hue from pink to blue directly. It appears that there was no obvious transition through violet in the experiments conducted at pH 8.0 and 10.0.

Figure 3-10 shows the morphology of gold nanoparticles deposited at different process times at a pH of 5.1. There is an increase of the coverage of the substrate, in agreement with the XPS results. The typical morphology of nanoparticles in the first stage is displayed in Figure 3-10 a, b. It is seen that the nanoparticles grew from 25 nm (Figure 3-10a) to 70 nm (Figure 3-10b). Most of the gold nanoparticles at this stage were isolated. Figure 3-10 c depicts the typical morphology of nanoparticles in the second stage of the development process. In this stage, many clusters formed inbetween isolated nanoparticles. The size of gold nanoparticles stayed at around 70 nm, however. After this the substrate became covered completely by the nanoparticles and clusters (Figure 3-10d), and aggregated gold nanoparticles merged into large irregular shapes of nanoscale dimensions, to form a continuous thin film. The shape of the original gold nanoparticles can still be discerned after this agglomeration.

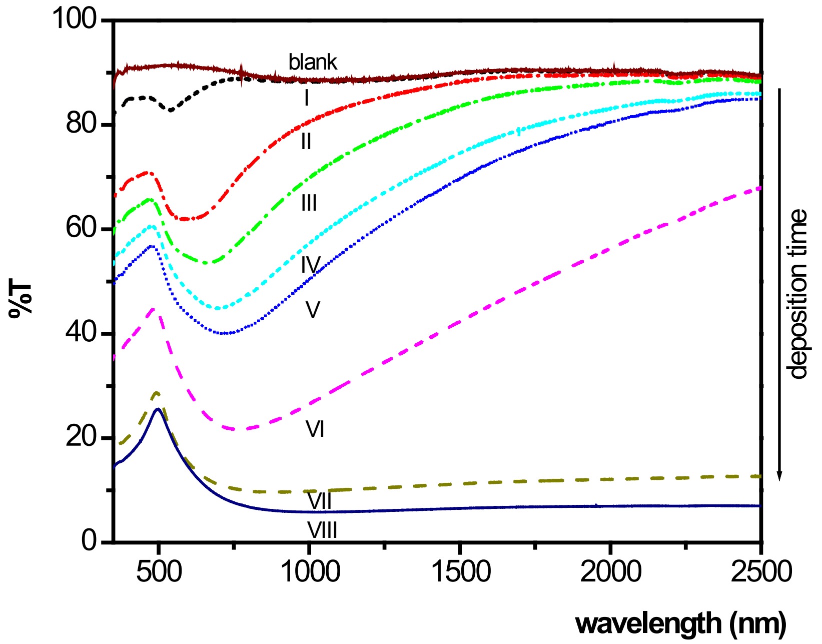

Figure 3-9 Transmittance spectra of gold nanoparticles deposited at pH 10.0

(Shown for deposition times of 2, 6, 12, 18, 24, 30, 35 and 40 minutes, corresponding to spectra I through VIII respectively.)

3.3.4 Morphology of gold nanoparticle coatings during different growth stages

In Figure 3-11, the morphology of gold nanoparticles deposited in different phases of the process at pH 10.0 is shown. In the first stage (Figure 3-11a) it is seen that the size of nanoparticles is similar to that deposited at pH 5.1, which is around 25 nm. However, the density of nanoparticles is quite high compared with that of those deposited at pH 5.1. In the second stage (Figure 3-11b, c, d), clusters of aggregated gold nanoparticles have been formed, and the substrate is completely covered by the clusters. The size of gold nanoparticles stayed at around 30 nm (Figure 3-11 b), which is significantly smaller than for the gold deposited at pH 5.1. Finally, the clusters merged into a continuous film. Once again, the shape of the original nanoparticles can still be observed (Figure 3-11c, d).

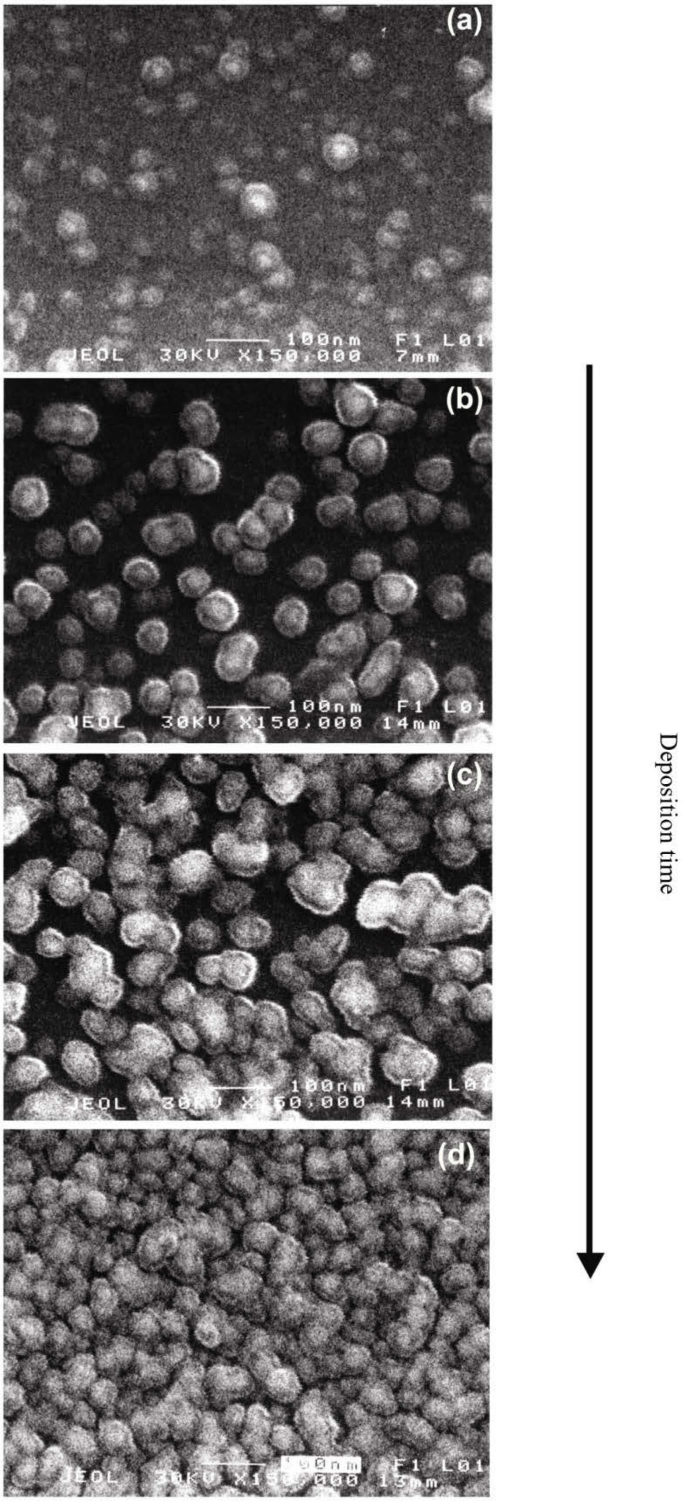

Figure 3-10 Morphology of gold nanoparticles deposited at pH 5.1

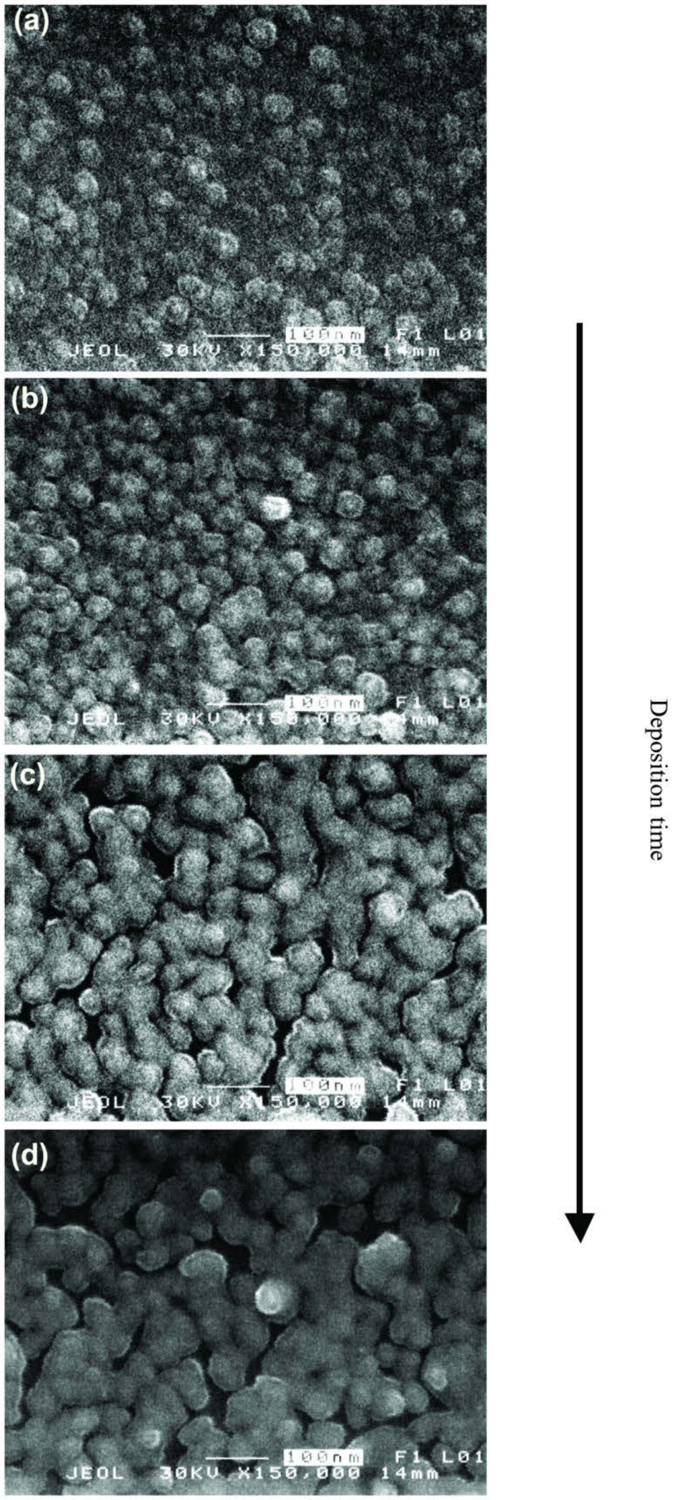

Figure 3-11 Morphology of gold nanoparticles deposited at pH 10.0

3.3.5 Crystal structure of gold nanoparticle coatings

The crystal structure of coatings of gold nanoparticles deposited by the wet chemical process was investigated with X-Ray diffraction (XRD) according to the procedure described in 3.2.4(c). Due to limitations of the XRD instruments, thicker films needed to be deposited. A typical XRD spectrum of the gold coatings is shown in Figure 3-12.

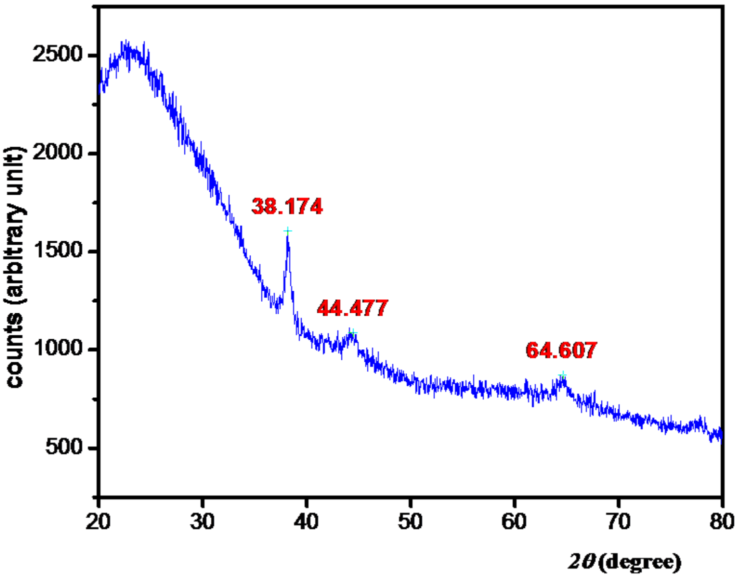

Figure 3-12 Crystal structure of Au film by XRD

The diffraction peaks and their relative intensity to the strongest one are indicated in Table 3-1. There three peaks are observed, with 2θ of 38.174°, 44.477° and 64.607° respectively.

Table 3-1 XRD results of gold nanoparticles on glass

Peak (°2θ)	Height (counts)	Rel.Int[1] (%)	Rel.Int[1]. (%)
38.174	440.40	100.00	100.00
44.4770	141.19	32.06	19.42
64.607	85.18	19.34	18.80

---

[1] Rel. Int: relative intensity.

The diffraction data of unstressed gold face-centred crystals are indicated in Table 3-2. The three strongest peaks for the reference sample are {1 1 1}, {2 0 0} and {2 2 0}.

Table 3-2 XRD data of Au reference sample (face-centred cubic)

Peak (°2θ.)	h k l	Rel.Int.[1] (%)	Peak (°2θ.)	h k l	Rel.Int.[1] (%)
38.184	1 1 1	100.00	81.721	2 2 2	12
44.392	2 0 0	52	98.133	4 0 0	6
64.576	2 2 0	32	110.79	3 3 1	23
77.547	3 1 1	36	115.25	4 2 0	22

It is clear that the gold coatings of nanoparticle deposited on glass substrates developed a typical face centred cubic (FCC) crystal structure. The {1 1 1}, {2 0 0}, {2 2 0} and {3 1 1} planes could all be located in the XRD spectrum of all gold nanocoatings. Other planes such as {2 2 2}, {4 0 0}, {3 3 1} and {4 2 0} are not apparent in the spectrum, due to their low relative intensities and noisy baseline.

Comparing the experimental data with the standard data indicates that the recorded peak positions are the same in the standard sample. Therefore the material is a normal unstressed cubic gold structure. Note that the relative intensities of {1 1 1} in the gold nanospheres are significantly higher than the data set of reference gold cubic samples, which would indicate the preferred orientation in the sample is {1 1 1}. The peak widths are, however, very wide, which indicates small particle size and/or high stress within the coating.

3.3.6 Scratching test

Quantitative information concerning the adhesion of the coating to the substrate is provided by the scratch test. The test usually applies to continuous films, while the films deposited here were either isolated particles or semi-continuous. However, scratch results determined from isolated gold nanoparticles on glass would give indications of the adhesion of film developed in the earlier stages of deposition.

The scratch test is produced by the combination of two loads applied to the stylus in the nanoindentation instrument: normal indentation and horizontal movement of the tip. In the conventional scratch test, a programmed increasing load is applied to the tip while the tip is moving [158] horizontally across the sample surface. The minimum critical load P_r, at which film and substrate start to detach, indicates the practical work of adhesion. The premise of operation is that the film itself is continuous and uniform, which is not the case in the system investigated in this work. Therefore, a fixed load was applied during the present scratch tests.

Figure 3-13 shows “before” and “after” 3D images of a 20 μN constant force scratch on a gold nanoparticle on a glass substrate. It can be seen that the scratch mark by the indentor tip passes over the gold particle rather than dislodgeing it from the substrate. Figure 3-14 shows “before” and “after” 3D images of a 30 μN constant force scratch test on the same sample. It is clear that the particle is displaced in this case. Due to the higher normal force during the scratch, the nanoparticles have been removed by the indentor [159].

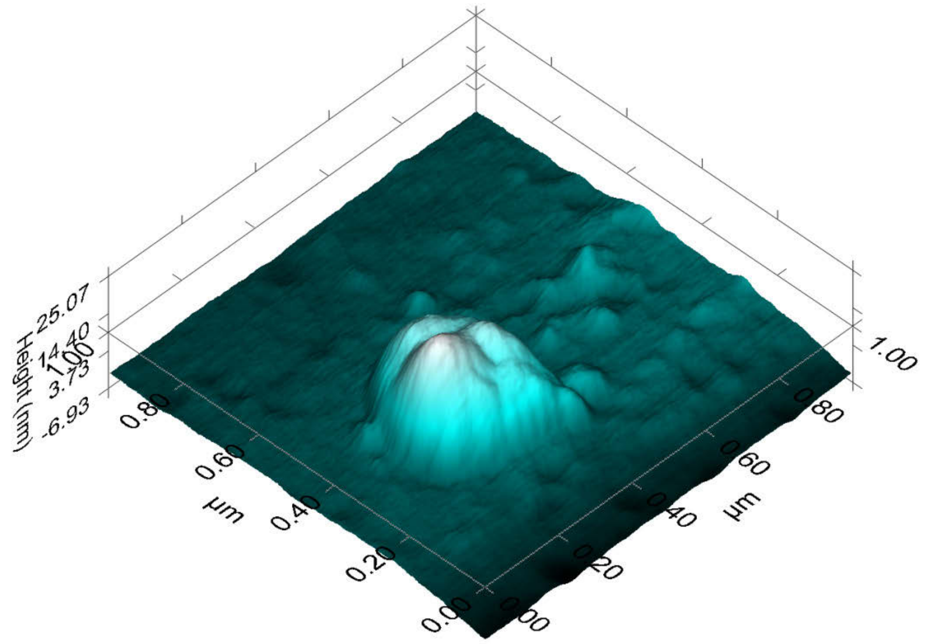

(a) before scratch

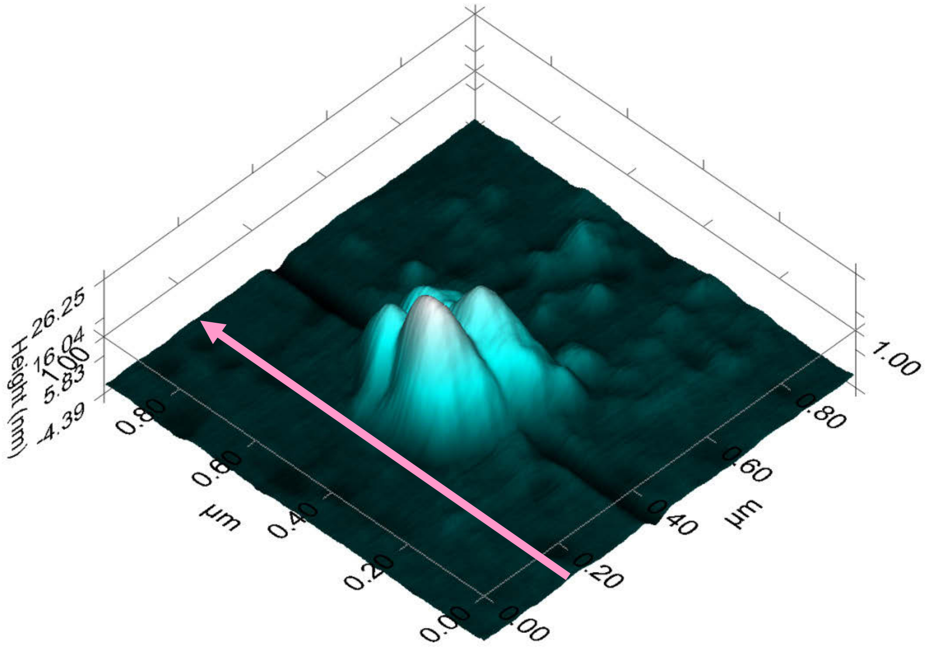

(b) after scratch

Figure 3-13 Adhesion test of gold nanospheres on glass substrate by 20 µN constant force scratch test[2]

---

[2] Test conducted by R. Stromberg, Hysitron Inc.

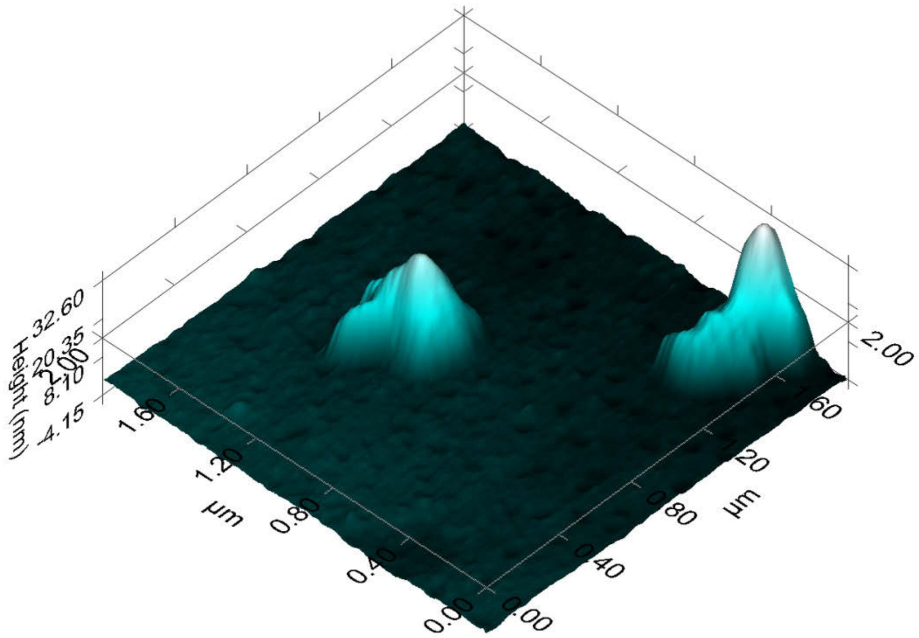

(a) before scratch

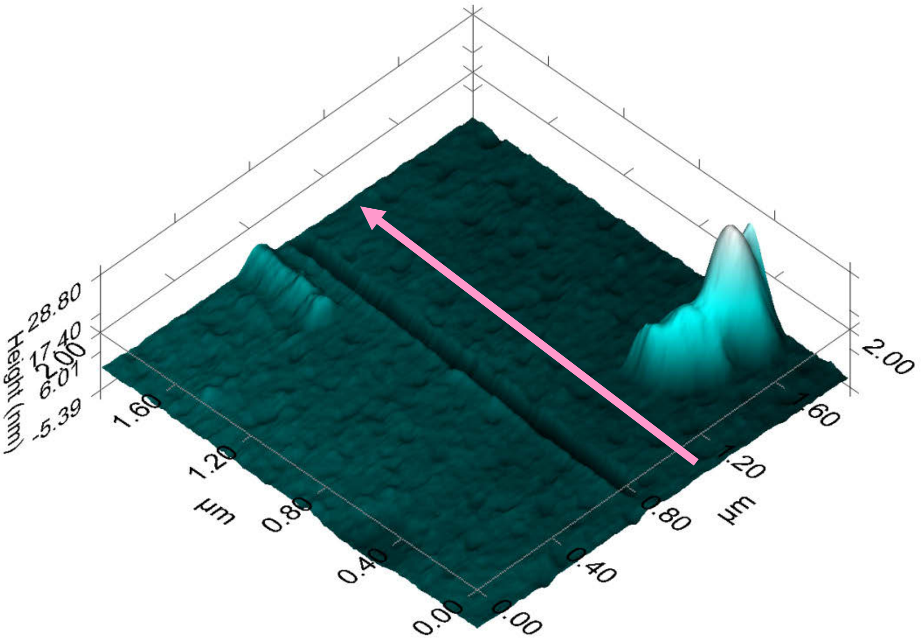

(b) after scratch

Figure 3-14 Adhesion test of gold nanospheres on glass substrate by 30 µN constant force scratch test[3]

---

[3] Test conducted by R. Stromberg, Hysitron Inc

3.4 Discussion

3.4.1 Effect of volume fraction of gold particles on colour

The colour of the coating can be considered from the point-of-view of transmission and reflection. The former is the colour displayed when light passes through the surface. The latter, in opposition, is the colour displayed when light is reflected from the surface. Here only transmittance colour is discussed because it is the more important for architectural applications (at least to individuals inside the building!). The colour of these coatings comes from their surface plasmon polariton, which is an electromagnetic mode existing at the interface between a metal and a dielectric substrate. Electromagnetic radiation from light can penetrate 20 to 30 nm into gold at visible wavelengths, which is comparable to the size of the nanoparticles themselves. In this case the electromagnetic wave forces oscillations of the free electrons in the particle with the same frequency as the applied electric field. A plasmon resonance will occur at a frequency depending on the type of material and geometry. The absorption peak for isolated gold nanoparticles in the 3 to 40 nm size range is at about 520 nm [160]., which produces the famous ruby-red or red wine colours in colloidal sols. The surface plasmon peak around 520 nm removes the green component of white light and causes the substance containing the nanoparticles to exhibit a red colour. The peaks in all series of spectra obtained in this work are caused by Au particles on the glass surface.

The surface plasmon peak from isolated particles is not the only reason for the colour of the coating. The second peak at around 700 nm can be explained by dipole-dipole interaction between nearby nanoparticles [161-163]. This is because an increase in packing density and/or aggregation of the particles, which would usually accompany an increase in particle size and volume fraction, is associated with the development of a second resonance, starting at 680 nm, and which red-shifts strongly into the near-infrared as the particles pack more closely together. The optical absorption of this effect is more important for architectural applications. Since this absorption peak removes the red part of the spectrum, the transmittance colour of coatings displays neutral blue or purple [12, 161]. Other than these, coating thickness and the dielectric properties of the surrounding matrix [12], the particle morphology [160], and the regularity of spacing also influence colour.

The optical absorption of the nanoparticles due to their interaction is proportional to $(R/d)^{2L+1}$, where R is particle radius, d is the interparticle distance, and L is the multipole order (L=1 for dipole, L=2 for quadrupole, etc.) [155]. It is obvious that reducing the interparticle distance and/or increasing the particle diameter will increase this source of absorption. The presence of this peak is therefore indicative of aggregation of the particles [41].

Genzel and Martin have shown that an approximate expression to model these effects may be obtained by noting that the plasmon resonance of non-contiguous nanoparticles will occur when [164]:

$$\varepsilon'_{Au}(\lambda) = -\varepsilon'_{m}(\lambda)\frac{(2+\phi)}{(1-\phi)} \qquad \text{(eq. 3-1)}$$

where λ is the wavelength of the light, $\varepsilon'_{Au}(\lambda)$ is the real part of the dielectric constant of gold, $\varepsilon'_{m}(\lambda)$ is the real part of the effective dielectric constant of the matrix surrounding the gold particle, and ϕ is the volume fraction of gold particles. Both $\varepsilon'_{Au}(\lambda)$ and $\varepsilon'_{m}(\lambda)$ may be functions of λ, however, $\varepsilon'_{m}(\lambda)$ is often taken as a constant [41, 164]. Experimental values for $\varepsilon'_{Au}(\lambda)$ may be found in the literature, and here we have fitted published data [1] with a fourth-order polynomial to yield an empirical expression.

$$\varepsilon'_{Au}(\lambda) \approx \sum_{i=0}^{4} a_i \lambda^i \qquad \text{(eq. 3-2)}$$

where $a_0 = 3.3777\times10^{1}$, $a_1 = 3.6141\times10^{-1}$, $a_2 = 1.3083\times10^{-3}$, $a_3 = -1.9057\times10^{-6}$ and $a_4 = 8.8682\times10^{-10}$. The particle size does not come explicitly into the Genzel-Martin expression. However, a more detailed analysis of the condition for plasmon resonance includes contributions from particle size [160], and it is these factors that explain the small red-shifting with increase in size, that is, also observed in practice.

The matrix around the particles consists of soda lime glass on one side, with ε of about 7, and air on the other, with ε of 1. Since the values of ε for air and glass are not particularly sensitive to wavelength whereas values for metals are, in this work $\varepsilon'_{m}(\lambda)$ in Equation (3-1) is replaced with a single value, that is, an average of the two media. The observed position of the plasmon resonance at the start of the experiments, for which $\phi \ll 1$, is 520 nm. Substitution of this value, $\phi=0$, and with the data of Equation (3-2) into Equation (3-1), indicates a value for ε'_{m} of approximately 1.75.

The position of the plasmon resonance due to dipole-dipole interactions can now be estimated as a function of ϕ. It is a simplified model in which no effect from shape and multipole interactions is considered. Thus this expression is correct only for discrete, mono-dispersed gold nanoparticles [165]. With high packing density, that is, ϕ above about 0.5, the effect of multipoles is not negligible [165]. Also, the shape of the particles does play a role as well, and the dipole-dipole interaction depends actually on interparticle distance, not on volume fraction. This latter point has been elegantly demonstrated by Rechberger *et al.* for lithographically prepared arrays of identical average volume fraction, and this will be discussed later [166].

The data of Ung *et al.* [12], derived for very precisely determined values of ϕ, are shown with Equation (3-1) in Figure 3-16. The agreement is excellent, especially for low-volume fractions up to ϕ=0.4. When the simulation results are examined for the higher volume fraction in detail, it can be noted that the experimental results from Ung *et al.* [12] are between the regression curves of the areal model and box model. Two trends, corresponding to the upper (areal) and lower (box) estimates of the volume fraction described earlier, are demonstrated. As discussed in section 3.2.4(e), the smallest volume fraction is from the box model while the largest is from the areal model (Figure 3-15), provided only a monolayer of particles is deposited on the substrate and no overgrowth of particles occurs during the deposition.

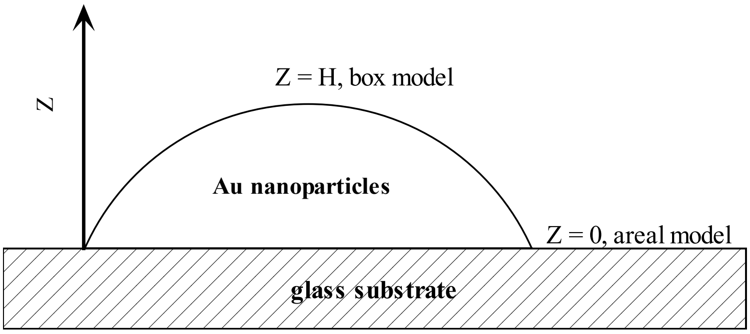

Figure 3-15 Illustration of area model and box model

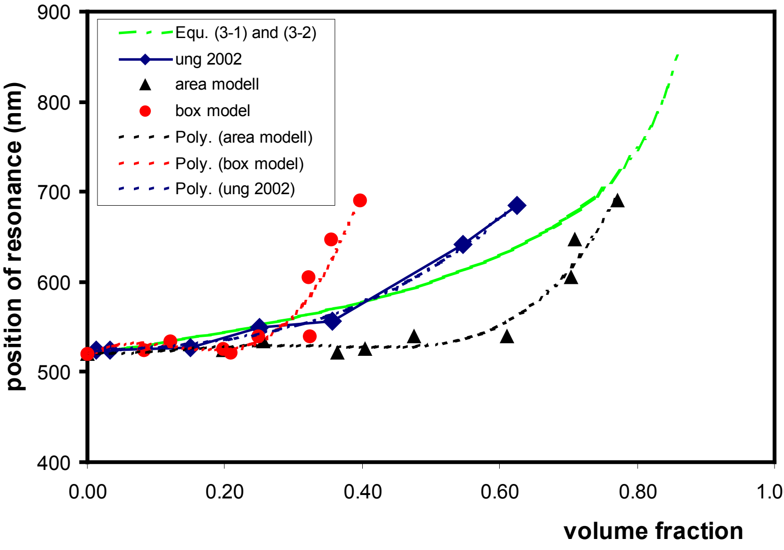

Figure 3-16 Effect of volume fraction on position of resonance peak

It is evident that, as expected, the areal estimate overestimates the volume fraction, while the box model underestimates it, and that these two alternatives straddle the predictions of Equation (3-1). In addition, the wavelength of maximum absorption increases somewhat faster, at higher volume fractions, than expected. This is due to the dipole interactions mentioned earlier. The fit of experimental data can be improved by re-addressing the nature of the “volume fraction” calculated, however, this will not be pursued at this point.

The smooth variation of hue of the coatings deposited at pH 5.1, pink through violet to blue, can therefore be explained as follows. Initially, the density of particles was low, so that most of the particles are isolated. This produces the well-known absorption peak at 520 nm without other peaks. In the second stage, while the density is still relatively low, two factors developed concurrently. First, the isolated particles grew and secondly, some of the particles aggregated as clusters. In this stage, two peaks (see Figure 3-7 III, V) coexisted, with the new peak at 700 nm due to the resonance of the aggregated nanoparticles, while the original plasmon resonance at 520 nm has red-shifted. In the third stage, there were few isolated nanoparticles left on the surface and the first plasmon resonance peak is no longer visible in the spectrum due to the significant broadening of the new peak. The 700 nm peak had also red-shifted due to the reduction of distance between dipoles caused by further agglomeration of the clusters.

At pH 10.0, the deposition rate was so fast that even at the first stage, the density of the nanoparticles was very high. There was not enough space for growth of isolated particles. Rather, a large number of agglomerated particles formed early during the deposition. These factors also restricted the growth of the nanoparticles. This explains why the peaks at 520 nm and 700 nm do not co-exist in these samples beyond the very earliest stages. As with the samples at pH 5.1, the decrease in interparticle distance led to red-shifting and broadening of the second peak.

3.4.2 Effect of particle morphology on film colour

The discussion of data obtained in this work has demonstrated that the colour is a function of the volume fraction of gold nanoparticles. However, this model ignores the effects of the morphology of the particles and other factors on the colour of the coating.

In Figure 3-17 and Figure 3-18, we show two coatings of similar density and particle size, but different styles of aggregation. Figure 3-17(a) shows substantially isolated particles of 60 nm diameter, and the corresponding spectrum (Figure 3-18(a)) shows a peak at 520 nm, as expected from individual particles. In Figure 3-17(b) it can be seen that nanoparticle clusters aggregated from much smaller particles. The corresponding spectrum (Figure 3-18(b)) was characterised by a broad absorption at ~655 nm, due to dipole-dipole interactions between the aggregated nanoparticles, and the peak at 520 nm has been almost swamped in the spectrum, except for the slight shoulder on the broadened peak at 520 nm.

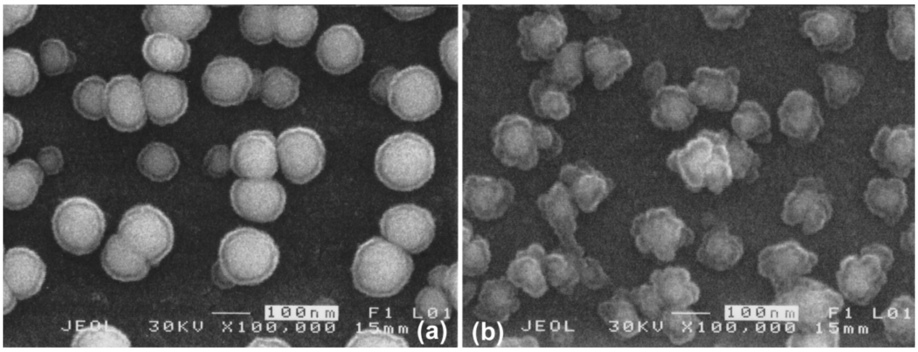

Figure 3-17 Different patterns of gold nanoparticle clusters

((a) Isolated 60 nm gold nanospheres, (b) Gold nanoclusters aggregated by smaller particles.)

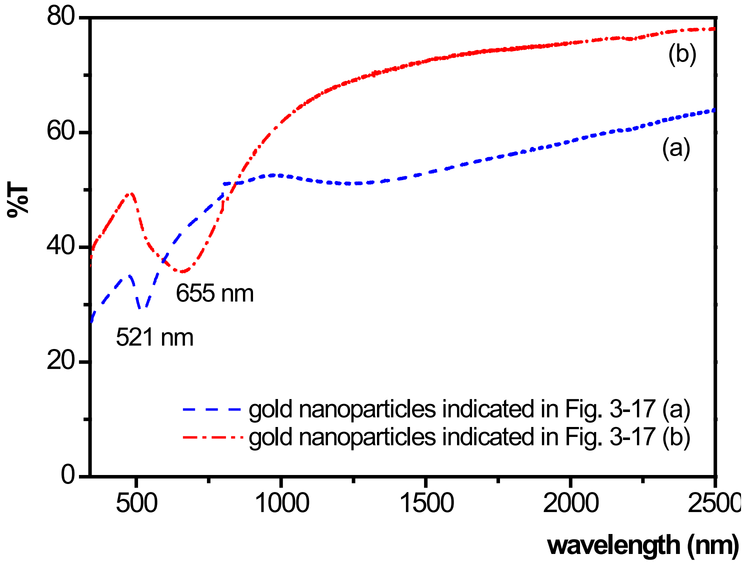

Figure 3-18 Optical properties of gold clusters with different morphologies

Table 3-3 Influence of aggregating mode on resonance plasmon peak.

Sample	Areal fraction	"Box" volume fraction	Average radius of hemisphere in model, nm	Plasmon resonance, nm
(a) Single isolated round	0.360 ± 0.102	0.175 ± 0.045	57.8 ± 16.7	521
(b)Aggregated small particles	0.375 ± 0.032	0.167 ± 0.021	21.4 ± 8.0	655

The areal and "box" volume fractions of the two samples are listed in Table 3-3. The statistical results are sampled from 956 and 1,448 particles individually. There are no substantial differences for volume fraction in either the areal model (0.36 and 0.375) or in the box model (0.175 and 0.167). Therefore, the change the spectra (Figure 3-18) comes only from the morphologies of the particles. In this case, the colour depends on particle morphology, and not on volume fraction. Our work further affirmed that different patterns of aggregation could result in quite different spectra, even in coatings of similar average density and similar nominal particle size. The importance of this observation is that it shows how red-shifted films can actually be obtained without necessarily overtly sacrificing the transparency of the coating. This is useful in the context of architectural applications, since better infrared shielding could be achieved with the same quantity of gold being applied.

The optical properties of gold nanoparticles on the glass substrate are therefore mainly determined by two factors: one is the property of the gold nanoparticles acting as well-isolated singular units, and the other is the collective property of particular clusters. The influence of the second factor is more pronounced at high particle densities. However, both contributions must be taken into consideration.

3.4.3 Adhesion of gold nanospheres on glass

Nanoindentation not only measures mechanical properties [167, 168], but also evaluates adhesive and abrasive properties of thin films [158]. In thin film adhesion testing, load is applied to the film until it delaminates from the under-layer or substrate. For isolated particles or semi-continuous film, the method is not appropriate [169].

The scratch test, which predominantly characterises the ability of a film to withstand abrasion, is more suitable for isolated particles and semi-continuous coatings. In this test, both normal and lateral forces are applied to the indenter, and removal of the particles under the different normal forces indicates the degree of adhesion of the film to the substrate [169, 170].

As pointed out by Burnett *et al.* [171], experimentally a number of other factors as well as interfacial strength control the minimum critical load (P_r) obtained from the scratch test. These factors include film thickness, mechanical properties of both film and substrate (Young's modulus), friction between stylus and coating, internal stress in the coating etc. [172]. Once critical load is exceeded, the detachment of gold nanoparticles on the glass substrate occurs. For the results obtained in this work, the critical load is between 20 and 30 μN. The disadvantage of this method is that there is no possibility of comparison between different systems. Comparisons are only appropriate for thin films prepared with identical situations.

3.4.4 Error analysis for mechanical properties of nanoindentation

Figure 3-19 shows plots of load-displacement for three indents on gold nanoparticles on the glass. The red curve indicates an indent performed on the substrate alone, and the load-displacement curve shows a typical brittle solid type material, that is, linear behaviour to fracture and little, or no permanent plastic deformation. The green curve indicates an indent made on a cluster of nanoparticles and shows primarily nanoparticle effects. The data in this case reveals a ductile solid with significant permanent deformation [156]. The blue curve represents an indent made on a small nanoparticle and initially follows the green curve, indicating primarily nanoparticle effects. Deviation from the green curves occurs as the tip encounters the stiffer substrate and the curve rises parallel to the red curve. The results suggest that, even with an applied force of as small as 5 µN in the measurement of nanoparticles, the substrate effect should be taken into consideration carefully. Figure 3-21 shows a 3D image of a 5 µN indentation on a cluster of nanoparticles. The depression resulting from the indentation is clearly imaged and thus shows the permanent deformation has occurred within the Au subjected to the load.

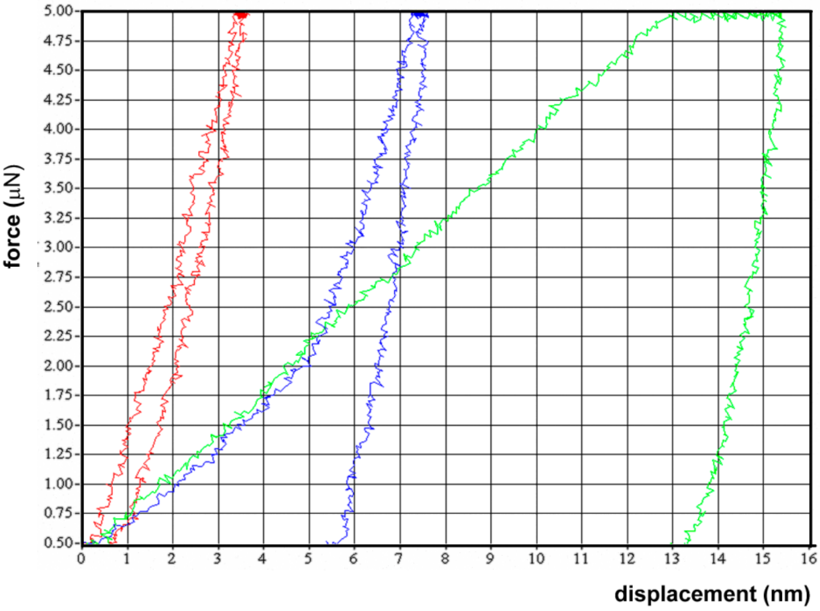

Figure 3-19 Plots of load versus displacement for three indents of film of gold nanoparticles on glass.

(The red curve shows effects of glass substrate, blue shows a combination of the substrate and nanoparticles, green shows effects of gold nanoparticles.)

It was noticed in the load-displacement curve of the gold nanoparticles that displacement occurred at a constant load of 5 µN. There are two apparent possibilities: one is creep as a result of the time-dependant plastic flow of the materials. The other is the thermal drift of the instrument due to thermal expansion or contraction. Thermal drift is thought to be the major causes since creep of gold at ambient temperature is unlikely.

The relative hardness and relative elastic modulus of gold nanoparticles can be calculated from the load-displacement curve. The hardness of gold nanoparticles is obtained from [156].

$$H = \frac{P}{A} \tag{eq. 3-3}$$

in which P is the maximum load applied, A is the area of the contact.

Since the cubic corner indenter tip is utilised during the experiment, the contact area is determined by:

$$A = 3\sqrt{3} h_P^{\ 2} tg^2 \theta \tag{eq. 3-4}$$

in which, h_P is the "plastic" depth of penetration, θ is the semi-angle (face angles of pyramidal face with the central axis of the indenter).

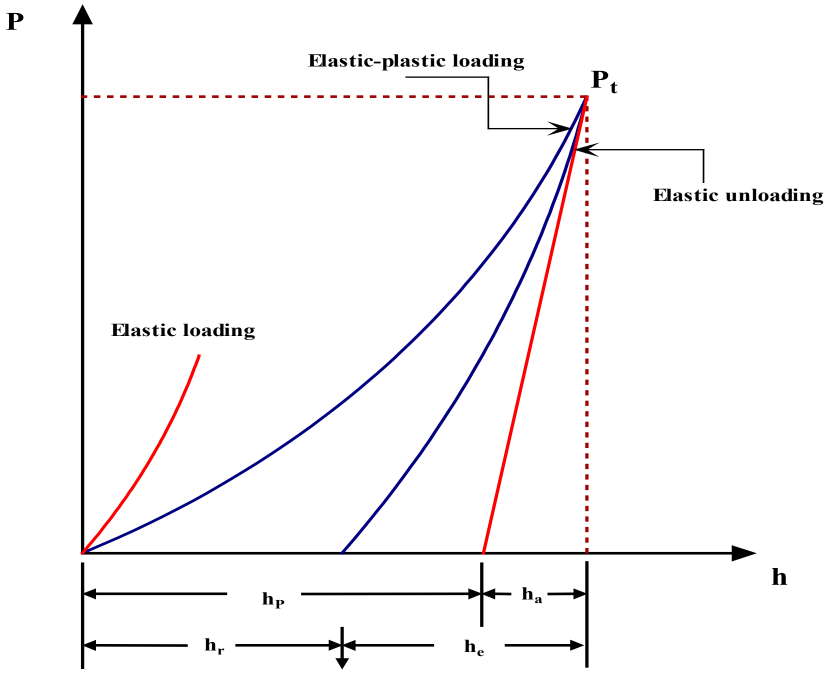

Figure 3-20 Load-displacement for elastic-plastic loading, followed by elastic unloading

(h_p is the depth of the residual impression, h_a is the distance from the edge of the contact to the specimen surface at full load, P_t is maximum load, h_e is the elastic displacement during the unloading of the actual cone, h_r is the depth of the residual impression, Redrawn from [156].)

The semi-angle (θ) of the cubic corner tip is 35.26°. Hence the hardness of the gold nanoparticles in this case, is derived as 9.41×10^9 N/m^2. The result is about 20 times higher than the bulk gold, which is around 4.0×10^8 N/m^2.

There are numbers of possible sources of error in nanoindentation measurements. The geometry of the actual indenter contributes significant factors [156]. Non-ideal geometry of the indenter may cause huge differences in the contact area, depending on the penetration depth. For the conical indenter with 10 nm of penetration depth, the area ratio of actual indenter to ideal indenter reaches as high as 10 [156]. This partly explains the extremely high results obtained from the nanoindentation test. The geometrical error is reduced by increasing the h_p. The correction factor (ratio of actual contact area to ideal contact area) reduces to 4 and 1.2 for the 50 nm and 100 nm penetration depths respectively.

The initial penetration depth of indenter also further exaggerates the error. The height measurement should start from the free surface of the sample, therefore the indenter has to reach the surface first. In practice, a minimum force has to be applied on the tip of the indenter to make sure of the initial contact. The actual measurement starts from the impression left from this initial contact. The force, should be as small as possible, was technically determined by the sensitivity of the instrument, that is, 1 μN in most of instruments. For the nanoindentation, the load is usually as small as 5 μN, thus the elastic-plastic deformation caused by initial penetration is not negligible.

The elastic-plastic depth of the cubic corner indenter of loading is given by:

$$h = \sqrt{P}\left\{\left(3\sqrt{3}Htg^2\theta\right)^{-\frac{1}{2}} + \left[\frac{2(\pi-2)}{\pi}\right]\frac{\sqrt{H\pi}}{2\beta E^*}\right\} \qquad \text{(eq. 3-5)}$$

upon unloading, the relationship between load and depth of elastic deformation is given by:

$$h_e = \sqrt{P}\frac{\pi}{2E^*}\cdot ctg\alpha' \qquad \text{(eq. 3-6)}$$

thus, the residue impression h_r is deduced from:

$$h_r = \sqrt{P}\left\{\left(3\sqrt{3}Htg^2\theta\right)^{-\frac{1}{2}} + \left[\frac{2(\pi-2)}{\pi}\right]\frac{\sqrt{H\pi}}{2\beta E^*} - \frac{\pi}{2E^*}\cdot ctg\alpha'\right\} \qquad \text{(eq. 3-7)}$$

In Equation (3-7), the hardness, H; semi-angle of indenter, θ; geometry correction factor, β; combined angle of the indenter and the residual impression, α'; and combined modulus E^* are all the same in both the initial contact and test loading. Therefore, the depth of initial penetration, h_r is proportional to the root of the load. When bulk gold data were substituted, it was found $h_r >> h_e$, thus the height caused by initial penetration h_i is:

$$h_i = \sqrt{\frac{P_i}{P}} \cdot h \qquad \text{(eq. 3-8)}$$

in which P_i is the load applied in the initial contact. In the experiments carried out here, the initial and following loadings are 1 and 5 μN accordingly, which indicates the displacement of the following loading should be expressed as:

$$h_p' = h_{pi} + h_p \approx (1 + \sqrt{\frac{P_i}{P}}) \cdot h_p \qquad \text{(eq. 3-9)}$$

Once these factors (geometry and initial penetration) are taken into consideration, the hardness of gold nanoparticles deposited on the glass is 4.5×10^8 N/m^2, which is very close to the literature value of bulk gold [173].

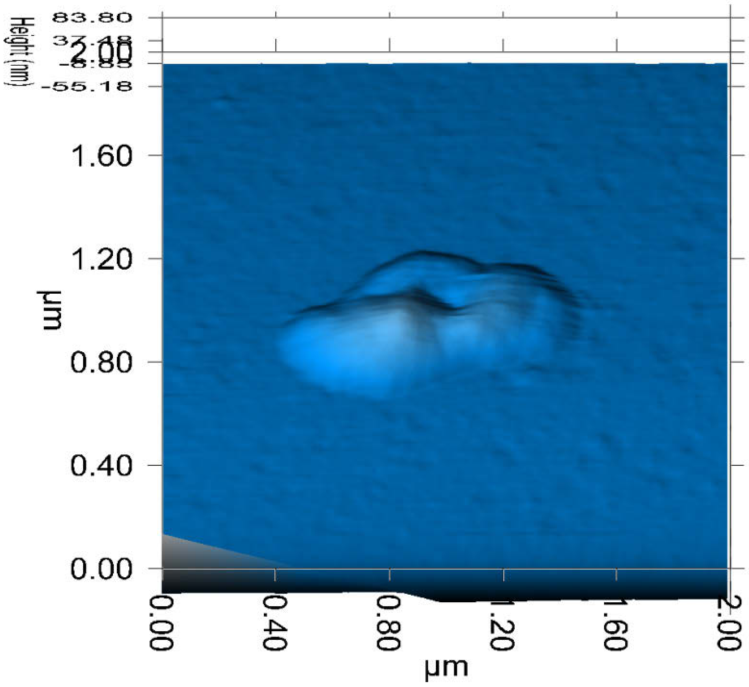

Figure 3-21 The gold nanoparticles after 5 μN of indentation

The other important mechanical property, derived from the load-displacement compliance curve, is modulus E*. The quantity E* combines the modulus of the indenter and the gold nanoparticles is given by:

$$\frac{1}{E^*}=\frac{1-\nu^2}{E}-\frac{1-\nu'^2}{E'} \qquad \text{(eq. 3-10)}$$

in which E' and ν' are the elastic modulus and Poisson's ratio of the indenter.

The combined modulus E* can be determined from the cubic corner tip indentation by the multiple-point unload method [156].

$$E^*=\frac{dP}{dh}\cdot\frac{1}{2}\cdot\frac{1}{\beta}\cdot\sqrt{\frac{\pi}{A}} \qquad \text{(eq. 3-11)}$$

if the previous error analysis is taken into consideration, the combined modulus for the gold nanoparticles *E**=44.5 GPa, which is within 4% of the literature value of bulk gold 46 GPa [173].

3.5 Summary

This study investigated the effect of pH on the optical properties of gold nanoparticle coatings formed on glass. The work has been motivated by the desire to develop window coatings that would attenuate solar radiation while exhibiting an acceptable hue. The obtained particles nucleate and grow directly on the surface of the glass, rather than in the coating solution. Coatings consisting of isolated gold nanoparticles exhibited the well-known plasmon resonance at ~520 nm on the glass substrate and were pink-coloured. However, the absorption peak due to particle-particle interactions, which is at about 700 nm, could be developed with an increase of coating density. This peak could be broadened and red-shifted by increasing the deposition time. Such coatings were blue or blue-grey in transmission, and would be more suitable in principle for architectural applications than the pink ones. The most desirable blue-grey coatings were obtained after deposition at pH 10, and displayed a significantly different morphology from those deposited at a pH of 5.1. The extent to which the position of the plasmon resonance can be modelled as a function of volume fraction was assessed, and the reasons for deviations from this model examined.

The crystal structure and mechanical properties of the gold nanocoating by wet chemical deposition were also investigated. The XRD results indicated that the gold nanospheres have the FCC structure with some degree of {1 1 1} texture. The width of the peaks in the spectrum also indicates small particle size and/or high intrinsic stress within the film. Young's modulus, microhardness and adhesion of gold nanoparticles on the glass substrate were also explored by nanoindentation. The errors relating to the nanoindentation measurement were analysed in detail. The results of the mechanical properties of gold nanoparticles are close to the literature value of bulk gold.

4. Nucleation of semi-transparent gold nanosphere coatings on glass

4.1 Introduction

In Chapter 3, aqueous deposition of gold nanosphere coatings on glass for architectural application has been demonstrated. We have previously argued that this low-temperature, wet chemical process has significant possibilities for this application [13], since it is potentially far cheaper than vacuum sputtering or chemical vapour deposition. Thin films with a neutral blue colour and useful solar-screening capabilities have been produced [13, 174], and the hue seems to be generally acceptable to the potential end-users. The process is quite flexible, and could, in principle, be applied on the tail end of an existing float glass production line, or off-line. The coating material is inert and, provided that it is not abraded, should survive for the lifetime of the window. However, there are still some disadvantages associated with these coatings. In particular, they exhibit only a modest degree of spectral selectivity between the visible and near-infrared region [175], with a Figure-of-merit, T_{vis}/T_{sol}, of ~0.8, where T_{vis} is the proportion of the visible spectrum, that is, transmitted and T_{sol} the proportion of the total solar spectrum transmitted [174, 176]. Ideally, a solar control application requires 100% blocking of the infrared, and 100% transmission of the visible, corresponding to a T_{vis}/T_{sol} of 2.08 for standard solar radiation [174]. In addition, it would be useful if a wider range of colour tones and greater control of them were available in these coatings.

In the previous chapter, it was found that the transmission spectra of the gold nanoparticle film directly relate to the nucleation process of the gold nanoparticles on the reaction interface. Coatings of similar average density and similar nominal particle size, but with different patterns of aggregation, could result in quite different spectra.

In this chapter, the relationship of the transmission spectra of the gold nanoparticle coatings with their nucleation and growth on the glass surface is investigated. The differences in the nature of nucleation and growth in the deposition process can cause coatings of similar gold content to exhibit quite different transmission spectra. These effects may be controlled by addressing the nature of the glass surface (which largely controls the rate of nucleation of particles) [177] or by manipulation of parameters such as the pH or temperature of the solution (which tend to control the rate of growth).

4.2 Experimental

4.2.1 Glass surface pre-treatments

Ethylene diamine, hydrazine, and sodium hydroxide were obtained from Aldrich, while HCl, HNO_3 were obtained from BDH, H_2SO_4, from Q-Store, $Na_2B_4O_7 \cdot 10H_2O$ was purchased from Unilab, $SnCl_2 \cdot 6H_2O$ and HF were from Sigma, NH_4HF_2 was from AJAX Univar. Gold was sourced from AGR-Matthey. All chemicals were used as received. All H_2O used was purified by double-distillation. A 0.10 M $HAuCl_4$ solution was prepared as described in the previous chapter. Buffered hydrofluoric acid (HF) was prepared by dissolving 20 g NH_4HF_2, 5 mL 49% HF and 100 mL of 37% HCl in 1 L of distilled water immediately before use.

Table 4-1 Different pre-treatment processes for the surface of glass

	(a)	(b)	(c)
Process	98% H_2SO_4 boiling for 30 minutes	1:1 H_2SO_4/H_2O boiling for 30 minutes[178]	Buffered hydrofluoric acid, 1 minute

Generic soda-lime glass microscope slides (1 mm thick) were obtained from Livingstone Scientific, and their surfaces were pre-processed in one of three ways (Table 4-1). These treatments were selected to provide different kinds of surface:

(a) because it is well known to oxidise organic contaminants,

(b) because it is known to both produce a nanoscale rough surface on glass and remove sodium [178];

(c) because it reputedly etches the glass to a smooth finish (it is an industry standard solution applied to pre-treat glass prior to coating [30, 179]).

Thereafter, the slides were pre-treated for two minutes in 0.1% aqueous $SnCl_2$, and rinsed with pure water before they were exposed to the coating solution.

4.2.2 Gold nanofilm deposition

The coating solution must be made up immediately before use, and comprised 0.0004 M

$HAuCl_4$, 0.015 M N_2H_4 and 0.03 M ethylene diamine in pH 8 buffer, which was made with 100 mL of 0.025 M $Na_2B_4O_7 \cdot 10H_2O$ (borax) and 41 mL of 0.1 M HCl. It was confirmed that the pH stayed constant during the deposition.

4.2.3 Materials characterisation

(a) Transmittance

A Cary 5E UV/Vis/IR spectrophotometer, working in the range of 170 nm to 4300 nm and with a resolution of 0.5 nm, was used to inspect the visible-IR transmission spectrum of the samples. The scanning rate was 5 nm/s with spectral bandwidth (SBW) of 2 nm.

(b) Surface composition of treated glass

X-ray photoelectron spectroscopy (XPS) spectra of the surface of the glass samples were recorded using Al K_α radiation (1486.6 eV) at 20 eV and 10^{-9} Torr. The experimental data were calibrated with the carbon peak that was always shown as a contamination at 285 eV.

(c) Dynamic contact angle

The dynamic contact angles (DCA) were obtained with a Cahn DCA-322 DCA analyser using double-distilled water. The reason for choosing water rather than other organic media is that the deposition occurs in aqueous solution. A stage speed of 200 mm/s was applied to advance and recede the sample from the liquid. The surface energies reported are the average of five measurements.

(d) Morphology of gold thin film

The morphology of deposited gold was characterised using an LEO scanning electron microscope (SEM) with in-lens images at 2-30 kV, and with a Dimension 3100 atomic force microscope (AFM) using an Ultrasharp® tip.

(e) Size distribution

The distribution of gold nanoparticle diameters at different stages of the deposition was obtained from the SEM images using ImageJ (National Health Institute). The software allowed the user to map an image of the coating into an array of hemispheres, which could then be analysed further. The height-to-diameter ratio of the particles was obtained from the AFM image files using WSxM 3.0 of Nanotec Electronica, Spain. Seventy particles were sampled on each surface. The radii measured on the AFM were corrected with Equation (4-1), which is determined from SEM images of the same samples and a hardball model of AFM tips [42], and accounts for the fact that the AFM over-estimates such distances, due to interference of the tip with the sides of the nanoparticle (Figure 4-1)

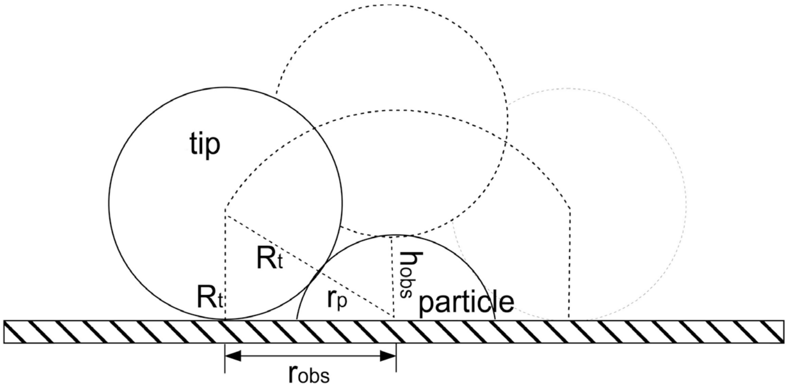

Figure 4-1 Hardball model to correct over-estimation of radius of gold nanoparticles by atomic force microscopy

$$r_P = \sqrt{R_t^2 + r_{Obs}^2} - R_t \qquad \text{(eq. 4-1)}$$

In Equation (4-1), r_P is the radius of a real gold nanoparticle, R_t is the radius of the AFM tip, r_{Obs} is the radius of gold nanoparticle observed with AFM. R_t was around 10 nm, according to the information from the manufacturer.

(f) Emissivity

The emissivity of glass slides with coatings of gold nanoparticles was measured with a Windbourn Emissometer. The glass slides with fresh thermally-deposited copper and/or gold were utilised as standards. The emissivity of a sample was calculated from Equation (4-2):

$$\varepsilon = 1 - \frac{V_{sample} - V_{zero}}{V_{s\tan dard} - V_{zero}} \cdot R_{s\tan dard} \qquad \text{(eq. 4-2)}$$

in which V_{sample}, V_{zero}, $V_{standard}$ are the potential of sample, blank, and standard respectively. $R_{standard}$ is coefficient of standard. For copper, $R_{standard}$ is 0.97.The result is the average of three measurements.

4.2.4 Simulation of nucleation process by classical nucleation theory

The effect of interfacial energy on the nucleation of gold in aqueous solution is simulated by classical nucleation theory [173, 180, 181]. It is based on the premise that random aggregations of atoms occur spontaneously to form nuclei of radius r. If W_f is the work required to form a nucleus, then any randomly formed nuclei can only grow if dW_f/dr is <0. The theory predicts that there is a critical size, r^*, and volume, V^*, of randomly formed nucleus, above which $dW_f/dr<0$, and below which re-dissolution will occur. W_f may be estimated from a consideration of the interplay of the driving force of the chemical reaction or phase transformation with the surface energies $\gamma_{Au/H20}$ and $\gamma_{Au/glass}$ required to create the nucleus.

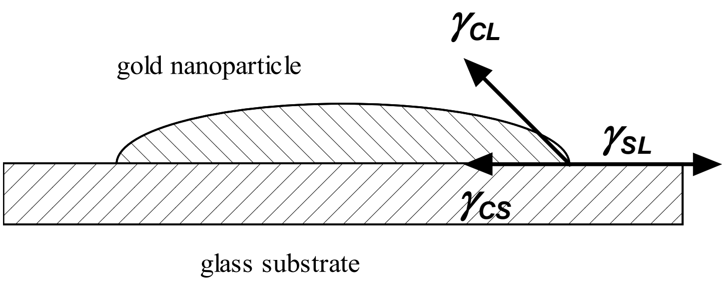

Figure 4-2 Gold nanosphere on glass substrate

For the cap-shaped particles of gold on the glass surface (Figure 4-2), the interfacial energy between substrate and liquid (SL), crystal and substrate (CS), crystal and liquid (CL) must be in equilibrium, expressed by:

$$\gamma_{SL} = \gamma_{CS} + \gamma_{CL} \cdot \cos\theta \qquad \text{(eq. 4-3)}$$

in which θ is the contact angle measured between the substrate and the nucleus cap, γ_{SL} is the interfacial energy of glass substrate and solution, γ_{CS} is the interfacial energy of gold nanoparticle and glass substrate and γ_{CL} is the interfacial energy of gold nanoparticle and solution. This relationship is the basis for a quantitative examination of heterogeneous nucleation and growth phenomena.

4.3 Results

4.3.1 Glass surface with different pre-treatment schemes

(a) Surface composition of etched glass surfaces

The surface composition of the glass substrate was characterised by XPS according to the procedure described in 4.2.3(b). The XPS spectra of the glass surfaces after different pre-treatments are shown in Figure 4-3. Sodium is found on untreated slides and on buffered HF-treated glass slides with a peak at 1075.4 eV. No sodium is found on the surface after etching with H_2SO_4, despite this element being a significant constituent of the type of glass used. On the other hand, the XPS spectra illustrated in Figure 4-4 indicate that glass slides with all three treatments showed a strong peak at 156.6 eV. This is due to the large amount of silicon remaining on the surface after etching with the buffered HF (Figure 4-4). Although it is well known that the HF is a strong silica stripper for soda glass, the content of silicon remained the same with the different treatments.

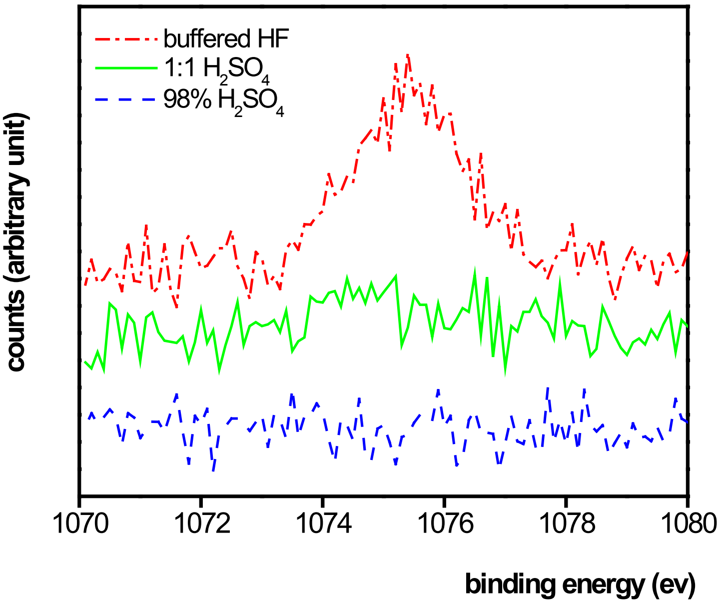

Figure 4-3 XPS spectrum for Na on glass surface with different pre-treatments

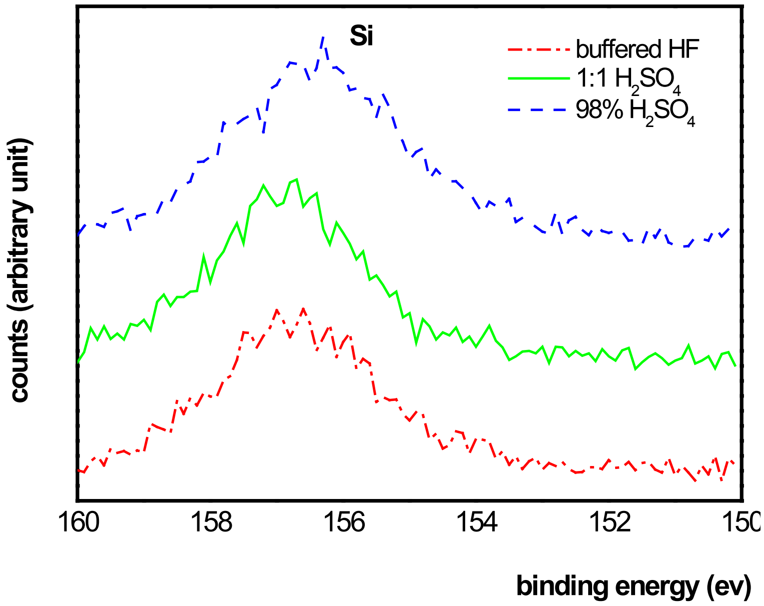

Figure 4-4 XPS spectrum for Si on glass surface with different pre-treatments

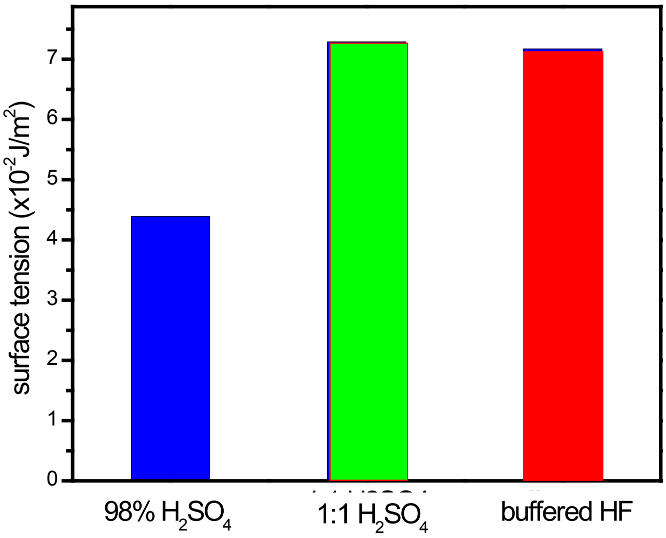

Figure 4-5 Surface tension of glass surface with different pre-treatments

(b) Dynamic contact angle of etched glass surfaces

The surface contact angles of glass slides with different pre-treatments were measured by dynamic contact angle. The average DCA results for 98% H_2SO_4, 1:1 H_2SO_4 and buffered HF are 0.044, 0.072 and 0.071 J/m^2 respectively (see Figure 4-5). After etching with 98% H_2SO_4, the surface of glass is hydrophobic rather than hydrophilic and its surface energy is markedly lower than those of the surfaces etched with 1:1 H_2SO_4 or buffered HF. The surface energies of the latter two were the same. It is believed that this was caused by difference of water-water interaction and water-substrate interaction [182].

(c) Morphology of etched glass surfaces

The morphologies of the etched glass surfaces with different pre-treatments were imaged by Dimension® 3100 atomic force microscope with tapping mode. The morphologies of the substrates are shown in Figure 4-6. The root mean square (RMS) of surface roughness is also reported for analyses of the AFM height information. Even though the RMS roughness for the glass surfaces treated with 98% H_2SO_4 and buffered HF are similar, 1.94 nm and 2.06 nm respectively, the textures of the surfaces are quite different. The morphology of the glass surface etched with HF displays an irregular lamellar structure, while that of the surface etched with H_2SO_4 shows a structure of mounds.

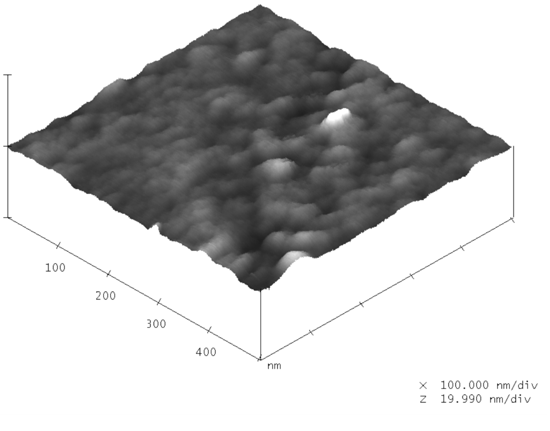

(a) 1:1 H_2SO_4

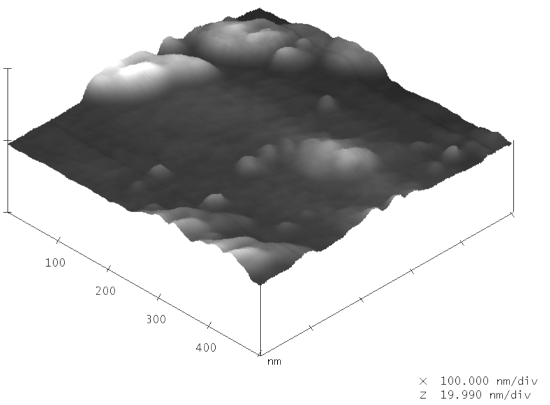

(b) 98% H_2SO_4

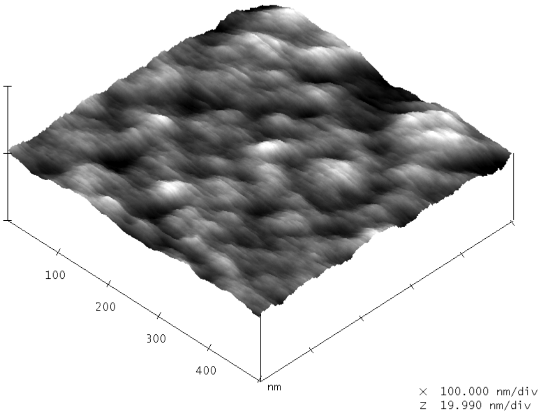

(c) Buffered HF

Figure 4-6 Typical morphology of glass surfaces produced by different etching processes

4.3.2 Optical transmittance of gold coatings on etched glass surfaces

The optical transmission spectra of gold coatings deposited on the different glass surfaces are indicated in Figure 4-7. Deposition on the HF-treated surface (surface Figure 4-6(c)) was observed to occur much more quickly than for the other two. To compare the optical properties, the pre-treated glass slides were therefore exposed in solution for various lengths of time to obtain similar transmittance in the visible region. It is found that gold particles grown on the surfaces treated with H_2SO_4 tended to develop dual absorption peaks at around 520 nm and 700 nm. However, coatings deposited on the glass surface treated with buffered HF manifested a single absorption peak at about 700 nm.

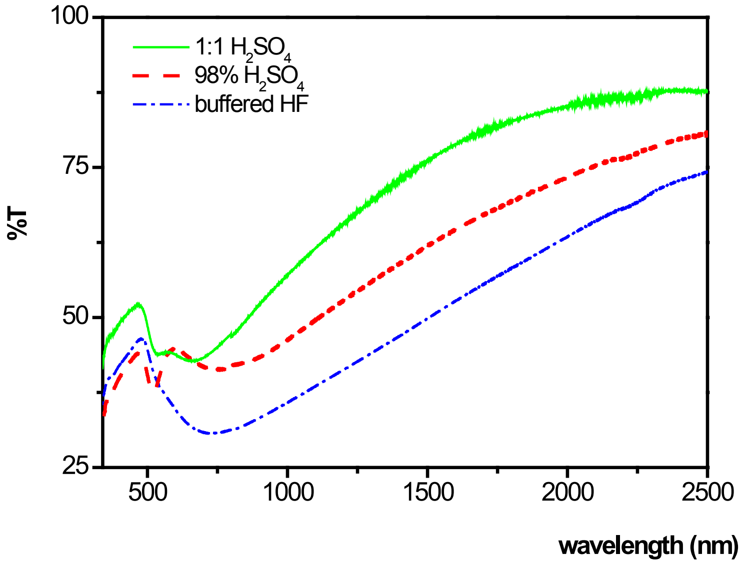

Figure 4-7 Transmittance spectra of gold nanohemisphere coatings on glass with different pre-treatments of the surface

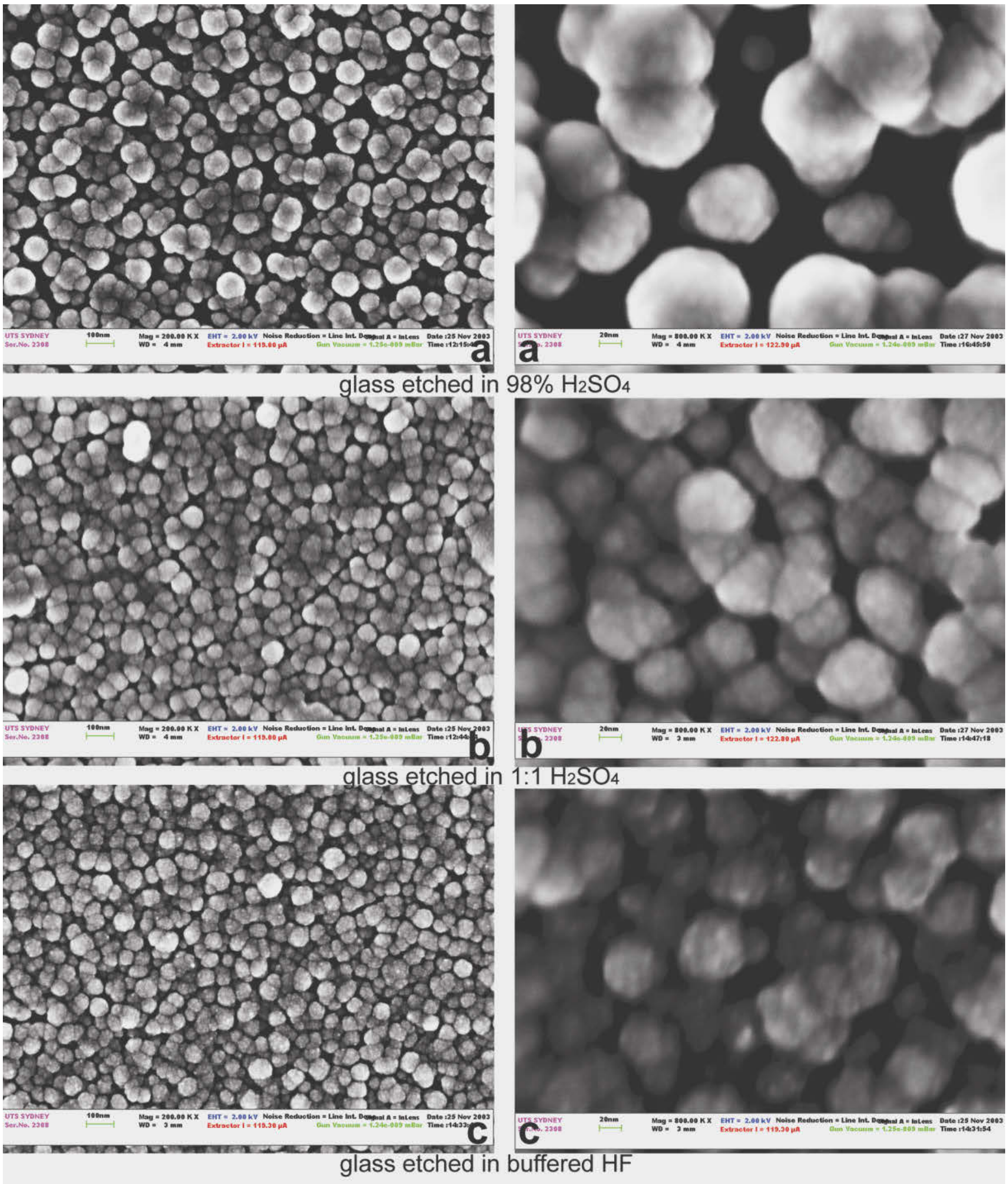

Figure 4-8 **Morphology of gold nanoparticles on glass with different pre-treatments of the surface**

4.3.3 Morphology of gold coatings on etched glass surfaces

(a) SEM images of gold nanofilms on etched glass surfaces

High resolution of SEM images was obtained using an LEO scanning electron microscope. The morphologies of the gold coatings on the different glass surfaces are shown in Figure 4-8, with the samples shown corresponding to the spectra in Figure 4-7. Both large and small particles co-exist for the substrate etched with 98% H_2SO_4. More isolated gold nanoparticles in the surface etched with H_2SO_4 (Figure 4-8 a, b) are observed, while most of the gold particles on the surface etched with buffered HF are within close proximity to one another. It is evident that the texture of the gold coating on the surface etched with HF is more uniform than that etched with H_2SO_4.

(b) Size distribution of gold nanoparticles on etched glass surfaces

Quantitative information of the size distribution of particles was obtained by analysis of the SEM images with Image J software. The average sizes of gold nanoparticles deposited on different pre-treated surfaces are listed in Table 4-2. The standard deviation shows that the distribution of particle size is broader on the surface etched with 98% H_2SO_4. The size distributions of gold nanoparticles are also indicated in Figure 4-9. The diameters of some particles are larger than 100 nm (Figure 4-9a), while others are around 40 nm. On the surface etched with buffered HF, the particles are more uniform and around 50 nm in diameter (Figure 4-9 c).

Table 4-2 Average particle size of gold nanoparticles on glass with different pre-treatments

Substrate	98% H_2SO_4	1:1 H_2SO_4	Buffered HF
Particle radius (nm)	39.0 ± 11.0	29.3 ± 8.4	23.3 ± 5.9

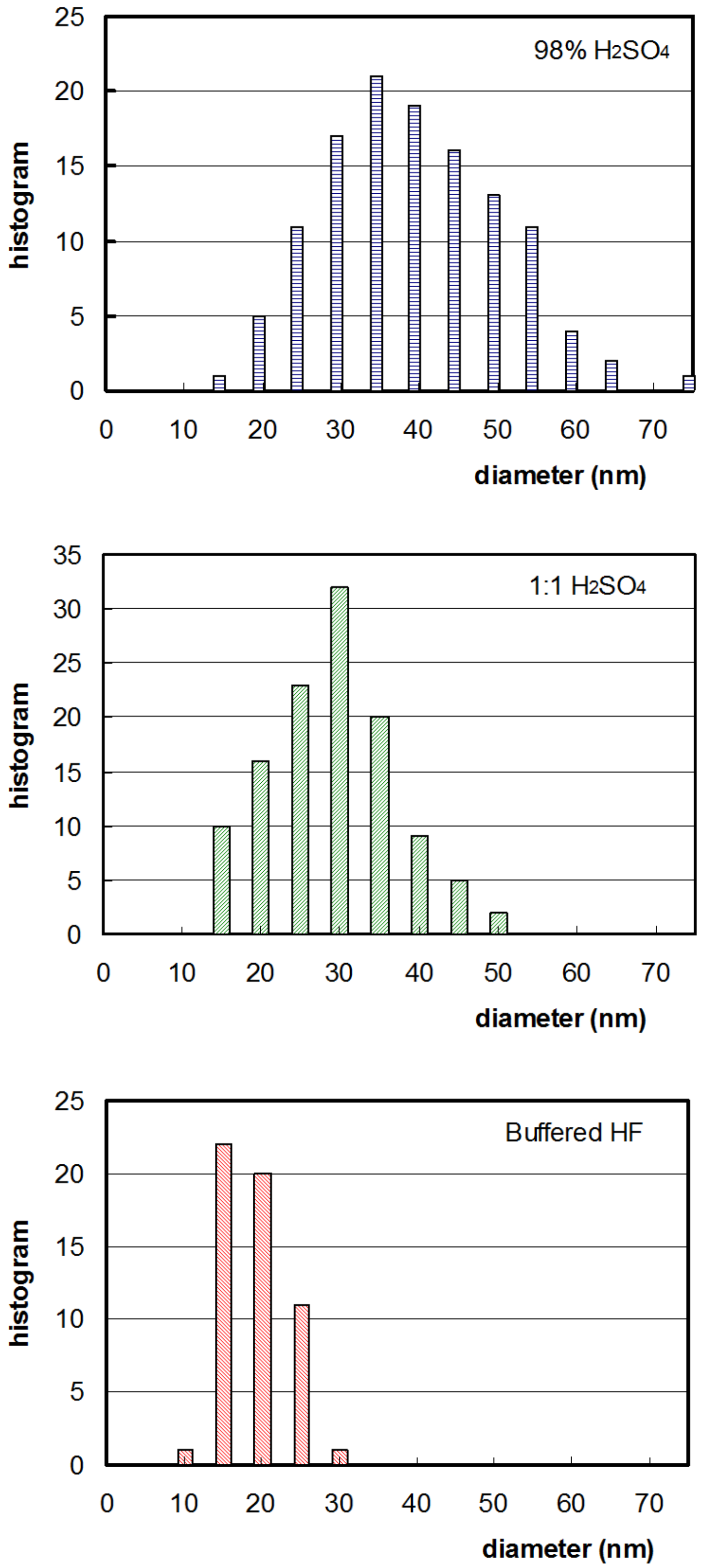

Figure 4-9 Size distribution of gold nanoparticles on glass with different pre-treatments

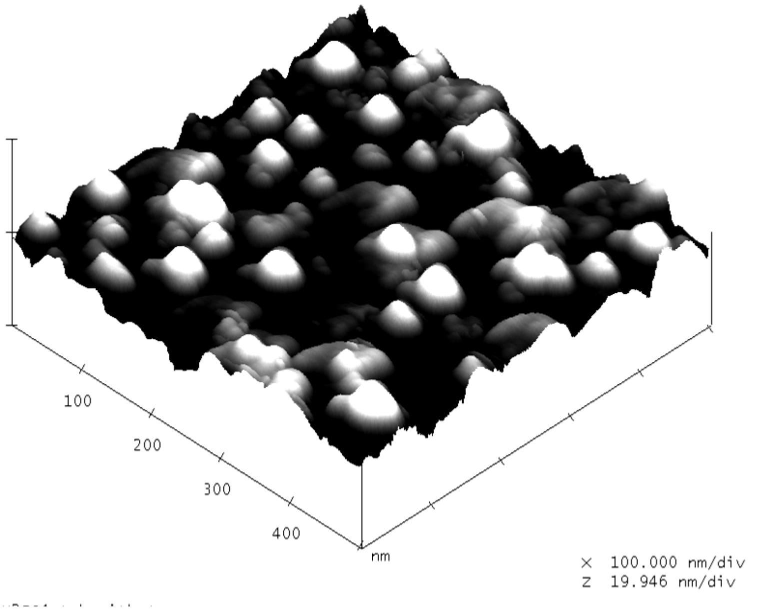

(a) glass etched with 98% H_2SO_4

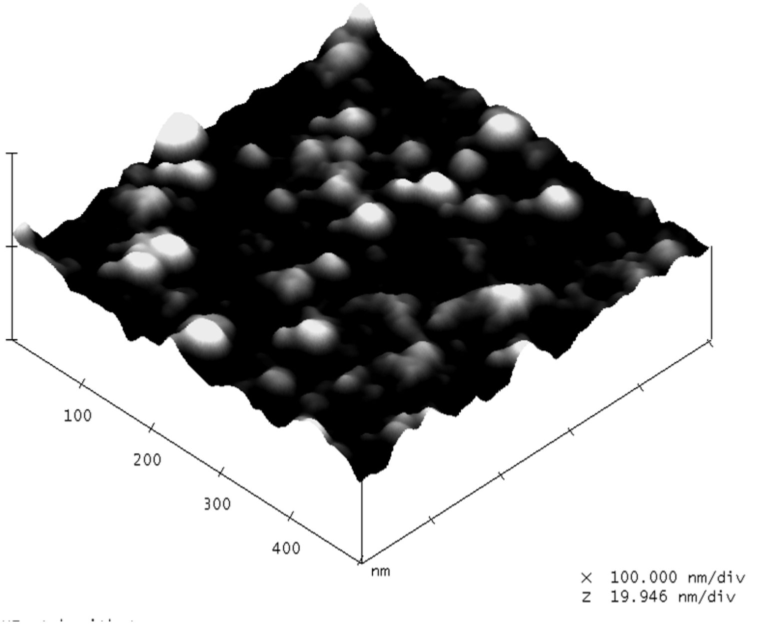

(b) glass etched with buffered HF

Figure 4-10 AFM images of gold nanoparticles on glass with different pre-treatments

(c) Morphology of gold nanoparticles in initial deposition stages on etched glass surfaces

To investigate the interfacial energy between the etched glass substrate and the gold nucleus, the shapes of gold nanoparticles in the very initial stages were imaged by Dimension® 3100 AFM. The glass substrates were only lightly tinted in order to obtain well separated gold nanoparticles. The radii of the nanoparticles from the AFM data were also corrected with Equation (4-1). The AFM images of gold nanoparticles in the initial stages are shown in Figure 4-10. Similar to the SEM images shown in Figure 4-8, the gold nanoparticles that nucleated on the surface pre-treated with buffered HF are smaller and more uniform. The shape of the particles is further explored in Figure 4-11, which shows the ratio of radius (R) to height (H) of the particles deposited on the surfaces etched with 98% H_2SO_4 and buffered HF, as measured using an AFM (Figure 4-10). These particular samples are treated in the deposition solution for a shorter length of time than the ones described in the preceding paragraph, in order that the particles would be smaller and sufficiently well separated for measurement of their dimensions. The mean value of R/H for the H_2SO_4-treated surface is 3.43 (σ =1.20) whereas, that of the buffered-HF-treated surface was 4.92 (σ =0.99). Thus, the particles deposited on the surface pre-treated with HF are on average considerably flatter than those formed on the surface pre-treated with 98% H_2SO_4. The relationship of size distribution and numbers of nucleation sites is evaluated by Kozisek *et al.* [183], who, in agreement with the above results, found that formation of new nuclei stopped due to the depletion of the active sites.

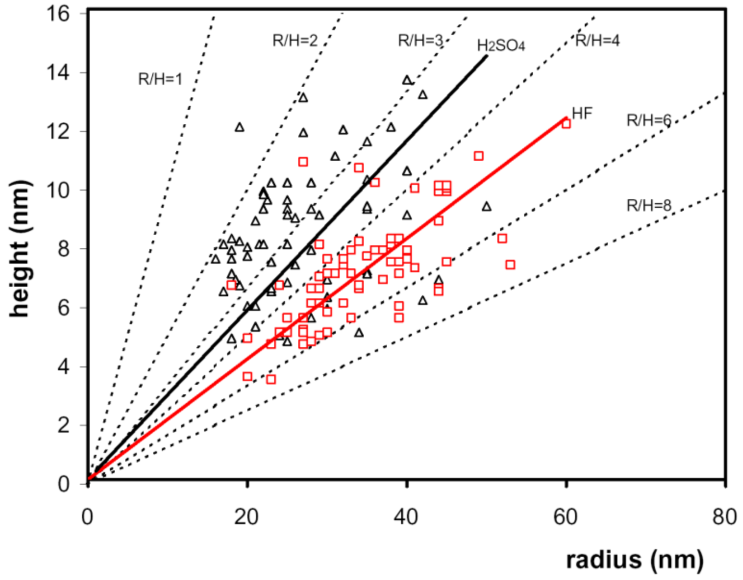

Figure 4-11 Aspect ratio (radius/height) of particles on different surfaces

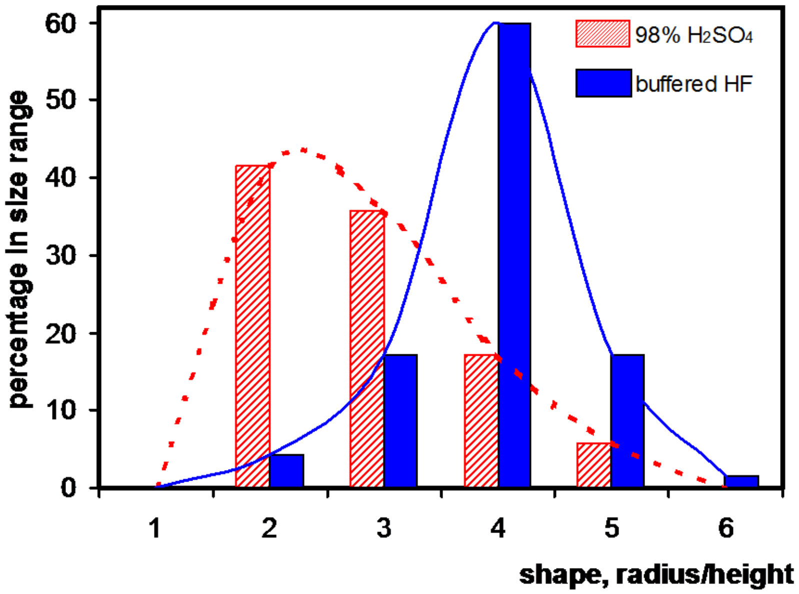

Figure 4-12 Aspect ratio (radius/height) of particles deposited on surface treated with 98% H_2SO_4 compared with that of particles deposited on surface treated with buffered HF.

(The trend lines shown are merely to guide the eye.)

The trend is further explored by a normalised histogram of R/H. It verifies that the aspect ratio (R/H) of particles deposited on the glass etched with buffered HF is flatter than those deposited on the substrate etched with 98% H_2SO_4. The data also show that the shapes of particles in both cases are “cap”-like, due to the very initial stage of deposition.

4.3.4 Emissivity of gold nanoparticle coating

The emissivities of different kinds of gold nanoparticle coatings were investigated. The samples represented different stages of deposition. The colours of coating varied from red to purple, blue, metallic blue and black, in transmittance (indicated in Figure 4-13).

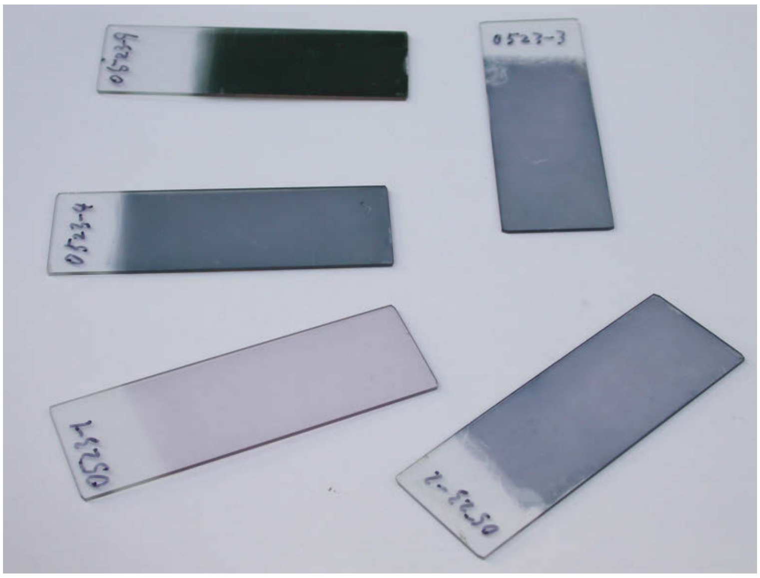

Figure 4-13 Colours of coatings of gold nanoparticles

The emissivity of the various coatings of gold nanoparticles are listed in Table 4-3. The colour of the coatings ranged from pinkish to purple, blue and metallic, which indicates different stages, extending from isolated particles, coalesced isolated particles, semi-continuous film and, finally, continuous film. The average result of three tests for each sample is listed. The variance of the measurements are indicated as standard deviation. It is evident that the very low emissivity of bulk metal surfaces does not apply to these nanostructured coatings.

Table 4-3 Emissivity of gold nanoparticle coatings

Sample	Colour	Emissivity	Sample	Colour	Emissivity
Glass	-	0.891±0.003	0517-6	Mix purple	0.907±0.001
0711-4	Reddish	0.897±0.011	0711-3	Blue	0.911±0.004
0521-6	Metal blue	0.802±0.040	0521-2	Purple	0.908±0.006
0521-4	Blue	0.896±0.016	0711-6	Purple	0.914±0.004
0517-16	Metallic	0.319±0.147	0711-1	Metal blue	0.378±0.041
Cu standard		0.030±0.005	Au standard		0.0479±0.040

The emissivity of a surface is the ratio of the energy radiated from it to that from a blackbody at the same temperature, the same wavelength and under the same viewing conditions. The emissivity scale, lying between 0 and 1, depends on the property of the materials. Higher emissivity indicates better absorbing capability.

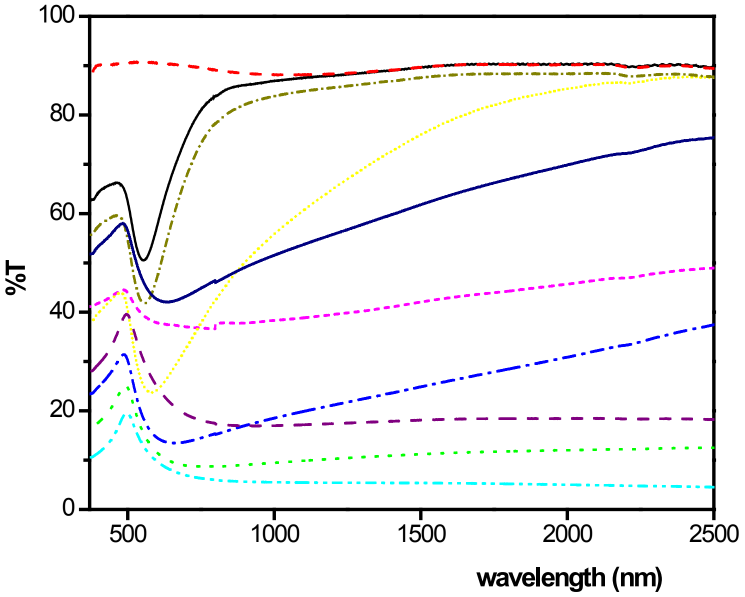

Figure 4-14 Transmittance spectrum of gold nanoparticle coating

Emissivities of different colours of gold nanoparticles coatings were measured. The transmittance spectra of these coatings are displayed in Figure 4-14. When the emissivity listed in Table 4-3 is matched to its optical transmittance spectrum, it is noted that the colour of the coating is not critical to the evolution of emissivity. The emissivity of gold nanoparticles remained similar while the colours of the coatings transited from red to purple and blue. According to the discussion in Chapter 3, it was realised that the colour of coatings of gold nanoparticles comes from isolated nanoparticles, which display pink, and particle-to-particle interaction, which display purple and blue. Therefore, the surface plasmons of gold nanoparticles and particle to particle interaction do not play an important role in the change of emissivity.

However, continuity of the film seems to play a very important role in the emissivity. There is an abrupt decline in emissivity with increasing thickness, which is also indicated by a drop of transmittance of the film in the infrared region. When the percentage of transmittance in 2500 nm changes slightly from 35% to 20%, the emissivity of the film drops from 0.95 to 0.03. From the discussion and morphology analysis in section 4.3.3, it was recognised that the formation of coatings of gold nanoparticles must go through various stages, from isolated particles to closely spaced particles, from semi-continuous islands to continuous film. So this critical point must also be the transition point for a coating going from semi-continuous islands to fully continuous film.

The finding is very useful in controlling the emissivity of coatings of gold nanoparticles, especially when regulations in some countries require the controlling of the reflectance to avoid “light pollution”. The existence of a critical point can help us find an “operating window”, in which a coating still has a quite high spectral selectivity but much lower reflectance.

4.4 Discussion

4.4.1 Effect of surface energy on nucleation of gold nanoparticles

Heterogeneous nucleation, although prevalent in the gold deposition process, is quite difficult to model because of a lack of knowledge of the interactions between the gold nanoparticles and the activated glass [184]. Nevertheless, the Gibbs free energy of the system is a reasonable indicator of the thermodynamic stability of different sizes of gold nanoclusters [185, 186].

The morphology, and hence the colour (for example [13, 62, 187]), of the coatings is largely controlled by the rate at which new particles nucleate on the surface, and their subsequent rate of growth. The critical size of nucleation r* depends on dW_f/dr. The smaller the r*, the less W_f is required. Classic nucleation theory may be somewhat simplified by a time-independent driving force, F of about -200 kJ per mole of Au, or about -2×10^{10} J/m^3 of Au^0 deposited, derived from the ΔG of the reduction reaction

$$2HAuCl_4 + 2N_2H_4 \rightarrow 2Au + 8HCl + 2N_2 + H_2 \qquad \text{(eq. 4-4)}$$

F is independent of time since, in this work at least, only the very early portion of gold deposited from the solution is taken up onto the test specimens, with the remainder being wasted by precipitation later on, after the test samples have already been removed from the bath.

For a spherical cap with n gold atoms, the reversible work of formation is given by:

$$\Delta G_n = n\Delta G' + \sum A_i \gamma_i \qquad \text{(eq. 4-5)}$$ ☐

where ΔG' is the difference in Gibbs free energy per atom of the new phase with reference to that of the initial phase, A_i is the surface area of a cluster of n atoms, and γ_i is the interfacial free energy per unit area.

According to classic nucleation theory and the geometrical relationship of this system, it can be shown that (Appendix 1):

$$\Delta G_n = n\Delta G' + \frac{f(\theta)\gamma_{CL}}{\beta \cdot r} \cdot 2n\pi r_{Au}^3 \qquad \text{(eq. 4-6)}$$

where β is the packing density of the face-centred crystal (FCC) lattice (0.74), θ is the contact angle of the crystal with the glass substrate.

$$f(\theta) = \frac{(2+\cos\theta)(1-\cos\theta)^2 \cdot \sin\theta}{1-\frac{3}{2}\cos\theta+\frac{1}{2}\cos^3\theta} \qquad \text{(eq. 4-7)}$$

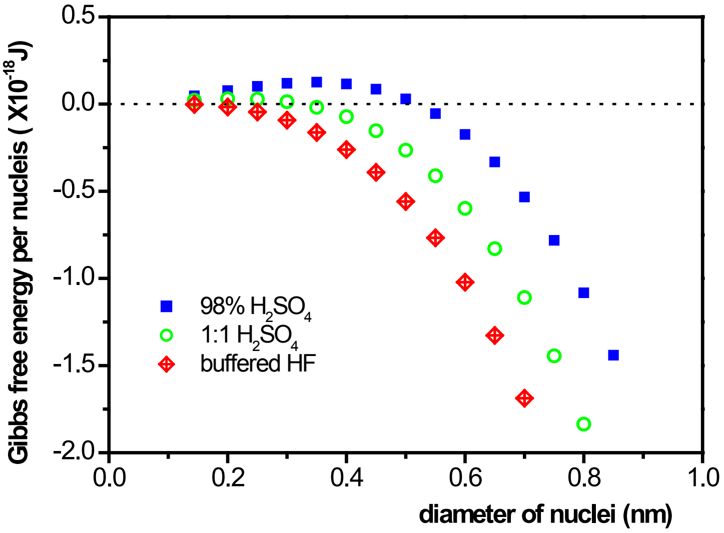

Figure 4-15 The critical nucleation size for different surface tensions substrate

The changes in free energy during the growth of gold nuclei are simulated in Figure 4-15, which shows the free energy of nuclei of different sizes and on different surfaces. For the lower interfacial free energy surface (pre-treated with buffered HF), the gold nucleation process appears to start very early. For the higher interfacial free energy surface (pre-treated with 98% H_2SO_4), the nucleation process is thermodynamically impossible before 0.5 nm in diameter, which indicates the nucleation process on the higher interfacial surface is more difficult than that on a lower interfacial free energy surface [188]. Here, we assume the nuclei were hemispheres. The nucleation took place sparsely without any coalescence during the process. Therefore, since nucleation was difficult on the surface pre-treated with 98% H_2SO_4, the nuclei tended to grow into fewer and bigger nanoparticles.

When the nuclei reach critical size r*, any further growth will result in dW/dr becoming negative, and therefore thermodynamically spontaneous.

The interfacial free energy, $\gamma_{Au/H20}$ of gold is likely to be in the range of 0.1-1 J/m^2, since that of a molten gold surface exposed to an inert vacuum environment is in the range 0.75 to 1.1 J/m^2 [189]. In aqueous environment, γ_{SL} is in the range of 0.3~0.4 J/m^2. Generally, certain other algebraic and geometric simplifications are also applied to this problem, and, since the driving force here is assumed to be a constant, the work to create such a particle may be expressed as [173]:

$$W_f = \left\{1 - \frac{3}{2}\cos\theta + \frac{1}{2}\cos^3\theta\right\}\left\{2\pi r^2 \gamma_{Au/H2O} - \frac{2\pi r^3}{3}F\right\} \qquad \text{(eq. 4-8)}$$

where θ in this case is the contact angle of the gold nucleus on the glass. θ may be derived from the shape of the particle (Figure 4-12), using the expression

$$\theta = 90 - \arccos\left[\frac{2RH}{R^2 + H^2}\right] \qquad \text{(eq. 4-9)}$$

Mean values for θ of 43.4º (σ=11.8º) and 29.7º (σ=6.6º) were obtained from the measurement of particles on the surfaces treated with 98% H_2SO_4 and buffered HF respectively. It is clear that the net effect of pre-treating the glass with buffered HF has been to lower $\gamma_{Au/glass}$ and thereby lower θ.

The free energy of 10^{-4} mol. of gold atoms deposited as uniform hemispherical caps on surfaces of different interfacial free energy is shown in Figure 4-16. The total free energy of these gold clusters was evaluated to indicate the stability of the system. From simulation, it can be seen, for the deposition on the lower interfacial energy surface, that the system is stable when the particle size is smaller than those deposited on the higher interfacial energy surface. This simulation result is also verified by the size distribution of the gold nanoparticles deposited on different pre-treated surfaces, indicated in Figure 4-9. For gold hemispheres deposited on the lower interfacial surface (pre-treated with buffered HF), most of the particles were within in the range of 40–70 nm. However, in the case of the higher interfacial surface (pre-treated with 98% H_2SO_4), most of particles grew to the range of 60–110 nm. From this simulation, it is evident that smaller clusters are stable on the surface etched with buffered HF.

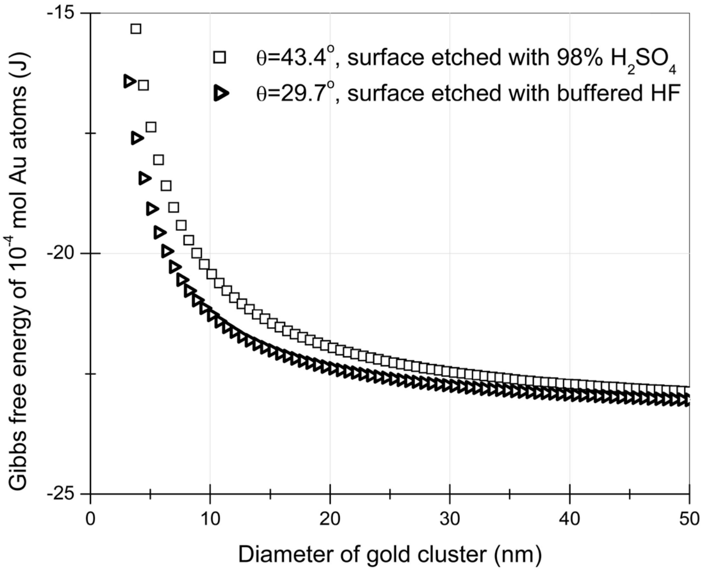

Figure 4-16 The free energy of 10^{-4} mol of gold caps compared for two surfaces as a function of particle size

The critical volume V^* of the nucleus can be obtained from (eq. 4-10):

$$V^* = \frac{16\pi}{3}\left(\frac{\gamma_{Au/H20}}{F}\right)^3 (1 - \frac{3}{2}\cos\theta + \frac{1}{2}\cos^3\theta) \qquad \text{(eq. 4-10)}$$

in which *F* is the time-dependent driving force of the reduction reaction, and *θ* is the contact angle of nucleus with the substrate.

V^* for the HF-treated surface ($\theta \approx 30°$) is reduced to only 24% that of V^* of the surface treated with the H_2SO_4 ($\theta \approx 43°$). Since a spontaneous aggregation of atoms must occur to achieve V^*, and the rate at which this event occurs at a certain temperature is given approximately by,

$$I \propto \exp^{-V^*} \qquad \text{(eq. 4-11)}$$

it follows that formation of critically sized nuclei will proceed at about twice the rate on the HF-treated surface.

A more accurate extraction of r^*, V^* or I from these data requires more analysis than can be presented here. However, it can be noted that the effect described will facilitate and accelerate the nucleation process on the HF-treated surface, causing a coating of more uniform particle size to form on it. Conversely, a slower rate of nucleation generally produces a broader distribution of particle sizes, with a less regular coating morphology, because particles formed earlier have more time and space to grow. These trends may be discerned in the histograms of Figure 4-9. Finally, it is noted that from Equations. 4-10 and 4-11 that since F is very large in this system and $\gamma_{Au/H20}$ is comparatively far smaller, V^* will always be very small, possibly less than 1 nm, and I will always be very large. Smaller V* is preferable in the proposed application because it produces fine and uniform particles on the glass with better spectral selectivity. However, there are also limitations. If the V^* is too small, the system will be very unstable, that is, spontaneous decomposition of the system would occur easily. This situation must be avoided during the operation for both engineering and economic reasons. Therefore, a proper pre-treatment is essential for successful control of the *in situ* deposition of spectrally selective gold coatings.

It has been demonstrated that interfacial energy plays a very important role since it affects the critical size of the nucleus (V*). With the right process of pre-treatment, the reaction will only occur at the selected substrate rather than anywhere else. These results strongly suggest that interlayers or pre-treatments that can promote the "wetting" ability of glass with regard to gold are essential in the production of transparent gold coatings on glass.

4.4.2 Effect of nucleation on transmission colour of coatings of gold nanoparticles

As discussed in Chapter 3, the colour of coatings comes from two surface plasmon absorption peaks in the visible and near-infrared region. The first peak is the isolated gold particle surface plasmon resonance peak around 520 nm. This peak is a weak function of size and dielectric constant of the surrounding media. For example, it may only be red-shifted a few tens of nanometres by an increase of the particle diameter or of the dielectric constant of the ambient medium. Rather, most of the useful functionality in the present system comes from the absorption peak at around 700 nm [190]. The peak at around 700 nm is clearly due to dipole-dipole interactions between particles that are close together [12, 152, 161, 164, 191].

Is the gap between particles on the surfaces treated with sulphuric acid (Figure 4-8) sufficiently great to support this explanation? Red-shifting of the plasmon resonance is acutely sensitive to the ratio of particle radius (r) to centre-to-centre distance (D) between particles. Published data shows that a plasmon resonance in the range of 520 to 550 nm is maintained as long as r/D is less than about 0.4 [192, 193], r/D=0.5 for two particles that touch. It is therefore clear, for example, that the surface-to-surface distance between two particles of 40 nm diameter must be less than 10 nm for the absorption peak to be red-shifted beyond 550 nm. The presence of the 520 nm peak in the spectra of coatings on the surfaces treated with sulphuric acid is evidence that many of the particles are effectively more than 10 nm distant from their neighbours.

The simulation results from the DDSCAT program also affirm the analysis. In Figure 4-17, two gold nanospheres approach with the same gap. Since the gaps between the particles are the same, that is, 10 nm in this simulation, the r/D is controlled by the radius of gold nanoparticles. Gold nanospheres of 10, 20 and 40 nm radius are chosen for the simulation, which give r/D of 0.33, 0.4 and 0.44 respectively. With the decrease of r/D (corresponding to an increase in the particle size), the surface plasmon peak around 520 nm shifts gradually to the red side. The side peak due to interaction of the particles only occurs if r/D ≥0.4

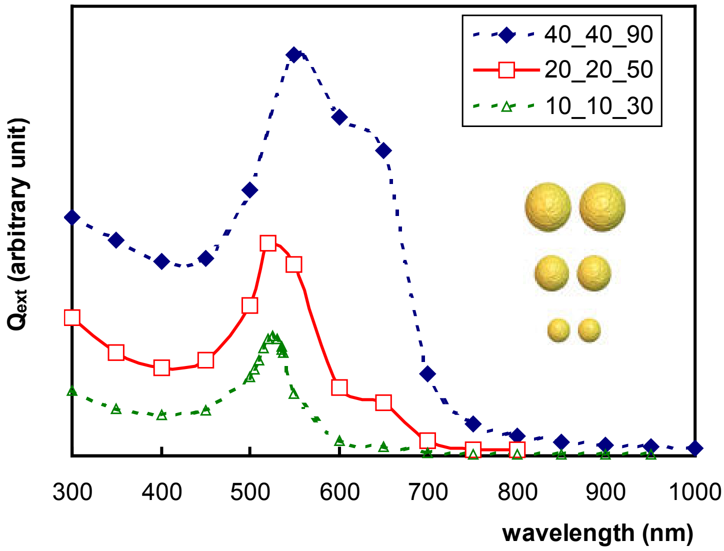

Figure 4-17 Simulation of spectrum for the approaching of different sizes of gold particles with the same gaps.

(10_10_30: two 10 nm gold nanoparticles with 10 nm gap between them,
20_20_50: two 20 nm gold nanoparticles with 10 nm gap between them,
40_40_90: two 40 nm gold nanoparticles with 10 nm gap between them)

Therefore, for the glass surface treated with sulphuric acid, the two peaks mentioned above developed concurrently. First, the isolated particles grew and second, some of the particles aggregated as clusters. Thus two plasmon resonances are evident in the spectrum. However, for the glass surface treated with buffered HF, nucleation happened so quickly that even at the very initial stage the density of gold particles was high. There was therefore no space for large, isolated particles to develop, and a large number of smaller particles agglomerated from an early stage during the deposition. These factors also restricted the growth of the nanoparticles themselves. The resulting plasmon resonance at 720 nm was so strong that it obscured any residual signal at 520 nm. Agreeing with the simulation, SEM images (Figure 4-8) show a large amount of isolated gold nanospheres with gaps larger than 20 nm for the case of the glass treated with concentrated sulphuric acid.

However, while the surface tension, $\gamma_{glass/H20}$ of the surface etched with 1:1 H_2SO_4 is quite similar to that etched with buffered HF, surprisingly, its optical spectrum and particle morphology was also like that of the surface treated with 98% H_2SO_4. The gold nanoparticle coating on this surface contained both agglomerated and isolated particles, and had the associated dual plasmon absorptions at 520 nm and 700 nm. The reason for this, it is believed, is that $\gamma_{Au/glass}$ is the more important factor controlling particle shape in this system, and it was evidently similar in magnitude for both of the surfaces treated with H_2SO_4.

4.4.3 Improvement of spectral selectivity by the nucleation process

There are different stages during the deposition process (Figure 4-18). First, the gold nuclei exist as isolated particles. Only part the of visible light is absorbed by their surface plasmon resonance. Infrared is not significantly reflected or absorbed in this stage (Figure 4-19). The coating in this stage shows a pinkish colour due to the part-absorption of the green part of the spectrum by isolated gold nanoparticles. However, the initial nature of the formation of gold nuclei and their growth at this stage is very important for the later coating. It is evident from their morphology that the nucleation process of chemically deposited gold on glass surfaces follows the so-called Volmer-Weber mode in so far as separate islands formed on the glass [194]. As discussed, this is the consequence of the value of θ. However, for high spectral selectivity between the visible and near-infrared region, the coating should be a continuous thin film rather than in the form of discrete islands (Figure 4-18). This requires coalescence of the gold hemispheres and the creation of a continuous macroscopic network characterised by a percolation threshold thickness. At this threshold, sufficient coalescence occurs to create a continuous pathway for electronic conduction through the film, which leads to dramatic changes of conductivity and optical properties. This is the ideal situation for solar control application. At this stage, infrared could be effectively reflected due to its longer wavelength, while the coating is still transparent in the visible region. The thickness at which this phenomenon occurs is very important in gold coatings for solar control. If it is thicker than 150 nm, the coating will be totally opaque and reflect almost all the radiation in both visible and the near-infrared region. In other words, the gold film displays the optical properties of bulk gold with a shining golden-yellow hue [195]. Therefore, every effort has to be made to minimise the threshold thickness of nanoscale gold coatings.

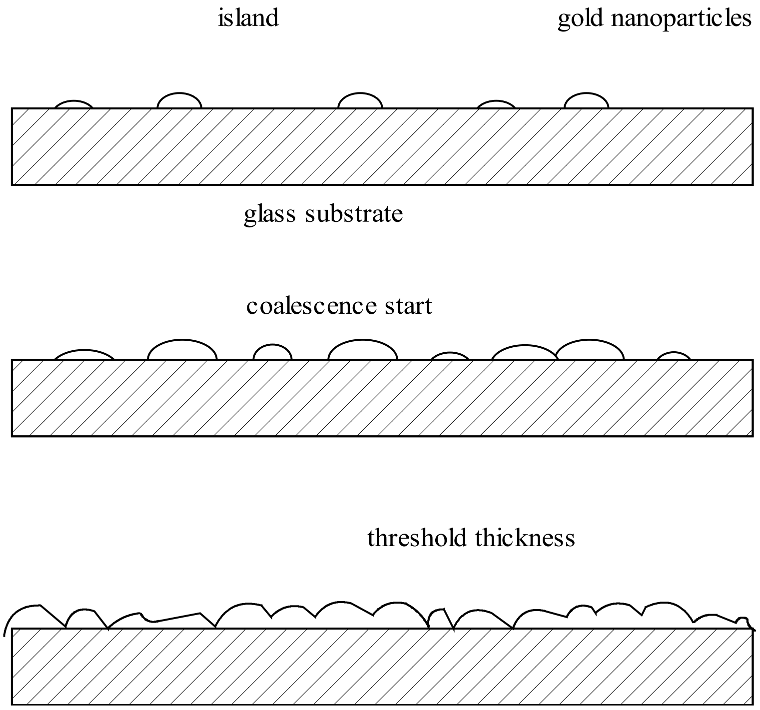

Figure 4-18 Nature of reflection off gold coatings at various stages in the deposition process

(Redrawn from [194].)

There are two possible strategies to achieve this. The first is to form the smallest particles possible and ensure that they are copiously nucleated. Growth of such a coating will cause coalescence into a continuous film. The second strategy is to alter the interfacial surface energy, which in its ultimate form will lead to the occurrence of the so-called Frank-van der Merwe mode of film formation [194]. In this mode, layers of coatings grow on top of each other (Figure 4-19**)**. Naturally, the two strategies can also be combined.

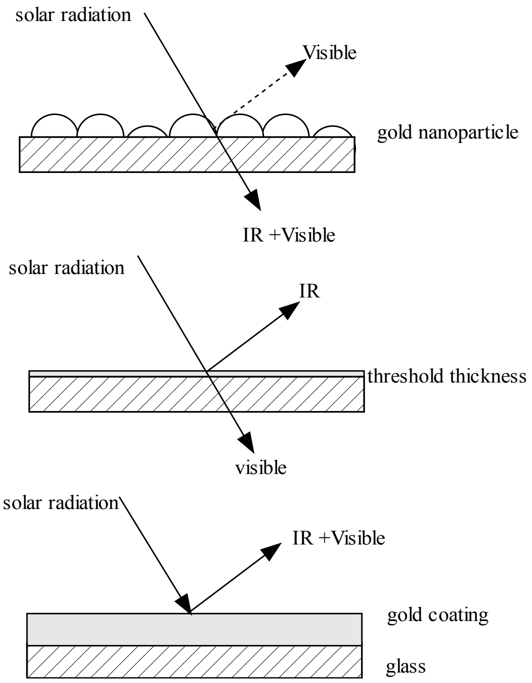

Figure 4-19 Illustration of the process of nucleation and growth of gold coatings on glass

(Redrawn from [194].)

4.5 Summary

Glass surfaces were pre-treated with 1:1 sulphuric acid (H_2SO_4), 98% H_2SO_4 and buffered hydrofluoric acid (HF). The surface obtained with buffered HF had higher sodium content and lower contact angle compared with that treated with 98% H_2SO_4. There was also a remarkable difference in the morphology and transmission spectra of the gold coatings that were subsequently deposited on the glass. This was evident in the texture of the coating on glass pre-treated with HF, which was more uniform than that of the sample pre-treated with sulphuric acid, and which exhibited only one absorption peak in its transmission spectrum. These trends could be explained in terms of classic heterogeneous nucleation and growth theory. The optimum microstructure for high spectral selectivity has been identified, and is a near-continuous monolayer of gold nanoparticles with minimum coating thickness.

The emissivity of gold nanoparticles coatings in different stages of deposition was investigated. It is evident that the colour, surface plasmon and particle-to-particle interaction are not critical factors for achieving low emissivity. However, forming a continuous film will abruptly change the coating's emissivity. The finding is useful to control the reflectance of the coating to avoid "light pollution".

5. Synthesis and mechanism of formation of gold nanorods

5.1 Introduction

Gold nanoparticles with reduced symmetry, including shapes such as rods, shells [196, 197] and caps, have attracted much attention for their unique optical properties [197]. Gold nanorods show particular promise for optoelectronic devices [18, 198, 199], medical imaging [198, 200, 201] and thermal therapy [202, 203], as well as for developing spectrally selective coatings. They have also been used as a template for further synthesis [204]. Background information on these particles was summarised in Chapter 2 of this thesis. There I showed that although the seed-mediated method of growth is now dominant for producing gold nanorods, there are still many unresolved issues.

Firstly, it is difficult to grow long aspect ratio rods with high yield [74, 82]. Multiple steps have to be applied to separate the long aspect ratio rods from the mixture of short ones and spheres. This process uses gold nanorods from previous steps as the seeds. It has been shown to be time-consuming and results in a low yield [68]. The instability of gold nanorods by this method is another issue. Not all the Au(I) in the growth solution is immediately consumed by the reductant, and the remaining Au(I) can still be reduced slowly in the growth solution over a few months. The morphology of gold nanorods is thus time-dependent. Consequently, the optical properties of gold nanorods are also time-dependent. This is very undesirable for practical applications. The control of mono-dispersed particle size is a significant challenge, as spherical particles grow simultaneously in the solution, and the spheres are extremely difficult to separate.

Different mechanisms have been suggested to explain the growth of gold nanorods by the seed-mediated method, and, so far, no single mechanism has been widely accepted. The soft micellar template theory [70, 205], the passive protection theory [72] and the electrical field diffusion theory [77] were reviewed in Chapter 2 and are the most discussed. None of them can provide a completely satisfactory explanation for the growth process. The ambiguity of the proposed mechanisms makes developing a new synthesis method difficult.

In this chapter, the effects of factors such as the nature of the seed solution, silver ion chemistry and concentration, and the surfactant chemistry and concentration will be investigated systematically. My goal has been to optimise the process to produce better gold nanorods for spectrally selective glass coatings. The properties of the resulting gold nanorods will be examined.

5.2 Experimental procedure

5.2.1 Materials

Hydrochloric acid (HCl) and nitric acid (HNO_3) were obtained from AnaLab®, hexadecyltrimethylammoniumbromide (CTAB) was purchased from Nanjing XuanGuang Ltd, China, potassium borohydride (KBH_4) and L-ascorbic acid were sourced from Sigma-Aldrich. All chemicals were used as-received. All H_2O used was purified by Millipore column with resistance of 18.6 MΩ. The $HAuCl_4$ solution was prepared as described previously. The gold nanorods were prepared by the modified seed-mediated growth method, which was reported by Nikoobakht [72] first, and briefly outlined here.

5.2.2 Seed solution

Two different kinds of seed solution were prepared :

(a) Seed A:

The seed solution was prepared by adding 0.10 mL of 0.02 M KBH_4 to 10.0 mL aqueous solution of 0.5mM $HAuCl_4$ and 0.2M CTAB, while stirring vigorously. The resulting brownish-yellow solution was used within 30 minutes as seed solution A.

(b) Seed B:

This was a control solution. The procedure was similar to that of Seed A except 10.0 mL of 0.2 M CTAB alone weres used instead. The resulting clear colourless solution was used within 30 minutes as seed solution B.

5.2.3 Growth of gold nanorods

0.10 mL 0.05 M L-ascorbic acid was added to a constantly stirred 10.0 mL of aqueous solution containing 0.2 M CTAB, 0.5 mM $HAuCl_4$, and various amounts of $AgNO_3$, ranging in concentration from 0 to 0.25 mM. The gold solution turned from brown-yellow to colourless immediately after mixing in 0.10 mL of 0.050 M L-ascorbic acid. 12 μL of seed solution, either in type A or B weres added to initialise the growth of gold nanorods. The stirring was stopped once all the ingredients were well mixed, and the nanorods grew in a still solution. The reaction can proceed at room temperature and lasts from tens of minutes to a few hours before the colour of the colloidal suspension becomes stable.

5.2.4 Purification of gold nanorods

The purposes of purification are to remove excess surfactant (CTAB) and gold nanospheres. The 40 mL of gold nanorods colloid were centrifuged at low speed to remove the largest spherical particles. In this work, typically 30 mL of solution were used in each centrifuge tube and centrifuged at 2,000 rpm for 5 min. The precipitate containing large spheres was discarded, and supernatant from each centrifuge tube was subjected to further processing. The collected supernatant was then spun at 12,000 rpm for 25 minutes, and supernatant from this centrifugation was decanted carefully by aspirator pump without disturbing the precipitate. The remaining mixture was redispersed in 40 mL of MilliQ water and the centrifugation repeated. The final product contains 50–100 times the concentration of gold nanorods particles of the original colloid, with approximately 2 mM of CTAB remaining.

5.2.5 Ag distribution

Four batches of gold nanorods were synthesised with method described in the section 5.2.3. Different concentration of silver ions were added in the growth solution. The final added silver concentrations in the growth solution were 0, 0.05, 0.10 and 0.20 mM respectively. The gold nanorods thereafter were purified by the centrifuging process. A colloidal suspension of 28.2 g was centrifuged at 12,000 rpm. The pellet of 1.0 ~1.5 mL volume was washed by MilliQ water while the supernatant was prepared for the analysis. The tube containing the pellet was refilled to 28.2 g by water and spun again to obtain the 1.0~1.5 mL of pellet again by the centrifuging process. The pellet was then digested by aqua regia and diluted to 20.0 mL for chemical analysis.

The supernatant was analysed by Inductively Coupled Plasma – Optical Emission Spectroscopy (ICP-OES) (Varian Vista Pro), while the pellet was analysed by Inductively Coupled Plasma – Mass Spectroscopy (ICP-MS) (Perkin Elmer ELAN 6000 DRC) for Ag. The analyses were carried out at the Australian National Measurement Institute. The separation procedure is illustrated in Figure 5-1.

5.2.6 Aging effect

Fresh synthesised gold nanorods are divided into two parts: one was kept in the growth solution and stored at room temperature for 10 months. The other part was purified according to the procedure described in section 5.2.4. The purified gold nanorods were redispersed in water and stored at room temperature for 10 months. The morphology and optical properties of aged gold nanorods were then examined and compared both with each other and with fresh gold nanorods.

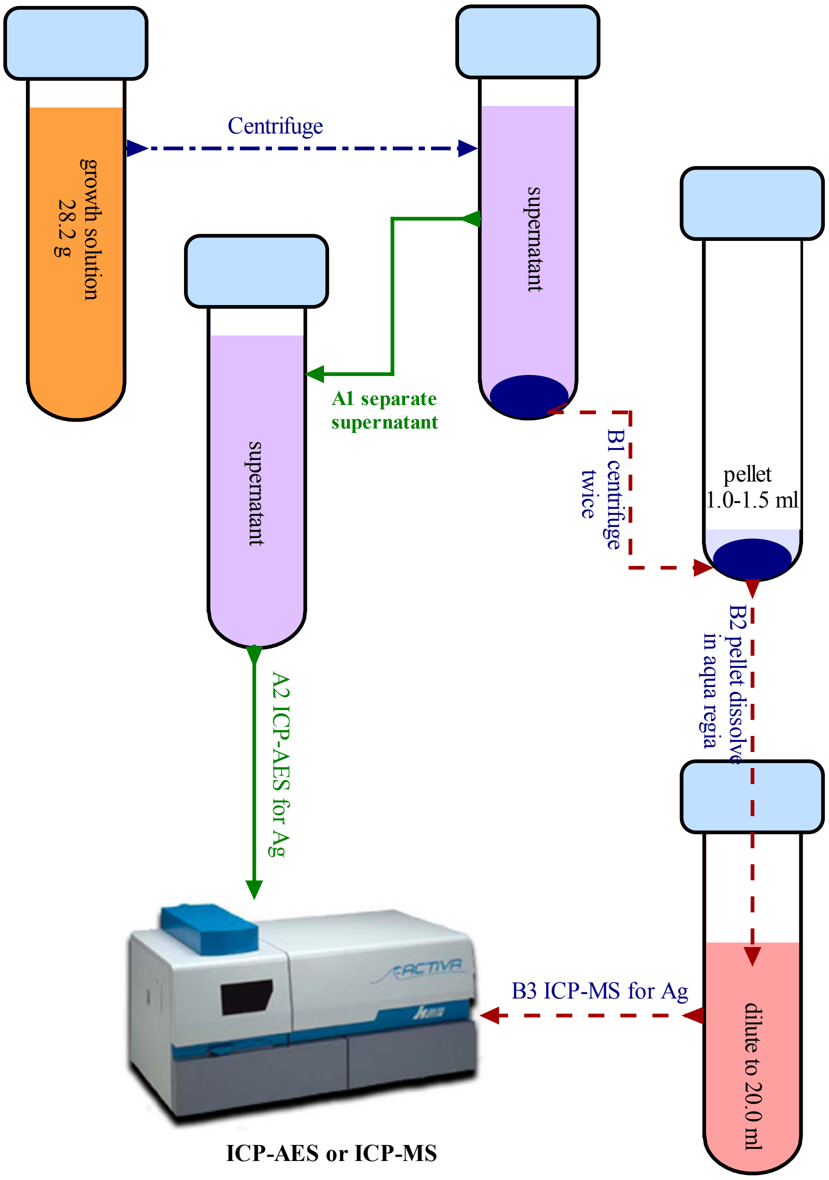

Figure 5-1 Scheme to determine Ag distribution between supernatant and gold nanorods

5.2.7 Characterisation of gold nanorods

(a) Transmittance

The gold nanorod colloids were analysed using a Cary 3E UV/VIS spectrophotometer, with a working range of 170 nm to 900 nm and with a spectral resolution of 0.5 nm, to obtain the visible-IR transmission spectrum of the samples. A 5 nm/s of scanning rate with spectral bandwidth (SBW) of 2 nm was set for the process.

(b) Morphology

The morphologies of gold nanorods were characterised using an LEO scanning electron microscopy (SEM) with in-lens images taken at 2–30 kV. Preparation of the nanorods for SEM characterisation was as follows. The purified, concentrated gold nanorods were dropped on the top of a graphite sample stud and dried overnight in a desiccator. Stainless steel or aluminium studs were avoided to obtain better contrast during imaging. Dried samples could be imaged directly, as no carbon sputtering is required.

5.2.8 Simulation of optical properties

(a) Spectrum by discrete-dipole approximation

The optical properties of gold nanorods were numerically simulated with the discrete-dipole approximation method (DDA). The Fortran code DDSCAT was developed by Bruce T. Drain (Princeton University) and compiled by M. Cortie (University of Technology, Sydney, Australia) for Windows. The advantage of DDSCAT is that there is no limitation on the shape of the target (although there are limits on size). It is an approximation method which converts the continuum target into a finite array of polarisable points, which acquire dipole moments in response to the local electric fields [206]. The extinction (α_{ext}) is expressed as [160]:

$$\alpha_{ext} = \eta(C_{abs} + C_{sca}) \qquad \text{(eq. 5-1)}$$

where η is the number of particles per unit volume; C_{abs} and C_{sca} are the absorption and scattering cross-sections. The absorption efficiency factor (Q_{abs}) is expressed as [160]:

$$Q_{abs} = C_{abs}/\pi a_{eff}^2 \qquad \text{(eq. 5-2)}$$

where C_{abs} is the absorption cross section. In DDSCAT the geometric cross-section is always that of a sphere of equal volume to the real target.

If multiple scattering is negligible, the irradiance of a beam of light is exponentially attenuated from I_i to I_t in traversing a distance h through a particulate medium, according to,

$$\frac{I_t}{I_i} = \exp(-\alpha_{ext}h) \qquad \text{(eq. 5-3)}$$

Extinction is the result of both absorption and scattering; absorbance is calculated according to the definition of absorbance:

$$A = -\log\frac{I_t}{I_i} \qquad \text{(eq. 5-4)}$$

An ellipsoid was applied as the physical model to simulate the optical properties of gold nanorods. The shape of the ellipsoid used in DDSCAT can be expressed as [207]:

$$(\frac{x}{a})^2 + (\frac{y}{b})^2 + (\frac{z}{b})^2 = \frac{d^2}{4} \qquad \text{(eq. 5-5)}$$

in which a and b are longitudinal and transverse radii of the ellipsoid, and d is the interdipole spacing. The aspect ratio of the ellipsoid (ε) is defined as $\varepsilon = a/b$. The complex refraction indices of gold and water were taken from the literature [189, 208]. Dipole arrays of about 25,000 nodes were applied in the calculations.

(b) Colour gamut

The CIE colour model is applied to map the colours of the gold nanorod sols. This model was developed by CIE (Commission Internationale de l'E Clairage) committee and is widely regarded as the most accurate colour model. It can map all possible colours made by mixing red, green and blue light sources. There are three parameters, X', Y' and Z', in the CIE model, in which only two are independent. Y' is defined to match the luminous-efficiency function of the human eyes. X' and Z' are obtained based on experiments involving human observers [209].

$$X' = \frac{X}{X+Y+Z},\; Y' = \frac{Y}{X+Y+Z},\; Z' = \frac{Z}{X+Y+Z},$$

The CIE-LAB definition is a 1976 revision of the CIE system, which uses three variables, that is, luminance, L*; red-green axis, A*; and blue-yellow axis, B*, to construct the colour gamut. A computer code developed by Cortie [210] was utilised to convert the transmittance spectrum to CIE L*, A* and B*. The model made it possible to use the Cartesian coordinate system to map all the colours of gold nanorods in all intermediate stages during their growth.

5.3 Results

5.3.1 Effect of pH of ascorbic acid

1.0 mL of 10 mM $AgNO_3$ solution and 1.0 mL of 0.05 M ascorbic acid were added to the 100.0 mL of CTAB-$HAuCl_4$ solution (0.5mM $HAuCl_4$ and 0.1M CTAB aqueous solution). Finally, 120 µL of seed A were added in. The pH of ascorbic acid was pre-adjusted with 1.0M NaOH to 2.0, 4.5 and 12 respectively. No reaction could be observed for the ascorbic acid at pH =2.0. The growth of gold nanorods in ascorbic acid at pH 4.5 and pH 12.0 can be seen in the spectra of Figure 5-2 and Figure 5-3 respectively. The higher the pH of the ascorbic acid, the faster the growth rate of the gold nanorods. The pH of the CTAB-$HAuCl_4$ solutions remained stable during the reaction process.

In contrast to the gold nanospheres described in previous chapters, the spectra of the nanorod sols were characterised by dual peaks; one at around 528 nm, associated with the surface plasmon resonance of isolated gold nanospheres, or with the transverse plasmon resonance of the rods. The other was at around 750 to 800 nm, and was believed to be the longitudinal surface plasmon resonance of elongated gold particles. This peak relates closely to the aspect ratio and dimensions of gold nanorods. In the different pH values, the second plasmon resonance peak of gold nanorods remained at about the same wavelength range.

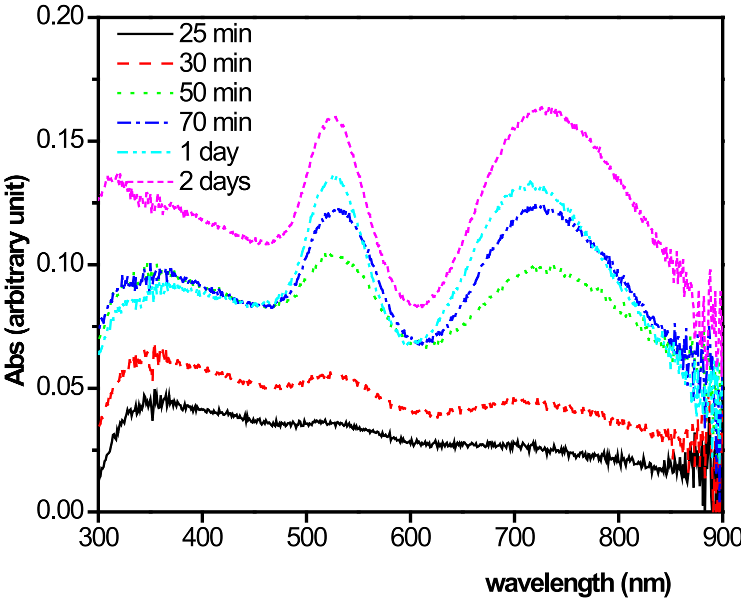

(a) pH 4.5 ascorbic acid

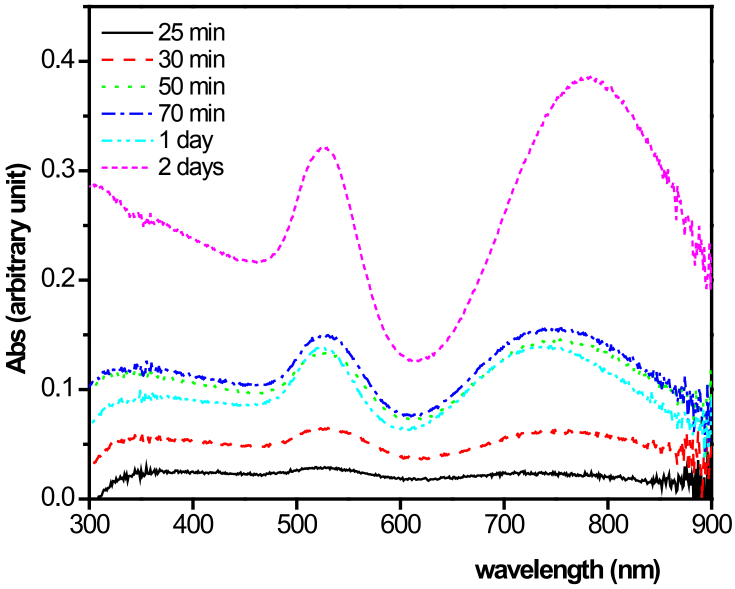

(b) pH 12.0 ascorbic acid

Figure 5-2 Growth of nanorods with various pH of ascorbic acid

5.3.2 Effect of Ag^+ on the growth of gold nanorods

(a) Evolution of the spectrum during the growth

The function of Ag^+ in the process of growth of gold nanorods was investigated by adding 0.5, 1.0, and 2.0 mL of 10 mM $AgNO_3$ to each 100.0 mL of CTAB-$HAuCl_4$

solution. A control without $AgNO_3$ was included as reference. The time dependence of the absorbance spectra of gold nanorods colloids is depicted in Figure 5-3.

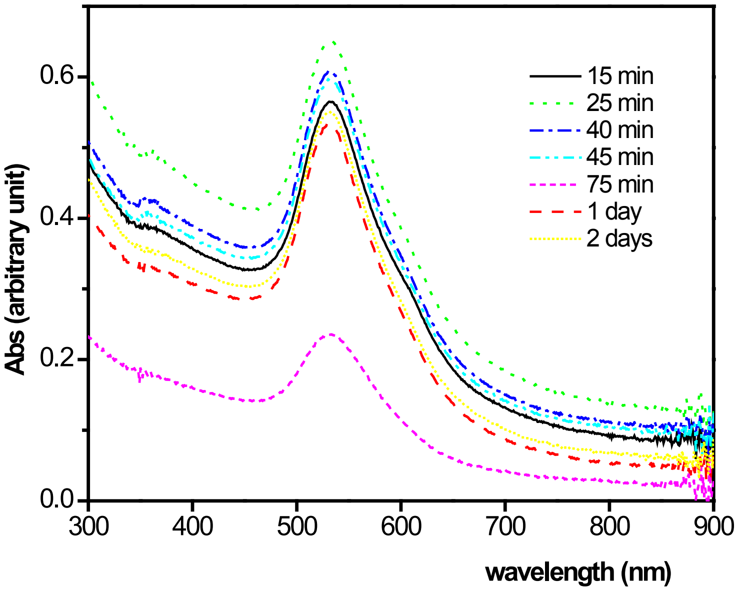

(a) no Ag^+

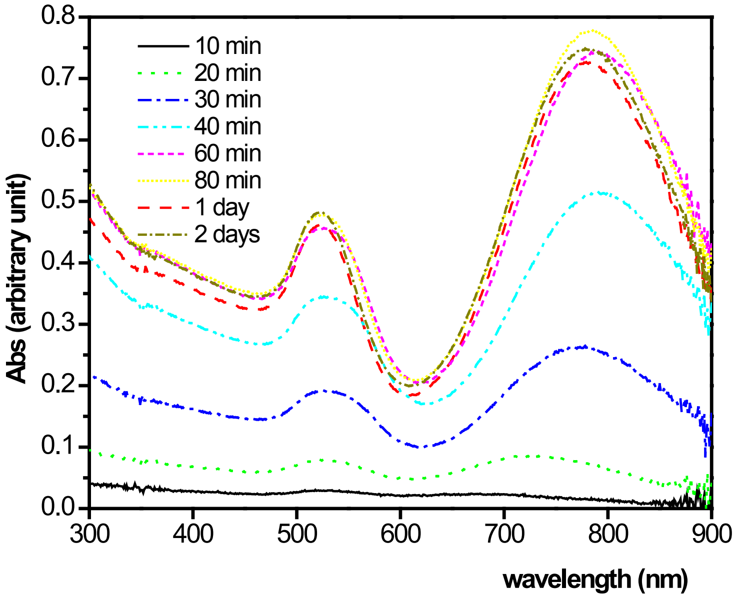

(b) 0.05 mM Ag^+

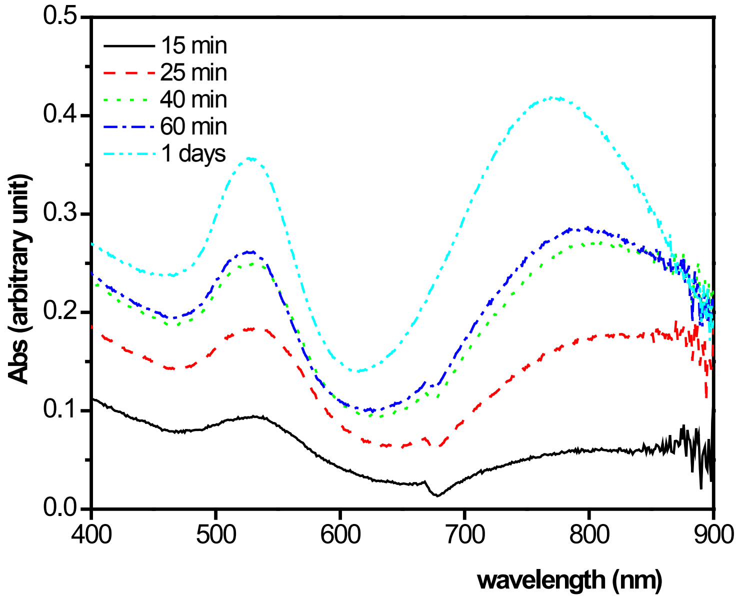

(c) 0.1 mM Ag^+

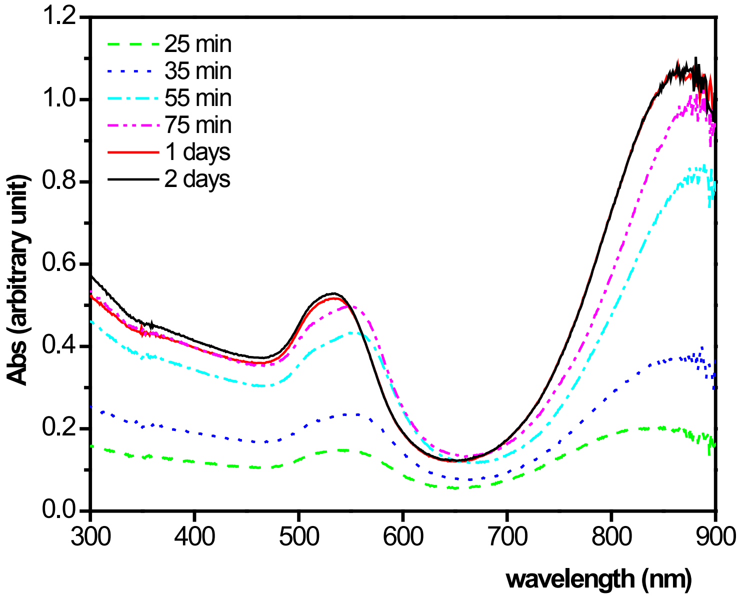

(d) 0.2 mM Ag^+

Figure 5-3 Growth of gold nanorods with different [Ag^+]

As found by other researchers [70], Ag^+ plays an important role in the formation of the gold nanorods. In the absence of Ag^+, a predominance of gold nanospheres was formed rather than the nanorods, with the product showing only one single surface plasmon peak at around 540 nm in the spectra. (Figure 5-3 (a)). With increasing silver concentration from 0.05 mM to 0.2 mM, the longitudinal surface plasmon peak appears and moves to the red end of the spectrum. This observation agrees with other reports [70]. At later stages of the reaction, some shifting of the longitudinal surface plasmon to the blue end of the spectrum was observed. The shifts of the longitudinal peak will be discussed in section 5.4.1.

(b) Shift of longitude peak with addition of Ag^+

The spectra of gold nanorods prepared with different additions of Ag^+ are illustrated in Figure 5-4. The spectra were sampled within three hours from the start of the reaction. The broad range of Ag^+ is investigated in order to determine its role in the synthesis of the gold nanorods.

The relationship of Ag^+ concentration with longitudinal plasmon resonance peak is indicated in Figure 5-5. An increase in the Ag^+ concentration results in the red-shift of the peak, but a further increase in the Ag^+ concentration beyond 0.2 mM did not help the growth of the rods. In fact, more than 0.2 mM Ag^+ shifted the longitudinal peak to the blue side. This is probably due to a decrease in the effective aspect ratio of the particles. With a very high concentration of Ag^+ (1.67 mM Ag^+), only one significant surface plasmon peak is identified. In this case, the yield of gold nanorods is very low. In the scope of our research, Ag^+ suppress this reduction-oxidisation reaction significantly.

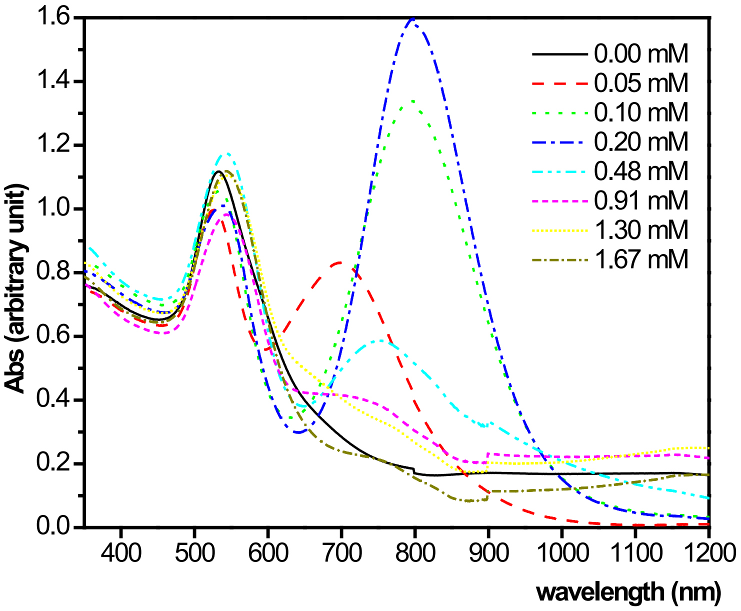

Figure 5-4 Effect of Ag^+ on position of longitudinal peak

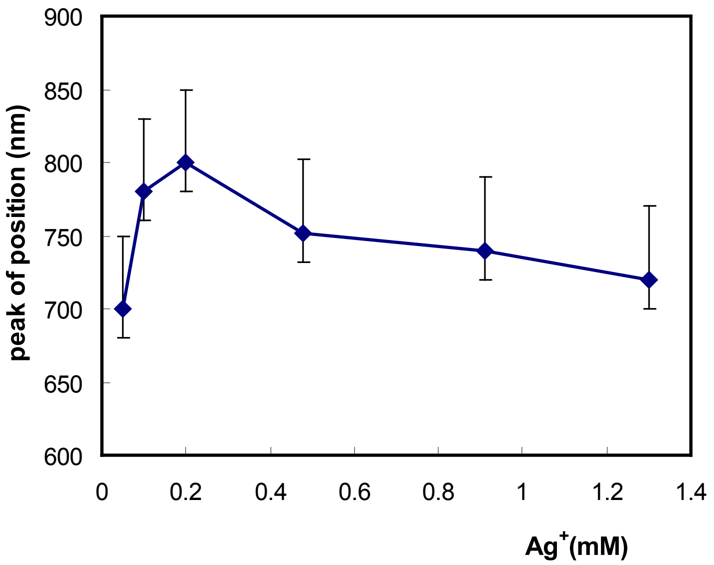

Figure 5-5 The correlation of position of longitudinal peak with [Ag$^+$]

A blank experiment was also carried out simultaneously, in which there was no $HAuCl_4$ and only $AgNO_3$ in the CTAB solution. It was found that the spectrum of the solution did not change during the duration of the experiment, which indicated the Ag^+ was not reduced by ascorbic acid under the experimental conditions. Ag^+ can only be reduced by ascorbic acid in very high pH, for example pH 12 above, in our experiments.

5.3.3 Effect of seeds on the growth of gold nanorods

(a) Gold nanorods induced by different seeds

The initialisation of the reactions by the seeds is thought to be the major reason for the repeatability of the synthesis of gold nanorods. Comparative experiments were conducted as verification. In experiment No. 1, normal seed solution, "seed A", was used, while in experiment No. 2, "seed B", in which only KBH_4 but no $HAuCl_4$ existed in CTAB solution, was used instead. The spectra of gold nanorod growth initialised by these two seeds are illustrated in Figure 5-6. The variation was not significant to be explained by the deviation of operation and seeds introduced.

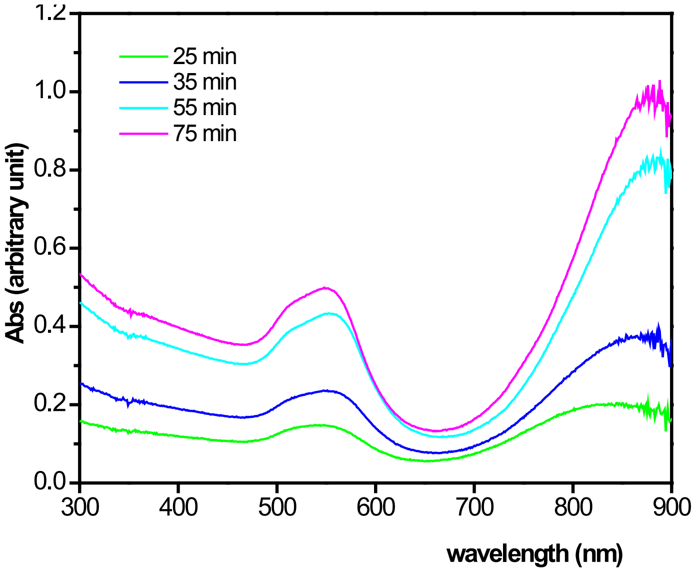

(a) seed A

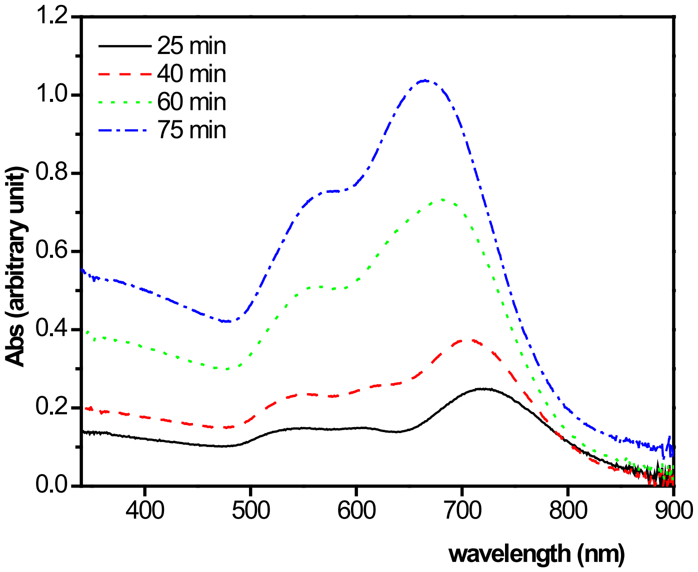

(b) seed B

Figure 5-6 Different spectra of gold nanorods with the same procedure initialised by different seeds

KBH_4, a good reducing agent for gold nanoparticles, is believed to be the possible reason for this kind of variation. It is well known that KBH_4 is unstable in aqueous solution and reacts with water, giving off hydrogen [20].

$$BH_4^- + H_2O \rightarrow BH_3OH^- + H_2 \qquad \text{(eq. 5-6)}$$

$BH_3OH^- + H_2O \rightarrow BH_2^- + H_2$ (eq. 5-7)

Considering the ratio of the concentration of BH_4^- to $AuCl_4^-$, there remains a large amount of BH_4^- in the seed solution following the reaction. The remaining BH_4^-, and its intermediate products, BH_2OH^- and BH_3OH^-, all participate in the reaction as reducing agents. As a result of the self-decomposing process of BH_4^-, the seed introduced into the solution is always in a different redox potential environment; even the samples were prepared in the same batch.

The morphological evolution of gold nanorods initialised by both seeds are shown in Figure 5-7 and Figure 5-8. It is demonstrated that although the seed B particles commenced with short-aspect ratios, they also grew into nanorods. Therefore, heterogeneous gold seeds are not absolutely necessary to produce nanorods. Under the right conditions, KBH_4 in the solution can also reduce the $AuCl_4^-$ and form the gold nuclei (Au^0), which are needed for the production of rods by ascorbic acid.

The evolution of morphology during the growth process is the result of an anisotropic reaction. The differential reduction rate of Au(I) on crystal planes transforms the seeds from spheres to ellipsoids. With further reaction, the ellipsoid turned into dogbones and dumbbells.

Perez-Juste *et al.* suggested that removal of excess BH_4^- in the seed solution by heating the solution at 50°C is helpful to obtain a more reproducible product [77]. Jana *et al.* reported that the size and its distribution of the seeds will also have significant influence on the morphologies of the gold nanorods synthesised [205].

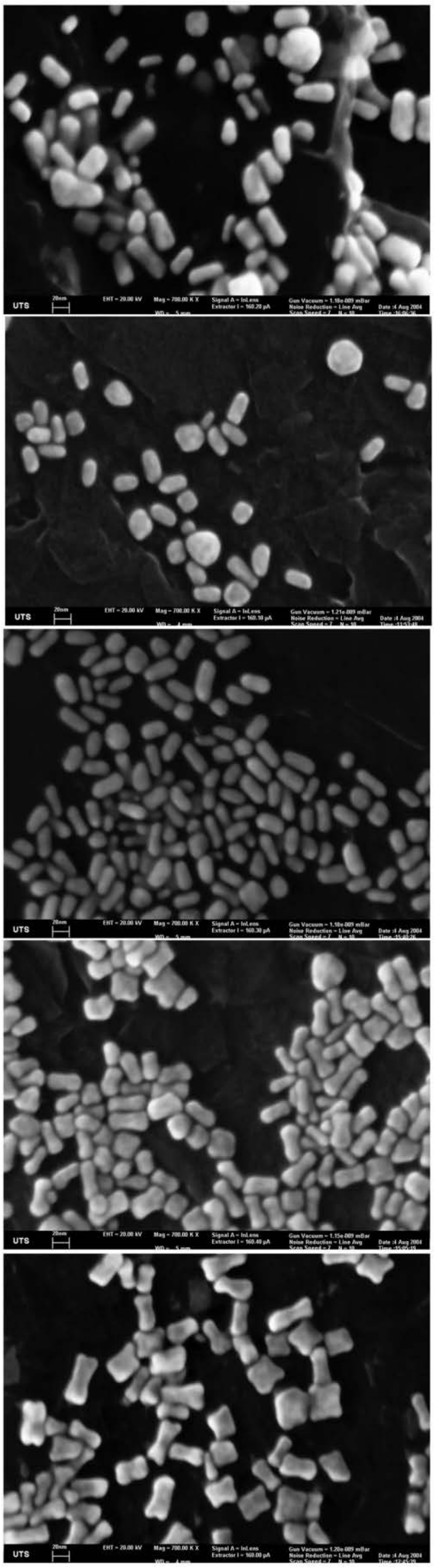

Figure 5-7 Evolution of gold nanorods initiated by seed A

(a. after 10 minutes; b. after 20 minutes; c. after 30 minutes;
d. after 40 minutes; e. After 60 minutes.)

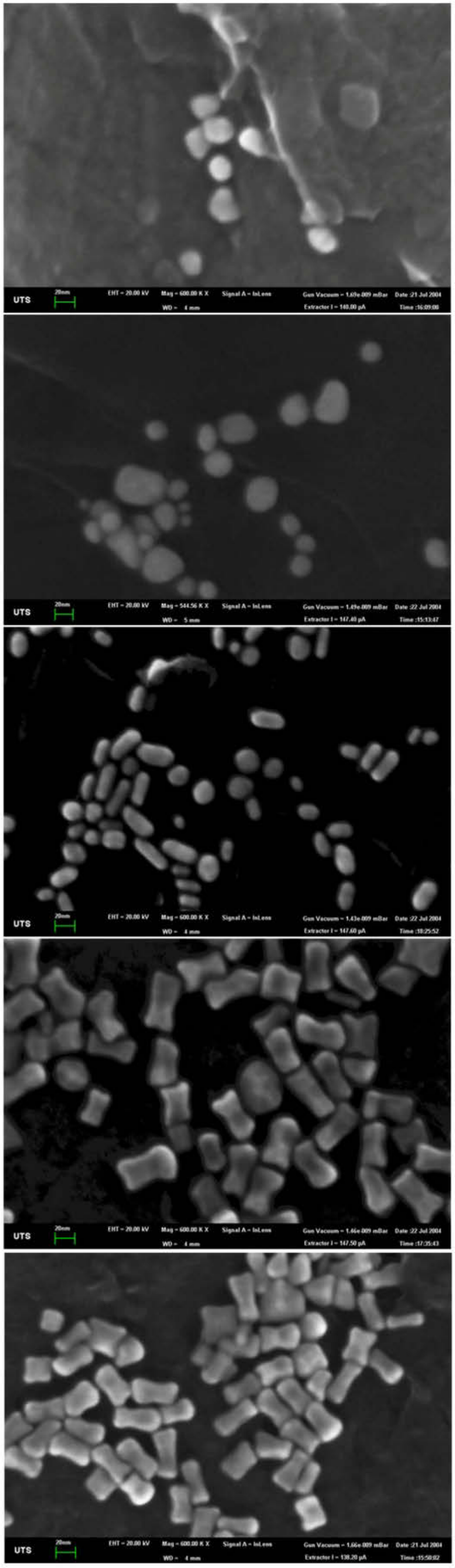

Figure 5-8 Evolution of gold nanorods initiated by seed B

(a. after 10 minutes; b. after 20 minutes; c. after 30 minutes;
d. after 40 minutes; e. after 60 minutes.)

(b) Effect of amount of seeds on the longitudinal peak

Not only the types of seeds but also the amount of seeds greatly influence the optical properties of the gold nanorods. Different amounts of seed A, ranging from 6 to 100 μL/10 mL, were also tried. The spectra of gold nanorods synthesised in 3 hours are indicated in Figure 5-9.

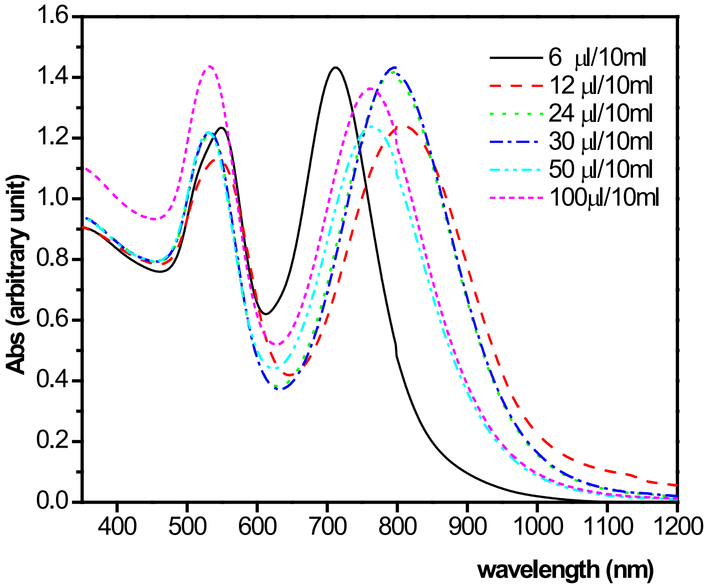

Figure 5-9 Effect of amount of seed solution

The correlation of position of the longitudinal peak with seeds added is shown in Figure 5-10. Similar to the effect of Ag^+, increasing the amount of seeds initially shifted the peak significantly to longer wavelengths, but after some optimum amount, further increases reduced the wavelength of longitudinal resonance again.

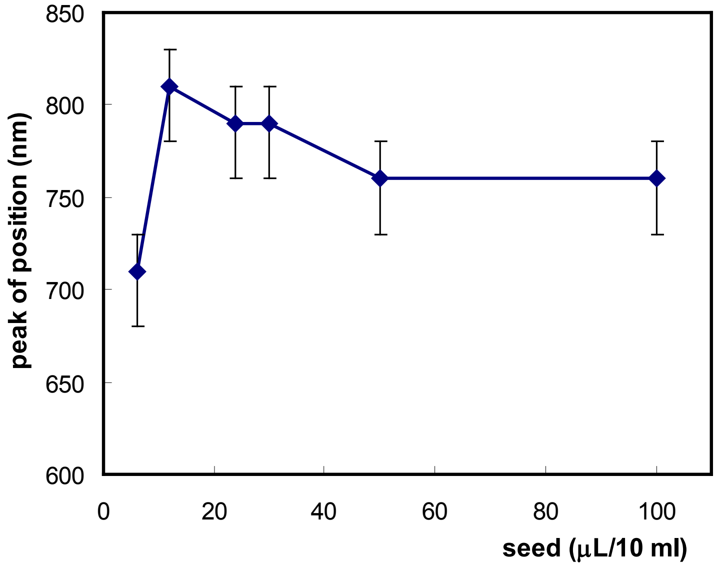

Figure 5-10 Shift of longitude peak with seed amount

5.4 Discussion

5.4.1 Time-dependent change of morphology and optical properties

(a) Evolution of morphology and optical properties during growth

It is clear that the peak due to the longitudinal plasmon blue-shifts and decreases in strength as the rods age. The literature is in agreement that this shift can only occur if the aspect ratio of the rods is decreasing. The numerical simulation growth of nanorods by the ellipsoidal model (Figure 5-11) with the discrete-dipole approximation method (DDA) has also verified this.

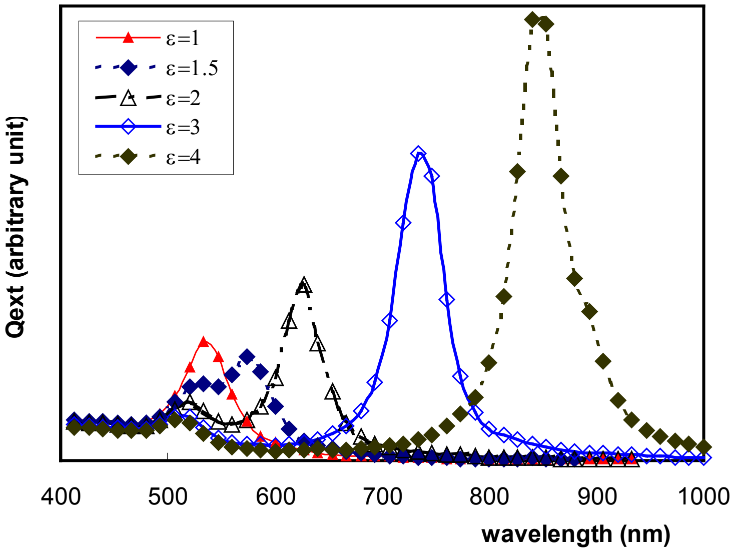

Figure 5-11 Optical properties of colloid with different aspect ratios of gold nanorod

In agreement with experimental results, such as in Figure 5-9, the simulation shows two surface plasmon peaks. There is a transverse surface plasmon peak at around 520 nm and a longitudinal peak that shifts to the infrared region with increasing aspect ratio. These simulation results compare conformably with the simulation carried by Link with Mie theory [146].

In the later stages of the growth, indicated in Figure 5-7 and Figure 5-8 d, e, the shape of the gold nanorods cannot be simply simulated by ellipsoids or cylinders anymore. The morphology of the gold nanorods at this stage shows irregular dogbone or dumbbell shapes. The changes in the optical properties of nanorods during the growth are shown in Figure 5-12.

Figure 5-12(a) gives the actual extinction spectra measured by the spectrometer. The spectrum developed a broad region of extinction below 350 nm, in combination with three peaks at ~520, 560 and ~700 nm. It is evident that the optical density of the suspension increases steadily during the synthesis stage, which is caused by the increase in the density of gold nanorods in the suspension and/or growth of the nanorods by reaction. Some of this increase is simply due to the increased content of metallic gold in suspension. This factor is evident in the spectrum between 300 and 500 nm, where absorption is mostly due to interband transitions and hence in proportion to the volume of metallic gold present. The proper relationship between the remaining peaks can be indicated by normalising the data with regard to the absorbance, shown in Figure 5-12(b). The changes in the normalised spectra may now be attributed to changes in shape of the metallic nanoparticles. In the normalised spectra (Figure 5-12 (b)), the longitudinal plasmon peak (around 700 nm) initially intensifies and shifts to shorter wavelengths (A to B) during the aging of the growth solutions. However, at aging times of greater than 1.5 hours (point B) it decreases in significance out to 24 hours (point C), while a third peak develops (D). In this stage, the spherical seeds become ellipsoidal. Further growth of the ellipsoidal particles results in dumbbell shapes.

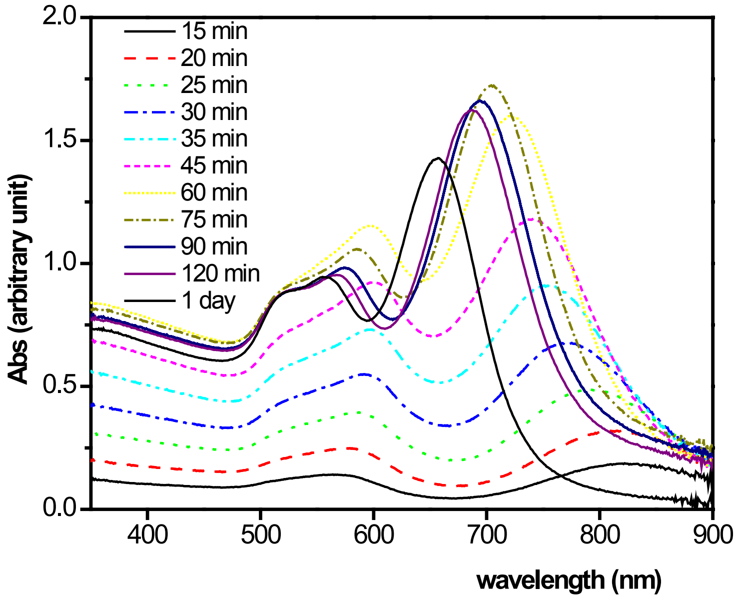

(a) optical extinction spectra to 24 hours

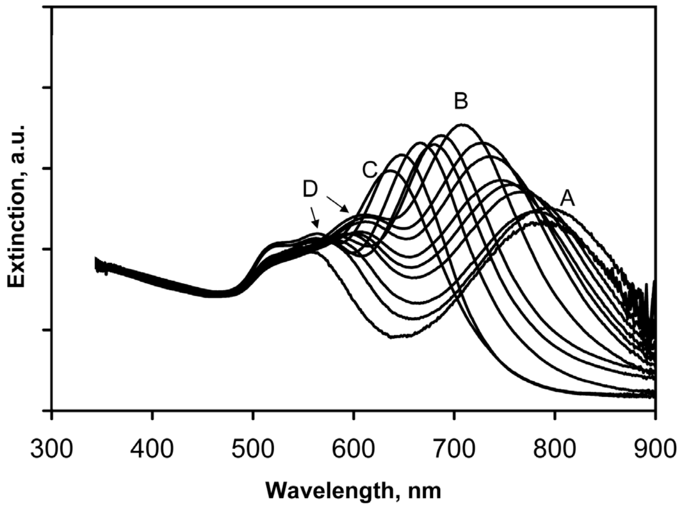

(b) normalised spectra to eliminate variation due to the volume of gold metal in suspension

Figure 5-12 Optical spectra of gold nanoparticles during growth

There are two peaks in the spectrum between 500 and 600 nm. One of these peaks red-shifts and strengthens as the particles age (Figure 5-12 (a)). The appearance of these peaks could result from the appearance of short aspect ratio gold nanorods in suspension or of new surface plasmons induced by the low symmetry of dogbone shape. However, examination of the evaporated suspensions corresponding to the long aging times (Figure 5-13(a)) shows that the nanoparticles consisted of a mixture of rods, dumbbells and dogbones, with insufficient spheres or short rods being present to explain either of these peaks. In addition, examination of these nanoparticles shows narrow size distribution. The length (L), minimum width (D1) and maximum width (D2) are 39.0 ± 6.7 nm, 17.4 ± 4.) nm, 19.6 ± 4.6 nm respectively. Therefore, they must have come from transverse resonances in the particles shown.

Using a code designed by Cortie [210], it is possible to simulate optical properties for arbitrary shapes of gold nanoparticles. The principle of the code is to assign the location and materials of each dipole in the arbitrary shape. When the shapes transit from ellipsoidal to dogbone, the emergence of the peak around 560 nm indicates a new transverse resonance.

(b) Evolution of morphology and optical properties in long time aging

The effect of long aging times on gold nanorods is indicated in Figure 5-16 and Figure 5-13. The gold nanorods are aged in different solutions. In the first case, the gold nanorods are left in the growth solution and stored at room temperature for 10 months. In the second case, the gold nanorods were purified first by centrifuging process described in 5.2.4. Purified gold nanorods are kept in de-ionised water and stored at room temperature for 10 months.

The nanorods show significant difference in both optical spectra and morphologies. For the purified gold aged in the water, the optical properties and morphologies are very similar to those as prepared. The rods maintain the same aspect ratio after their 10 months, aging process. For the gold nanorods aged in the growth solution, the first impression is that the morphologies of gold particles have changed dramatically. This includes the diminishing of dogbone shapes and regeneration of ellipsoids; moreover, size increase is apparent. The particles also develop clear crystal planes during the long aging process (Figure 5-13). Particle size distribution analysis also affirms this impression. The average results of 250 particles in each case are displayed in
Table 5-1. The aging process does not change the average dimension and aspect ratio of purified gold nanorods. However, the length and width of gold nanorods aged in the growth solution increased 21.8% and 40.2% respectively. The normalised dimensional distributions of gold nanorods are also shown in Figure 5-14 and Figure 5-15.

Compared with the gold nanorods depicted in Figure 5-13(a) and (c), there are two important differences. The first is that the sharp features of the particles, such as corners and edges, have been etched away with the long period aging in the growth solution. Also, the small particles that can be seen commonly in Figure 5-13(a) have diminished. The phenomenon is called Oswald Ripening [211].

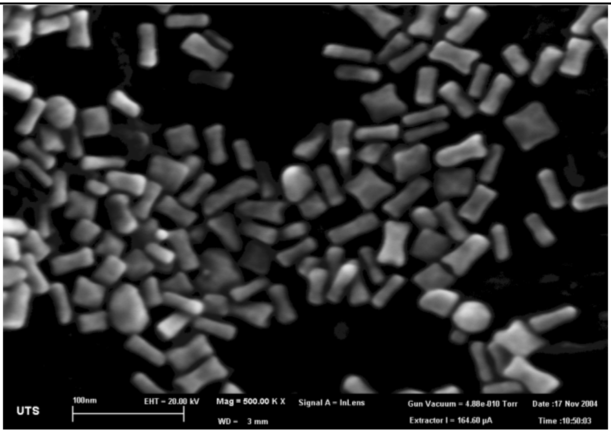

(a) as prepared

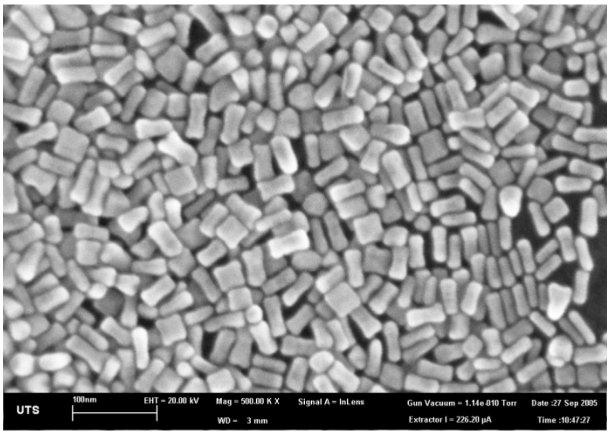

(b) purified/redispersed nanorods aged for 10 months

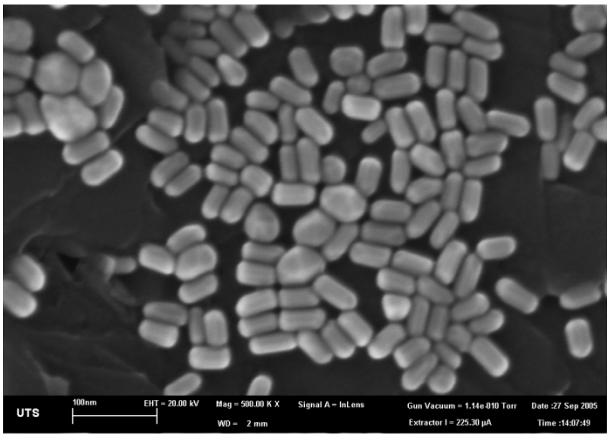

(c) nanorods aged in growth solution for 10 months

Figure 5-13 Aging effect on morphologies of gold nanoparticles

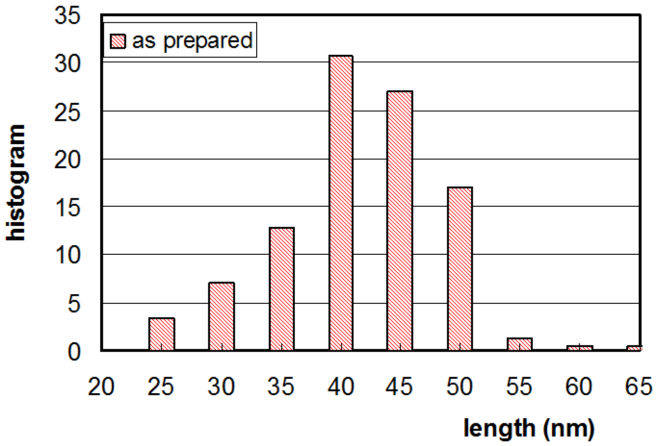

(a) as prepared

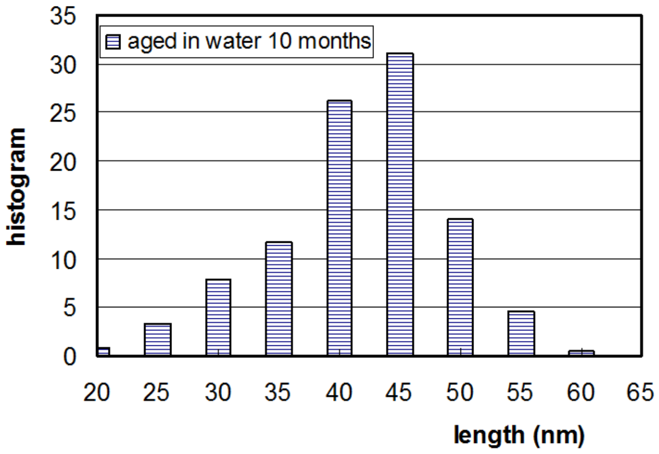

(b) purified and aged in water for 10 months

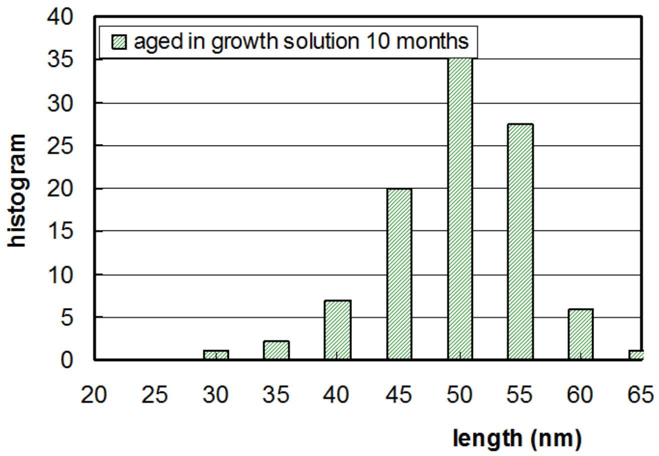

(c) aged in growth solution for 10 months

Figure 5-14 Change in length of gold nanorods during different aging processes

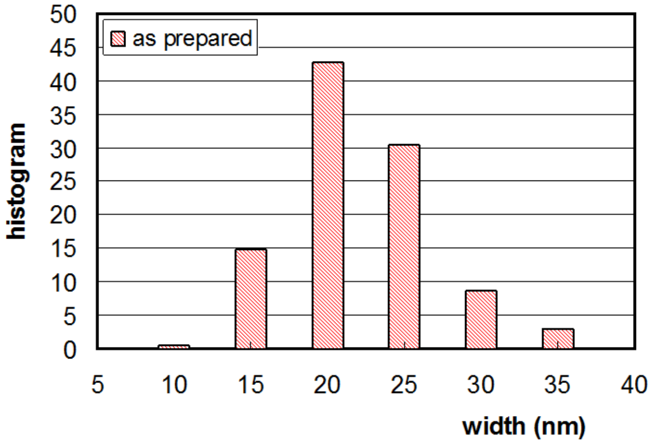

(a) as prepared

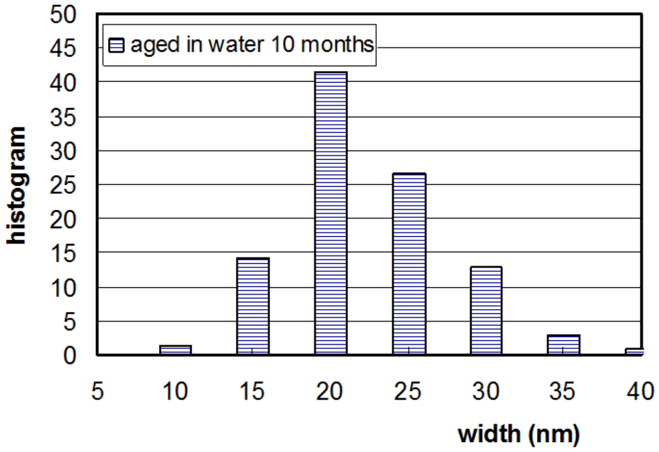

(b) purified and aged in water for 10 months

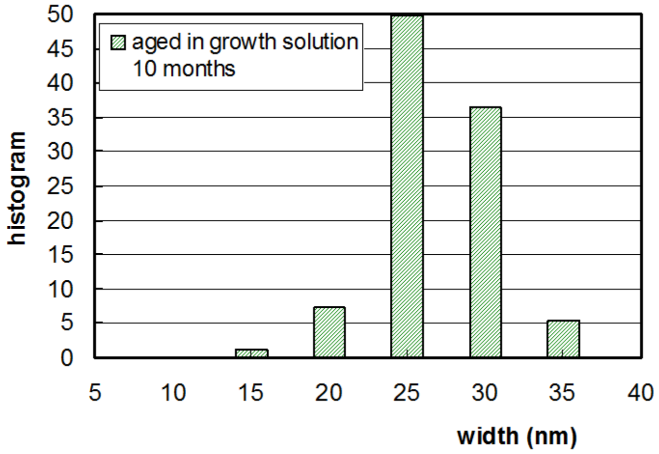

(c) aged in growth solution for 10 months

Figure 5-15 Change in width of gold nanorods during different aging processes

Table 5-1 Average size of gold nanoparticles during extended aging

	L (nm)	D_1 (nm)	D_2 (nm)	Φ_1(L/D1)
As prepared	39 ± 7	17 ± 5	20 ± 5	2.23
Purified and aging in water for 10 months	39 ± 7	18 ± 5	20 ± 5	2.24
Aging in growth solution for 10 months	47 ± 6	24 ± 3	---	1.94

The measured optical spectra support the observation of the morphological changes of the nanoparticles. The purified nanorods display a similar spectrum to that of the initially prepared samples. On the other hand, the rods that were aged in the growth solution show some discrepancies in optical properties. First, the blue-shift of the longitudinal surface plasmon peak is remarkable, and the transverse peak around 560 nm is diminished.

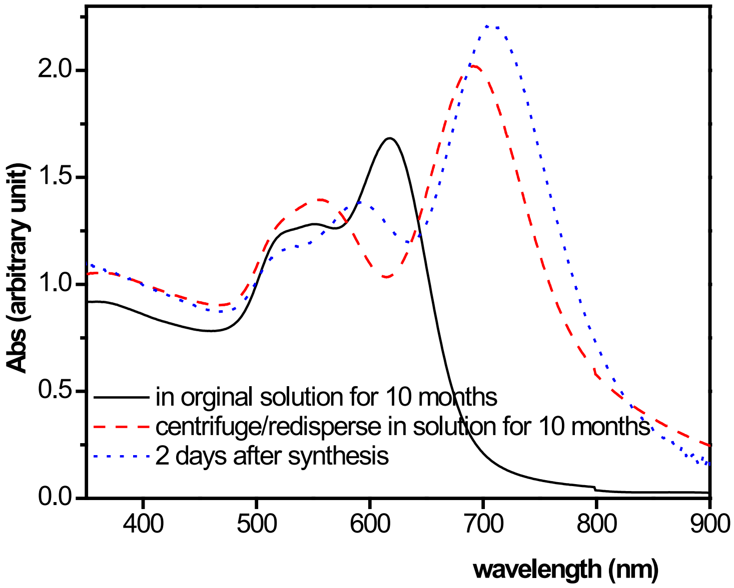

Figure 5-16 Aging effect on suspensions of gold nanoparticles

Calculation of the stoichiometry indicates the gold complex ion in the growth solution could not be completely reduced by the addition of ascorbic acid. This excess of gold complex ions in the growth solution will take part in further reactions during aging. The formation of gold nanorods depends on anisotropic growth, which indicates that the reaction rate in various directions is different. However, the increase of rods in both longitudinal and transversal directions is 8.5 nm and 7.0 nm respectively. Isotropic growth in the aging process eventually decreases the aspect ratio of the particles.

Therefore, aging brings two contrasting effects to the longitudinal surface plasmon peak. In one respect, a decrease in the aspect ratio will shift the longitudinal peak to the short wavelength side. On the other hand, an increase in the particle size will shift the longitudinal peak to the longer wavelength side. This latter point is confirmed by simulation in Figure 5-17. In this simulation, gold nanorods with lengths of 41.5, 83 and 125 nm, but with fixed aspect ratio, of 3 are utilised. It is evident that the longitudinal peak is shifted to the red side for the larger volume nanorods.

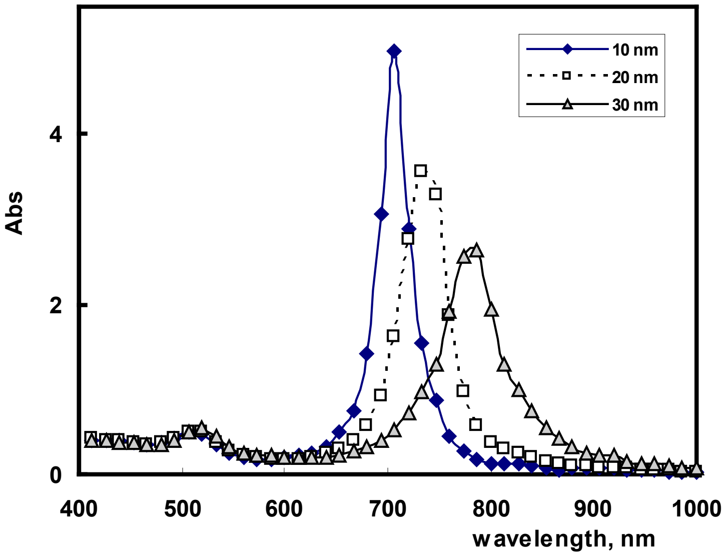

Figure 5-17 The simulated optical properties of gold nanorods with aspect ratio 3

As mentioned, during aging in the growth solution the volumes of gold nanorods increased, while their aspect ratios were simultaneously reduced. The geometric parameters of gold nanorods at different stages are listed in Table 5-2.

Table 5-2 Geometrical parameters for simulating nanorods growth.

Effective radius (nm)	Length (L) (nm)	Radius (D) (nm)	Φ_1(L/D)
10	7.4	18.4	2.5
11.8	9.0	20.2	2.24
15.25	12.2	23.7	1.94

Simulated spectra corresponding to the particles listed in the table above are plotted in Figure 5-18. It can be seen that the longitudinal peak shifts to the blue side, in spite of the increase of the volume. It is apparent that the aspect ratio has a greater influence on the shift of the longitudinal peak than the volume does The simulation results display a good match with the experimental results, for example, those of Figure 5-16, in which the longitudinal peak was seen to shift to the blue side during the aging process.

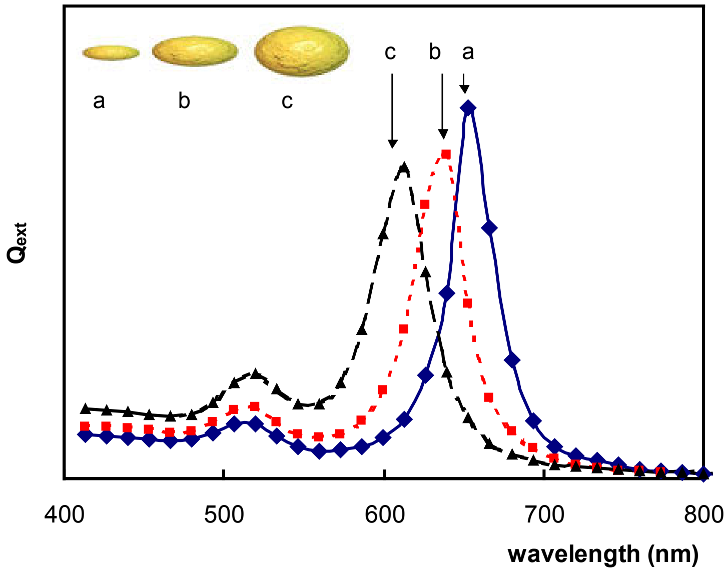

Figure 5-18 Simulated nanorods absorbance in growth

5.4.2 Role of Ag^+ in growth of gold nanorods

(a) Influence of addition of Ag^+ on morphology of gold nanorods

Although there is still controversy in relation to the role of the Ag^+ in the growth of nanorods, it is well accepted that Ag^+ plays an important part during the nanorods' growth. It was clear from the results obtained within our work that, without Ag^+, use of the CTAB alone produces a very low yield of nanorods (Figure 5-20(a)). This was also previously reported by Jana *et al.* [70]. In Figure 5-4, it was verified that the morphology of gold nanorods is dependent on the silver ion content in the growth solution. With the same concentration of CTAB, the morphologies of gold nanoparticles differ due to the presence of Ag^+, as well as how the Ag^+ is introduced. The typical morphologies of the various shapes of gold nanoparticles are indicated in(Figure 5-19). 2 mM of Ag^+ were introduced in the growth solution in the conventional form of $AgNO_3$ in Figure 5-19(b), while in Figure 5-19(c) an unknown amount of Ag^+ was introduced as a lightly silver-tinted diced glass slide. In the latter case the Ag^0 was oxidised in the growth solution by Au(I) and entered the growth solution as Ag^+. In Figure 5-19, the Ag tinted diced glass was further tinted in the electroless gold solution described in section 3.2.3 before it was introduced into the growth solution as seed. In that case, gold spheres predominate due to the lack of Ag^+. If silver ions are in the solution, they result in preferred growth of certain crystal planes and form rod-like particles. The “gold flowers” with spiked notches were such an example and were derived from lightly silver-tinted diced glass. The Ag^+ was introduced into the system by oxidisation of Ag^0 by Au^{1+}. Use of lightly gold tinted diced glass with Ag^+ in the solution resulted in gold nanoparticles appearing more like irregular tetrahedrons. The tetrahedron and “flower” morphologies are believed to have arisen as a result of Ag^+ only having access to the Au^0 nuclei in restricted directions.

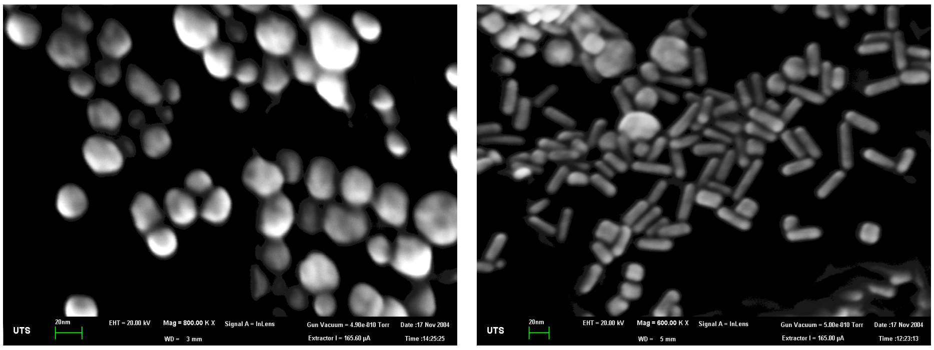

(a) without Ag^+ (b) 0.2 mM Ag^+ in solution

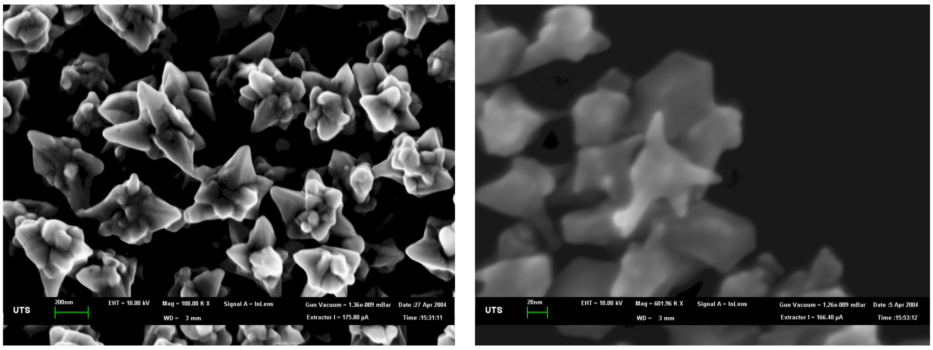

(c) plated Ag on diced glass (d) plated Au/Ag on diced glass

Figure 5-19 Different morphologies of gold nanoparticles due to Ag^+

However, silver is only effective in the presence of CTAB. When the same concentration of Ag^+ was added to different concentrations of CTAB (Figure 5-20(b)), the spectra of gold nanorods showed significant differences. The longitudinal peak was diminished for the growth solution with very low concentration of CTAB (0.008 M), which indicates that spheres rather than rods developed during the process. With an increase in the CTAB concentration from 0.02–0.04 M, the longitudinal peak was enhanced. At even higher concentrations, in the range of 0.08–0.2 M, CTAB has little influence on the intensity of the longitudinal peak. As a control, the role of CTAB without Ag^+ was also investigated (Figure 5-20(a)). Evidently CTAB alone has little effect on the development of nanorods within the scope of my experiments.

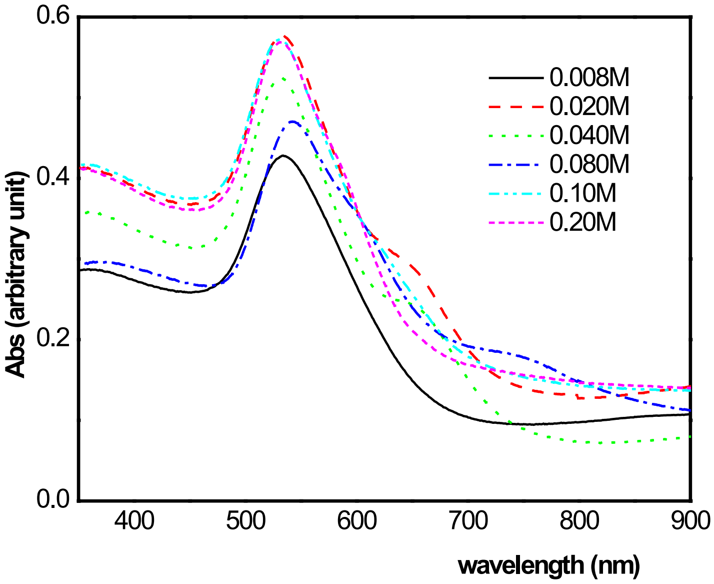

(a) without Ag^+

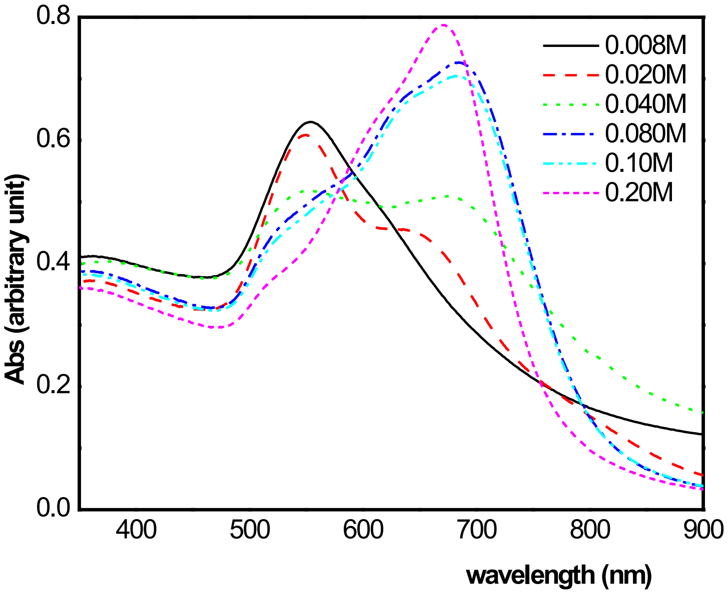

(b) with 0.025 mM Ag^+

Figure 5-20 Spectra of gold nanorods prepared with various concentrations of CTAB combined with Ag^+

(b) Distribution of Ag between gold nanorods and surfactant

The analysis results of Ag^+ for both pellet and supernatant are listed in Table 5-3 and Table 5-4. The concentration of Ag^+ in the pellet is significantly higher than that in the supernatant. Control analyses of blanks proved that the Ag content was negligible in both $HAuCl_4$ and CTAB, which indicates that all the silver in the experiments must have come from the added $AgNO_3$. This is also strong evidence that the Ag was either adsorbed on the surface of the nanorods or incorporated as an inclusion in the gold nanorods.

Table 5-3 Concentration of Ag^+ in pellets of centrifuge

		Ag in pellet		
Added Ag (mM)	Added Ag (ppt)	Before centrifuge (ppt)	After dilution (ppt)	Total (g)
0	0	94.5~142	7.1	1.42×10^{-7}
0.05	5390	1.45×10^{4}~2.20×10^{4}	1110	2.20×10^{-4}
0.1	10800	1.77×10^{4}~2.70×10^{4}	1370	2.70×10^{-4}
0.2	21600	1.88×10^{4}~2.91×10^{4}	1490	2.91×10^{-4}

Table 5-4 Concentration of Ag^+ in supernatant after each dilution

		Ag in supernatuant		
Added Ag (mM)	Added Ag (ppt)	Growth solution (ppt)	first centrifuge (ppt)	after dilution (ppt)
0	0	2.3	0.12	0
0.05	5.39×10^{3}	4.92×10^{3}	262	20
0.1	1.08×10^{4}	9.91×10^{3}	527	40
0.2	2.16×10^{4}	1.99×0^{4}	1058	79

Table 5-5 Molar ratio of Au/Ag in gold nanorods

Added Ag/Au in growth solution (mmol/mmol)	Ag/Au in gold nanorods (mmol/mmol)
1:10	1:1.8
1:5	1:1.5
1:2.5	1:1.4

It is worth pointing out that the [Ag^+] in the growth solution increased proportionally with added [Ag^+], while the concentration and the total amount of Ag^+ in the pellet remained at the same levels. This indicates that the amount of Ag being adsorbed in or on the rods is approximately the same. Even while the molar ratio of added Ag and Au ranged significantly from 1:10 to 1:2.5, the analytical results indicate that the ratio only varies slightly from 1: 1.8 to 1: 1.4 in the rods. Furthermore, the addition of Ag^+ retarded the reaction rate significantly. These factors suggest that the Ag was adsorbed in some way on the surface of gold nanoparticles. In support of this, Jana *et al*. have suggested that AgBr adsorbs on the surface of gold nanorods and selectively restricts the growth of certain crystal planes [70].

(c) Behaviour of Ag in reaction

Up to this point, it has been shown that there is a strong possibility that the Ag may be adsorbed on the surface of the gold nanoparticles. However, the form of the Ag is still not known, that is, in which species, either as AgBr, $AgBr_2$- or Ag0. There are different viewpoints on the behaviour of silver in reaction. Liu *et al*. suggested a mechanism of underpotential deposition (UPD) [212]. With this theory, Ag^0 could be deposited on the gold surface as a monolayer or sub-monolayer, even though Au is more easily reduced in the system. Jana *et al*. believed that Ag(I) worked as a passivation layer in the form of AgBr [70]. However, Perez-Juste *et al.* suggested that $AgBr_2$- is the species contributing to the passivation [77].

The reduction of Ag from Ag+ to Ag0 can be probed by looking for the surface plasmon peak of silver at around 400 nm. The experimental results of this work showed no such plasmon peak during the growth of gold nanorods, which indicates Ag+ is not reduced by ascorbic acid in the CTAB solution in the scope of the experimental condition in the work. Jana and Pal *et al.* showed that Ag+ could only be reduced in a very high pH solution, which is not a normal operating mode for gold nanorods [70, 213].

For the system without CTAB, even with the equivalent of Br^- (provided by KBr) present in the solution, the Ag(I) will be reduced. The plasmon peak of 399 nm in Figure 5-21 indicates the reduction Ag(I) to Ag^0.

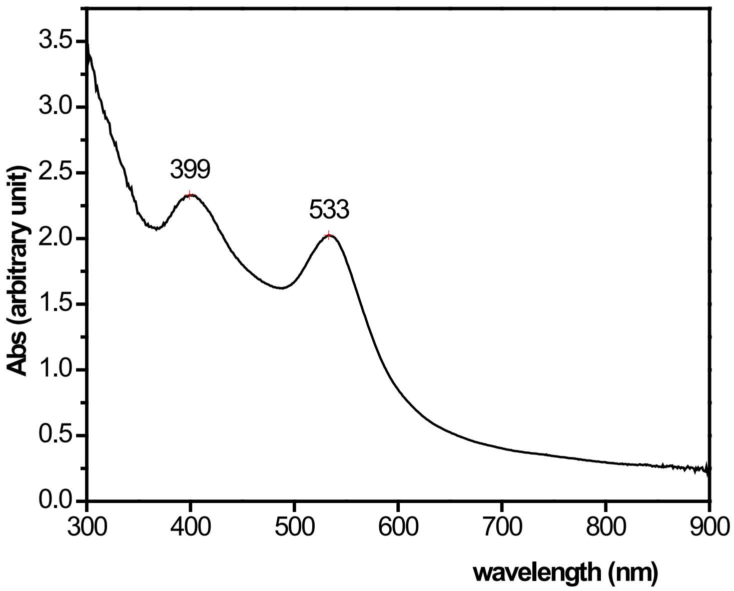

Figure 5-21 Reduction of Ag^+ and $AuCl_4^-$ with no CTAB by ascorbic acid

Simulation by Cortie *et al.* also affirmed, a with monolayer of Ag0 on gold nanoparticles, the surface plasmon peak at around 400 nm, which indicates the existence of silver, is strong enough to be detected (Figure 5-22). For gold nanorods, there is no surface plasmon peak around 400 nm. However, for the nanorods with silver "ear", the 400 nm peak is very obvious (Figure 5-22).

In this simulation, the geometric parameters of gold particles come from the analysis of 264 particle shapes produced by aging suspensions for 50 minutes. The values of the length of gold nanorods (L), minimum width (D_1) and maximum width (D_2) were (45.6 ± 9.2) nm, (22.6 ± 6.1) nm, and (24.3 ± 6.3) nm respectively, where the range given is the standard deviation of the measurement. The resulting aspect ratios, L/D_1 and L/D_2 were 2.18 ± 0.74 and 2.00 ± 0.63 nm.

Both simulation and experimental results confirm that there is no Ag0 in the final products of gold nanorods. The Ag must exist as the form of Ag(I) in gold nanorods. So, the question is whether Ag works as AgBr colloid or $AgBr_2$-. Mixing Ag+ and Br^- results in the AgBr yellow precipitate, and the precipitate dissolves instantly with shaking in 0.1 M CTAB solution. However, it does not dissolve in 1 M KBr. there is no clear evidence whether the products are AgBr colloid or $AgBr_2$-. Nanoparticles of AgBr were not found in any samples from this work. Thus, $AgBr_2$- is the more likely form in the reaction of gold nanorods.

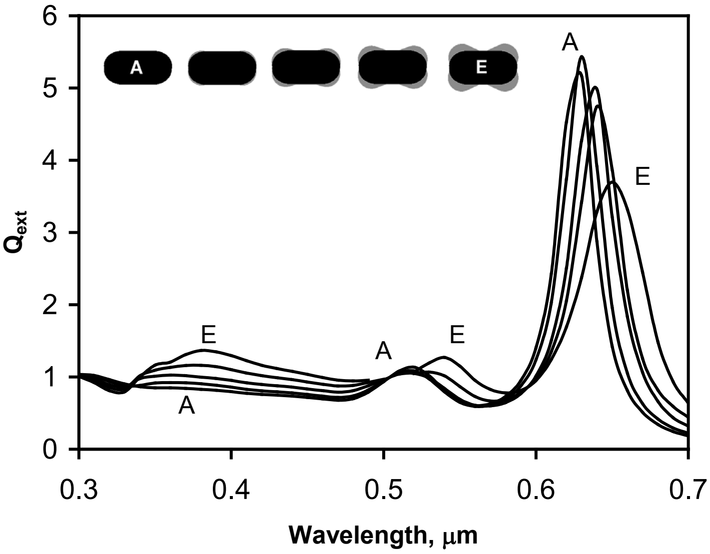

Figure 5-22 Simulation of optical properties of the effect of Au/Ag nanorods

The degree of CTAB micellar dissociation, expressed by α =p/n (where p is the effective charge per micelle of aggregation number n), is 0.091-0.12 [214]. This indicates that 10% of Br^- is retained in solution as counterions. Considering the extremely small $K_{sp,AgBr}$ (5.0 × 10-13) [189, 215], Ag+ in the solution actually exists as $AgBr_2$- and is stabilised by CTAB in the working range.

5.4.3 Effect of CTAB

The CTAB has an important role in the reaction of forming gold nanorods. Besides collaborating with Ag^+ (as discussed in section 5.4.2(a), CTAB also converts $AuCl_4^-$ into $AuBr_4^-$ [155]. It has also been reported by Aguirre *et al.* that CTAB might induce the shape change of the nanoparticles [216].

$$AuCl_4^- + 4Br^- = AuBr_4^- + 4Cl^- \qquad \text{(eq 5-8)}$$

There have been reports that CTAB micelles worked as the soft template for the gold nanorods [72]. In the scope of this research, different concentrations of CTAB (concentration range of 0.02 M to 1.0 M) were used for producing gold nanorods. The spectra of gold nanoparticles generated under different CTAB concentrations are indicated in Figure 5-23. The spectra were collected at around 1.5 hours after the reaction started. For the low concentration of CTAB (0.02 M), the intensity of the longitudinal peak at around 670 nm was too weak to be noted, compared with the gold surface plasmon peak. With increasing concentration of CTAB, the longitudinal peak appeared initially at around 850 nm, and then gradually blue-shifted. In 1.0 M CTAB, the longitudinal peak almost merged with the transverse surface plasmon peak to form a broad peak. This result indicates that nanorods could be produced in the CTAB concentration range from 0.05 M to 0.7 M. For the CTAB outside the range, gold nanospheres are the more preferred shape.

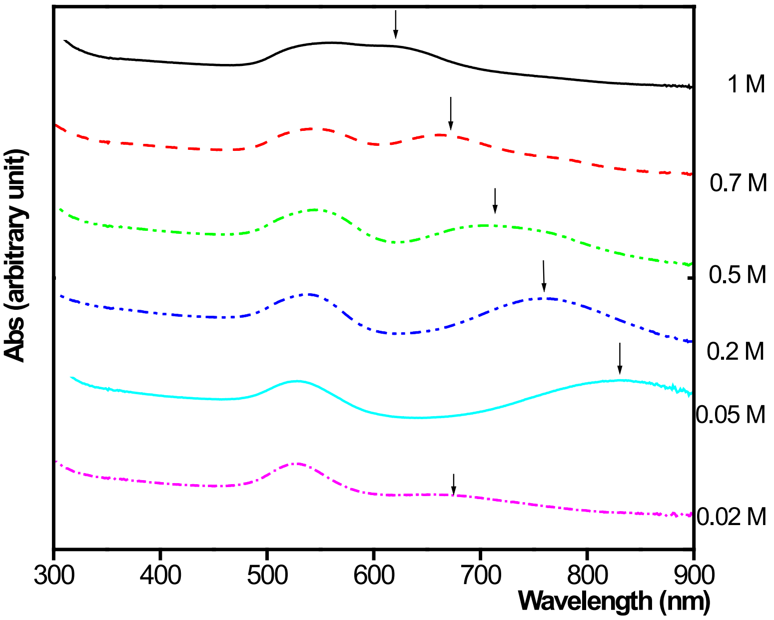

Figure 5-23 The spectra of gold nanorods produced in different concentrations of CTAB

This observation is consistent with the micelle shape of CTAB. It has been reported that CTAB has two critical micelle concentrations (CMC) [217]. CMC_1 is around 1 mM; a concentration greater than that forms spherical micelles [218]. NMR relaxation measurements and small-angle X-ray scattering measurements on CTAB have found that CMC_2 is at a concentration of 0.05M at room temperature. Above this concentration, there is a transition of the shape of CTAB micelles from sphere to rod. The long axis and short axis of the micelles are around 200 nm and 8 nm respectively [219, 220]. In very high concentrations of the CTAB solution, that is, greater than 0.5M, cubic and lamellar liquid crystal structures dominate [221].

The above viewpoint was further supported by reduction of $HAuCl_4$ in a cetyl trimethyl ammonium chloride (CTAC) solution. It was reported that a poor yield of nanorods was produced if CTAC was used in place of CTAB or as cosurfactant [77]. Coincidentally, it was also reported that CTAC formed the spherical micelles over the whole range of concentrations from the CMC to its solubility limit [222].

If the shapes of CTAB micelles are compared with the shapes and sizes of gold nanorods at different stages, close similarities can be found. There are spherical and oblate spheroid micelle shapes present in the CTAB solution. Israelachvili *et al*. proposed a cylindrical micelle with swollen hemispherical ends in further micelle growth, a model also favoured by other researchers [222]. Gold nanoparticles with all these three shapes are found during the different synthesis conditions. This evidence suggests the "soft template" viewpoint.

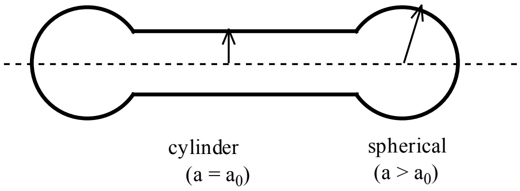

Figure 5-24 Micelle shape proposed by Israelachvili *et al.*

(Redrawn from [222].)

5.4.4 Proposed synthesis mechanism

In a previous discussion, another bilayer micelle mechanism for the growth of gold nanorods was suggested. It is different from Gao's "zipping" bilayer mechanism [79], but CTAB micelles still have an important function during the growth. Other researchers have demonstrated the existence of bilayers of surfactant in the system [109] The structure of a bilayer micelle is suggested as illustrated in Figure 5-25. The headgroups of the inner layer of CTAB are arranged with their heads to the surface of the gold surface. The tails tangle with tails from the outer layer of CTAB and headgroups interact directly with the aqueous phase. On the hydrophilic gold surface, CTAB cannot easily displace water adsorbed on the surface. Instead, a hydrophobic interface is built up by the tail of the monomer. In this way, CTAB is strongly adsorbed on positively charged hydrophilic surfaces [214, 223].

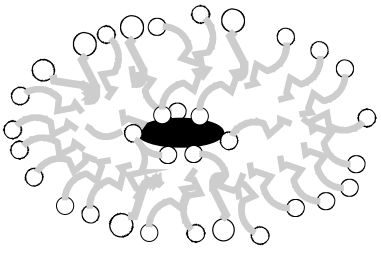

Figure 5-25 Illustration of gold nanorods in CTAB micelle

In the presence of $AgBr_2$-, the inner layer of CTA^+ headgroups binds to the gold surface through $AgBr_2$-. It has been further assumed that the AgBr or $AgBr_2$- is selectively adsorbed on the different crystal planes: binding of AgBr or $AgBr_2$- with {110} (side of rod) is stronger than its binding with {111} facets (ends of rod) [72], which leads to the anisotropic growth of particles. In the absence of Ag^+, the CTAB adsorbs evenly on the gold surface with the headgroups attached, in which isotropic growth results in spherical particles.

The growth of nanorods can be outlined as follows:

a). $AuCl_4^-$ is converted into $AuBr_4^-$, The anisotropic growth of gold particles is due to $AgBr_2$- selectively adsorbed onto the gold seed.

b). The disassociation and re-absorbing of particular monomers should be controlled by $AgBr_2$-

c). The shape and relaxation time of micelles influences the mass transportation of both $AuBr_4^-$ and $AgBr_2$-. The tails of CTAB inhibit the mass transfer of Au(I) onto the surface planes, which retards the growth of gold nanorods along particular crystal planes. The transportation of $AgBr_2$- and Au(I) controlled by equilibrium can be explained by the electric-field-directed mechanism of Perez-Juste *et al.* [77].

d). The shape of the micelle is essential to stabilise the gold nanorods.

Most of the experimental observations can be explained via this model, which combines a “soft template” with $AgBr_2$- adsorption. As mentioned above, introducing Ag^+ into the system leads to slowing of the reaction rate. It is believed that adsorbed $AgBr_2$- retards the mass transportation of $AuBr_4^-$. The impact of Ag^+ on the aspect ratio of nanorods is also explainable by this model. An increase in the concentration of Ag^+ initially causes $AgBr_2$-- to adsorb on the {110} sides of the gold nanorods, which restricts the sideways growth of nanorods and leads to a larger aspect ratio. A further increase in Ag^+ concentration is expected to result in adsorption of $AgBr_2$- on {111} facets, which leads to a smaller aspect ratio, while the nanorods grow. In this system, $AgBr_2$- works as a stabiliser, and causes an anisotropic reaction rate.

The process of growth is illustrated in Figure 5-26. In the initial stage, when the seed is surrounded by a CTAB micelle, the rate-determining step of the reaction is mass transportation. In this case, anisotropic growth results. When the rods grow larger, the micelle structure can no longer accommodate them and the CTAB is adsorbed onto the gold surface as a bilayer. Easier access of Au(I) to particular crystal planes makes the dogbone shape possible. In the long aging process, depletion of ascorbic acid significantly reduced the reaction rate. Therefore, in this case the transport of reactant is uniform to all facets of the nanorods and the reaction becomes isotropic.

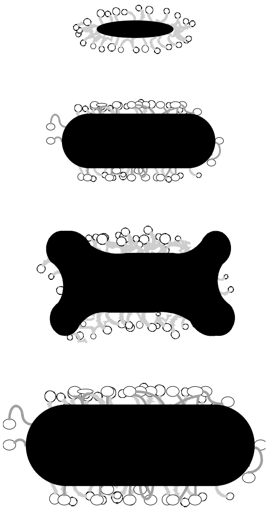

Figure 5-26 Growth scheme of gold nanorods from seeds

5.4.5 Colour gamut

Mixing of gold nanorods of different aspect ratios is a feasible way to produce a neutral blue colour with high infrared absorbance. Furthermore, control of the colour of suspensions or coatings of gold nanorods may be important in some applications. The “gamut” of a particular colour-producing technology is defined as the range of possible colours that it can produce. However, no study seems to have been made previously of the gamut of gold nanorods, an omission which is remedied here by mapping the colours of suspensions of the rods to the a* and b* colour coordinates of the CIE-LAB system. Figure 5-27 shows values measured during various growth experiments. It is evident that gold nanorods display a surprisingly wide colour gamut, from purple, through blue, to red depending on their particular shapes. An important consideration is that the longitudinal peak of gold nanorods with short aspect ratios is in the visible region. The resulting extinction of part of the upper visible region makes the colour of such gold nanorods purple or blue. During growth and/or an increase in concentration, the colour starts from light pink, becoming purple and then dark blue.

During the process of growth, gold nanorods of different aspect ratios behave quite differently. For gold nanospheres, the colour remains in the red region all the time, the absorbance increases rapidly in the beginning and then remains constant. For the high aspect ratio gold nanorods, the colour is red initially, and then turns to lighter pink in the later stages. In this case, the longitudinal peak is located in the invisible near-infrared region. That peak has little influence on the colour perceived by the human eye, and coatings or suspensions of the nanorods consequently display a pink-purple colour. In contrast, the colour change of nanorods of intermediate aspect ratio behaves quite differently. First, the colour starts from light pink, changing to purple and then becoming dark blue. After a certain stage, the colour tends to shift back to light blue or purple. One possible explanation is given in the simulation results discussed earlier, in which the formation of dogbone and dumbbell shapes shifts the longitudinal peak to shorter wavelengths.

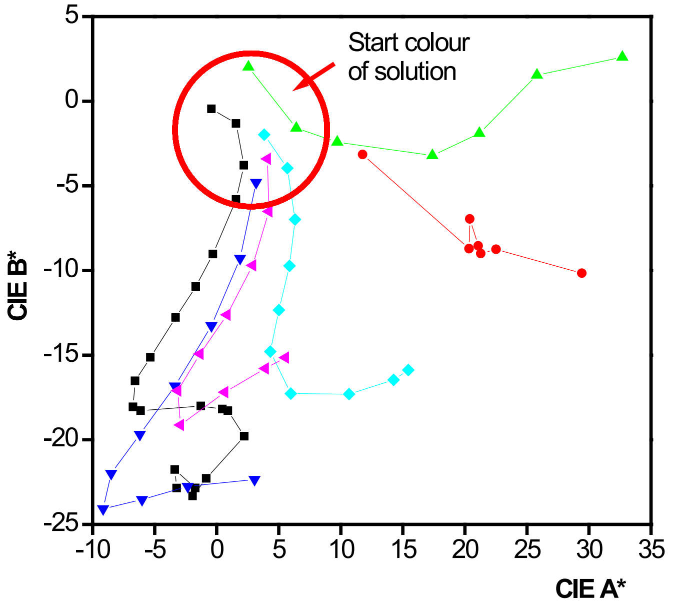

Figure 5-27 Colour changes of gold nanorods during growth

The results imply the importance of quenching reagents in the preparation of gold nanorods of particular optical properties. Otherwise, the morphology of gold nanorods during later service might be hugely different from the nanorods at the time of manufacture.

5.5 Summary

In this chapter, different process parameters, such as the pH of ascorbic acid, Ag^+ concentration, CTAB, and amount of gold seed are explored for their effect on the growth of gold nanorods. It is found that at a pH of 2, ascorbic acid cannot reduce Au(I), and a higher pH of ascorbic acid solution is preferred for the production of gold nanorods. The proper concentration of Ag^+ as well as seed is essential to form the gold nanorods. Rod formation is suppressed both in the absence of Ag^+ or with an excess of Ag^+ in the system. The results also confirmed that the Ag^+ needs to interact with the CTAB to assist the formation of the nanorods. A complex mechanism for the formation of gold nanorods is proposed. In the mechanism, the adsorbed $AgBr_2$- acts as the bridge between the CTAB micelle soft template and gold seed. The function of the CTAB micelle is to stabilise the gold nanorods and transport both Au(I) and $AgBr_2$- to particular crystal planes, in which differential reaction rates are achieved for the anisotropic growth of the particle.

Optical properties of gold nanorods were simulated. During the growth process, the aspect ratio is more important than the increase in volume, and this causes the longitudinal peak to shift into the blue in the later stages of growth. The simulation results agreed qualitatively with the experimental data. The colour of nanorods during the growing processes was examined using the CIE colour model. The colour change of shorter nanorods behaved significantly differently from that of longer rods. The difference is due to the position of the longitudinal peak. The longitudinal peak of long aspect ratio rods is located in the near-infrared region, and the colour of these rods depends on the transversal plasmon peak, which is around 520 nm. Thus, the rod show a pink colour. However, the longitudinal peak of short rods is located in the visible region, and the colour of these rods is due to the complex effect of both transversal and longitudinal peaks. The rods are purple to blue, depending on the positions of both peaks and their relative absorption intensities.

6. Spectrally selective coatings on windows by self-assembled gold nanorods

6.1 Introduction

A significant portion of the exterior surface area of modern buildings is covered by plate glass. Unfortunately, normal plate glass is not only a window for visible light, but also provides a free pathway for much of the infrared part of solar radiation as well. In summer the presence of windows may increase the burden on air-conditioning units [194].

In Chapter 3, it was shown that the gold nanosphere coatings deposited onto plate glass through an aqueous process had a somewhat inferior spectral selectivity between visible and infrared radiation, compared with other products. In Chapter 4, it was concluded that the optical properties of such coatings are controlled by the nucleation of gold on the surface of the substrate and on the threshold thickness required to make a continuous film [224]. Single, isolated gold nanospheres have only one surface plasmon absorption peak, around 520 nm. Any absorption of gold nanospheres in the infrared region indicates a dipole-dipole interaction of approaching gold nanospheres.

The recent, intensive research on precious metal nanoparticles other than spheres, such as nanorods [16], triangles [67, 225], star shapes [226], branched shapes [227], nanotubes [228], nanoshells [17] and “caps” [19], have inspired us to consider the potential of these less symmetrical particles for solar glazing. Unlike gold nanospheres, these shapes of gold nanoparticles not only have a surface plasmon peak at 520 nm, but also have other peaks at longer wavelengths. This may produce coatings that contain better spectral selectivity between the infrared and visible regions. We consider gold nanorods to have especially attractive properties for solar control applications. In Chapter 5, it was shown how gold nanorods of tunable aspect ratio could be produced in high yield by a bench-top wet chemical process. This makes gold nanorods an ideal material for this application. By controlling the morphology, the longitudinal absorption peak can be shifted from the visible region down to the near-infrared (1200 nm) region, which gives better spectral selectivity. Furthermore, it has been proposed that gold nanorods could be assembled as a “light switch” [210]

This could also be the prototype of the future “smart window”; that is, by turning the orientation of gold nanorods, the window changes its infrared absorption as required.

Optical properties of gold nanorods deposited on surfaces have attracted a lot of research interest recently. There are two possible strategies to apply the gold nanorods onto the glass surface; they are (1) growing of nanorods directly on the surface, and (2) self-assembling of nanorods on the surface. Wei, Taub *et al*. [108, 141, 142] modified the seed-mediated method [68] by attaching gold seeds to a functionalised surface, and then introducing a growth solution. The growth of the gold nanorods, attached to the surface, was monitored [108], imaged and manipulated by AFM [144]. The disadvantage of this strategy is that only a low density of seeds on the surface, 1-10 particles/μm^2, become attached, and therefore the gold nanorods are not dense enough to effectively shield the substrate from the infrared.

Self-assembling of gold nanorods on glass currently appears to be a more feasible method [126-129, 229]. An appropriate pH was found to be one of the most important factors in controlling the self-assembly process [129, 139]. It not only triggered immobilisation of gold nanorods but also controlled the density of immobilised nanorods on the surface [133]. The pH value also played an important role in the orientation of aggregated nanorods on the surface. Orendorff *et al*. found that at pH 8.0, gold nanorods formed side-by-side conjugates, rather than the isolated and disordered aggregation formed at pH 3.0 [131].

Ions have been reported as additional factors affecting assembly. Cl^- was reported to control segregation structures. For a particular concentration of [Cl^-], gold nanorods oriented in nearly head-to-tail shapes in the microscopic scale [133].

The surface charge of the nanorods was also reported as an influence on assembly. Gold nanorods with either negative or positive charges were explored in the immobilisation process. The surfaces of gold nanorods were modified by coatings of polyelectrolyte. The step converted the surface charge from positive to negative. The tuning of the surface charge of gold nanorods gives more flexibility for the application of gold nanorods in the immobilisation process [134]. The transfer of gold nanorods from the aqueous to the organic phase was studied by Wei *et al*.. The process did not require addition of thiol or amine. The morphology of the gold nanorods persisted after transferring. This will be very useful in the immobilisation of gold nanorods on certain non-linear optical surfaces [125]. All these reports prompted me to conclude that self-assembly is a promising technical solution for producing coatings of gold nanorods.

However, the thermal instability of gold nanorods is a major concern for many potential applications. It has been reported that the gold nanospheres can melt at as low as 500^{o}C [230]. There have been several reports on the melting of gold nanorods under irradiation by different wavelengths of laser light [81, 118]. Since gold nanorods are a thermodynamically unstable structure, how their microstructure will be changed and how that will affect their optical properties over long periods still needs to be examined. Finally, uniformity of self-assembled coatings at the macroscopic level remains a concern relevant to the use of gold nanorods for solar-control purposes.

6.2 Experimental

6.2.1 Materials

HCl, HNO_3, hexadecyltrimethylammoniumbromide (CTAB), γ-aminopropyltriethoxy-silane (APTES), potassium borohydride (KBH_4), L-ascorbic acid and gold were sourced from diverse suppliers. All chemicals were used as-received. Generic soda-lime glass microscope slides were obtained from Livingstone. All H_2O used was purified by double-distillation or Millipore® system. $HAuCl_4$ solution was prepared according to the procedure described in section 3.2.2.

6.2.2 Deposition of gold nanorods on glass via self-assembling method

(a) Synthesis and purifying of gold nanorods

The method of synthesis and purifying of gold nanorods has been described extensively in Chapter 5.

(b) Substrate functionalisation with *APTES*

The diced glass slides (30 × 15 mm^2) were cleaned in 50°C of Piranha solution ($Vol_{30\%\ H_2O_2} : Vol_{98\%\ H_2SO_4} = 1 : 5$) for 30 minutes. They were rinsed with distilled water and methanol in sequence before use. Cleaned glass slides were dipped into APTES solution (1:5, $Vol_{silane} / Vol_{ethanol}$) for 15 minutes. The coated glass slides were then rinsed with methanol before the coating was cured at a temperature of 110°C in an oven for 20 minutes.

(c) Self-assembly of gold nanorods on the glass

The silanised glass slides were then dipped into 20 mL of gold nanorod colloid for the derivatisation. The purified and concentrated gold nanorods colloids were diluted by double-distilled water (1:5) immediately before use. The derivatisation lasted up to three days. The density of nanorods on the coatings could be controlled by varying the deposition time.

6.2.3 Growth of gold nanorods on glass

(a) Initialised with gold seed

The diced glass slides were pre-treated according to the procedure described in sections 4.2.1 and 4.2.2. The slides were immersed in deposition solution for 1 ~ 2 minutes. Afterwards, the lightly tinted glass slides were cleaned and transferred to the gold nanorod growth solution, which contained 0.20 M CTAB and 0.5 mM of $AuCl_4^-$ and 0.5 mM ascorbic acid. No additional seeds were added in.

(b) Initialised with silver seed

The diced glass slides were pre-treated according to the procedure described in section 4.2.1 and then immersed in silver deposition solution for 0.5 ~ 1 minute. The silver deposition solution contains 0.015M $AgNO_3$, 0.028 M D-glucose and 0.13 M NH_4H_2O [39, 231, 232]. The lightly tinted glass slides were cleaned and transferred to the gold nanorod growth solution which contained 0.20M CTAB and 0.5mM of $AuCl_4^-$ and 0.50mM ascorbic acid. No additional seeds were added in.

6.2.4 Annealing of gold nanorods coating

The coated glass slides were annealed in a clean oven under atmospheric conditions at various temperatures. To optimise the annealing time, a drop each of gold nanorod colloid was placed on a series of carbon stubs in a desiccator overnight. Once the solution dried, the stubs were kept in the oven with designated temperature steps for different times.

6.2.5 Gold nanorod film characterisation

(a) Transmittance

The glass slides with the gold nanorods as-deposited and annealed were inspected with a Cary 5E UV/VIS/IR spectrophotometer, over the range 170 nm to 4300 nm and with a resolution of 0.5 nm. The visible-IR transmission spectra of the samples were obtained at a 5 nm/s scanning rate with a spectral bandwidth (SBW) of 2 nm. Due to the small dimension of the sample, half-beam height was utilised during all the measurements.

(b) Morphology

The morphology of gold nanorods as-deposited and annealed was characterised using a LEO scanning electron microscopy (SEM) with in-lens images at 2 30 kV.

(c) Near-field optical properties

The annealed gold nanorod sample was imaged using the NSOM-100® system from Nanonics®. Local excitation was provided by 100 nm aperture multi-wavelength probe, driven by a 20 mW, 514 nm laser source at the other end of the optical fibre. The light signal was collected by a 50× objective lens. Photons were counted by Avalanche Photo-diode (APD). The sample was illuminated through the probe by the laser, and the reflected light signal from the sample surface was collected by APD. The near-field optical image and topological image were imaged simultaneously by NSOM-100®.

(d) Thermal stability

The thermal stability of the gold nanorod coatings was examined by thermogravimetric analysis. Simultaneous DTA and TGA measurements were obtained using an SDT 2960 (TA Instruments). The sample was under high purity Ar as a protective atmosphere. The weight losses of the purified gold nanorods and CTAB were measured over a temperature range of 25°C to 350°C, with a temperature ramp rate of 5°C/min.

6.2.6 Simulation of optical properties

The optical properties of gold nanorods were numerically simulated with the discrete-dipole approximation method (DDA), as described in previous chapters.

6.3 Results

6.3.1 Morphology of gold nanorods in colloid and as a deposit.

The nanorods as produced in suspension are shown in Figure 6-1(a), and are 20-40 nm long with a typical aspect ratio of 1.5 ~ 2. The nanorods immobilised on glass are shown in Figure 6-1(b) It is clear that the immobilised gold nanorods appear to have a different morphology from those on the carbon stubs (Figure 6-1 (a)). The particles appear flatter and relatively spherical, compared with those on the carbon stubs. This may be an artefact due to the less conductive nature of the glass substrate under the electron beam of the SEM. Low-density coatings showed gold nanorods dispersed on the substrate with random orientation. The gold nanorods are mostly isolated as deposited.

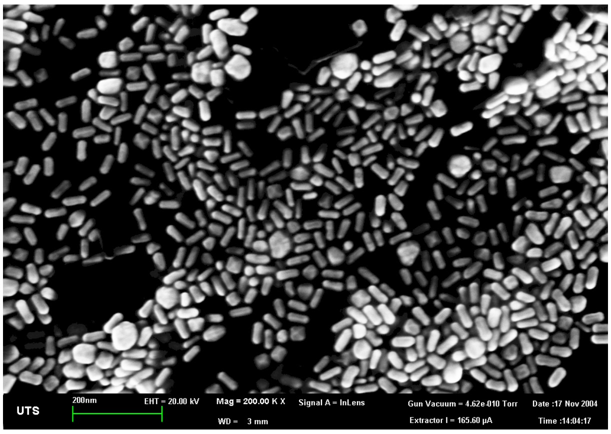

(a) in colloid

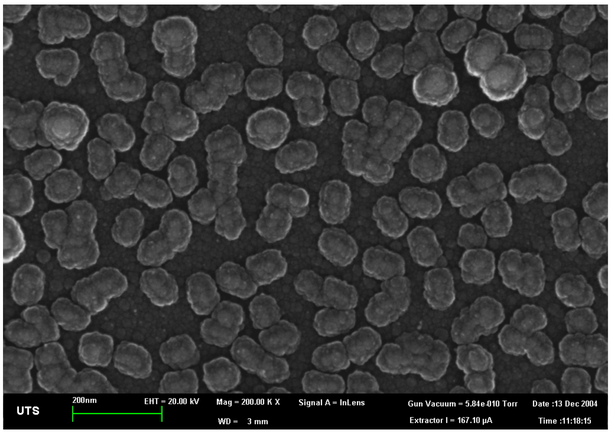

(b) as immobilised

Figure 6-1 Morphology of gold nanorods

6.3.2 Colour of colloids of gold nanorods

The colours of gold nanorods with different aspect ratios are indicated in Figure 6-2. From left to right, the aspect ratio of gold nanorods increases gradually. The colour turns from red to violet, and then blue, and eventually ends up as pink-red.

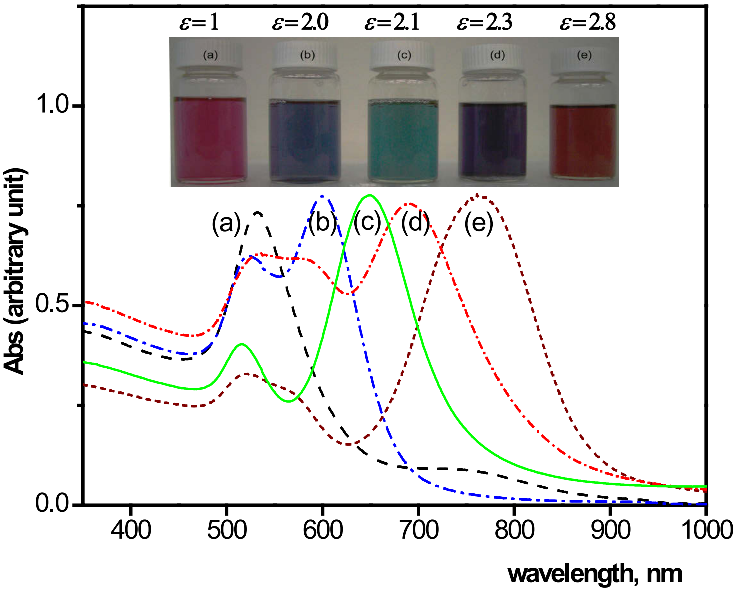

Figure 6-2 Gold nanorods with different aspect ratios

The change in colour of the gold nanorods depends on the absorption caused by the longitudinal peak, since the transverse peak was constantly located at around 520 nm . As the longitudinal peak shifted from the visible region to the infrared region, the colours of the colloids changed accordingly. The colour is also related to the ratio of absorbances of these two peaks. The gamut of colour for the gold nanorods has been discussed in section 5.4.5.

6.3.3 Simulation of optical properties of gold nanorods

The simulation affirmed the analysis above. The optical properties of gold nanorods for different aspect ratios are simulated by DDSCAT. For the gold nanoparticles with aspect ratio of 1 (nanosphere), there is only one absorption peak at 520 nm, which removes the green part of the spectrum. The colloid displays red in transmission. Prolonging of rod shape generates a second peak in the longer wavelengths of the visible region, and this brings a purple and/or blue colour to the colloid. A further increase in the aspect ratio results in the longitudinal peak shifting into the near-infrared region. At this point only the 520 nm absorption peak from transverse resonance exists in the visible region, which turns the colour of the gold nanorods with long aspect ratio back into red again, as simulated in Figure 5-11.

6.3.4 Comparison of transmittance of gold nanorod coating and colloid

The optical absorption spectra of glass coated with gold nanorods and the gold nanorod colloid on its own were measured by Cary 5E (Figure 6-3) according to the procedure described in section 6.2.5(a). It was found that the spectrum of the low-density coating of gold nanorods was identical to that of the gold nanorods in the colloid. Apparently, the gold nanorod coating inherited the optical properties of gold nanorods.

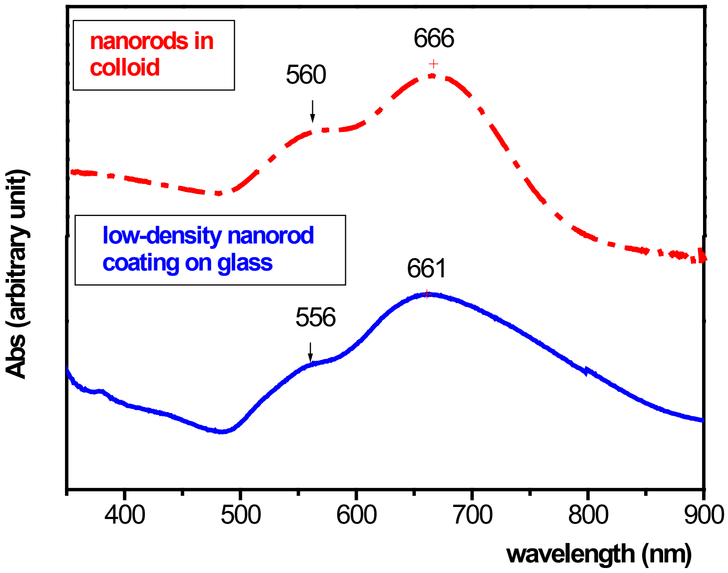

Figure 6-3 Spectra of gold nanorod colloid and gold nanorod coating

6.3.5 Annealing of gold nanorods on the graphite sample stud

The gold nanorods were annealed on graphite sample studs for various times and temperatures to determine their thermal stability. Samples were annealed at temperatures between 160 and 240°C. The morphology of gold nanorods after annealing was imaged with SEM and is indicated in Figure 6-4. The data suggest that the upper temperature limit for a stable gold nanorod coating is actually below 160°C.

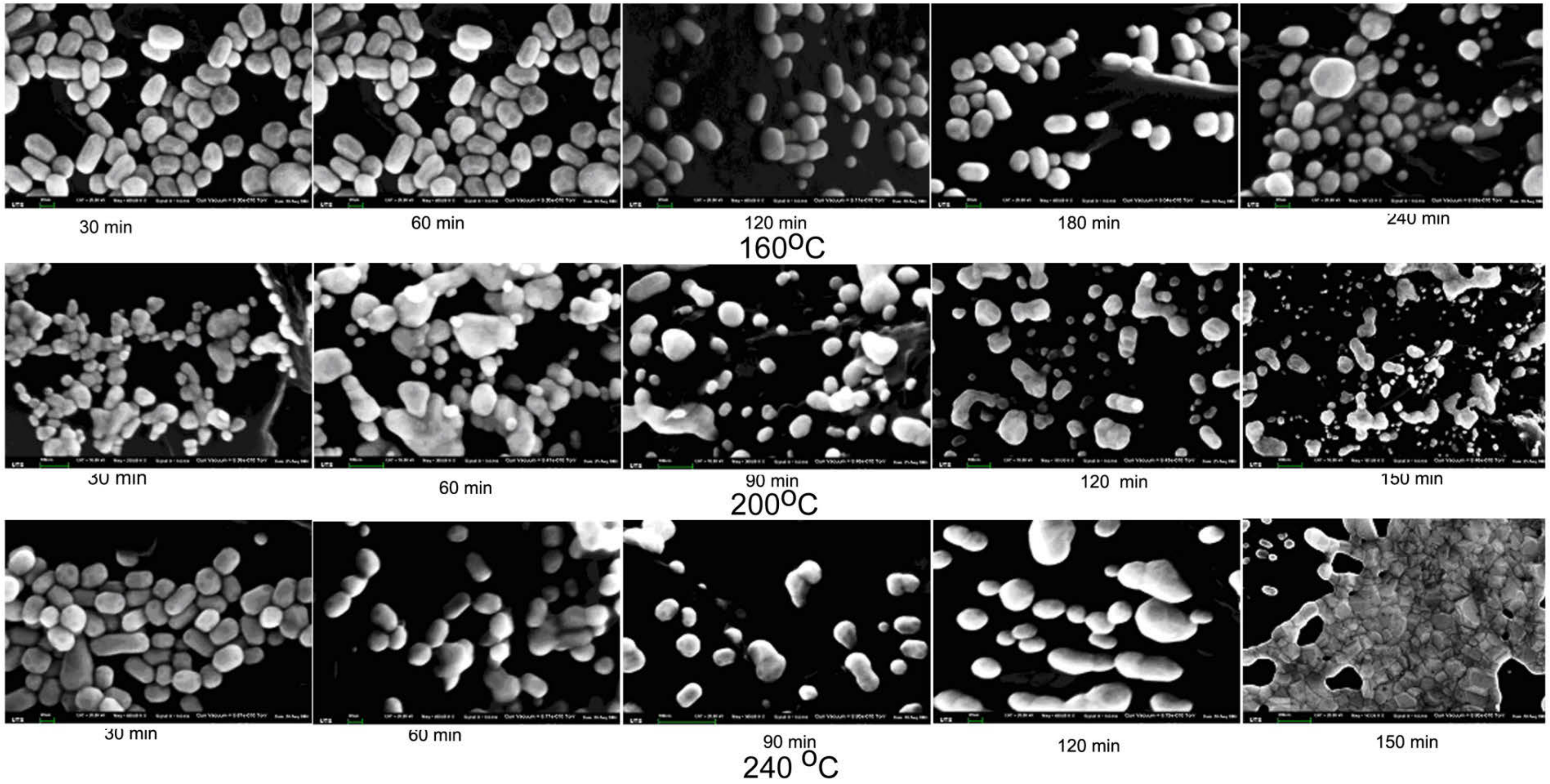

Figure 6-4 Morphologies of gold nanorods after annealing

6.3.6 Optical properties of various coatings

The typical spectra of gold nanorod coatings of high and low packing density are compared in Figure 6-5 to coatings of gold nanospheres. The coatings displayed quite different optical properties. Compared with the nanosphere coatings, the low-density nanorod coating showed similar transmittance in the near infrared range from (1500–2500)nm, but higher transmittance in the visible region. The high density nanorod coating showed the opposite effect; its visible transmittance is quite close to that of the nanosphere coating, while it has high shielding efficiency in the near-infrared region. Moreover, the absorption peak of the gold nanorod coating is displaced to longer wavelengths. This indicates that the nanorods would have a higher efficiency in solar screening.

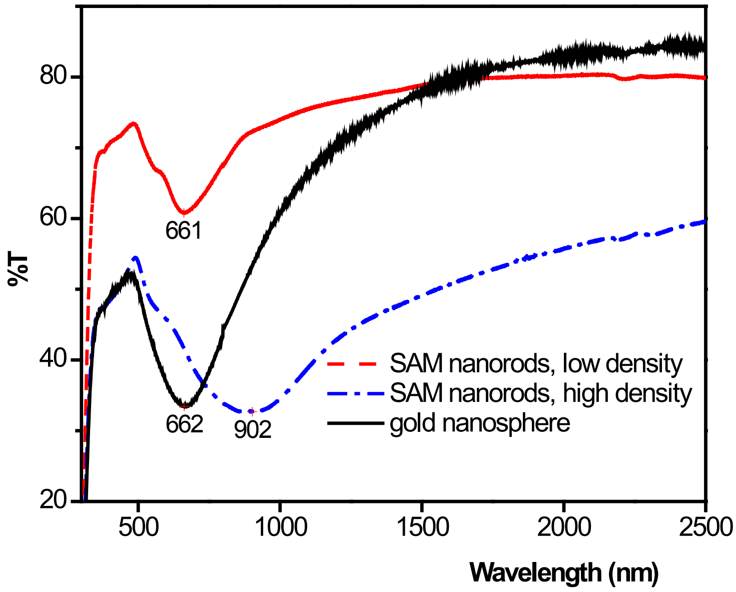

Figure 6-5 Transmittance spectra of gold nanorod and gold nanosphere coatings

6.3.7 Effect of annealing

Figure 6-6 shows the optical properties of the low-density coatings after annealing. The transverse absorption peak at around 540 nm becomes significant with the increase in the annealing temperature. Meanwhile, the broad longitudinal peak at around 750 nm diminished during the annealing process. The colour of the coating evolved from blue to reddish during the annealing. Close examination of the spectra produced by annealing at the different temperatures showed that the peak at 750 nm not only vanished gradually, but also also blue-shifted with the elevation of the annealing temperature. It has been noted that the 520 nm absorption became stronger, while absorption in the infrared region decreased slightly with the increase the annealing temperature (Figure 6-6).

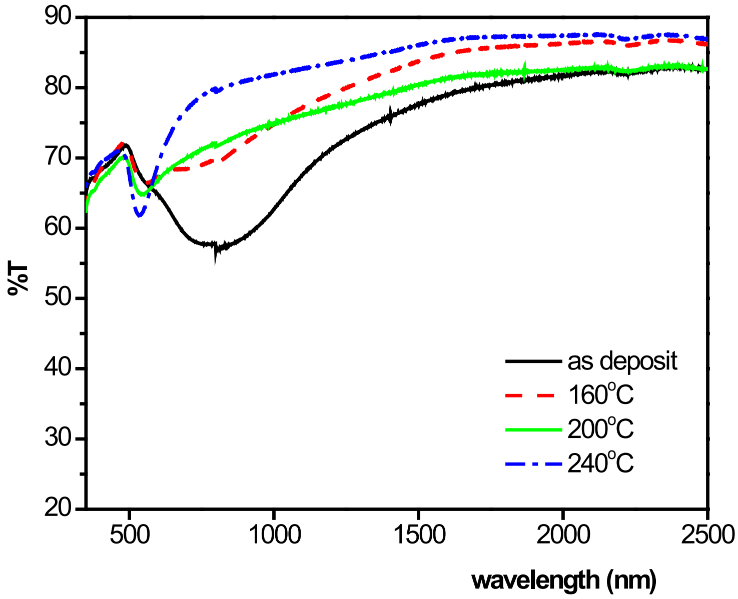

Figure 6-6 Transmittance of coatings with lower density of gold nanorods after annealing

Typical SEM images of annealed, low-density gold nanorod coatings are indicated in Figure 6-8(a). For the low-density coating, in which most of the nanorods are isolated, the growth of particle size and change of shape from rod to sphere develops with the elevation of the annealing temperature, due to the reorganisation of the gold nanorods [233]. Surrounding nanorods aggregate and form large clusters during the annealing process. The boundary of small particles could be clearly seen for the coating annealed under 160°C (Figure 6-8(a)). With the increase in the annealing temperature, the boundaries between individual particles became less obvious and larger hemispherical-shaped clusters formed. These hemispherical clusters kept growing at the higher annealing temperature and eventually formed irregular-shaped chunks (Figure 6-8(a)).

The spectra of high-packing-density coatings are shown in Figure 6-7. These gold nanorod coatings displayed different trends from those of low packing-density-coatings. It is difficult to see the side absorption peak around 540 nm even for the nanorods coating as deposited. Similar to the lower packing-density coating, the broad peak around 700 to 800 nm shifts to the blue side during the annealing process. Contrary to the low packing density of gold nanorod coatings, the transmittance of the coating after annealing decreased in the infrared region, while it remained unchanged in the visible region.

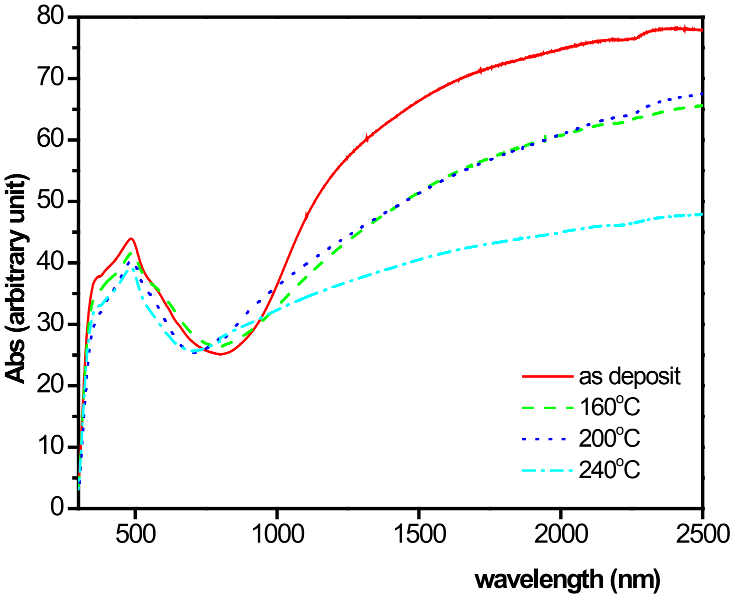

Figure 6-7 Transmittance of coatings with higher density of gold nanorods after annealing

Typical SEM images of high-density gold nanorod coatings produced by annealing are presented in Figure 6-8(b). The change in the morphology of the coatings depended not only on the temperature, but also on their packing density. The growth of individual particles in the case of high-packing-density coatings was not as clear as in the low-density coatings. The individual gold nanoparticles only grew slightly under high-temperature (240°C) annealing. However, there was shape evolution during the annealing process. Densely packed gold nanorods started to coalescence into gold nanospheres or hemispherical clusters. This is different from the case of the lower packing density coating; the boundary of the nanoparticles could be clearly seen in the SEM images, even at a higher annealing temperature (240°C).

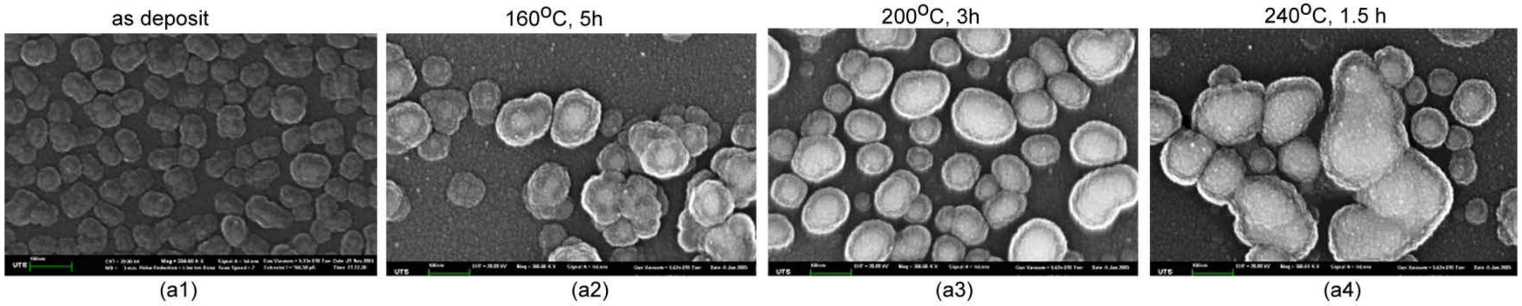

(a) low-density gold nanorod coating

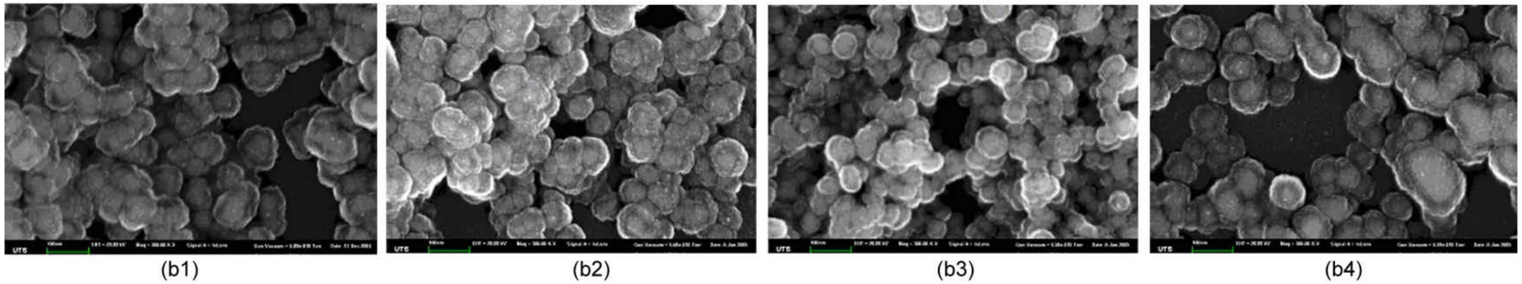

(b) high-density gold nanorod coating

Figure 6-8 Evolution of coatings of gold nanorods after heat treatment

6.3.8 Scratching test for gold nanorods coating via self-assembling method

Figure 6-9 shows the morphology of the coating of self-assembled gold nanorods imaged by an in-situ SPM module of nanoindentation. As seen in the image, the gold nanorods appear to be partially submersed in the silane interlayer on the top of the glass substrate. The rougher surface made locating and scanning the surface very difficult. This, in addition to the relatively soft nature of the silane interlayer, made attempts at accurate adhesion and hardness measurements unsuccessful.

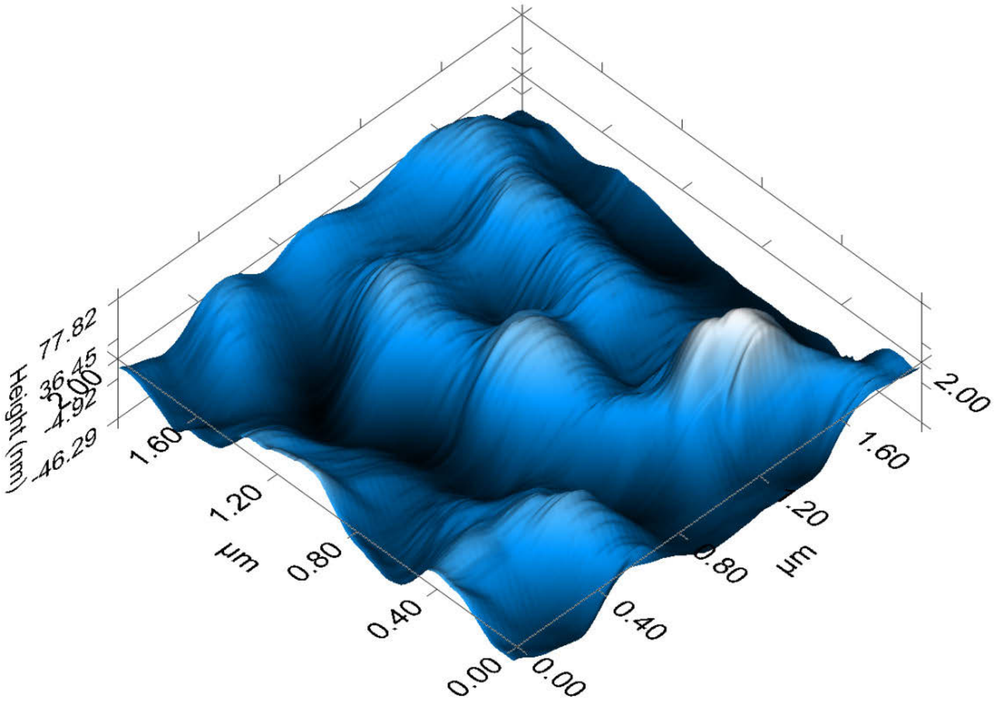

Figure 6-9 Morphology of SAM gold nanorod coating on glass substrate as deposit

6.3.9 Interaction of annealed gold nanorod coating with light

The near-field optical properties of gold nanoparticles is also of interest [234, 235]. The effect has potential applications [236], such as in waveguides etc. [237, 238].

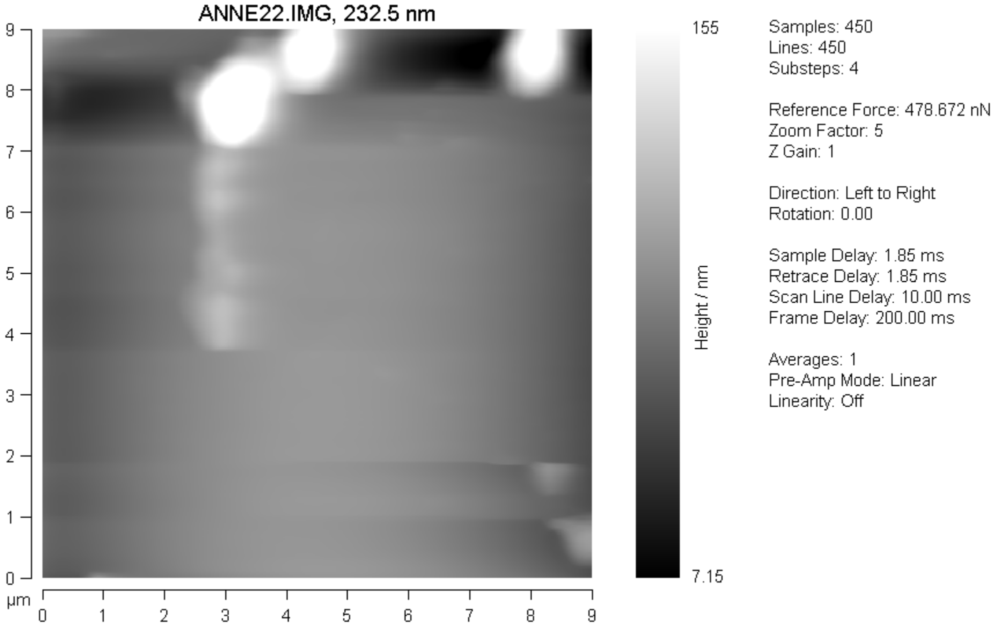

Samples: 450
Lines: 450
Substeps: 4

Reference Force: 478.672 nN
Zoom Factor: 5
Z Gain: 1

Direction: Left to Right
Rotation: 0.00

Sample Delay: 1.85 ms
Retrace Delay: 1.85 ms
Scan Line Delay: 10.00 ms
Frame Delay: 200.00 ms

Averages: 1
Pre-Amp Mode: Linear
Linearity: Off

(a) AFM channel

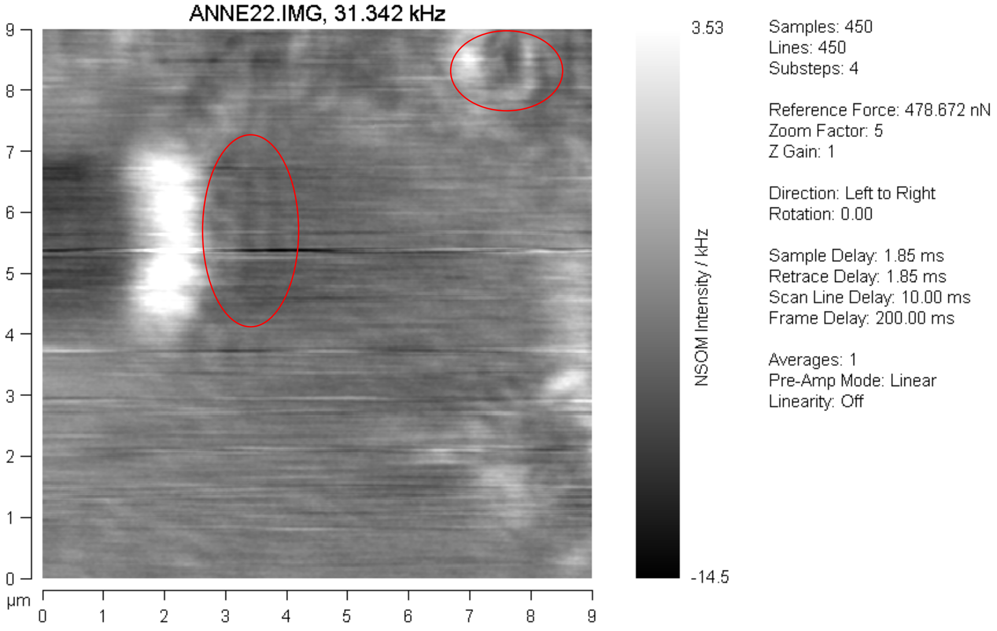

Samples: 450
Lines: 450
Substeps: 4

Reference Force: 478.672 nN
Zoom Factor: 5
Z Gain: 1

Direction: Left to Right
Rotation: 0.00

Sample Delay: 1.85 ms
Retrace Delay: 1.85 ms
Scan Line Delay: 10.00 ms
Frame Delay: 200.00 ms

Averages: 1
Pre-Amp Mode: Linear
Linearity: Off

(b) NSOM channel

Figure 6-10 Topological and NSOM images for annealed gold nanorods

Gold nanorods annealed at 200°C were imaged using a Nanonics® NSOM-100, according to the procedure described in section 6.2.5(c). The resultant images are shown in Figure 6-10. The AFM image is presented in Figure 6-10 (a) and the NSOM image in Figure

6-10 (b). The NSOM images showed a distinctive shadow effect. The NSOM signal is very high in the adjacent area of gold particles. When the probe tip was located at the actual position of the particles, the NSOM intensity was relatively low. A similar finding was reported by Bakker *et al*. [239] in transmission mode NSOM, in that case for 128 nm gold dots on top of Ti/TiO_2 coated glass. The NSOM signal was also blocked out by dots. The intensity ratio between the shadow of the dots and the adjacent bright area was as high as 25.

An interference pattern due to the annealed gold nanorods could be clearly observed, with an oscillating behaviour appearing in the vicinity of the gold clusters. The ripples of the interference patterns followed the boundary of the gold cluster. These fringes are thought to be caused by interference between light reflected by neighbouring gold particles. The sides of the particles reflect parts of the light which interfere in the surrounding region. Similar interferences were reported by Jalocha *et al*. [240]. Jalocha *et al.* believed these interferences to have been created between the light emitted by the tip and the light reflected by the sample surface. Both insulating and conductive surfaces showed similar interference.

6.3.10 An attempt to grow rods directly on glass

The disadvantages of the self-assembly method to prepare spectrally selective coatings of gold nanorods on glass are clear. Firstly, the gold nanorods prepared from the seed-mediated method were dispersed in very diluted surfactant. Therefore enrichment, separation and purification were required before the rods could be used for the assembly. These processes are intricate and time-consuming. Secondly, according to existing recipes, only about half of the $AuCl^-_4$ was reduced during the reaction [75]. According to the mechanism discussed in Chapter 5, we believe this is the intrinsic nature of the seed-mediated method. A particular ratio of [ascorbic acid]/[$AuCl^-_4$] has to be maintained to provide differential growing rates on passivated crystal orientations, to result in anisotropic growth of gold nanoparticles with a rod shape. In return, the overall recovery of gold is low.

Growth of gold nanorods directly onto the glass surface, as mentioned in the literature review chapter, can overcome all these drawbacks. However, the reported density of gold nanorods by this method was only around 1-10 per μm^2, which is far below that required for spectrally selective purposes. To achieve higher seed density, I pre-treated the glass surface with $SnCl_2$, initialised it with silver, and then dipped the activated glass into the gold nanorod growth solution, as described in section 6.2.3. The morphology of the coating on the glass is indicated in Figure 6-11. Unfortunately, the gold nanoparticles grown by this method tend to be spherical rather than rod-like.

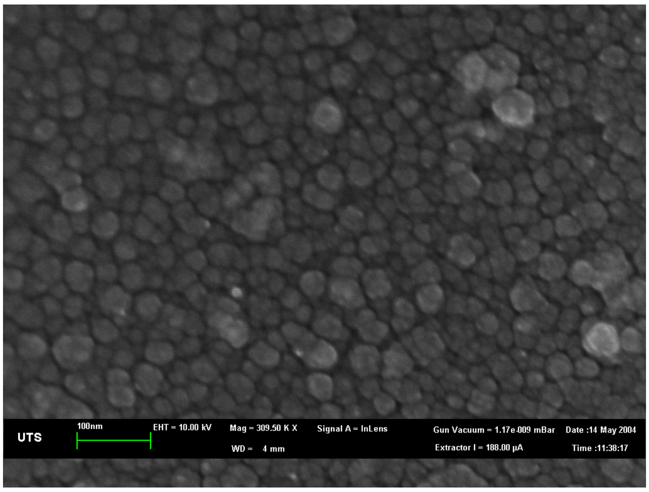

Figure 6-11 Gold nanoparticles growing directly on glass by seed-mediated method

During the direct growth process, shedding of gold nanoparticles from the surface was observed. Pink, silk-like threads rose from the glass surface, at the bottom of the reaction vessel, to the top of the growth solution and ultimately turned the whole solution pink. This process indicates that the adhesion between gold nanoparticles and the surface is not strong enough to hold the particles in the presence of quaternary ammonium surfactant. Once the initial layer of gold nanoparticles was formed by the replacement reaction, the anisotropic reaction which previously shaped the gold nanorods was absent. Moreover, the gold nanoparticles shed into the solution did not develop into rod shapes either. The morphology of the particles varied from irregular cubic (Figure 6-12(a)) to flower petal-like (Figure 6-12(b)) in the system.

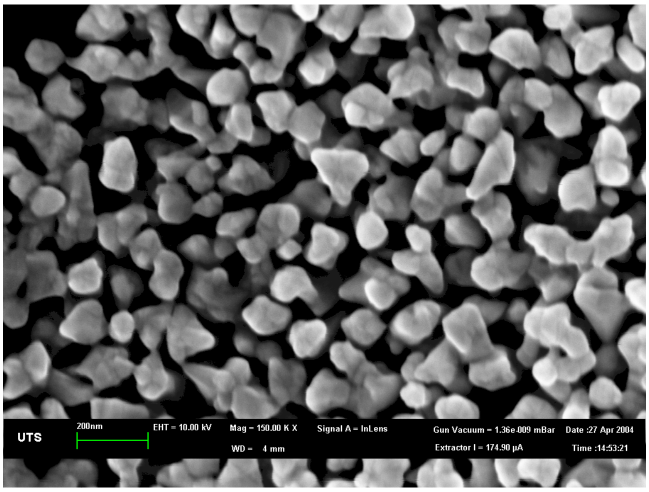

(a) irregular shape in solution

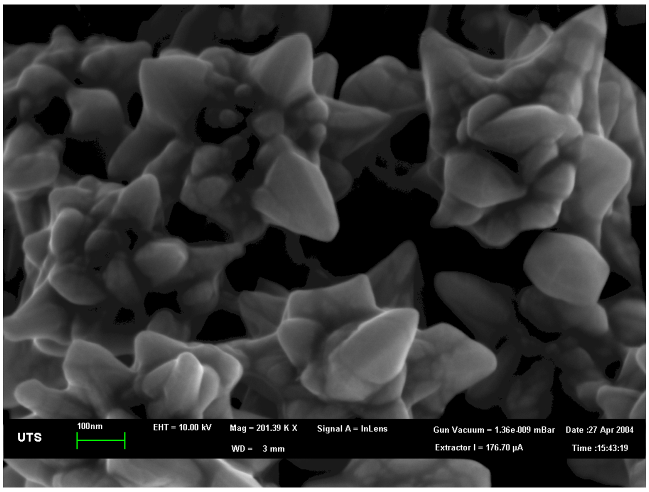

(b) flower-petal shape in suspension

Figure 6-12 Various shapes of gold nanoparticles in growth solution during attempts to grow nanorods directly on glass

6.4 Discussion

6.4.1 Simulation of optical properties of low-packing-density gold nanorod coatings during annealing

(a) Changing of optical properties with aspect ratio during the annealing

DDSCAT simulation results confirmed how the annealing process shifted the optical properties of the low-density coatings. In these simulations, the aspect ratio of the gold nanorods was reduced from 3 to 1. The longitudinal peak shifted in the blue direction with annealing and diminished in intensity. However, the absorbance of the transverse peak around 540 nm was enhanced.

The simulation results agree with the experimental data. After heat treatment of low-density coatings, the longitudinal peak around 750 nm did not present, while the transverse surface plasmon peak became significant.

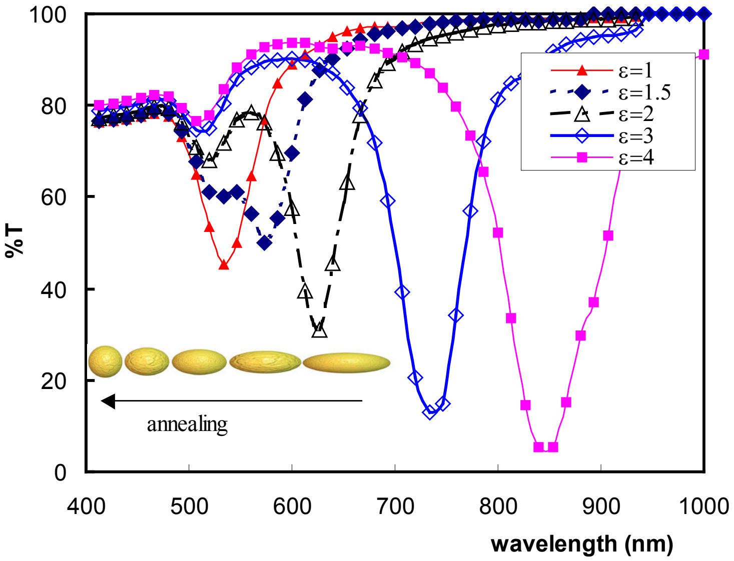

Figure 6-13 Simulation of evolution of optical properties of coatings of low-density gold nanorods during annealing

(b) Particle-to-particle interaction in late annealing stage

Close examination of SEM images (Figure 6-8) reveals that nanorods are replaced by a different morphology after they have been annealed above 160°C,. Therefore, there are two stages of transformation of gold nanoparticles during the annealing process. When gold nanorods were annealed under 200°C, they altered to a spherical shape. At a later stage, the small spherical particles coalesced to develop larger spheres.

This stage was also simulated by DDSCAT. In the simulation of section 4.4.2, the optical properties of particles of varying size, but separated by the same gap, were simulated. Three different particles size were used, that is, 40 nm, 20 nm and 10 nm in radius. The gap between the particles, which is measured between the shortest paths of the surface of the particles, was set to 10 nm in each case. Thus, the inter-particle spaces, which were measured between centres of the particles, were 90 nm, 50 nm and 30 nm respectively. The simulation results indicated that the larger the size of the particles, the stronger the interparticle effects, indicated in a strong peak at around 650 nm.

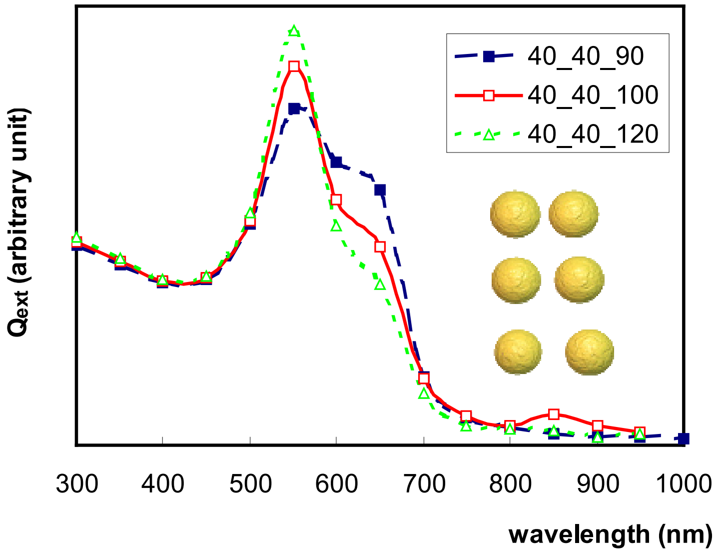

Figure 6-14 Simulation of absorption spectra of gold spheres with sa

(The spectra are normalised, 40_40_90: two 40 nm gold nanoparticles with 10 nm gap between them, 40_40_100: two 40 nm gold nanoparticles with 20 nm gap between them, 40_40_120: two 40 nm gold nanoparticles with 40 nm gap between them.)

In Figure 6-14, the optical properties of the same size of particles with different gaps between the particles were simulated. Three different gaps are simulated in this case, that is, 10 nm, 20 nm and 40 nm respectively. The radius of the particles in this simulation is 40 nm. Thus, the inter-particle spaces were 90 nm, 100 nm and 120 nm respectively. The results indicated that the smaller the gaps between the particles, the stronger the particle-to-particle effects. The interaction of particles caused by the gap and size has been well discussed in section 4.4.2.

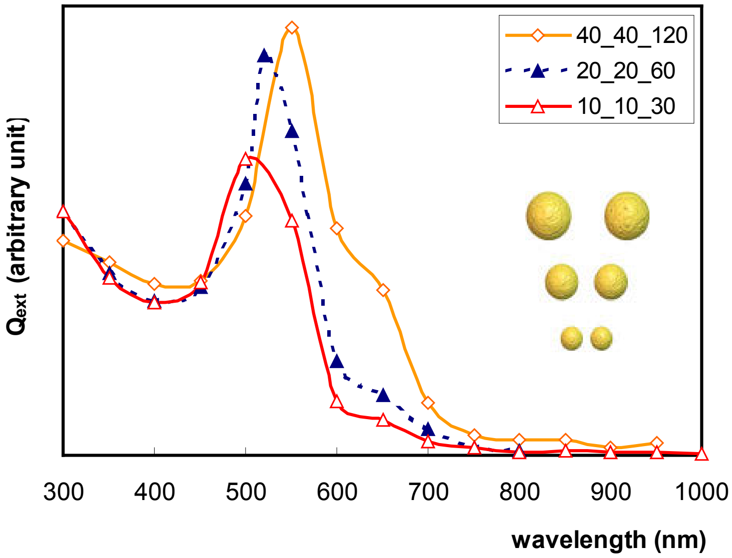

Figure 6-15 Simulation of absorption spectra of gold nanorod coating in later annealing stage

(The spectra are normalised, 40_40_120: two 40 nm gold nanoparticles with 40 nm gap between them, 20_20_60: two 20 nm gold nanoparticles with 20 nm gap between them, 10_10_30: two 10 nm gold nanoparticles with 10 nm gap between them.)

During the annealing process, the growth of the nanospheres must be accompanied by an enlargement of the gap between the particles, due to the fixed amount of gold available. This eventually brings some adverse effects to the particle-to-particle interaction. The situation is simulated in Figure 6-15. Larger particle size strengthens the absorption, however, larger particle space counteracts this size effect. Furthermore, growth of particles not only intensified, but also broadened, the surface plasmon absorption peak around 520 nm. The optical properties of gold nanoparticles on the glass are mainly based on two elements, namely, particle size and interparticle spacing. Both contributions must be taken into consideration.

6.4.2 Evolution of optical properties of coating

It was initially a little surprising to find that the packing density of gold nanorods had a significant influence on the optical behaviour during the annealing (compare Fig 6-7 and Figure 6-7). The difference may come from the behaviour of gold nanorods at higher temperatures. It is relatively straightforward to explain the evolution of the optical properties for coatings of low packing density from their morphologies. Isolated gold nanorods on the substrate inherited the optical property of colloid as deposited (Figure 6-5). The longitudinal and transversal surface plasmon resonances were indicated at around 700 nm and 540 nm peaks respectively in the spectra. However, as a result of the annealing process, the aspect ratio of the nanorods decreased and they formed nanospheres or hemispheres (Figure 6-6(a)). The surrounding nanoparticles also merged to form larger spheres. Since these spheres are isolated, they have a strong plasmon absorption peak at around 540 nm, but no other peaks. The colour of the coatings shifted from blue to pink during annealing. Furthermore, the decrease with packing density of the gold nanospheres, as a result of merging of the small particles, actually resulted in a slight increase of transmittance of the coatings in the infrared region.

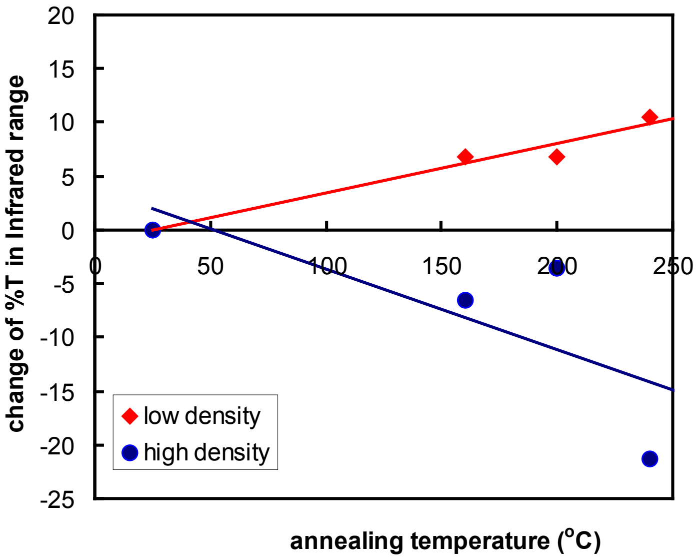

Figure 6-16 Change of transmittance in infrared range of gold nanocoatings during annealing

The peak around 700 nm for high-density coatings appears to be influenced by two effects of the gold nanoparticles: shape change and particle-to-particle interaction. Change in the morphology of the gold nanoparticles from rods to spheres eliminates the longitudinal peak around 700 nm. However, a decrease in the spacing between gold nanospheres results in strong absorption in the range at 650 to 700 nm by dipole-to-dipole interaction, which in turn counteracts the disappearance of the longitudinal peak of the gold nanorods. The slight blue shift of the peak at 700 nm can be attributed to be the equilibrium of these contrasting effects. However, even though there was some coarsening of the particles, it was not enough to explain the substantial improvement of the infrared shielding ability in the high-density coatings, due to annealing.

Thermogravimetric analysis (TGA) of pure CTAB crystals shows (Figure 6-17(a)) that pure CTAB crystal decomposition started from 180^{o}C and was completed at 250^{o}C. TGA results of the purified gold nanorods (Figure 6-17(b)) shows that they were capped with 20 %w/w of CTAB, which was driven off at temperatures greater than 250^{o}C. When present, the dielectric layer inhibits the movement of free electrons within the film. Annealing destroys the insulating micellar layer and improves conductivity in the network structure of the coating, which causes the annealed coatings to shield infrared more efficiently. The process appears similar to the growth of island metal films. When the particles were separate, the movement of free electrons was restrained by the boundaries, and the gold nanoparticles interacted with light with surface plasmons. The free electrons only oscillated within individual grains. In this case, the gold particles strongly absorbed some part of visible radiation at the plasmon resonant wavelengths but had no reflection of infrared. However, once these boundaries merged during annealing, the transparent film provided strong infrared reflectance [194].

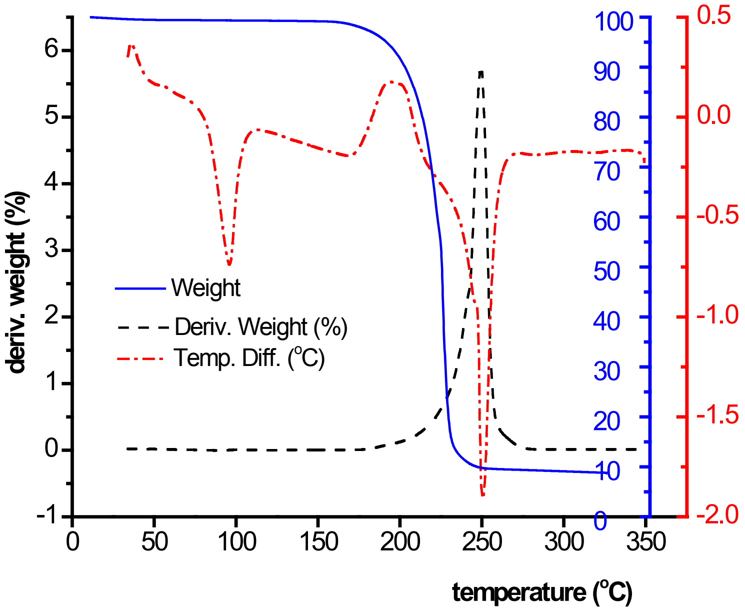

(a) pure CTAB

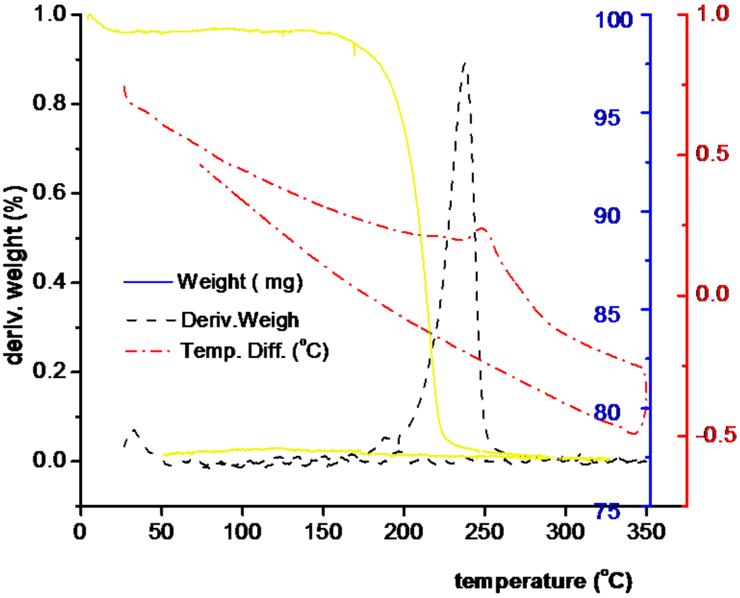

(b) gold nanorods capped with CTAB

Figure 6-17 TGA results for CTAB and gold nanorods capped with CTAB

The TGA results were similar to those of Nikoobakht *et al.* [109]. Three bands were identified in their experiments. The first band, around 230°C, was attributed to free monomers of surfactant, while the other two, around 275°C and 345°C, were believed to be due to unbound and bound headgroups of surfactant. The authors found that weight loss occurred at 300-330°C, which is significantly higher than the work presented here. However, the earlier study used a different surfactant system. In their report, a bi-surfactant system in which cetyltrimethylammonium bromide (CTAB) was used as the cationic surfactant and tetraoctylammonium bromide (TOAB) as a cosurfactant..

The function of an insulating layer was also established in the work of Ung *et al.* [90]. In that study, 13.2 nm gold spherical nanoparticles coated with different thicknesses of SiO_2 were immobilised on the substrate by the Layer By Layer (LBL) method. The optical experiments showed that the coupled peak red-shifted from 520 nm to 700 nm, with a decrease of thickness of insulating layers from infinity to 0.5 nm. For particles separated by 3 nm SiO_2, the inter-dipolar absorption peak appeared around 580 nm. Simulation results from the Maxwell-Garnett model gave good agreement with the experimental data, in which a volume fraction was used as the only variable to calculate the position of the coupling absorption peak. The Genzel and Martin model also gave a reasonable agreement between experiments and simulations in the case of gold nanohemispheres [13].

6.4.3 Improved spectral selectivity by composite coating of gold nanorods

The key to improving the spectral selectivity of these coatings is to blend nanorods of varying aspect ratios in a controlled fashion. The simulated performance of an example of such a mixture, which notionally contains a blend of rods with aspect ratios spread between 3.0 and 10.0 and an effective radius of 20 nm, is presented in Figure 6-18. A coating containing this mixture would have T_{vis}/T_{sol} of 1.44. As we mentioned in section 4.1, T_{vis} is the proportion of the visible spectrum, that is, transmitted and T_{sol} the proportion of the total solar spectrum transmitted [174]. If applied at a gold loading of 0.29 g/m^2 of window, the coating shown would transmit 52% of incident solar radiation falling on it, and would have a pale pink colour in transmission [241]. Actual transmission of incident solar energy in practice would be slightly less than the 52% calculated for the coating alone, since even a 3 mm plate glass substrate only transmits about 86% of incident solar radiation, due to reflection and absorption.

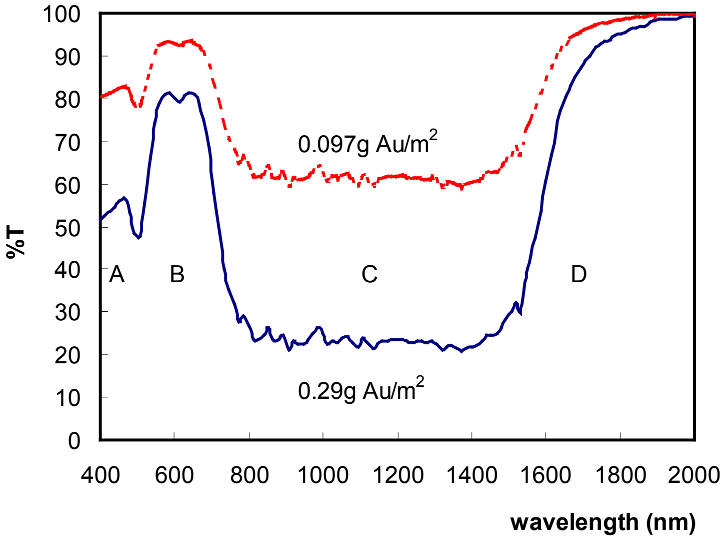

Figure 6-18 Simulated optical properties for coatings of mixtures of gold nanorods

6.4.4 Prototype for smart window

The anisotropic optical properties of gold nanorods have aroused interest in terms their potential application for “smart windows”. If the orientation of the nanorods could be tuned *in situ*, the transmittance and colour of glass could also be changed according to the seasons.

The optical extinction of gold nanorods is strongly influenced by their orientation with regard to the electric field vector **e** of the light. When the rods are parallel to the unpolarised incident radiation, the **e** of the light must be directed across the transverse direction of the rod. This will lead to only the weak transverse absorption peak around 520 nm. However, both longitudinal and transverse peaks are excited for rods that are perpendicular to the incident radiation. In Figure 6-19, the absorption of the gold nanorods in the polarised radiation is simulated by DDSCAT. It is shown that only weak absorption around 520 nm occurs when the rods are parallel to the radiation. In this situation, the rod is equivalent to the spherical particles and shows a pink colour. When the rods are perpendicular to the incident ratio, their colour depends on the effects of both transverse and longitudinal peaks excited by the incident radiation. In this case, the colour of the coating will vary from purple, through blue to red, depending on the aspect ratios of the rods.

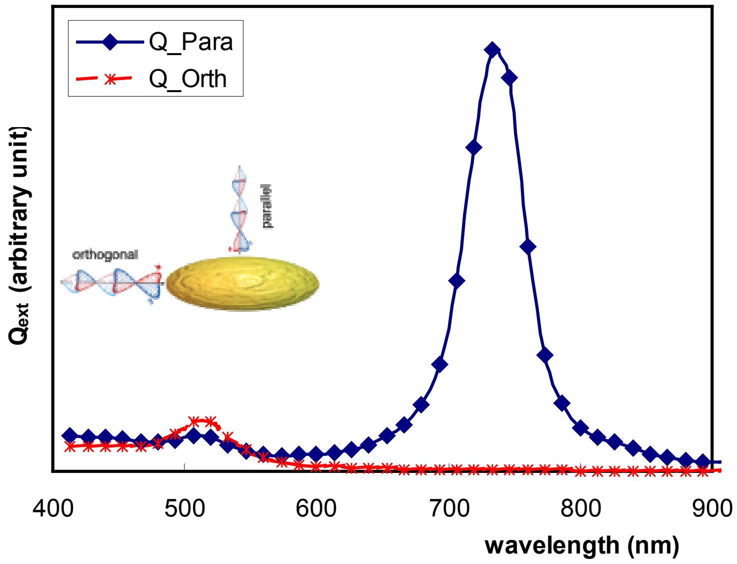

Figure 6-19 Surface plasmon of gold nanorod with radiation

This "smart window" is conceptually illustrated in Figure 6-20. Simulation of the optical properties of the nanorods by DDSCAT in Figure 6-19 supported the model. When the rods are parallel to the electric field of the incident radiation, they absorb the infrared strongly. When they are orthogonal to the electric field, they show no longitudinal peak and only the surface plasmon resonance peak at 520 nm.

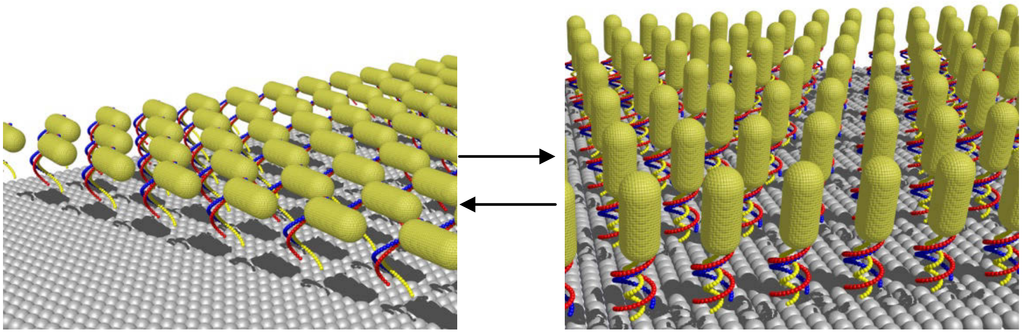

Figure 6-20 Illustration of a conceptual "smart window" based on gold nanorods

Cortie *et al*. suggested that changing the orientation of the gold nanorods could be achieved by using folding and unfolding of organic molecules [242]. By adjusting the pH value, the denaturing and refolding of DNA molecules [243, 244] will align the gold nanorods, and, as a consequence, tune the colour and infrared transmittance accordingly. Some molecular species, such as 16-mercaptohexadecanoic acid, have been shown to be rigid enough to support the gold nanorods [133]. The challenge in developing the “smart window” will be to determine or generate a molecular structure in which the folding and denaturing process is reversible.

6.5 Summary

The unique optical properties of gold nanorods, which exhibit tuneable absorption as a result of their aspect ratio, strongly suggested their potential application of this coating in solar control. In this chapter, I have described efforts to prepare coatings of gold nanorods on glass by the self-assembly method and by direct growth. The self-assembly method proved an effective way to deposit gold nanorods on the glass substrate. However, the attempt to grow gold nanorods directly on a glass substrate was unsuccessful. The self-assembled coatings of gold nanorods on glass provided better spectral selectivity between infrared and the visible regions than was the case for coatings of spheres or hemispheres.

The colour of gold nanorod coatings of low packing density changed from blue to purple and finally to pink during annealing. The transmittance of these coatings in the infrared region also increased. However, the colour of the high-density coatings remained blue, and their shielding ability in the infrared was improved by annealing. The results show that the optical properties of gold nanorod coatings are related to their packing density.

A mixture of gold nanorods of various long aspect ratios might be a good way to further improve the spectral selectivity of the coatings. Simulation indicates that with 0.29 g/m^2 of Au of a mixture of gold nanorods (with aspect ratios up to 10), T_{vis}/T_{sol} can reach 1.44. Finally, the anisotropic optical properties of gold nanorods are essential to develop the prototype “smart window” of Cortie, which could actively control infrared transmission.

7. Conclusion

Although it has been known for decades that transparent coatings of gold on glass can block the infrared component of sunlight while allowing the visible through, use of this system has fallen out of favour due to the high cost of the vacuum deposition equipment required to produce it. In this study, an alternative approach is explored, in which tailored gold nanoparticles of the appropriate optical properties were synthesised by wet chemistry and deposited onto glass. Gold nanospheres, hemispheres, rods, aggregates and "dogbones" all have possible use in this application. While good coatings of neutral blue-grey colour can be obtained by exploiting dipole-dipole plasmon resonances between closely spaced nanospheres, gold nanorods appear to offer a more versatile technological solution.

In situ precipitation of coatings of gold nanoparticles coatings were developed for solar screening. Coatings that comprised isolated gold nanoparticles exhibited the well-known plasmon resonance at ~520 nm on the glass substrate and were pink-coloured. However, the absorption peak due to particle-particle interactions, at about 700 nm, could be developed with an increase in coating density. This peak could be broadened and red-shifted by the packing density of gold nanoparticles. Such coatings were blue or blue-grey in transmission, and would be more suitable in principle for architectural applications than the pink-coloured coatings.

It was found that the optical properties of gold nanosphere coatings depend upon the nature of nuclei and their growth on the glass surface. This resulted in coatings of similar gold content, but different patterns of aggregation, which exhibited quite different transmission spectra. These effects may be controlled by the high surface energy of the glass surface, which largely controls the rate of nucleation.

The properties of gold nanoparticles coating were investigated. The mechnical properties such as adhesion of gold nanoparticle on glass substrate, and the nanohardness of gold nanoparticles were characterised by nanoindentation. The scratching test revealed at by increasing the lateral force from 20 to 30 μN, the particles could be removed easily by the nanotip. The indentation also verified that the gold nanoparticle deposited displayed similar mechnical properties to the bulk metal gold. The XRD data indicated that the gold nanosphere coating shows FCC crystal structure with strong {111} preference.

The gold nanorods could possibly provide better spectral selectivity than gold nanospheres and gold nanohemispheres. Synthesis of gold nanorods either, in colloid or on the substrate, is the premise for the application of gold nanorods for solar control purposes. The gold nanorods synthesised by the seed-mediated method were investigated in this study. Different process parameters such as the pH of ascorbic acid, Ag^+ concentration, CTAB, and gold seed were explored for the growth of gold nanorods. It was found that the ascorbic acid with pH 2 can not reduce Au(I), while ascorbic acid with higher pH is preferred for producing the gold nanorods. The proper concentration of Ag^+ as well as seed is essential to form the gold nanorods. The absence or excess of Ag^+ in the system prevents the formation of the nanorods. The results also confirmed that the Ag^+ needs to collaborate with CTAB to assist the formation of the nanorods. One complex gold nanorod growth mechanism was proposed. In the mechanism, the adsorbed $AgBr_2^-$ acts as the bridge between the CTAB micelle soft template and the gold seed. The function of the CTAB micelle is to stabilise the gold nanorods and transport both Au(I) and $AgBr_2^-$ to particular crystal planes, in which differential reaction rates are achieved for the anisotropic growth of the particles. Optical properties of gold nanorods were simulated by DDSCAT. During the growth process, the aspect ratio is more important than the volume which shifts the longitudinal peak into the blue in the later growing stage. The simulation results agreed with the experimental data. The colour of the nanorods during the growing processes was plotted by CIE colour model. The colour change of shorter nanorods was observed behave significantly different from that of longer rods. The difference is due to the position of the longitudinal peak caused by aspect ratios. The longitudinal peak of long aspect ratio rods is locates in the near-infrared region; the colour of these rods depends on the transversal plasmon peak around 520 nm. Thus, the rods show a pink colour. However, the longitudinal peak of short rods is located in the visible region; the colour of these rods is the complex effect of both transversal and longitudinal peaks. These rods show a purple to blue colour depending on the positions of both peaks and the relative absorptions of these peaks.

Coatings of gold nanorods were also explored, due to their unique optical properties. In particular, the peak absorption of gold nanorods can be readily tuned from 520 nm (green light) through to ~1400 nm (the near-infrared), simply by varying their aspect ratio. This phenomenon has led to these particles being considered for solar-control coatings on windows. The high efficiency of the effect and the fact that mass production of gold nanorods is technically feasible have opened the way for possible commercialisation of this idea.

Two different approaches were applied for the production of gold nanorod coatings. In the first approach, the gold nanorods were synthesised and purified first before they were assembled on the functionalised glass substrate. In the second approach, an attempt was made to grow the gold nanorods directly on the substrate. The first was demonstrated as a successful method. The gold nanorod coating displays better spectral selectivity between infrared and visible. Further study revealed that better spectral selectivity can be achieved with a mixture of different aspect ratios of the gold nanorods. The direct growth approach was not very successful, due to a lack of methods for manipulating the seeds on the substrate.

In this study, it has been demonstrated that two methods are available to deposit nanoscale gold coatings on glass for solar-control purposes. Coatings produced by *in situ* deposition resulted in a blue colour in transmission, caused by the inter-particle interaction of gold nanospheres. The absorption peak is in the upper visible and near-infrared regions. Self-assembled coatings of gold nanorods showed high spectral selectivity between the infrared and visible regions. Numerical simulation indicated that a mixture of nanorods of varying aspect ratios could achieve good spectral selectivity with a low gold loading. However, further development of gold nanorod coatings requires the availability of an efficient method to produce long rods.

8. References

[1] T.E. Johnson, *Low-E Glazing Design Guide*. 1991, Boston: Butterworth Architecture.

[2] Anonymous, ASTM G159-98 Standard Tables for References Solar Spectral Irradiance at Air Mass 1.5: Direct Normal and Hemispherical for a 37^o Tilted Surface. 1998, PA: American Society for Testing and Materials.

[3] N. Wruk. Energy balance of coated double glazings. Glass Processing Days. 1997. Tampere, Finland.

[4] V. Block. Reducing carbon dioxide. Glass Processing Days. 2001. Tampere, Finland.

[5] J.A. Savage, Infrared Optical Materials and Their Antireflection Coatings. 1985, Bristol, England: Adam Hilger Ltd.

[6] J.M. Bell and J.P. Matthews, *Glazing materials.* Materials Forum, 1998. **1**: 22.

[7] S.J. Nadel and R.J. Hill. Durable low-e coated glass for use in warm temperature climates. Glass Processing Days. 1997. Tampere, Finland.

[8] G.B. Smith, C.A. Deller and P.D. Swift, *Nanoparticle-doped polymer foils for use in solar control glazing.* Journal of Nanoparticle Research, 2002. **4**: 157.

[9] H. Takeda, K. Yabuki and K. Adachi, Coating solution for forming a film for cutting off solar radiation and the film formed therefrom, 2001. US Patent 6319613.

[10] P. Mulvaney, Surface plasmon spectroscopy of nanosized metal particles. Langmuir, 1996. **12**: 788.

[11] N. Felidj, J. Aubard, G. Levi, J.R. Krenn, G. Schider and A. Leitner, *Enhanced substrate-induced coupling in two-dimensional gold nanoparticle arrays.* Physical Review B, 2002. **66**: 245407.

[12] T. Ung, L.M. Liz-Marzan and P. Mulvaney, *Gold nanoparticle thin films.* Colloids and Surfaces A: Physicochemical Engineering Aspects, 2002. **202**: 119.

[13] X. Xu, M. Stevens and M.B. Cortie, In situ precipitation of gold nanoparticles onto glass for potential architectural applications. Chemistry of Materials, 2004. **16**: 2259.

[14] Y. Golan, L. Margulis and I. Rubinstein, *Vacuum-deposited gold films.* Surface Science, 1992. **264**: 312.

[15] K.L. Choy, *Chemical vapour deposition of coatings.* Progress in Materials Science, 2003. **48**: 57.

[16] T.K. Sau and C.J. Murphy, Seeded high yield synthesis of short Au nanorods in aqueous solution. Langmuir, 2004. **20**: 6414.

[17] K.E. Peceros, X. Xu, S.R. Bulcock and M.B. Cortie, *Dipole-dipole plasmon interactions in gold-on-polystyrene composites.* Journal of Physical Chemistry B, 2005. **109**: 21516

[18] G. Raschke, S. Brogl, A.S. Susha, A.L. Rogach, T.A. Klar, J. Feldmann, B. Fieres, N. Petkov, T. Bein, A. Nichtl and K. Ku1rzinger, *Gold nanoshells improve single nanoparticle molecular sensors.* Nano Letters, 2004. **4**: 1853.

[19] J. Liu, A.I. Maaroof, L. Wieczorek and M.B. Cortie, *Fabrication of hollow metal nanocaps and their red-shifted optical absorption spectra.* Advanced Materials,

2005. **17**: 1276.

[20] G.O. Mallory and J.B. Hajdu, *Electroless Plating: Fundamentals and Applications*, Orlando, Florida, USA: American Electroplaters and Surface Finishers Society.

[21] L.M. Svedberg, K.C. Arndt and M.J. Cima, *Selective substrate metallization,* 2001. US Patent 6194032.

[22] M. Nakazawa, Substitutional electroless gold plating solution, electroless gold plating method and semiconductor device, 2002. US Patent 6398856.

[23] M. Nakazawa, M. Yoshitani and S. Wakabayashi, *Electroless gold plating solutions,* 1993. US Patent 5258062.

[24] F. Vratny, *Electroless deposition of gold,* 1979. US Patent 4154877.

[25] J. Vanaglash, Gold plating process and product produced thereby, 1978. US Patent 4082908.

[26] J.F. McCormack and R. Heights, *Autocatalytic gold plating solutions,* 1971. US Patent 3589916.

[27] A.R. Burke, W.V. Hough and G.T. Hefferan, *Electroless gold plating baths,* 1979. US Patent 4142902.

[28] R.G. Miller, Novel method for the rapid deposition of gold films onto non-metallic substrates at ambient temperatures, 1977. US Patent 4005229.

[29] T.L. Ward and R.R. Benerito, *Process for etching glass on ceramic surface,* 1977. US Patent 4013493.

[30] S.H. Gimm and J.H. Kim, *Glass etching composition,* 1994. US Patent 5281350.

[31] N.P.D. Bastiani and R.J. Boucher, *Faux glass etch product and process of preparing same,* 1996. US Patent 5571557.

[32] I. Riegl, Process of etching glass surfaces particularly in the manufacture of optical waveguides, 1983. US Patent 4415404.

[33] R.D. Hardy and J.E. Jarufe, Method and composition for etching glass ceramic and porcelain surfaces, 2002. US Patent 6337029.

[34] I.-H. Loh, *Plasma surface modification in biomedical applications.* Medical Device Technology, 1999. **10**: 24.

[35] R. Nickerson, *Plasma Surface Modification for Cleaning and Adhesion.* www.astp.com.

[36] M. Charbonnier and M. Romand, Tin-free electroless metallization of glass substrates using different PACVD surface treatment processed. Surface and Coatings Technology, 2002. **162**: 19.

[37] Anonymous, *Controlled Chemical Plasma Etching for Advanced Technology Applications.* www.marchplasma.com.

[38] R.G. Miller, Transparent copper and improved electroless method for producing said articles, 1969. US Patent 3457138.

[39] G.A. Krulik, N.V. Mandich and R. Singh, *Plating rate improvement for electroless silver and gold plating,* 1994. US Patent 5318621.

[40] S.-H. Park, J.-H. Im, J.-W. Im, B.-H. Chun and J.-H. K, *Adsorption kinetics of Au and Ag nanoparticles on functionalized glass surfaces.* Microchemical Journal. **63**: 71.

[41] M.J. Natan and B.E. Baker, Self-assembled metal colloid monolayers having size and density gradients, 2001. US Patent 6242264.

[42] A. Doron, E. Joselevich, A. Schlittner and I. Willner, *AFM characterization of the*

structure of Au-colloid monolayers and their chemical etching. Thin Solid Films, 1999. **340**: 183.

[43] R. Gesemann, J. Spindler and F. Richter, *Combination of aqueous baths for electroless gold deposition,* 1994. US Patent 5320667.

[44] D.M. Tench, L.F. Warren and J.T. White, *Controlled plating on reactive metals,* 2003. US Patent 6503343.

[45] H. Franz and J.V. Vanek, *Electroless gold plating bath,* 1978. US Patent 4091128.[46] H. Matsubara, Y. Yonekawa and Y. Ishino, Observation of initial deposition process of electroless nickel plating by quartz crystal microbalance method and microscopy. Electrochimica Acta, 2002. **47**: 4011.

[47] S. Ravaine, R. Saliba, C. Mingotaud and F. Argoul, *Electroless formation of gold deposits under positively charged surfactant monolayers.* Colloids and Surface A: Physicochemical and Engineering Aspects, 2002: 401.

[48] H. Yang, T. Lu and K. Xue, Electrocatalytic mechanism for formaldehyde oxidation on the highly dispersed gold microparticles and the surface characteristics of the electrode. Journal of Molecular Catalysis A: Chemical, 1999. **144**: 315.

[49] D.J. Levy and M. View, *Deposition of gold films,* 1970. US Patent 3515571.

[50] A.O. Davlin, Method for adhering precious metal to vitreous substances, 2001. US Patent 6231925.

[51] Anonymous, *ASTM D 3359 Measuring Adhesion by Tape Test*, PA: American Society for Testing and Materials.

[52] R. Garcia and P. Ruben, *Dynamic atomic force microscopy methods.* Surface Science Reports, 2002. **47**: 197.

[53] K. Okamoto, M. Loncar, T. Yoshie, A. Scherer, Y. Qiu and P. Gogna, *Near-field scanning optical microscopy of photonic crystal nanocavities.* Applied Physics Letters, 2003. **82**: 1676.

[54] Anonymous, *Handbook of Analytical Method for Materials*, http://www.mee-inc.com: Materials Evaluation and Engineering Inc.

[55] S. Warren, A. Retzle, A. Kazimirov, O. Bunk, L.X. Cao, F.U. Renner, D.M. Kolb, M.J. Bedzyk and J. Zegenhagen, *A structure study of the electroless deposition of Au on Si (111) : H.* Surface Science, 2002. **496**: 287.

[56] H. Miyake, S. Ye and M. Osawa, Electroless deposition of gold thin films on silicon for surface-enhanced infrared spectroelectrochemistry. Electrochemistry Communications, 2002. **4**: 973.

[57] D.G. Duff, A. Baiker and P.P. Edwards, A new hydrosol of gold clusters. 1. Formation and particle size variation. Langmuir, 1993. **9**: 2301.

[58] D.G. Duff, M. Baiker, I. Gameson and P.P. Edwards, A new hydrosol of gold clusters. 2. A comparison of some different measurement techniques. Langmuir, 1993. **9**: 2310.

[59] S.K. Ghosh, S. Nath, S. Kundu, K. Esumi and T. Pal, *Solvent and ligand effects on the localized surface plasmon resonance (LSPR) of gold colloids.* Journal of Physical Chemistry B, 2004. **108**: 13963.

[60] J. Hernandez, J. Solla-Gullon, E. Herrero, A. Aldaz and J.M. Feliu, *Characterization of the surface structure of gold nanoparticles and nanorods using structure sensitive reactions.* Journal of Physical Chemistry B, 2005. **109**: 12651.

[61] C.J. Murphy, T.K. Sau, A.M. Gole, C.J. Orendorff, J. Gao, L. Gou, S.E. Hunyadi and T. Li, *Anisotropic metal nanoparticles: Synthesis, assembly, and optical applications.* Journal of Physical Chemistry B, 2005. **109**: 13857.

[62] L.M. Liz-Marzan, *Nanometals: Formation and color.* Materials Today, 2004: 26.

[63] C. Sonnichsen, T. Franzl, T. Wilk, J. Feldmann, O. Wilson and P. Mulvaney, *Drastic reduction of plasmon damping in gold nanorods.* Physical Review Letters, 2002. **88**: 077402.

[64] C.J. Murphy and N.R. Jana, *Controlling the aspect ratio of inorganic nanorods and nanowires.* Advanced Materials, 2002. **14**: 80.

[65] K.L. Kelly, E. Coronado, L.L. Zhao and G.C. Schatz, *The optical properties of metal nanoparticles: The influence of size, shape and dielectric environment.* Journal of Physical Chemistry B, 2003. **107**: 668.

[66] C.J. Orendorff, L. Gearheart, N.R. Jana and C.J. Murphy, *Aspect ratio dependence on surface enhanced Raman scattering using silver and gold nanorod substrates.* Physical Chemistry Chemical Physics, 2006. **8**: 165.

[67] Y. Sun and Y. Xia, Triangular nanoplates of silver: Synthesis, characterization, and use as sacrificial templates for generating triangular nanorings of gold. Advanced Materials, 2003. **9**: 695.

[68] N.R. Jana, L. Gearheart and C.J. Murphy, *Wet chemical synthesis of high aspect ratio cylindrical gold nanorods.* Journal of Physical Chemistry B, 2001. **105**: 4065.

[69] N.R. Jana, Nanorod shape separation using surfactant assisted self-assembly. Chemical Communications, 2003: 1950.

[70] N.R. Jana, L. Gearheart and C.J. Murphy, Seed-mediated growth approach for shape-controlled synthesis of spheroidal and rod-like gold nanoparticles using a surfactant template. Advanced Materials, 2001. **13**: 1389.

[71] N.R. Jana, L. Gearheart and C.J. Murphy, Evidence for seed-mediated nucleation in the chemical reduction of gold salts to gold nanoparticles. Chemistry of Materials, 2001. **13**: 2313.

[72] B. Nikoobakht and M.A. El-Sayed, Preparation and growth mechanism of gold nanorods (NRs) using seed-mediated growth method. Chemistry of Materials, 2003. **15**: 1957.

[73] S.K. Kang, S. Chah, C.Y. Yun and J. Yi, *Aspect ratio controlled synthesis of gold nanorods.* Korean Journal of Chemical Engineering, 2003. **20**: 1145.

[74] B.D. Busbee, S.O. Obare and C.J. Murphy, *An improved synthesis of high-aspect-ratio gold nanorods.* Advanced Materials, 2003. **15**: 414.

[75] L. Gou and C.J. Murphy, *Fine-tuning the shape of gold nanorods.* Chemistry of Materials, 2005. **17**: 3668.

[76] P.L. Gai and M.A. Harmer, Surface atomic defect structures and growth of gold nanorods. Nano Letters, 2002. **2**: 771.

[77] J. Perez-Juste, L.M. Liz-Marzan, S. Carnie, D.Y.C. Chan and P. Mulvaney, *Electric-field-directed growth of gold nanorods in aqueous surfactant solutions.* Advanced Functional Materials, 2004. **14**: 571.

[78] A. Gole and C.J. Murphy, Seed-mediated synthesis of gold nanorods: Role of the size and nature of the seed. Chemistry of Materials, 2005. **16**: 3633.

[79] J. Gao, C.M. Bender and C.J. Murphy, Dependence of the gold nanorod aspect ratio on the nature of the directing surfactant in aqueous solution. Langmuir, 2003.

19: 9065.

[80] Y. Sun and Y. Xia, Shape-controlled synthesis of gold and silver nanoparticles. Science, 2002. **298**: 2176.

[81] S.-S. Chang, C.-W. Shih and C.-D. Chen, *The shape transition of gold nanorods.* Langmuir, 1999. **15**: 701.

[82] H.-Y. Wu, H.-C. Chu, T.-J. Kuo, C.-L. Kuo and M.H. Huang, *Seed-mediated synthesis of high aspect ratio gold nanorods with nitric acid.* Chemistry of Materials, 2005. **17**: 6447.

[83] D.A. Zweifel and A. Wei, *Sulfide-arrested growth of gold nanorods.* Chemistry of Materials, 2005. **17**: 4256.

[84] M.J. Tierney and C.R. Martin, *Transparent metal microstructures* Journal of Physical Chemistry, 1989. **93**: 2878.

[85] C.R. Martin, *Membrane-based synthesis of nanomaterials.* Chemistry of Materials, 1996. **8**: 1739.

[86] B.M.I.V.D. Zande, M.R. Bohmer, L.G.J. Fokkink and C. Schonenberger, *Aqueous gold sols of rod-shaped particles.* Journal of Physical Chemistry B, 1997. **101**: 852.

[87] S. Matthias, J. Schilling, K. Niellsch, F. Muller, R.B. Wehrspohn and U. Gosele, *Monodisperse diameter-modulated gold microwires.* Advanced Materials, 2002. **14**: 1618.

[88] M. Liu and P. Guyot-Sionnest, *Synthesis and optical characterization of Au/Ag core/shell nanorods.* Journal of Physical Chemistry B, 2004. **108**: 5882.

[89] M. Mandal, S. Kundu, S.K. Ghosh, S. Panigrahi, T.K. Sau, S.M. Yusuf and T. Pal, *Magnetite nanoparticles with tunable gold or silver shell.* Journal of Colloid and Interface Science, 2005. **286**: 187.

[90] T. Ung, L.M. Liz-Marzan and P. Mulvaney, *Optical properties of thin films of Au@SiO_2 particles.* Journal of Physical Chemistry B, 2001. **105**: 3441.

[91] L. Wang, J. Luo, Q. Fan, M. Suzuki, I.S. Suzuki, M.H. Engelhard, Y. Lin, N. Kim, J.Q. Wang and C.-J. Zhong, *Monodispersed core-shell Fe_3O_4@Au nanoparticles.* Journal of Physical Chemistry B, 2005. **109**: 21593.

[92] J. Lin, W. Zhou, A.Kumbhar and J. Wiemann, Gold-coated iron (Fe@Au) nanoparticles: Synthesis, characterization, and magnetic field-induced self-assemble. Journal of Solid State Chemistry, 2001. **159**: 26.

[93] H. Wang, D.W. Brandl, F. Le, P. Nordlander and N.J. Halas, *Nanorice: A hybrid plasmonic nanostructure.* Nano Letters, 2006. **6**: 827.

[94] M.T. Reetz and W. Helbig, *Size-selective synthesis of nanostructured transition metal clusters.* Journal of American Chemistry Society, 1994. **116**: 7401

[95] Y.-Y. Yi, S.-S. Chang, C.-L. Lee and C.R.C. Wang, *Gold nanorods: Electrochemical synthesis and optic.* Journal of Physical Chemistry B, 1997. **101**: 6661.

[96] J.H. Song, F. Kim, D. Kim and P. Yang, Crystal overgrowth on gold nanorods: Tuning the shape, facet, aspect ratio, and composition of the nanorods. Chemistry A– European Journal. **11**: 910

[97] H. Yao, T. Onishi, S. Sato and K. Kimura, *High aspect ratio gold nanorods grown normal to high-energy surfaces.* Chemistry Letters, 2002. **4**: 458.

[98] C.-D. Chen, Y.-T. Yeh and C.R.C. Wang, *The fabrication and photoinduced melting of networked gold nanostructures and twisted gold nanorods.* Journal of

Physics and Chemistry of Solids, 2001. **62**: 1587.

[99] F. Kim, J.H. Song and P. Yang, *Photochemical synthesis of gold nanorods.* Journal of the American Chemical Society, 2002. **124**: 14316.

[100] O.R. Miranda and T.S. Ahmadi, *Effects of intensity and energy of CW UV light on the growth of gold nanorods.* Journal of Physical Chemistry B, 2005. **109**: 15724.

[101] Y. Niidome, K. Nishioka, H. Kawasaki and C.J. Murphy, Rapid synthesis of gold nanorods by the combination of chemical reduction and photoirradiation process morphological changes depending on the growing process. Chemical Communications, 2003: 2376.

[102] Y.-J. Zhu and X.-L. Hu, Microwave-polyol preparation of single-crystalline gold nanorods and nanowires. Chemistry Letters, 2003. **32**: 1140.

[103] F.-K. Liu, Y.-C. Chang, F.-H. Ko and T.-C. Chu, *Microwave rapid heating for the synthesis of gold nanorods.* Materials Letters, 2004. **58**: 373.

[104] G. Canizal, J.A. Ascencio, G.-T. J. and M.J. Yacaman, *Multiple twinned gold nanorods grown by bio-reduction techniques.* Journal of Nanoparticle Research, 2001. **3**: 475.

[105] J. Perez-Juste, I. Pastoriza-Santos, L.M. Liz-Marzan and P. Mulvaney, *Gold nanorods: Synthesis, characterization and applications.* Coordination Chemistry Reviews, 2005. **249**: 1870.

[106] A.M. Gole, C. Sathivel, A. Lachke and M. Sastry, *Size separation of colloidal nanoparticles using a miniscale isoelectric focusing technique.* Journal of Chromatography A, 1999. **848**: 485.

[107] M.E. Cates and S.J. Candau, *Statics and dynamics of worm-like surfactant micelles.* Journal of Physics: Condensed Matter, 1990. **2**: 6869.

[108] Z. Wei and F.P. Zamborini, Directly monitoring the growth of gold nanoparticle seeds into gold nanorods. Langmuir, 2004. **20**: 11301.

[109] B. Nikoobakht and M.A. El-Sayed, Evidence for bilayer assembly of cationic surfactants on the surface of gold nanorods. Langmuir, 2001. **17**: 6368.

[110] Z.L. Wang, M.B. Mohamed, S. Link and M.A. El-Sayed, *Crystallographic facets and shapes of gold nanorods of different aspect ratios.* Surface Science, 1999. **440**: L809.

[111] Z.L. Wang, R.P. Gao, B. Nikoobakht and M.A. Ei-Sayed, *Surface reconstruction of the unstable {110} surface in gold nanorods.* Journal of Physical Chemistry B, 2000. **104**: 5417.

[112] J. Yacaman, M. Ascencio and J.A. Canizal, Observation of surface relaxation, surface steps and surface reconstruction in gold nanorods. Surface Science, 2001. **486**: L449.

[113] P.Z. Coura, S.B. Legoas, A.S. Moreira, F. Sato, V. Rodrigues, S.C.O. Dantas, D. Ugarte and D.S. Galva, *On the structural and stability features of linear atomic suspended chains formed from gold nanowires stretching.* Nano Letters, 2004. **4**: 1187.

[114] S. Link, C. Burda, B. Nikoobakht and M.A. El-Sayed, How long does it take to melt a gold nanorod? A femtosecond pumb-probe absorption spectroscopic study. Chemical Physics Letters, 1999. **315**: 12.

[115] S. Link, Z.L. Wang and M.A. El-Sayed, *How does a gold nanorod melt.* Journal of Physical Chemistry B, 2000. **104**: 7867.

[116] H. Takahashi, Y. Niidome, T. Sato and S. Yamada, Effects of capping thiols on

the laser-induced fusion of gold nanoparticles and deposition onto glass substrates in cyclohexane. Colloids and Surfaces A: Physicochemical Engineering Aspects, 2004. **247**: 105.

[117] S. Mandal, P. Selvakannan, S. Phadtare, R. Pasricha and M. Sastry, *Synthesis of a stable gold hydrosol by the reduction of chloroaurate ions by the amino acid, aspartic acid.* Proceeding of Indian Academic Science (Chemical Science), 2002. **114**: 513.

[118] M.B. Mohamed, K.Z. Ismail, S. Link and M.A. Ei-Sayed, *Thermal reshaping of gold nanorods in micelles.* Journal of Physical Chemistry B, 1998. **102**: 9370.

[119] A. Al-Sherbini, *Thermal instability of gold nanorods in micellar solution of water/glycerol mixture.* Colloids and Surfaces A: Physicochemical Engineering Aspects, 2004. **246**: 61.

[120] Y. Wang and C. Dellago, Structural and morphological transitions in gold nanorods: A computer simulation study. Journal of Physical Chemistry B, 2003. **107**: 9214.

[121] J. Perez-Juste, M.A. Correa-Duarte and L.M. Liz-Marzan, *Silica gels with tailored, gold nanorod-driven optical functionalities.* Applied Surface Science, 2004. **226**: 137.

[122] Y. Huang, X. Duan, Y. Cui, L.J. Lauhon, K.-H. Kim and C.M. Lieber, *Logic gates and computation from assembled nanowire building blocks.* Science, 2001. **294**: 1313.

[123] H. Zhu, C. Tao, S. Zheng, S. Wu and J. Li, *Effect of alkyl chain length on phase transfer of surfactant capped Au nanoparticles across the water/toluene interface.* Colloids and Surfaces A: Physicochemical Engineering Aspects, 2005. **256**: 17.

[124] T. Ohgi, H.-Y. Sheng and H. Nejoh, *Au particle deposition onto self-assembled monolayers of thiol and dithiol molecules.* Applied Surface Science, 1998. **130–132**: 919.

[125] G.-T. Wei, Z. Yang, C.-Y. Lee, H.-Y. Yang and C.R.C. Wang, *Aqueous-organic phase transfer of gold nanoparticles and gold nanorods using an ionic liquid.* Journal of American Chemistry Society, 2004. **126**: 5036.

[126] O.-H. Kwon, S. Lee and D.-J. Janga, Mesoscopic linear alignment and thermal-relaxation dynamics of aggregated gold nanorods. European Physics Journal D, 2005. **34**: 243.

[127] E. Dujardin, L.-B. Hsin, C.R.C. Wang and S. Mann, *DNA-driven self-assembly of gold nanorods.* Chemical Communications, 2001: 1264.

[128] J.K.N. Mbindyo, B.D. Reiss, B.R. Martin, C.D. Keating, M.J. Natan and T.E. Mallouk, *DNA-directed assembly of gold nanowires on complementary surfaces.* Advanced Materials, 2001. **13**: 249.

[129] Y. Niidome, H. Takahashi, S. Urakawa, K. Nishioka and S. Yamada, *Immobilization of gold nanorods on the glass substrate by the electrostatic interactions.* Chemistry Letters, 2004. **33**: 454.

[130] J. Liao, Y. Zhang, W. Yu, L. Xu, C. Ge, J. Lin and N. Gua, *Linear aggregation of gold nanoparticles in ethanol.* Colloids and Surface A: Physicochemical and Engineering Aspects, 2003. **223**: 177.

[131] C.J. Orendorff, P.L. Hankins and C.J. Murphy, *pH-triggered assembly of gold nanorods.* Langmuir, 2005. **21**: 2022.

[132] S.K.S. Angelo, C.C. Waraksa and T.E. Mallouk, *Diffusion of gold nanorods on*

chemically functionalized surfaces. Advanced Materials, 2003. **15**: 400.

[133] A. Gole, C.J. Orendorff and C.J. Murphy, Immobilization of gold nanorods onto acid-terminated self-assembled monolayers via electrostatic interactions. Langmuir, 2004. **20**: 7117.

[134] A. Gole and C.J. Murphy, Polyelectrolyte-coated gold nanorods: Synthesis, characterization and immobilization. Chemistry of Materials, 2005. **17**: 1325.

[135] K.K. Caswell, J.N. Wilson, U.H.F. Bunz and C.J. Murphy, *Preferential end-to-end assembly of gold nanorods by biotin-streptavidin connectors.* Journal of American Chemistry Society, 2003. **125**: 13914.

[136] D. Chen and L. Gao, Large-scale growth and end-to-end assembly of silver nanorods by PVP-directed polyol process. Journal of Crystal Growth, 2004. **264**: 216.

[137] J.-Y. Chang, H. Wu, H. Chen, Y.-C. Lingb and W. Tan, *Oriented assembly of Au nanorods using biorecognition system.* Chemical Communications, 2005: 1092.

[138] N.R. Jana, L.A. Gearheart, S.O. Obare, C.J. Johnson, K.J. Edler, S. Mann and C.J. Murphy, *Liquid crystalline assemblies of ordered gold nanorods.* Journal of Materials Chemistry, 2002. **12**: 2909.

[139] K.G. Thomas, S. Barazzouk, B.I. Ipe, S.T.S. Joseph and P.V. Kamat, *Uniaxial plasmon coupling through longitudinal self-assembly of gold nanorods.* Journal of Physical Chemistry B, 2004. **108**: 13066.

[140] S. Ravaine, R. Saliba, C. Mingotaud and F. Argoul, *Control of the morphology of gold deposits grown at the gas/liquid interface.* Materials Science and Engineering C, 2002. **C22**: 209.

[141] N. Taub, O. Krichevski and G. Markovich, *Growth of gold nanorods on surfaces.* Journal of Physical Chemistry B, 2003. **107**: 11579.

[142] Z. Wei, A.J. Mieszawska and F.P. Zamborini, Synthesis and manipulation of high aspect ratio gold nanorods grown directly on surfaces. Langmuir, 2004. **20**: 4322.

[143] A.J. Mieszawska and F.P. Zamborini, *Gold nanorods grown directly on surfaces from microscale patterns of gold seeds.* Chemistry of Materials, 2005. **17**: 3415.

[144] S. Hsieh, S. Meltzer, C.R.C. Wang, A.A.G. Requicha, M.E. Thompson and B.E. Koel, *Imaging and manipulation of gold nanorods with an atomic force microscope.* Journal of Physical Chemistry B, 2002. **106**: 231.

[145] M.M. Alvarez and J.T. Khoury, *Optical absorption spectra of nanocrystal gold molecules.* Journal of Physical Chemistry B, 1997. **101**: 3706.

[146] S. Link, M.B. Mohamed and M.A. El-Sayed, Simulation of the optical absorption spectra of gold nanorods as a function of their aspect ratio and the effect of the medium dielectric constant. Journal of Physical Chemistry B, 1999. **103**: 3073.

[147] S. Link and M.A. El-Sayed, *Addition and correction for 103B.* Journal of Physical Chemistry B, 2005. **109**: 10531.

[148] B. Yan, Y. Yang and Y. Wang, Comment on "Simulation of the optical absorption spectra of nanorods as a function of their aspect ratio and the effect of the medium dielectric constant". Journal of Physical Chemistry B, 2003. **107**: 9159.

[149] J. Zhu, L. Huang, J. Zhao, Y. Wang, Y. Zhao, L. Hao and Y. Lu, *Shape dependent resonance light scattering properties of gold nanorods.* Materials Science and Engineering B, 2005. **121**: 199.

[150] A. Brioude, X.C. Jiang and M.P. Pileni, *Optical properties of gold nanorods:*

DDA simulations supported by experiments. Journal of Physical Chemistry B, 2005. **109**: 13138.

[151] O. Seitz, M.M. Chehimi, E. Cabet-Deliry, S.P. Truong, N. Felidj, C. Perruchot, S.J. Greaves and J.F. Watts, *Preparation and characterisation of gold nanoparticle assemblies on silanised glass plates* Colloids and Surface A: Physicochemical and Engineering Aspects, 2003. **218**: 225.

[152] S.L. Westcott, S.J. Oldenburg, T.R. Lee and N.J. Halas, Formation and adsorption of clusters of gold nanoparticles onto functionalized silica nanoparticle surfaces. Langmuir, 1998. **14**: 5396.

[153] B.M. Luce, *Electroless plating of gold,* 1967. US Patent 3300328.

[154] D.K. Breitinger and W.A. Herrmann, *Synthetic Methods of Organometallic and Inorganic Chemistry*. Vol. 5. 1999, New York: George Thieme Verlag, Stuttgart.

[155] H. Schmidhauer, *Gold: Progress in Chemistry, Biochemistry and Technology*. 1999, Chichester: John Wiley and Sons.

[156] A.C. Fischer-Cripps, *Nanoindentation*. 2002, New York: Springer.

[157] B. Bechtloff, P. Justen and J. Ulrich, The kinetics of heterogeneous solid-liquid reaction crystallizations: An overview and examples. Chemie Ingenieur Technik, 2001. **73**: 453.

[158] W.W. Gerberich and A.A. Volinsky, *Thin Film Adhesion by Nanoindentation-Induced Superlayers.* Project Report, http://www.osti.gov, 2001.

[159] Anonymous, Sample Analysis Report NRL-D-054. Hysitron Inc.

[160] C.F. Bohren and D.R. Huffman, *Absorption and Scattering of Light by Small Particles*. 1998, New York: Wiley-Interscience.

[161] J. Turkevich, Colloidal gold. Part II. Color, coagulation, adhesion, alloying and catalytic properties. Gold Bulletin, 1985. **18**: 125.

[162] Z.X. Liu, H. Wang and H. Li, Redshift of plasmon resonace frequency due to the interacting Ag nanoparticles embedded in single crystal SiO_2 by implantation. Applied Physics Letters, 1998. **72**: 1823.

[163] S.A. Maier, P.G. Kik and H.A. Atwater, Observation of coupled plasmon-polariton modes in Au nanoparticle chain waveguides of different lengths: Estimation of waveguide loss. Applied Physics Letters, 2002. **81**: 1714.

[164] L. Genzel and T.P. Martin, Infrared absorption by surface phonons and surface plasmons in small crystals. Surface Science, 1973. **34**: 33.

[165] G.B. Smith, University of Technology Sydney, Personal Communication, July, 2003.

[166] W. Rechberger, A. Hohenau, A. Leitner, J.R. Krenn and B. Lamprecht, *Optical properties of two interacting gold nanoparticles.* Optics Communications, 2003. **220**: 137.

[167] K. Gall, J. Diao and M.L. Dunn, *The strength of gold nanowires.* Nano Letters, 2004. **4**: 2431.

[168] M. Hu, P. Hillyard, G.V. Hartland, T. Kosel, J. Perez-Juste and P. Mulvaney, *Determination of the elastic constants of gold nanorods produced by seed mediated growth.* Nano Letters, 2004. **4**: 2493.

[169] T.-H. Fang, W.-J. Chang and C.-M. Lin, *Nanoindentation and nanoscratch characteristics of Si and GaAs.* Microelectronic Engineering, 2005. **77**: 389.

[170] W. Tanga, L. Shen and K. Xu, Hardness and elastic modulus of Au/Ni/Cr/Ta multilayers on Al_2O_3 substrate by nanoindentation continuous stiffness

measurement technique. Thin Solid Films, 2005. **485**: 72.

[171] P.J. Burnett and D.S. Rickerby, *The scratch adhesion test: An elastic-plastic indentation analysis* Thin Solid Films, 1988. **157**: 233.

[172] P.J. Burnett and D.S. Rickerby, *The relationship between hardness and scratch adhession.* Thin Solid Films, 1987. **154**: 403.

[173] M.F. Ashby and D.R.H. Jones, *Engineering Materials 2: An Introduction to Microstructures, Processing and Design*. International series on materials science and technology. Vol. 39. 1986, Oxford: Pergamon Press.

[174] H. Chowdhury, X. Xu, P. Huynh and M.B. Cortie, *Radiative heat transfer across glass coated with gold nano-particles,.* ASME Journal of Solar Energy Engineering, 2005. **127**: 70.

[175] S. Chaudhuri, D. Bhattacharyya and A.B. Maity, *Surface coatings for solar application.* Materials Science Forum, 1997. **246**: 181.

[176] M. Cortie, X. Xu, H. Zareie, H. Chowdhury and G. Smith. Plasmonic heating of gold nanoparticles and its exploitation. Smart Materials, Nano-, and Micro-Smart Systems II. 2005. Sydney, Australia.

[177] J. Christoffersen and M.R. Christoffersen, *A revised theory for the growth of crystals by surface nucleation.* Journal of Crystal Growth, 1992. **121**: 608.

[178] H.K. Jang, Y.D. Chung and S.W. Whangbo, *Effects of chemical etching with sulfuric acid on glass surface.* Journal of Vacuum Science and Technology, A, 2000. **18**: 401.

[179] H. Niederprum, H.G. Klein and J.-N. Meussdoerffer, *Etching glass with HF and fluorine-containing surfactant,* 1977. US Patent 4055458.

[180] T. Nomura, Y. Kousaka and M. Fukunaga, *A model for simultaneous homogeneous and heterogeneous nucleation in the case of slow reaction rate.* Journal of Colloid and Interface Science, 2000. **221**: 195.

[181] T. Nomura, M. Alonso, Y. Kousaka and K. Tanaka, *A model for simultaneous homogeneous and heterogeneous nucleation.* Journal of Colloid and Interface Science, 1998. **203**: 170.

[182] M.A. Henderson, The interaction of water with solid surfaces: Fundamental aspects revisited. Surface Science Reports, 2002. **46**: 1.

[183] Z. Kozisek, P. Demo and K. Sato, *Nucleation on active sites: Evolution of size distribution.* Journal of Crystal Growth, 2000. **209**: 198.

[184] A.L. Greer, P.V. Evans, R.G. Hamerton and D.K. Shangguan, *Numerical modelling of crystal nucleation in glasses.* Journal of Crystal Growth, 1990. **99**: 38.

[185] M.J. Stowell, *The initial stages of thin films growth.* Journal of Crystal Growth, 1974. **24/25**: 45.

[186] I. Markov and D. Kashchiev, *Nucleation on active centres: I General theory.* Journal of Crystal Growth, 1972. **16**: 170.

[187] B. Kim, S.L. Tripp and A. Wei, *Tuning the optical properties of large gold nanoparticle arrays.* Materials Research Society Symposium Proceeding, 2001. **676**: Y6.1.1.

[188] A.W. Adamson and A.P. Gast, *Physical Chemistry of Surfaces*. 6th ed. 1997, New York: John Wiley & Sons, Inc.

[189] R.C. Weast, *Handbook of Chemistry and Physics*. 56th ed. 1975, Cleveland, Ohio: CRC Press.

[190] V. Salgueirino-Maceira, F. Caruso and L.M. Liz-Marzan, *Coated colloids with tailored optical properties.* Journal of Physical Chemistry B, 203. **107**: 10990.

[191] M. Quinten, *Optical effects associated with aggregates of clusters.* Journal of Cluster Science, 1999. **10** 319.

[192] M. Schmeits and L. Dambly, *Fast-electron scattering by bispherical surface-plasmon modes.* Physical Review B, 1991. **44**: 12706.

[193] H. Wang, G.P. Goodrich, F. Tam, C. Oubre, P. Nordlander and N.J. Halas, *Controlled texturing modifies the surface topography and plasmonic properties of Au nanoshells.* Journal of Physical Chemistry B, 2005. **109**: 11083.

[194] N. Kaiser and H.K. Pulker, *Optical Interference Coatings*. 2003, Berlin: Springer.

[195] O.S. Heavens, *Thin Film Physics*. 1970, London: Methuen & Co. Ltd.

[196] Y.T. Lim, O.O. Park and H.-T. Jung, Gold nanolayer-encapsulated silica particles synthesized by surface seeding and shell growing method: Near infrared responsive materials. Journal of Colloid and Interface Science, 2003. **263**: 449.

[197] C.L. Nehl, N.K. Grady, G.P. Goodrich, F. Tam, N.J. Halas and J.H. Hafner, *Scattering spectra of single gold nanoshells.* Nano Letters, 2004. **4**: 2355.

[198] C. So1nnichsen and A.P. Alivisatos, Gold nanorods as novel nonbleaching plasmon-based orientation sensors for polarized single-particle microscopy. Nano Letters, 2005. **5**: 301.

[199] L. Lu, H. Wang, Y. Zhou, S. Xi, H. Zhang, J. Hub and B. Zhao, Seed-mediated growth of large, monodisperse core–shell gold–silver nanoparticles with Ag-like optical properties. Chemical Communications, 2002 144.

[200] Y. Kim, R.C. Johnson and J.T. Hupp, Gold nanoparticle-based sensing of "spectroscopically silent" heavy metal ions. Nano Letters, 2001. **1**: 166.

[201] A. Yu, Z. Liang, J. Cho and F. Caruso, Nanostructured electrochemical sensor based on dense gold nanoparticle films. Nano Letters, 2003. **3**: 1203.

[202] H. Liao and J.H. Hafner, *Gold nanorod bioconjugates.* Chemistry of Materials, 2005. **17**: 4636.

[203] I.H. El-Sayed, X. Huang and M.A. El-Sayed, Surface plasmon resonance scattering and absorption of anti-EGFR antibody conjugated gold nanoparticles in cancer diagnostics: Applications in oral cancer. Nano Letters, 2005. **5**: 829.

[204] S.O. Obare, N.R. Jana and C.J. Murphy, Preparation of polystyrene- and silica-coated gold nanorods and their use as templates for the synthesis of hollow nanotubes. Nano Letters, 2001. **1**: 601.

[205] N.R. Jana, Gram-scale synthesis of soluble, near-monodisperse gold nanorods and other anisotropic nanoparticles. Small, 2005 **1**: 875.

[206] B.T. Draine and P.J. Flatau, *Discrete-dipole approximation for scattering calculations.* Journal of Optical Society American A, 1994. **11**: 1491.

[207] B.T. Draine, *User Guide for the Discrete Dipole Approximation Code DDSCAT.6.0.* http://arxiv.org/abs/astro-ph/0309069, 2003.

[208] P.B. Johnson and R.W. Christy, *Optical constant of the noble metals.* Physical Review B, 1970. **6**: 4370.

[209] M. Robert, *The CIE Colour System.* http://www.cs.bham.ac.uk/.

[210] M. Cortie, X. Xu and M. Ford, Effect of composition and packing configuration on the dichroic optical properties of coinage metal nanorods. Physical Chemistry Chemical Physics, 2006. **8**: 3520

[211] B.Q. Li and J.M. Zuo, Self-assembly of epitaxial Ag nanoclusters on H-

terminated SiN (111) surfaces. Journal of Applied Physics, 2003. **94**: 743.

[212] M. Liu and P. Guyot-Sionnest, *Mechanism of silver (I) assisted growth of gold nanorods and bipyramids.* Journal of Physical Chemistry B, 2005. **109**: 22192.

[213] T. Pal, S. De, N.R. Jana, N. Pradhan, R. Mandal, A. Pal, A.E. Beezer and J.C. Mitchell, *Organized media as redox catalysts.* Langmuir, 1998. **14**: 4724.

[214] R.J. Hunter, *Introduction to Modern Colloid Science*. 1993, Oxford: Oxford University Press.

[215] S. Budavari and M.J. O'Neil, The Merck Index: An Encyclopaedia of Chemicals, Drugs and Biologicals. 11th ed. 1989: Merck & Co.

[216] C.M. Aguirre, T.R. Kaspar, C. Radloff and N.J. Halas, *CTAB mediated reshaping of metallodielectric nanoparticles.* Nano Letters, 2003. **3**: 1707.

[217] R.J. Hunter, *Foundations of Colloid Science*. 2nd ed. 2001, Oxford; New York: Oxford University Press.

[218] S. Matzinger, D.M. Hussey and M.D. Fayer, Fluorescent probe solubilization in the headgroup and core regions of micelles: fluorescence lifetime and orientational relaxation measurements. Journal of Physical Chemistry B, 1998. **102**: 7216.

[219] F. Reiss-Husson and V. Luzzati, The structure of the micellar solutions of some amphiphilic compounds in pure water as determined by absolute small-angle X-ray scattering techniques. Journal of Physical Chemistry, 1964. **68**: 3504.

[220] U. Henriksson, Lars Odberg, J.C. Eriksson and L. Westmant, Nitrogen-14 nuclear magnetic relaxation in aqueous micellar solutions of n-hexadecyltrimethylammonium bromide and chloride. Journal of Physical Chemistry, 1977. **81**: 76.

[221] N.K. Raman, M.T. Anderson and C.J. Brinker, *Template-based approaches to the preparation of amorphous, nanoporous silicas.* Chemistry of Materials, 1996. **8**: 1682.

[222] D. Attwood and A.T. Florence, *Surfactant Systems: Their Chemistry Pharmacy and Biology*. 1983, London: Chapman and Hall.

[223] E. Koglin, A. Tarazona, S. Kreisig and M.J. Schwuger, *In-situ investigations of coadsorbed cationic surfactants on charged surfaces: a SERS microprobe study.* Colloids and Surface A: Physicochemical and Engineering Aspects, 1997. **123–124**: 523.

[224] X. Xu, M.B. Cortie and M. Stevens, *Effect of glass pre-treatment on the nucleation of semi-transparent gold coatings.* Materials Chemistry and Physics, 2005. **94**: 266.

[225] G.S. Me´Traux, Y.C. Cao, R. Jin and C.A. Mirkin, *Triangular nanoframes made of gold and silver.* Nano Letters, 2003. **3**: 519.

[226] C.L. Nehl, H. Liao and J.H. Hafner, *Optical properties of star-shaped gold nanoparticles.* Nano Letters, 2006. **6**: 683.

[227] E. Hao, R.C. Bailey, G.C. Schatz, J.T. Hupp and S. Li, *Synthesis and optical properties of "branched" gold nanocrystals.* Nano Letters, 2004. **4**: 327.

[228] M. Steinhart, Z. Jia and A.K. Schaper, *Palladium nanotubes with tailored wall morphologies.* Advanced Materials, 2003. **15**: 706.

[229] B. Nikoobakht, Z.L. Wang and M.A. El-Sayed, *Self-assembly of gold nanorods.* Journal of Physical Chemistry B, 2000. **104**: 8635.

[230] M.B. Cortie, *The weird world of the nanoscale.* Gold Bulletin, 2004. **37**: 12.

[231] H. Bahlss and P. Wayne, *Method for applying metallic silver to a substrate,* 1976. US Patent 3983288.

[232] B.V. Sodervall and T. Lundeberg, *Deposition of silver layer on nonconducting substrate,* 1998. US Patent 5747178.

[233] Y. Wang, S. Teitel and C. Dellago, *Surface-driven bulk reorganization of gold nanorods.* Nano Letters, 2005. **5**: 2174.

[234] T.J. Norman, C.D. Grant, D. Magana, J.Z. Zhang, J. Liu, D. Cao, F. Bridges and A.V. Buuren, *Near infrared optical absorption of gold nanoparticle aggregates.* Journal of Physical Chemistry B, 2002. **106**: 7005.

[235] M.R. Beversluis and A. Bouhelier, Continuum generation from single gold nanostructres through near-field mediated intraband transitions. Physical Review B, 2003. **68**: 115433.

[236] C. Girardy and A. Dereuxz, *Near-field optics theories.* Reports on Progress in Physics, 1996. **59**: 657.

[237] M. Salerno, N. Felidj, J.R. Krenn, A. Leitner and F.R. Aussenegg, *Near-field optical response of a two-dimensiional grating of gold nanoparticles.* Physical Review B, 2001. **63**: 165422.

[238] A. Lewis, H. Taha, A. Strinkovski, A. Manevitch, A. Khatchatouriants, R. Dekhter and E. Ammann, *Near-field optics: From subwavelength illumination to nanometric shadowing.* Nature Biotechnology, 2003. **21**: 1378.

[239] R.M. Bakker, V.P. Drachev, H.-K. Yuan and V.M. Shalaev, *Enhanced transmission in near-field imaging of layered plasmonic structures.* Optics Express, 2004. **12**: 3701.

[240] A. Jalochat and C. Pieralli, *A scanning optical profilometer using the SNOM architecture.* Pure Apply Optics, 1994. **3**: 793.

[241] D. Bedeaux, *Optical Properties of Surfaces*. 2002, London: Imperial College Press.

[242] M.B. Cortie, A. McDonagh and P. Mulvaney, Devices having a variable optical property and processes of making such devices 2004 902439.

[243] Y.-L. Liu, H.-T. Lee, C.-C. Chang and L.-S. Kan, *Reversible folding of cysteine-rich metallothionein by an overcritical reaction path.* Biochemical and Biophysical Research Communication, 2003. **306**: 56.

[244] C.-C. Chang, Y.-C. Su, M.-S. Cheng and L.-S. Kan, *Protein folding by a quasi-static-like process: A first-order state transition.* Physical Review E, 2002. **66**: 621903.

9. Appendix 1: Application of classic nucleation theory

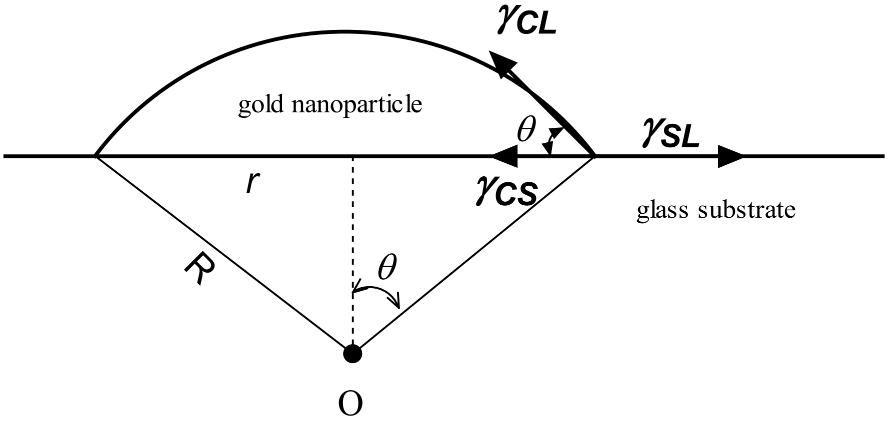

Appendix 1 Illustration of gold nucleus

For the cap-shaped particle of gold on the substrate, the interfacial energy between substrate and liquid (SL), crystal and substrate (CS), crystal and liquid (CL) must be in equilibrium, expressed by :

$$\gamma_{SL} = \gamma_{CS} + \gamma_{CL} \cdot \cos\theta \tag{1}$$

for the 0≤ θ≤ 90°, the contact area between crystal and liquid is:

$$A_{CL} = 2\pi R^2(1-\cos\theta) \tag{2}$$

the contact area between crystal and substrate is:

$$A_{CS} = 2\pi R^2(1-\cos^2\theta) \tag{3}$$

the volume for the nucleus (crystal) is:

$$V = \frac{2\pi R^3}{3}(1-\frac{3}{2}\cos\theta+\frac{1}{2}\cos^3\theta) \tag{4}$$

n gold atoms can form of such nuclei:

$$n' = \frac{2n}{(1-\frac{3}{2}\cos\theta+\frac{1}{2}\cos^3\theta)}\frac{r_{Au}^3}{R^3\beta} \tag{5}$$

in which :

$$R = \frac{r}{\sin\theta} \tag{6}$$

r is the measuring radius of the particle, β is the packing density of the gold atoms in the nucleus. r_{Au} is the radius of gold atoms.

For spherical caps of n gold atoms, the reversible work of formation is given by:

$$\Delta G_n = n\Delta G' + \sum A_i \gamma_i \tag{7}$$

when we substitute these results in

$$\Delta G_n = n\Delta G' + n'(A_{CS}\gamma_{CS} - A_{CS}\gamma_{SL} + A_{CL}\gamma_{CL}) \tag{8}$$

it gives:

$$\Delta G_n = n\Delta G' + \frac{f(\theta)\gamma_{CL}}{\beta \cdot r} \cdot 2n\pi r_{Au}^3 \tag{9}$$

$$f(\theta) = \frac{(2+\cos\theta)(1-\cos\theta)^2 \cdot \sin\theta}{1 - \frac{3}{2}\cos\theta + \frac{1}{2}\cos^3\theta} \tag{10}$$